Interventional Systems Neuroscience Group
Imperial College of Science, Technology and Medicine
Department of Brain Sciences

Biophysical investigation of temporal interference neuromodulation

---

Charlotte Emily Luff

Submitted in part fulfilment of the requirements for the degree of
Doctor of Philosophy
in
Clinical Medicine Research
and the Diploma of Imperial College,
January 2022

Abstract

Temporal Interference (TI) stimulation is a non-invasive deep brain stimulation technique that has promise for treating brain diseases caused by aberrant neural activity. During TI, two high frequency electric fields are applied to the brain. These fields differ in frequency by a small amount termed the difference frequency. Neurons are stimulated at the difference frequency, however, it has not been determined how this occurs. The mechanism of action of TI is currently unknown, and elucidation of this is pivotal for development of the technique. In this thesis, I present work that probes the mechanisms of TI stimulation, and the nonlinear processes underlying it. Additionally, I investigate whether these processes are present in endogenous neural activity.

I investigated the mechanism and parameter space of TI stimulation. I found that a neural frequency conversion process that originates at the single neuron membrane, is occurring during stimulation, resulting in subthreshold polarisation at the difference frequency. This nonlinear frequency conversion occurs at a wide range of applied frequencies, suggesting that it is being mediated by Frequency Mixing (FM). The strength of this nonlinear process and thus the strength of TI stimulation, is dependent on the applied frequency, but not on the difference frequency. Additionally, I found that the strength of TI stimulation is dependent on the summed amplitude of the applied currents. These findings aid in the elucidation of the mechanisms by which TI exerts its effects, which may help development of the technique, and have implications for the focality of the stimulation.

Additionally, I investigated the presence of FM in endogenous neural activity by testing a new methodology for detection of FM via a three-way phase relationship between the signals involved. I found evidence for this nonlinear process in human cortical activity. I suggest that it may be disturbed in Traumatic Brain Injury (TBI), where large-scale functional networks are disrupted.

Lastly, I validated a novel technique for non-invasive deep brain stimulation called Pulse-Width Modulated-Temporal Interference (PWM-TI). I found that PWM-TI can effectively stimulate neurons at the difference frequency, with comparable efficiency to traditional TI.

Acknowledgements

I would like to express my sincere gratitude to the following people:

To my supervisor Dr Nir Grossman. Thank you for your continued support and guidance throughout the last four years. It has been a privilege to be your first PhD student, and complete this chapter of my journey as a scientist under your mentorship. I especially appreciate your patience during all of the late night physics lessons.

To Professor Edward Boyden. Thank you for your guidance during my time as a transient member of the Synthetic Neurobiology lab. Additionally, thank you to Dr Ho-Jun Suk for taking me under your wing.

To my parents David and Marian. Thank you for providing the foundations from which I am able to grow as a scientist and a person. You have made everything I have achieved up to this point possible with your love and support.

To my sister Mel. Thank you for your unwavering love and encouragement, especially throughout the last four years. Achieving anything seems possible with the support of my best friend. Thank you also to Louis, for your support, and for providing your home as a peaceful place from which I could work.

To all of my closest friends, Jane, Cerys, Alexi, Ryan, Ben, Jamie, Kyle, Kara, Phil, Sean and Nico. Thank you for the adventures, the laughs, and all the things that make life great.

To all of the Interventional Systems Neuroscience team, and my colleagues within the UK DRI. Thank you for the inspiration and help with experiments.

To my colleagues and friends: Pat, Kety, Matteo, Eddy, Marieke, and Nawal. Thank you for your support during the challenging times, and for making the ISN lab a fun and exciting place to work the rest of the time.

To the amazing global community of scientists on "science twitter", who readily shared their knowledge every time I encountered an obstacle in my research.

Finally, to Mother Nature. Thank you for providing the peace and clarity to quieten even the busiest PhD student's mind.

Statement of Publications

The data in Chapters 3 and 4 are being prepared for submission to Cell.

The data in Chapter 5 are being prepared for submission to Brain Stimulation.

Statement of Originality

The novel computational method for three-way phase detection, as well as the analysis pipeline for this, (outlined in Chapter 2 and deployed in Chapter 4) was developed by Dr Robert Peach.

All human Electroencephalography (EEG) data (presented in Chapter 4), was collected by Dr Emma Jane Mallas. The EEG data was supplied for analysis by myself.

All other work contained in this thesis is my own and conforms to the rules and guidelines set out for PhD theses by Imperial College London.

Copyright Declaration

The copyright of this thesis rests with the author. Unless otherwise indicated, its contents are licensed under a Creative Commons Attribution-NonCommercial 4.0 International Licence (CC BY-NC).

Under this licence, you may copy and redistribute the material in any medium or format. You may also create and distribute modified versions of the work. This is on the condition that: you credit the author and do not use it, or any derivative works, for a commercial purpose.

When reusing or sharing this work, ensure you make the licence terms clear to others by naming the licence and linking to the licence text. Where a work has been adapted, you should indicate that the work has been changed and describe those changes.

Please seek permission from the copyright holder for uses of this work that are not included in this licence or permitted under UK Copyright Law.

Acronyms

AC Alternating Current.

aCSF Artificial Cerebrospinal Fluid.

AD Alzheimer's Disease.

AM Amplitude Modulation.

AP Action Potential.

BG Basal Ganglia.

CFC Cross-Frequency Coupling.

DA Dopaminergic.

DBS Deep Brain Stimulation.

DC Direct Current.

EEG Electroencephalography.

ET Essential Tremor.

FEM Finite Element Method.

FM Frequency Mixing.

GLM Generalised Linear Model.

GP Globus Pallidus.

GPe Globus Pallidus external.

GPi Globus Pallidus internal.

HEK Human Embryonic Kidney.

HOI Higher Order Interaction.

IPI Inter-Pulse Interval.

LFP Local Field Potential.

MCI Mild Cognitive Impairment.

OCD Obsessive Compulsive Disorder.

PAC Phase-Amplitude Coupling.

PD Parkinson's disease.

PPC Phase-Phase Coupling.

PSD Power Spectral Density.

PWM Pulse-Width Modulated.

PWM-TI Pulse-Width Modulated-Temporal Interference.

RC Resistor-Capacitor.

RKHS Reproducing Kernel Hilbert Space.

SNc Substantia Nigra pars Compacta.

STN Subthalamic Nucleus.

tACS Transcranial Alternating Current Stimulation.

TBI Traumatic Brain Injury.

tDCS Transcranial Direct Current Stimulation.

TES Transcranial Electrical Stimulation.

TI Temporal Interference.

TTX Tetrodotoxin.

List of Tables

3.1 **Frequencies of applied stimulation current waveforms** 56

3.2 **Nonlinear artefact across applied frequencies** 67

3.3 f_Σ **Nonlinear:linear artefact ratio** 67

3.4 Δ **Artefact-corrected normalised PSD at** f_Δ **and** f_Σ 71

3.5 **Artefact-corrected normalised PSD at** f_Δ **and** f_Σ 72

3.6 Δ **Normalised PSD at** f_Δ **and** f_Σ **(no stimulation)** 72

3.7 **Normalised PSD at** f_Δ **and** f_Σ **(no stimulation)** 73

3.8 Δ **Normalised PSD at** f_Δ 80

3.9 **Measures of neural frequency conversion strength when electric field strength is of constant amplitude across applied frequency** 81

3.10 **Repeated-measures ANOVA results for measures of neural frequency conversion strength when electric field strength is of constant amplitude across applied frequency** 81

3.11 **Post-hoc comparisons of measures of neural frequency conversion strength when electric field strength is of constant amplitude across applied frequency** 82

3.12 **Normalised threshold across difference frequency when electric field strength is of constant amplitude** 86

3.13 **Repeated-measures ANOVA results for normalised threshold when electric field strength is of constant amplitude across difference frequencies** 86

3.14 **Δ Normalised PSD at f_Δ** 92

3.15 **Normalised PSD at f_Δ** 93

3.16 **Δ Normalised PSD at f_Δ** 96

3.17 **Normalised PSD at f_Δ** 97

3.18 **Measures of temporal interference strength** 102

3.19 **Results of step-wise GLM for normalised threshold** 102

3.20 **Δ Normalised PSD at f_Δ** 103

4.1 **Correlation measures for HOI strength vs average band power** 129

5.1 **Envelope modulation depth** 158

5.2 **Δ PSD at f_Δ** 158

5.3 **Measures of temporal interference strength** 159

5.4 **Repeated measures ANOVA results for measures of temporal interference strength** 159

5.5 **Post-hoc comparisons of measures of temporal interference strength** . 160

List of Figures

1.1 **Principle of temporal interference non-invasive deep brain stimulation** 10

1.2 **Stimulation of a neuron by temporal interference non-invasive deep brain stimulation** 11

1.3 **The neuron as an electrical circuit** 19

2.1 **Schematic of *ex vivo* whole cell patch clamp setup with extracellular stimulation** 28

2.2 **Schematic of whole cell patch clamp equivalent circuit during voltage recording in the absence of injected current** 30

2.3 **Workflow for detection of significant three-way phase relationships** . . 37

2.4 **Testing three-way phase relationship methodology with synthetic data** 42

2.5 **Testing the robustness of frequency mixing detection** 43

3.1 **Schematic of potential temporal interference mechanisms** 54

3.2 **Schematic of applied amplitude modulated stimulation waveforms** . . . 57

3.3 **Schematic of fixed sum amplitude, fixed envelope amplitude, and fixed product waveforms** 58

3.4 **Characterisation of nonlinear stimulation artefact in recordings** 66

3.5 **Evoked neural frequency conversion in single neuron subthreshold activity during temporal interference stimulation** 70

3.6 **Evoked neural frequency conversion in single neuron subthreshold activity across a range of applied stimulation frequencies** 75

3.7 **Evoked neural frequency conversion in single neuron subthreshold activity across a range of applied stimulation frequencies cont.** 77

3.8 **Dependency of neural frequency conversion strength and temporal interference-induced neural activity on applied frequency** 83

3.9 **No dependency of neural frequency conversion strength and temporal interference-induced neural activity on difference frequency** 87

3.10 **Characterisation of the contribution of the neural network to neural frequency conversion** 91

3.11 **Characterisation of the contribution of tetrodotoxin-sensitive conductance to neural frequency conversion** 95

3.12 **Characterisation of the driving force of temporal interference stimulation** 100

4.1 **Detection of frequency mixing in spontaneous single neuron activity** . 123

4.2 **Characterisation of frequency mixing in spontaneous single neuron activity in the absence of tetrodotoxin-sensitive conductance and synaptic input** 126

4.3 **Detection of frequency mixing in spontaneous cortical activity in the healthy human brain** 130

4.4 **Characterisation of frequency mixing in spontaneous cortical activity in the healthy human brain** 131

4.5 **Characterisation of frequency mixing interactions that correlate with memory misbinding in the spontaneous brain activity of healthy and traumatic brain injury patients** 135

4.6 **Characterisation of frequency mixing interactions that correlate with sustained attention in the spontaneous brain activity of healthy and traumatic brain injury patients** 138

5.1 **Pulse-width modulated temporal interference waveform** 147

5.2 **Computational model schematics** 152

5.3 **Characterisation of pulse-width modulated temporal interference induced polarisation of a pyramidal neuron model, and comparison to traditional temporal interference stimulation** 156

5.4 **Passive neural membrane response to pulse-width modulated temporal interference-induced polarisation** 162

5.5 **Pulse-width modulated-temporal interference can stimulate single neurons at the difference frequency with comparable efficacy to traditional sinusoidal temporal interference** 166

Contents

Abstract i

Acknowledgements ii

Publications iii

Statement of Originality iv

Copyright Statement v

LIST OF ACRONYMS vi

LIST OF TABLES viii

LIST OF FIGURES xi

1 General Introduction 1

1.1 Electrical brain stimulation 1

1.1.1 Introduction to neural activity 1

1.1.2 Introduction to electrical brain stimulation 2

1.1.3 Non-invasive brain stimulation . . . 3
1.1.4 Invasive deep brain stimulation . . . 7
1.1.5 Non-invasive deep brain stimulation . . . 9
1.2 Electrical brain stimulation at the single cell . . . 15
1.2.1 The neuron as an equivalent circuit . . . 15
1.2.2 Nonlinearity in electrical circuits . . . 16
1.2.3 Nonlinearity in neurons . . . 17
1.3 Frequency mixing . . . 19
1.3.1 Introduction to frequency mixing . . . 19
1.3.2 Evidence of frequency mixing in neural activity . . . 20
1.3.3 Cross-frequency coupling . . . 21
1.3.4 Frequency mixing in temporal interference . . . 22
1.4 Envelope Detection via rectification . . . 23
1.4.1 Introduction to envelope detection via rectification . . . 23
1.4.2 Envelope detection in temporal interference . . . 24
1.4.3 Summary . . . 24

2 Methods and Materials **25**

2.1 Overview . . . 25
2.2 Extracellular electrical stimulation . . . 26
2.2.1 Principles . . . 26
2.2.2 Mechanisms . . . 26

2.2.3 Application in this thesis 27

2.3 Whole cell patch clamp electrophysiology 29

2.3.1 Principles 29

2.3.2 Measuring membrane potential 29

2.3.3 Principles of data analysis 31

2.4 Electroencephalography 31

2.4.1 Principles 31

2.4.2 Measuring synchronous cortical neural activity 32

2.4.3 Analysis of recorded signals 33

2.5 Detecting frequency mixing using three-way phase relationships 34

2.5.1 Three-way phase relationship detection method 34

2.5.2 Methodology testing 37

3 Nonlinear frequency conversion at the single neuron 44

3.1 Introduction 44

3.1.1 Mechanism of temporal interference 44

3.1.2 Nonlinear frequency conversion by individual neurons 50

3.1.3 Nonlinear frequency conversion in subthreshold neural activity 51

3.1.4 Exploration of nonlinear frequency conversion and temporal interference parameter space 51

3.1.5 Characterisation of nonlinear stimulation and recording artefacts 52

3.1.6 Aims 53

3.2 Methods 53

3.2.1 *Ex-vivo* brain slice preparation 53

3.2.2 Electrical stimulation 55

3.2.3 Whole cell patch clamp recording 59

3.2.4 Pharmacology 59

3.2.5 Data analysis 60

3.3 Results 63

3.3.1 Characterisation of nonlinear stimulation artefact 63

3.3.2 Temporal interference evoked subthreshold neural oscillation at the difference frequency: evidence of neural frequency conversion 68

3.3.3 Neural subthreshold frequency conversion can be evoked across a broad range of frequencies 73

3.3.4 Strength of evoked neural subthreshold frequency conversion drops at higher stimulation frequencies 78

3.3.5 Strength of evoked neural subthreshold frequency conversion is dependent on applied frequency across a range of difference frequencies 80

3.3.6 Strength of evoked neural subthreshold frequency conversion does not depend on difference frequency 84

3.3.7 Evoked neural subthreshold frequency conversion is sustained under synaptic input block: evidence of a cell membrane origin 88

3.3.8 Evoked neural membrane subthreshold frequency conversion involves voltage-gated ion channels 93

3.3.9 Strength of temporal interference stimulation and neural frequency conversion is dependent on the summed amplitude of the applied stimulating electric fields . . . 97

3.4 Discussion . . . 103

3.4.1 General discussion of results . . . 103

3.4.2 Limitations . . . 110

3.4.3 Future directions . . . 111

3.4.4 Conclusions . . . 112

4 Higher order nonlinear frequency interactions in spontaneous neural activity 113

4.1 Introduction . . . 113

4.2 Methods . . . 115

4.2.1 *Ex-vivo* brain slice preparation . . . 115

4.2.2 Whole cell patch clamp recording . . . 115

4.2.3 Participants . . . 115

4.2.4 Electroencephalogram acquisition . . . 116

4.2.5 Cognitive testing . . . 116

4.2.6 Detection of significant three-way phase relationships . . . 118

4.3 Results . . . 122

4.3.1 Three-way phase relationships indicative of frequency mixing are present in spontaneous neural activity detected at the single neuron . . . 122

4.3.2 Blockade of voltage-gated ion channels and synaptic input reduces frequency mixing strength in spontaneous neural activity detected at the single neuron . . . 124

4.3.3 Frequency mixing can be detected in large-scale spontaneous human cortical activity . . . 127

4.3.4 Frequency mixing is significantly different in spontaneous neural activity in traumatic brain injury compared to spontaneous neural activity in the healthy brain . . . 133

4.4 Discussion . . . 139

4.4.1 General discussion of results . . . 139

4.4.2 Limitations and future direction . . . 142

4.4.3 Conclusions . . . 144

5 Pulse-width modulated temporal interference: validation and mechanistic investigation 145

5.1 Introduction . . . 145

5.2 Methods . . . 148

5.2.1 *Ex-vivo* brain slice preparation . . . 148

5.2.2 Electrical stimulation . . . 148

5.2.3 Computational modelling . . . 149

5.2.4 Whole cell patch clamp recording . . . 150

5.2.5 Data analysis . . . 150

5.3 Results . . . 153

5.3.1 Pulse-width modulated temporal interference can evoke action potentials at the difference frequency in a model pyramidal neuron 153

5.3.2 The neuronal membrane interprets pulse-width modulated temporal interference as an amplitude modulated signal due to passive neuronal resistor-capacitor properties 160

5.3.3 Pulse-width modulated temporal interference produces neural polarisation at the difference frequency with similar efficiency to traditional temporal interference 163

5.4 Discussion 167

5.4.1 General discussion of results 167

5.4.2 Limitations 170

5.4.3 Future directions 171

5.4.4 Conclusions 173

6 General Discussion **175**

6.1 Overview of experimental chapters 175

6.1.1 Chapter 3 175

6.1.2 Chapter 4 176

6.1.3 Chapter 5 177

6.2 Implications 177

6.3 Future directions 179

References **180**

Chapter 1

General Introduction

1.1 Electrical brain stimulation

1.1.1 Introduction to neural activity

In the brain, information is encoded in the firing rate and spike timing of neurons. The timing of spikes has been implicated in many processes across brain regions. These include the processing of position in space in the hippocampus, perception in the visual cortex, and working memory in the parietal cortex (O'Keefe and Recce, 1993; Vinck et al., 2010; Pesaran et al., 2002). Synchronous neural network activity, or oscillations, can lead to coordinated firing activity locally and between regions. Neural oscillations are a fundamental feature of the brain, that are conserved across species and thought to be critical for intra-region and global communication across and within networks of neurons, by providing time periods when discrete neuronal assemblies are temporally coherent (Buzsáki et al., 2013). In endogenous brain activity, these oscillations are generally thought to be created by microcircuits using rhythmic inhibitory input to create periodic excitability or by networks termed central pattern generators (Grillner, 2006; Buzsáki et al., 1983; Lindsley, 1952). In addition, intrinsic subthreshold oscillations have been found across a variety of brain regions, in numerous classes of neurons (Desmaisons et al., 1999; Llinás et al., 1991), and are thought to play a critical role in timing of spike or Action Potential

(AP) firing (Desmaisons et al., 1999; Giocomo et al., 2007), and the emergence of network oscillations (Lee et al., 2018). Neural oscillations fall across a range of frequencies, with different frequencies being implicated in different neural processes and behavioural states. For example during sleep, slow waves in the delta frequency band (1-4Hz) are typical, and though to reflect the cycling between up and down states of cortical neurons (Nir et al., 2011). Local networks can have a preferred frequency that has been linked to the membrane resonance frequency of individual neurons and their resulting subthreshold oscillations (Hutcheon and Yarom, 2000; Tohidi and Nadim, 2009), highlighting the important role of the single cell and its subthreshold dynamics in synchronous brain activity.

1.1.2 Introduction to electrical brain stimulation

Electrical brain stimulation is a technique involving the application of electric fields to targeted regions of the brain, in order to manipulate the electrical activity of neurons and ultimately modulate behaviour, often in neurological disorders and disease. At its core, delivery of an electric field to the brain generates a transmembrane voltage change or depolarisation across the neuronal membrane, which, if large enough in amplitude, leads to activation of voltage-gated sodium channels that produce a spike or AP. Induced electric fields of ~ 1V/m can affect timing of APs, and increasing field strength can directly evoke APs in neurons (Terzuolo and Bullock, 1956). These APs initiate the release of neurotransmitters, which facilitate communication between neurons in pathways of neuronal networks. The exact effect of brain stimulation at the neuronal network level depends on the location of stimulation, and if present, specific circuitopathy in the region being stimulated. Fundamentally in disease, the aim of electrical brain stimulation is to override and/or replace the pathological, symptom-causing neural activity, the root of which is the electrical activity of single neurons. Electrical brain stimulation can be broadly split into two categories, non-invasive and invasive, depending on whether the hardware for stimulation penetrates the skull.

1.1.3 Non-invasive brain stimulation

Technique

Transcranial Electrical Stimulation (TES) is a form of non-invasive brain stimulation, and is applied via electrodes placed on the intact scalp and skull. TES can be split into Transcranial Direct Current Stimulation (tDCS) and Transcranial Alternating Current Stimulation (tACS), the former typically involving application of a constant unidirectional current from anode to cathode and the latter referring to application of current, typically with a sinusoidal waveform, from anode to cathode in one half cycle and cathode to anode in the other (Liu et al., 2018). In tDCS, depolarisation of neurons is induced underneath the anode, increasing cortical excitability in this area, whereas a hyperpolarisation-induced decrease in cortical excitability occurs underneath the cathode (Nitsche et al., 2008). Comparatively, tACS generally produces modest increases in cortical excitability. The value in this technique however lies in its ability to modulate synchronous neural activity, with effects that are dependent on the frequency of the sinusoidal current being applied (Zaghi et al., 2010).

Mechanism of action

TES is proposed to modulate neural activity in a number of different ways. These include via stochastic resonance, rhythm resonance, biasing of neuronal spike timing, entrainment of endogenous oscillatory activity and imposition of new oscillatory activity, with effects happening concurrently and being dependent on the strength of the applied electric field (Liu et al., 2018). Alternating Current (AC) and Direct Current (DC) electric fields typical of those experienced by neurons during tDCS and tACS, modulate firing rate of rodent hippocampal neurons in brain slices at low field strengths (<10V/m), as measured by Local Field Potential (LFP) recordings, with fields strengths as low as 0.2-0.5V/m being shown to alter spike timing when frequency of stimulation matches the resonance frequency of neuronal properties (Reato et al., 2010; Francis et al., 2003). As frequency of stimulation increases, membrane polarisation induced by the same field strength is reduced due to low-pass filtering properties of the neuronal membrane, which

limit the speed at which the membrane can follow fluctuations in the electric field (Deans et al., 2007; Vaidya and Johnston, 2013). Thus, at similar electric field strengths, higher frequency stimulation is more likely to modulate spike timing than affect firing rate (Liu et al., 2018).

Neurons measured during tACS of the anaesthetised rat brain *in vivo* show entrainment to the extracellular electrical stimulation. That is, single unit neural spiking and LFP recordings show temporal alignment with the phase of the exogenous electrical field. Entrainment increases with increasing intensity of stimulation but field strengths as low as 1V/m are capable of phase-biasing neuronal spiking. Stimulation intensities capable of phase-locking spikes induce 2-3mV of membrane polarisation, measured intracellularly (Ozen et al., 2010), highlighting the role of polarisation at the single neuron on network entrainment and activity. Results showing that multiple cells are stimulated at the same phase of the stimulation also suggest that a large proportion of the cells driven by tACS are directly activated by the stimulation, as opposed to being activated via polysynaptic mechanisms, although this form of activation likely occurs concurrently (Ozen et al., 2010). The aforementioned results have been corroborated in rats and humans, with neuronal spiking and subthreshold currents being modulated with tACS, however a minimum electric field strength of 1V/m is required (Vöröslakos et al., 2018).

Uses

In humans, much of the clinical application of TES derives from the prevailing hypothesis that endogenous neural oscillations can be augmented, and neuronal networks entrained, with electrical stimulation at a matching frequency (Helfrich et al., 2014; Ozen et al., 2010; Deans et al., 2007; Thut et al., 2012). This has proved difficult to test definitively however, due to the technical challenge of separating small amplitude neural activity from the large amplitude extracellular stimulation artifact of the same frequency which is created when TES and large scale non-invasive neural recording in the form of Electroencephalography (EEG) is done concurrently. Whilst possible (Kohli and Casson, 2019), true artifact removal and recovery of neurophysiological signals is difficult due to challenges such as nonlinear distortion of stimulation artifacts by physiological processes (Noury et al., 2016). Consequently, many studies

investigating therapeutic effects of TES in disease rely on behavioural outcomes to assess efficacy. TES has been investigated in a multitude of neurological diseases and disorders including but not limited to epilepsy, stroke, schizophrenia, Alzheimer's Disease (AD) and Mild Cognitive Impairment (MCI) (Yang et al., 2021; Teselink et al., 2021). In a study investigating the effect of 40Hz tACS on AD-MCI patients, a significant increase in memory performance was reported in patients undergoing tACS compared to sham (Benussi et al., 2021). Furthermore, an increase in intracortical connectivity measures was observed. This was interpreted as a restoration of cholinergic neurotransmission, thus suggesting that tACS targets the pathological decrease in gamma frequency oscillations underlain by loss of inhibition and cholinergic innervation in AD, to modulate behaviour (Benussi et al., 2021). For the treatment of cognitive deficits in Parkinson's disease (PD), tDCS has been explored. Across seven studies that used tDCS for treatment of cognitive impairment in PD, significant improvements in cognitive measures were reported following stimulation of the dorsolateral prefrontal cortex in five of the studies (Beheshti and Ko, 2021).

Advantages and limitations

In general, TES is well tolerated, painless, low-cost, and importantly non-invasive, meaning that in theory it could be widely administered as an intervention (Antal et al., 2017). *In-vivo* primate, and human electric field measurements, suggest that a maximum electric field strength of $\sim$0.5V/m can be achieved per 1mA applied current (Opitz et al., 2016; Huang et al., 2017), which with typically applied currents of 1-2mA, is strong enough to affect neural activity (Ozen et al., 2010; Liu et al., 2018). Despite preclinical studies showing effective modulation of neural activity at achievable electric field strengths of $\sim$1V/m however, there is yet to be wide-scale clinical adoption of the TES technique, partially due to small and inconsistent alterations in neurophysiological, and behavioural measures such as attention, working memory, and vigilance observed in clinical trials (Horvath et al., 2015; Berryhill and Martin, 2018; Begemann et al., 2020). This could be due to a number of factors, including variability of stimulation paradigms across studies, and variable human brain anatomy leading to varied field strengths across studies and even individuals. Furthermore, in some disease states such as AD, the brain regions

implicated in early stages of the disease, and thus most pertinent to neuromodulation, are sub-cortical, and currently used TES techniques cannot effectively activate neural tissue below the cortex (Saturnino et al., 2019). This is due to electric field amplitudes dropping at depth, resulting in field strengths at the lower limit of what is believed to be effective (<0.5V/m) (Opitz et al., 2016).

There is also seemingly a disconnect between preclinical and clinical studies when it comes to important stimulation parameters. It has been reported that rodent studies use current and therefore electric field intensities that are ten times larger than those used in human TES studies (Ozen et al., 2010). This could in part be due to unintended loss of current, due to shunting across the human skull and scalp, which is potentially leading to electric field strengths that are too low to effectively modulate neural activity (Liu et al., 2018). One study suggests that 75% of transcranially applied currents are attenuated by the skull and overlying tissue, and that 6mA of current is actually required to induce the 1V/m intracerebral electrical field required for effective neuromodulation, albeit this was calculated from cadaver brain tissue which is biophysically very different to alive tissue (Vöröslakos et al., 2018). It is important to note here that the study reported their stimulation intensity in amperes, but for strength of neurostimulation, current density or electric field strength is the important metric. Whilst 6mA was required in this study, this amplitude may not be directly applicable to other set ups. Nonetheless, a large attenuation of the applied current was observed. Increasing TES intensity is not trivial however, as surpassing typically used 1-2mA current amplitudes can cause side effects such as prickling and burning sensations on the skin, and phosphenes (Antal et al., 2017). Furthermore, it has been shown that during tACS *in vivo* in rats, increasing stimulus intensity recruits an increasingly larger percentage of the neuronal population (Ozen et al., 2010). This suggests that at electric field strengths capable of effective neuromodulation, TES focality will be relatively poor. Incidentally, poor focality and stimulation of multiple brain regions is another potential reason for the weak, nonspecific behavioural outcomes in TES trials, although potential avenues for improvements in this area are being investigated (Bikson et al., 2010; Edwards et al., 2013; Dmochowski et al., 2011; Datta et al., 2009).

1.1.4 Invasive deep brain stimulation

Technique

Contrary to TES, Deep Brain Stimulation (DBS) typically refers to a form of invasive electrical brain stimulation that involves focal (on the order of millimetres) delivery of current, in the form of short ($60-100\,\mu s$), biphasic rectangular pulses at a relatively high frequency (130-180Hz), via an electrode positioned in the brain (Mottaghi et al., 2020).

Uses

DBS is most commonly utilised in the clinical treatment of movement disorders, such as PD and Essential Tremor (ET), however, it is also being investigated as a therapeutic intervention in other brain disorders stemming from aberrant neural activity such as depression, and Obsessive Compulsive Disorder (OCD) (Lozano et al., 2019). PD is generally characterised by a loss of Dopaminergic (DA) neurons in the Substantia Nigra pars Compacta (SNc) of the Basal Ganglia (BG), leading to a lack of DA innervation to other nuclei such as the Globus Pallidus (GP), however the exact pathophysiology is complex and not fully understood (Chiken and Nambu, 2016). One hypothesis is that the loss of DA neurons in PD causes an over-activation of glutamatergic neurons in the Subthalamic Nucleus (STN), which in turn, over-stimulate inhibitory BG output neurons, thus inhibiting the thalamo-cortical network and ultimately the motor cortex (Albin et al., 1989). In PD, electrical stimulation of the STN or Globus Pallidus internal (GPi) can lead to improvement of symptoms characteristic of the disease such as bradykinesia, rigidity, tremor and gait abnormalities (Perlmutter and Mink, 2006).

Mechanism of action

A prevailing hypothesis is that DBS alters pathological firing rate, pattern and synchrony of BG neuronal discharge (Wichmann and Delong, 2006; McConnell et al., 2012). Evidence that DBS elicits direct activation of neurons exists in the form of *in vivo* electrophysiological recordings

in non-human primates, which suggest that in the BG, axonal APs are elicited and propagated to the GP in response to DBS of the STN at therapeutic amplitudes and frequencies. This was manifested in an increase in average firing rate and a more regular pattern of discharge in 86% and 88% of Globus Pallidus external (GPe) and GPi neurons respectively (Hashimoto et al., 2003). Regularisation of neuronal discharge during DBS could in part be explained by entrainment of neurons in the motor thalamus to the stimulation frequency, as shown in non-human primates during GPi-DBS (Muralidharan et al., 2016). Thus, frequency of stimulation is an important factor, evidenced by that fact that high frequency DBS (>90Hz) improves motor symptoms whereas low frequency (<50Hz) doesn't, and can even exacerbate them (McConnell et al., 2012). Rescue of pathological changes in single cell cortical pyramidal neuron properties, such as firing rate and pattern, which have been suggested to be underlain by alterations in the neuronal membrane properties (such as the input resistance and resting membrane potential), has been observed with application of STN-DBS (Degos et al., 2014). Thus, the importance of the single cell on network activity and outcomes of electrical brain stimulation cannot be overstated.

Despite much evidence of direct neuronal stimulation, the exact mechanisms of action of DBS at the network level are greatly debated. This is due to the complexity of the vastly interconnected underlying circuits, and the number of neurons being stimulated despite relative focality (therapeutic DBS in humans is thought to directly stimulate $\sim$ 30% of STN projection neurons (Chaturvedi et al., 2010), of which there are thought to be 400,000 (Hardman et al., 2002)). Due to its high frequency and the similar effects of DBS to direct lesion of the STN (subthalamotomy), DBS has been proposed to create a functional lesion of the overactive STN, thus rescuing thalamo-cortical activity (Benazzouz et al., 1993).

Advantages and limitations

The clinical benefits of DBS in properly selected patients are evident and relatively long lasting. A recent study of PD patients found that time spent with dyskinesia was still reduced by 75% when STN-DBS was switched on compared to when it was was switched off, 15 years after

electrode implantation (Bove et al., 2021). The technique is also seemingly required, with over 160,000 people having undergone DBS so far worldwide, however it is not without limitations (Lozano et al., 2019). DBS requires an invasive surgery to implant the electrode into subcortical regions of the patient's brain. This must be carried out by a skilled neurosurgeon and carries the risk of intraoperative and post-surgical complications, thus the number of reachable patients is critically limited (Rezai et al., 2006).

1.1.5 Non-invasive deep brain stimulation

Non-invasive electrical deep brain stimulation techniques have the potential to address limitations of both traditional non-invasive and deep brain stimulation techniques, such as surgical complications and inability to stimulate subcortical brain regions. One such technique is Temporal Interference (TI) (Grossman et al., 2017).

Technique

TI brain stimulation is derived from the concept of interferential current therapy, which is routinely used in physiotherapy (Goats, 1990). During TI, two high frequency (>1kHz)(f_1 and f_2) oscillating electric fields are applied to the brain via two pairs of current-delivering electrodes placed on the scalp. The frequencies of these fields are at least an order of magnitude higher than those used in traditional invasive DBS. In theory, these oscillating electric fields are too fast to activate neural tissue, due to low-pass filtering of the neuronal membrane (Deans et al., 2007). The two oscillating electric fields differ in frequency by a small amount (on the order of 10Hz and within the frequency range of endogenous neural activity), which is termed the difference frequency (f_Δ). Therefore if the fields are engineered to overlap at a point in the brain, the resulting electric field in this region oscillates at the mean of the two applied field frequencies and is amplitude modulated at f_Δ, due to periodic constructive and destructive interference of the two fields (Figure 1.1 A, B). *In vivo* patch-clamp experiments in rodents suggest that neurons exposed to only a singular high frequency oscillating field, for example those in superficial

layers directly underneath the electrodes, are not depolarised (Figure 1.2 B). It is suggested that the neurons exposed to the amplitude modulated field however, are able to demodulate the signal and follow the envelope (which oscillates at f_Δ) and thus can be stimulated to fire at f_Δ (Figure 1.2 A)(Grossman et al., 2017). These results were validated when TI was targeted to the hippocampus in anaesthetised mice, and subsequent immunohistochemical staining for cFos, an early immediate gene indicative or neuronal activation, suggested that indeed, only neurons in the hippocampus and not the overlying cortex had been stimulated.

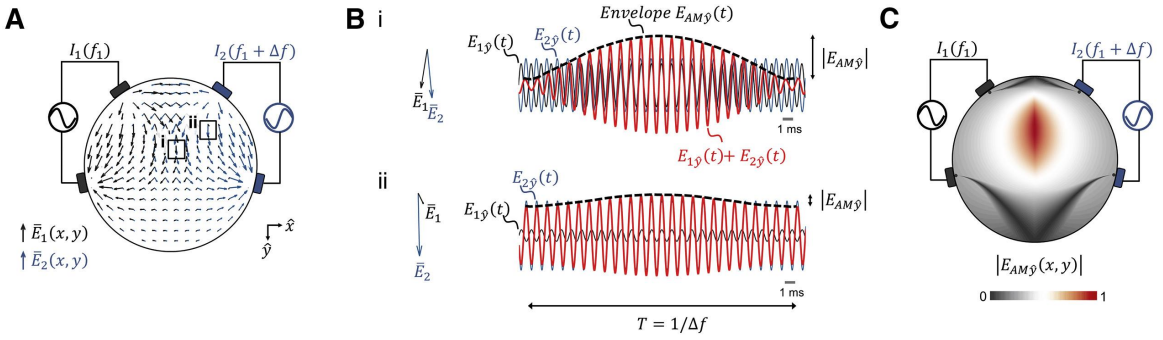


Figure 1.1: **Principle of temporal interference non-invasive deep brain stimulation** (A) Electric field vectors representing the induced Temporal Interference (TI) stimulation electric field. (B) Magnified views of the electric field vectors in (A), showing amplitude modulation of electric fields in TI where the two applied fields do (top), and do not (bottom), overlap fully. (C) Colour map of the spatial spread of TI, as indicated by the envelope modulation amplitude. Figure taken from Grossman et al. (2017). You are not required to obtain permission to reuse this article.

Potential mechanisms of action

The mechanism of action of TI is unknown. The simple summation of two fields with different frequencies does not result in a frequency component at f_Δ (see section 3.2.2)(Figure 3.2). As evidence of TI stimulation exists at the level of the single neuron, the following concepts will be explained in the context of how TI stimulation can lead to supra-threshold stimulation of a single neuron.

Thus far, evidence for TI stimulation at f_Δ exists in the suprathreshold domain, meaning that the response at f_Δ has been observed in a neuron which is firing APs. This could be achieved by a simple linear superposition of the two fields if the neuron is polarised at the applied

kHz frequencies. For example, once the amplitude of the kHz frequency amplitude modulated electric field is large enough that the cell membrane is depolarised above the threshold for neuronal activation, an AP is evoked. One could alternatively hypothesise that the nonlinear properties of the neural depolarisation process leads to nonlinear frequency conversion (envelope detection) via rectification (Cheng and Liu, 2020) (see section 1.4 and section 3.1.1) or nonlinear frequency conversion via multiplication (Frequency Mixing (FM))(see section 1.3 and section 3.1.1)(Breed, 2011). In the case of nonlinear conversion via multiplication, direct polarisation at the difference and sum frequencies of the applied electric fields, as well as higher order mixing terms are produced. In the case of nonlinear frequency conversion via rectification, the envelope of the amplitude modulated signal is extracted from the neural polarisation and thus polarisation at f_Δ is produced.

Currently the assumption is that TI-induced neural activity will be maximal at the site of maximum envelope amplitude, and this is reflected in the Finite Element Method (FEM) modelling done in the original paper (Figure 1.1 C) (Grossman et al., 2017). Based on this assumption, tissue phantom and *in vivo* mouse experiments probing evoked motor response were performed. These suggested that steering of TI-induced polarisation is possible by alteration of the current ratio applied across the two electrode pairs and that indeed neurons in the region

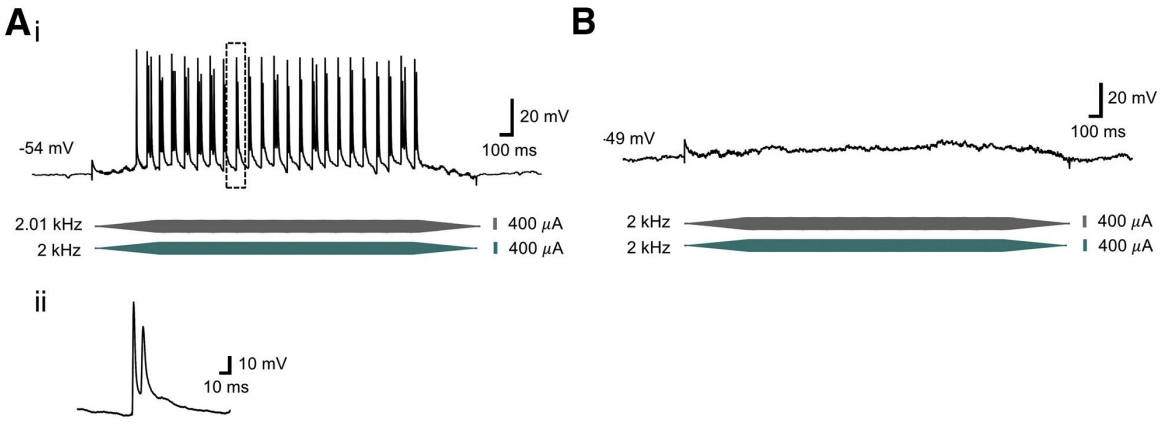


Figure 1.2: **Stimulation of a neuron by temporal interference non-invasive deep brain stimulation** Figure taken from Grossman et al. (2017).(A) Response of a single hippocampal neuron to Temporal Interference (TI) stimulation ($f_1 = 2000$Hz, $f_2 = 2010$Hz). (B) Response of a single hippocampal neuron to pure kHz sinusoidal stimulation ($f_1 = 2000$Hz, $f_2 = 2000$Hz). You are not required to obtain permission to reuse this article.

of the maximal envelope amplitude are being stimulated (Grossman et al., 2017). However, it is important to note that no direct electrophysiological validation of this assumption has been done in living tissue and if nonlinear processes are occurring, the spatial distribution of TI-induced activity may be quite different.

Assuming that TI with a specific f_{Δ} produces the equivalent of tACS of the same frequency just at depth (i.e. the site of maximum envelope amplitude), the neurophysiological effects of TI would be similar (see section 1.1.3). For example, TI may be able to influence spike timing, entrain neurons at specific frequencies, and even impose new rhythms upon neural activity, depending on the electric field that results from the overlap of the two applied fields. Thus far, evidence for entrainment of spikes in cortex and hippocampus by TI stimulation has been observed at the level of the single cell in rodents (Grossman et al., 2017).

Uses

In theory, TI stimulation could be investigated for efficacy in treatment of the same neurological diseases and disorders as TES and DBS (see section 1.1.3 and section 1.1.4) (Grossman et al., 2018). A computational study utilising FEM modelling of human and rodent brains has suggested that indeed, TI is scale-able to the human brain, and that electric field strengths similar to those used in tACS are achievable in deep brain regions with TI (Rampersad et al., 2019). Additionally, the expected areas of stimulation (determined by the maximum amplitude-modulated electric field strength) were smaller compared to tACS, suggesting that TI may be able to exert more focal neurostimulation (Rampersad et al., 2019). It is important to note, that these modelling experiments, as with the original modelling, are based on the assumption that the envelope amplitude of the electric field is the parameter that determines strength of TI.

As the technique is in its infancy, there are few studies on its application. One early report suggests that TI with difference frequencies of 20Hz and 70Hz improved reaction time and increased excitability of the motor cortex, as measured by transcranial magnetic stimulation-evoked motor evoked potentials (Ma et al., 2021). This finding supports previous work sug-

gesting that electric fields in the beta range (12-30Hz) significantly increase excitability of the motor cortex (Wischnewski et al., 2019), and suggests that TI may be effective in humans.

In epilepsy, electrical brain stimulation can be used to probe which regions of the brain are epileptogenic (Munari et al., 1993). It has been suggested that TI is potentially an effective non-invasive alternative for this, with orientation-tunable TI being used to successfully evoke seizure-like events focally in the mouse hippocampus (Missey et al., 2021). Important to note is that this study used what was termed TI, but the applied stimulation used biphasic square waveforms with different frequencies, assuming that it would produce the same effect as sine wave TI. Critically, the summation of two biphasic square waveforms does not result in a signal that is amplitude modulated at f_Δ, rather, it creates a waveform that has a pulse-width that is periodically modulated at f_Δ. Thus, if indeed this kind of waveform is able to stimulate neurons at f_Δ as in TI, it may suggest that neurons are also able to demodulate a pulse-width modulated signal to recover f_Δ, or a completely different and un-hypothesised mechanism is at play. If it is the former, this could signify that the envelope amplitude is not the important parameter in TI stimulation, or that nonlinear processes are instrumental. Regardless, elucidation of the mechanism of this technique termed Pulse-Width Modulated (PWM)-TI, may be able to validate these results and also give clues as to the mechanism of traditional TI.

As research into TI stimulation ramps up, it important to note that as the stimulation artifact during TI is at a different frequency ($(f_1+f_2)/2$) to the brain activity of interest (f_Δ), this should more easily allow concurrent TES and LFP/EEG recordings (see section 1.1.3). Thus, the previously challenging task of gleaming deeper insight into the mechanisms of TES, may be achievable with this technique.

Advantages and limitations

TI stimulation has the potential to be a safe, effective, and widely used neuromodulation technique that couples the non-invasive nature of TES with the ability of DBS to target subcortical structures (Grossman et al., 2017). However, as TI stimulation is a transcranial method, it is subject to some of the same considerations as traditional TES. As previ-

ously mentioned, it has been suggested that TES with multiple electrodes may be capable of stimulating deep brain regions (Huang and Parra, 2019), although naturally, greater current amplitudes will likely be required to achieve sufficient electric field strengths at depth. This results also in large electrical field strengths at the cortex, leading to poor focality for traditional TES. Assuming that conductivity and resistivity of brain tissue is similar for both low and high frequency oscillating electric fields (Gabriel et al., 1996) (https://itis.swiss/virtual-population/tissue-properties/database/dielectric-properties/), strength of the amplitude modulated kHz frequency electric field superficially and at depth, should match that of low frequency fields used in traditional TES. The proposed benefit of TI lies in the notion that the non-amplitude modulated fields (in superficial regions where electric field strength is largest) should not activate neural tissue, and that stimulation is dependent on the amplitude of the electric field envelope, which is maximal at depth. As expected and in line with previous models, FEM modelling suggests that the electric field strength of the un-modulated superficial field during TI ($\sim$0.5 V/m per 1mA applied current), is larger than the amplitude modulated field at depth ($\sim$0.35 V/m) (Esmaeilpour et al., 2021). Thus critically, it is imperative that un-modulated kHz electric fields do not have an activating effect on neurons, if focality is to be achieved. Nonetheless theoretically, and based on current evidence and assumptions, TI stimulation should be able to address this issue of poor focality with increased applied current amplitude, as it should be possible to have activated brain regions only at depth, the distribution of which should match FEM modelling (Figure 1.1 C)(Grossman et al., 2017). Additionally, kHz fields appear to induce less sensation on the scalp, and thus may enable modest increases in applied current amplitudes (Hsu et al., 2021).

Focality of stimulation however, approximated by FEM modelling, and based on the assumption that stimulation is maximal at the site of maximal envelope amplitude, is suggested to be on the order of centimetres (Figure 1.1 C). Thus, it is far from being able to rival current DBS techniques. As previously mentioned, focality of stimulation is vital for controlled and effective neurostimulation (see section 1.1.4). Elucidation of the mechanism(s) of TI stimulation and the role of nonlinear processes such as FM, can inform strategies to improve the focality and support the adoption in clinical neuroscience.

In summary, regarding TI, open questions in the field include:

1) What is the mechanism of action of TI stimulation?

2) How does strength of TI depend on the parameters of stimulation?

3) Can PWM-TI exert similar neurostimulation to TI and if so, what is the mechanism of action?

1.2 Electrical brain stimulation at the single cell

1.2.1 The neuron as an equivalent circuit

In order to understand how electrical stimulation such as TI affects the single neuron and ultimately the brain, it is required that we understand how neurons respond to applied currents. Although a great oversimplification, the electrical property of the neural membrane can be represented as an equivalent RC circuit, that is, it is composed of a resistor and capacitor in parallel (Figure 1.3 A). The battery is the difference in the intracellular vs extracellular ion concentration, which creates an electrochemical gradient, or a voltage difference across the membrane- the resting membrane potential (V). The resistor represents the reciprocal of the conductance across the membrane, and the capacitor represents the bilipid membrane which is an insulator, and the intra- and extra-cellular ionic solutions which are conductors. The value of the capacitance depends on the properties of the bilipid membrane. The wires in the circuit are the ionic solutions, i.e. the medium which carries the current. In this model, the resistance and the capacitance are constant, and thus this is a linear system.

As the neuron has both a resistance and a capacitance it also has a time constant. The time constant of a neuronal membrane is defined as the time required to charge the capacitor through the resistor, from a charge voltage equalling zero to approximately 63.2% of the value of the applied voltage. Thus, the time constant determines how fast the membrane voltage (V) can change in response to extracellular current/voltage or current/voltage injection (Koch et al.,

1996). The time constant τ of the neuronal membrane (s) is

$$\tau = \mathrm{R}_m \mathrm{C}_m \tag{1.1}$$

where R_m is the specific membrane resistance (Ω cm^2) and C_m is the specific membrane capacitance (μF/cm^2). τ determines the frequency at which the output of the system (V) begins to be attenuated (the cutoff frequency f_c (Hz)) by

$$\mathrm{f}_c = \frac{1}{2\pi R_m C_m} \tag{1.2}$$

thus the time constant is inversely proportional to the cutoff frequency and determines the low-pass filtering properties of the neuron. This circuit composed of just a resistor and a capacitor with constant values, is typically considered to be a model of the passive neuron.

1.2.2 Nonlinearity in electrical circuits

A nonlinear system is by definition a system in which the change of the output is not proportional to the change of the input. When we talk about linearity or nonlinearity in the context of an electrical circuit, it refers to the relationship between the voltage (V) or potential difference, and the current (I). If you take a very simple circuit comprised only of a battery and a resistor, if the resistor has a fixed resistance (R), according to Ohm's Law,

$$\mathrm{V} = \mathrm{IR} \tag{1.3}$$

the relationship between the voltage and current will be linear, or Ohmic, that is, V is propor-

tional to I, with a proportionality constant that is equal to the resistance. This is true also if you add a capacitor with a constant capacitance C to the circuit. The current across the capacitor is

$$\mathrm{I}_{cap} = \mathrm{C}\frac{\partial v}{\partial t}. \tag{1.4}$$

A capacitor is a linear element because the capacitive current has the scaling property and differentiation follows the superposition principle (Popescu, 2018). For a nonlinear relationship between current and voltage to exist, the resistor or the capacitor (or both) in this circuit must be variable and dependent on the current or the voltage. For example, if a resistor has a variable resistance which depends on the voltage across it, conductance (the reciprocal of resistance) will also be variable, and the relationship between I and V will be nonlinear.

1.2.3 Nonlinearity in neurons

Neurons indeed are nonlinear systems. While still an oversimplification, a more accurate representation of the cell as an equivalent circuit consists of a capacitor representing the cell membrane capacitance, a fixed resistor representing the leak conductance, plus multiple variable resistances or conductances to multiple ions such as sodium, potassium and chloride, in parallel (Figure 1.3 B). This model was first described by Hodgkin and Huxley in their seminal paper (Hodgkin and Huxley, 1952). In the model, sodium and potassium conductances are variable as they depend on the opening of voltage-gated ion channels in the cell membrane. Thus these circuit elements are an origin of nonlinearity, and even at the most basic level, the relationship between membrane voltage and transmembrane current in a neuron is considered to be nonlinear.

The elements of the neuron that are traditionally considered to have a constant value and thus be voltage-independent are known as the passive membrane components. These elements

are the cell membrane capacitance and the leak conductance. Leak channels underlying the leak conductance include the TASK potassium channel (González et al., 2012), the CIC-2 chloride channel (Jentsch et al., 2005), and TTX insensitive NALCN sodium channel (Ren, 2011). Traditionally approximated as linear (Hodgkin and Huxley, 1952), recent work has suggested that the leak conductance is in fact nonlinear, as it shows a dependence on membrane potential. It is theorised that whilst the channels themselves are not dependent on voltage, i.e. do not exhibit any gating, the conductance and thus the leak current does depends on the ionic concentration gradients, something which is inextricably linked to membrane potential or voltage (Huang et al., 2015). Additionally, numerous studies have suggested that cell membrane capacitance is also nonlinear in artificial lipid bilayers (Alvarez and Latorre, 1978), and Human Embryonic Kidney (HEK) cells (Farrell et al., 2006). It has been theorised that the origin of this nonlinearity is electrostriction, which is the process by which the bilipid membrane compresses when a voltage is applied across it (Mosgaard et al., 2015; Heimburg, 2012). This phenomenon is suggested to be likely to occur when the lipid membrane is close to a chain melting phase transition (Heimburg, 2012). Capacitance is dependent on the area of the capacitor (A) and the distance between the capacitive plates (d) such that

$$\mathrm{C} = \epsilon \frac{\mathrm{A}}{\mathrm{d}} \tag{1.5}$$

where (ϵ) represents the absolute permittivity of the dielectric material (the bilipid membrane). Therefore, compression of the membrane, which changes the distance between the plates (the extra- and intra-cellular solutions), also changes the capacitance. This would indeed make capacitance a variable element and introduce nonlinearity to the I-V relationship. In fact, infrared nerve stimulation is thought to be driven by a transient change in capacitance which induces depolarisation, suggesting indeed that the capacitance in a neuron may not be a biological constant, especially under unnatural conditions (Shapiro et al., 2012). Together, these results suggest that nonlinearity may also originate in the "passive" elements of the neuronal equivalent circuit which were previously assumed to be of fixed value, and independent of voltage.

1.3 Frequency mixing

1.3.1 Introduction to frequency mixing

In electronics, Frequency Mixing (FM) refers to the creation of signals with new frequencies when two signals of different frequencies are multiplied within a nonlinear mixer. In its purest form, a frequency mixer takes signals with frequencies f_1 and f_2 and creates signals with frequencies at the difference ($f_\Delta = f_2$-f_1) and sum ($f_\Sigma = f_1$+f_2), as well as the harmonics, of the two applied frequencies (here assuming $f_2 > f_1$). However in reality, the signal at the output of the mixer usually contains new frequency components (f_Δ and f_Σ) but also the original frequency components (f_1 and f_2). When coupled with a process for separating f_Δ, for example via low pass filtering of the resulting signal, FM can be a means for detecting the difference in frequency between two signals (Figure 3.1 B). This is typically how it is thought that the brain uses such a phenomenon. Nonlinear mixers and the process of FM is also used to shift the frequency of a signal from one frequency range to another. Frequency mixers do not require

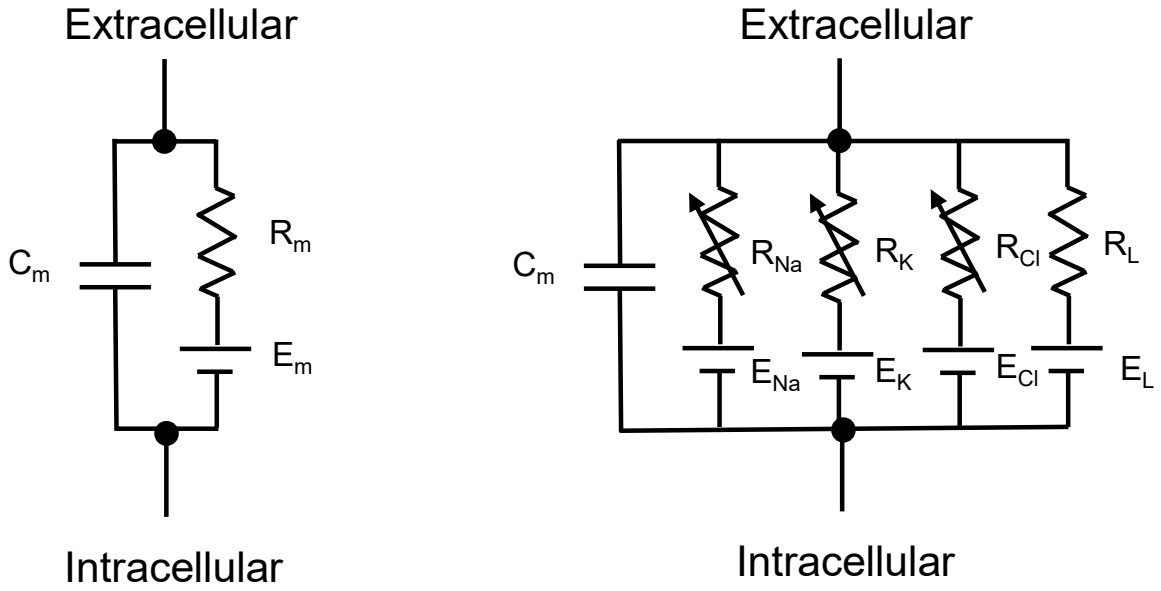


Figure 1.3: **The neuron as an electrical circuit** (A) The neuron as an RC electrical circuit, where C_m is the cell membrane capacitance, R_m is the cell membrane resistance, and E_m is electrochemical gradient across the membrane. (B) The Hodgkin-Huxley model of the neuron as an equivalent circuit. C_m is the cell membrane capacitance, R_L is the leak resistance, R_{Na}, R_K, and R_{Cl} are variable resistances to each ion, and E_L, E_{Na}, E_K and E_{Cl} represent the electrochemical gradient driving the flow of the respective ion(s).

an input of an amplitude modulated signal, however the summation of two signals of different frequencies results in an amplitude modulated signal that contains frequency components at both input frequencies, so this signal is a fine input for a frequency mixer.

1.3.2 Evidence of frequency mixing in neural activity

Evidence for FM of neural activity has been seen previously in human EEG measurements, where the power spectrum of activity in response to two superimposed visual gratings, which are modulated at two different frequencies f_1 and f_2, showed components at $2f_1 + 2f_2$ (Regan and Regan, 1987). Additionally, recordings of the spiking activity of a single sensory nerve cell in paddlefish (*Polyodon spathula*) have also demonstrated the phenomena (Neiman and Russell, 2004). In this case, it was shown that the recorded cell, which receives input from two oscillatory populations with different endogenous frequencies (f_1 and f_2), has resulting activity with frequency components at the terms f_1-f_2, f_1+f_2 and $2f_1$-f_2, suggesting nonlinear mixing of the inputs (Neiman and Russell, 2004). In the rat brain, it has been proposed that spectral mixing of signals in the vibrissa primary somatosensory cortex encoding position and contact with whisker, allows the phase difference of the two signals to be computed. This is important because it is hypothesised that the phase of one of these signals relative to the other allows the position of an object relative to the head to be deciphered (Ahissar and Kleinfeld, 2003; Ahrens et al., 2002). Additionally in this brain region, FM firstly between an anaesthesia-evoked oscillation at one frequency (f_1) and a mechanical whisker-evoked oscillation at another frequency (f_2), and secondly, between two mechanical whisker-evoked oscillations at different frequencies (f_1 & f_2), can be observed. Evidence for this was in the form of frequency components at f_1-f_2 and f_1+f_2 in LFP recordings. Higher order mixing terms were also observed, although these are likely harmonics due to the non-sinusoidal nature of the stimulus rather than as a direct result of nonlinear mixing of the fundamental frequencies (Ahrens et al., 2002). More recently, detection of FM has been achieved via computation of the three-way phase relationship between two root signals R1 and R2 at f_1 and f_2, and one of the emergent signals either f_1-f_2 (E1), f_1+f_2 (E2), $2f_1$ (H1) or $2f_2$ (H2), in LFP

recordings of endogenous rodent neural activity. These results suggest that FM occurs in spontaneous neural activity at the network level, in a state and region dependent manner, and furthermore, that oscillatory signals resulting from FM are sufficient to entrain neural network activity, thus suggesting that the signals emerging from FM may play a functional role in neural dynamics (Haufler and Paré, 2019). Together, these studies have shown evidence of the FM phenomenon in endogenous oscillatory brain activity (Haufler and Paré, 2019) and sensory-induced oscillatory brain activity (Ahrens et al., 2002). It has been hypothesised that the nonlinearity underlying FM originates in the AP threshold properties of the neuron and a simple phenomenological model was proposed based on this (Kleinfeld and Mehta, 2006), although there is no experimental evidence to support this.

1.3.3 Cross-frequency coupling

The concept that neuronal rhythms of different frequencies exhibit a relationship, or are dependent on one another, is not limited to FM, and other forms of two-way dependency or coupling, are well established in the brain and implicated in neuronal function and dysfunction (Salimpour and Anderson, 2019). This phenomena is thought to aid in the coordination of signals across the frequency, spatial and temporal domains and play a functional role in behaviour.

One important interaction between neuronal signals of different frequencies has been observed in the form of cross-frequency Phase-Amplitude Coupling (PAC), where the power of a signal (typically in the gamma frequency range ($>$ 30Hz)) is dependent on the phase of another (typically theta (4-8Hz)) (Canolty and Knight, 2010). It has been suggested that this form of PAC is involved in working memory and task performance in both rodents and humans (Tort et al., 2008; Axmacher et al., 2010).

Additionally, Phase-Phase Coupling (PPC), where dependency exists between the phases of the two signals, has been posited to exist (Belluscio et al., 2012; Siebenhühner et al., 2020). Original studies suggest the existence of PPC between theta and gamma oscillations in the rodent hippocampus (Belluscio et al., 2012), however this coupling is thought to be an artifact

due to the statistical methods applied (Scheffer-Teixeira and Tort, 2016). Ultimately however, it is still believed that in endogenous human brain activity, PPC exists between theta and alpha oscillations in networks linking brain regions, as detected by a different method, with the strength of these networks being a predictor of cognitive performance (Siebenhühner et al., 2020).

In PAC and PPC, one signal modulates the phase or amplitude of the other, but the frequency of the resulting brain activity remains limited to the frequencies of the fundamental signals. Conversely, in FM, the interaction between signals of two different frequencies results in new frequencies. The relevance of this to neural activity and ultimately behaviour is completely unknown.

The importance of CFC is hypothesised to lie in its ability to facilitate information transfer from widespread neural networks operating at low-frequency timescales relevant to behaviour, to high-frequency local networks (Canolty and Knight, 2010). The functional importance of FM in the brain, and whether it could be similarly involved in the integration of signals of different frequencies has never been empirically tested.

1.3.4 Frequency mixing in temporal interference

Given that a number of nonlinear processes occur in neurons, and FM is a phenomena which has been detected in neural activity, it seems logical to suggest that the mechanism of TI stimulation, which requires the application of two signals with different frequencies to brain tissue, involves a nonlinear process such as FM. Hitherto electrophysiological investigation of TI stimulation focused on supra-threshold activity, and as alluded to previously (see section 1.1.5), f_{Δ} in suprathreshold neural activity can actually be produced by other nonlinear and linear processes. Furthermore, whether TI involves generation of FM products (i.e.both f_{Δ} and f_{Σ}) was not tested, thus definitive evidence for the existence of FM during TI has never been observed.

In summary, regarding FM, open questions in the field include:

1) What is the origin of FM in neural activity?

2) Can exogenous electric fields at different frequencies be directly mixed by neurons?

3) If exogenous electric fields at different frequencies can be mixed, can TI stimulation be mediated (at least partially) by a FM phenomenon?

1.4 Envelope Detection via rectification

1.4.1 Introduction to envelope detection via rectification

Whilst frequency mixers can be components of product detectors used for envelope detection or amplitude demodulation, they are not the only method of creating nonlinearity in the system, and thus isolating f_Δ from a signal. Envelope detection via rectification is another way in which f_Δ may be extracted from an amplitude modulated signal (see section 3.1.1 for more detail). Rectification is the process by which an AC, which periodically reverses direction, is converted to a DC, which flows in only one direction. This can be done for example, by a half-wave rectifier and the most simple element of a circuit that can act as a half-wave rectifier is a diode.

Half wave rectification of an amplitude modulated signal results in a voltage where only the positive part of the AC current is passed, and this is reflected in the resulting voltage change across the resistor. When the rectification is coupled with a process for signal smoothing, for example via a capacitor, it can lead to envelope detection (Figure 3.1 C). The capacitor in the circuit acting as an envelope detector, stores charge when the voltage signal is rising and and releases this charge, slowly through the resistor in the circuit, when the voltage signal starts to fall. In short, an envelope detector that works via rectification, takes a high-frequency amplitude modulated signal as an input and provides an output which is the demodulated envelope of the input signal.

1.4.2 Envelope detection in temporal interference

As TI is an amplitude modulated signal, one could hypothesise that the production of f_Δ in TI, is via envelope detection. In fact, a recent modelling study suggested that indeed, envelope detection or demodulation, mediated via rectification of ionic currents is the mechanism by which neurons are able to respond to f_Δ during TI (Mirzakhalili et al., 2020). In this study however, the conclusion is drawn purely from the observation that total current through ion channels is rectified, and the origin of capacitance that can both allow for polarisation at the applied kHz frequency, and filter out the kHz frequency rectified signal, such that the low-frequency envelope can be extracted, is not at all clear. Regardless, whether nonlinear processes such as envelope detection or FM are potentially the driving force of TI is an open question. Investigation into the previously raised open questions will help in uncovering of the exact mechanism of TI and potentially aid in improvement, and eventually wide-scale clinical adoption, of the technique.

1.4.3 Summary

Electrical brain stimulation techniques are used clinically to treat a variety of disorders underpinned by aberrant electrical brain activity. There is a clear need for brain stimulation techniques that are both non-invasive, focal, and able to reach deep brain structures. TI shows promise as a novel brain stimulation strategy, however the mechanism by which it exerts its effects is currently unknown.

In this thesis, I use electrophysiological techniques and novel methodologies for detecting higher order nonlinear frequency interactions, to investigate the mechanism of TI stimulation. Furthermore, I explore the neuronal response to brain stimulation, and what it can tell us about the biophysics of neural activity.

Chapter 2

Methods and Materials

2.1 Overview

Methods pertaining to multiple chapters in this thesis are described in detail in this methods chapter. Additionally, an overview of the utilised methods of neural recording are covered (see section 2.3 and section 2.4).

Chapter 3 investigates the potential mechanisms of action of TI stimulation, and the presence of nonlinear integration of input signals at the single neuron in mice. All data are from single neuron recordings obtained using the whole cell patch clamp method (see section 2.3). The data in Chapter 4 investigates the presence of nonlinear interactions in endogenous neural activity both at the level of the single neuron in mice, and in wide scale cortical network activity in humans. This data was obtained using whole cell patch clamp (see section 2.3) and EEG (see section 2.4) respectively. Chapter 5 presents evidence for the efficacy of a novel brain stimulation technique based on TI, again at the level of the single neuron in mice, with data obtained using whole cell patch clamp (see section 2.3). Extracellular electrical stimulation is utilised in Chapter 3 and Chapter 5 and thus is covered in this chapter (see section 2.2).

A novel data analysis method for detecting nonlinear three-way phase relationships between neural signals of different frequencies is used in Chapter 3 and Chapter 4 and is thus explained

in detail in this methods chapter (see section 2.5).

2.2 Extracellular electrical stimulation

2.2.1 Principles

Extracellular electrical stimulation of neurons can be achieved by applying a current or voltage across the neuron to induce an electric field. For the experiments in this thesis, a constant current source is used, meaning that a current is applied, and this current is kept constant regardless of the impedance of the load, by alteration of the supplied voltage. Additionally, throughout the thesis for the application of TI stimulation, AC stimulation is used. During AC stimulation, the direction of the flow of charge or current reverses periodically. The time it takes for the flow of charge to complete one complete cycle of this reversing process is known as the period and the reciprocal of this is the frequency of the stimulation, expressed in Hertz (Hz).

2.2.2 Mechanisms

The electric field that is induced by the applied current produces a force on the charges (ions) in the medium which mobilises these ions and creates a current. If the current being applied is AC, the direction of the electric field is changing direction at a rate indicated by frequency of the applied current, and the ions in the medium oscillate around somewhat of a fixed point in space. Thus AC stimulation can be thought of as causing periodic positive charge build up on the outside of the cell membrane. As positive charge builds up, the cell membrane capacitor is charged and positive charge on the inside of the membrane is repelled. This movement of charge either side of the capacitor looks like current flowing across the capacitor and is thus termed capacitive current. With AC, this charge buildup, and consequently the capacitive current, inverts when the polarity of the applied current does. In neurons, ion channels facilitate the movement of ions across the membrane, therefore current also flows across the membrane in

this way. As mentioned previously (see section 1.2.3), the current that flows via these channels can be voltage dependent due to the existence of voltage gated ion channels. Thus extracellular electric fields polarise membranes, firstly via charging of the cell membrane capacitance which induces a capacitive current and secondly, via movement of ions across the membrane via a resistive current. Whilst this described mechanism of action outlines the processes by which a theoretical portion of membrane is polarised by extracellular current application, in reality, multiple factors can influence the actual amount of membrane polarisation. The electric field and thus the current being experienced by the neuron can be perturbed by the presence of the neuron itself, with orientation with respect to the field and biophysical and morphological properties being important factors (Ye and Steiger, 2015).

2.2.3 Application in this thesis

In all of the experiments outlined in this thesis that utilised extracellular stimulation, stimulation was applied across electrodes placed in a bath of Artificial Cerebrospinal Fluid (aCSF). The stimulation was delivered via a current source. A 0.25mm diameter platinum wire stimulating electrode (VWR, Lutterworth, UK) was positioned just touching the slice, on L2/3 cortex before commencement of whole cell patch clamp recordings. A return stimulation electrode consisting of two 2x2mm Ag/AgCl pellet electrodes (VWR, Lutterworth, UK) in a y-shape configuration (Figure 2.1), was placed in the bath (ventral side of the slice). Electrical stimulation was delivered using a custom-built MATLAB GUI via a DAQ (USB-6216 BNC; National Instruments, Newbury, UK) and constant current isolator (LCI1107; Soterix Medical Inc, New York, NY, USA). Specific waveforms for experiments are outlined in the relevant results chapter methods sections.

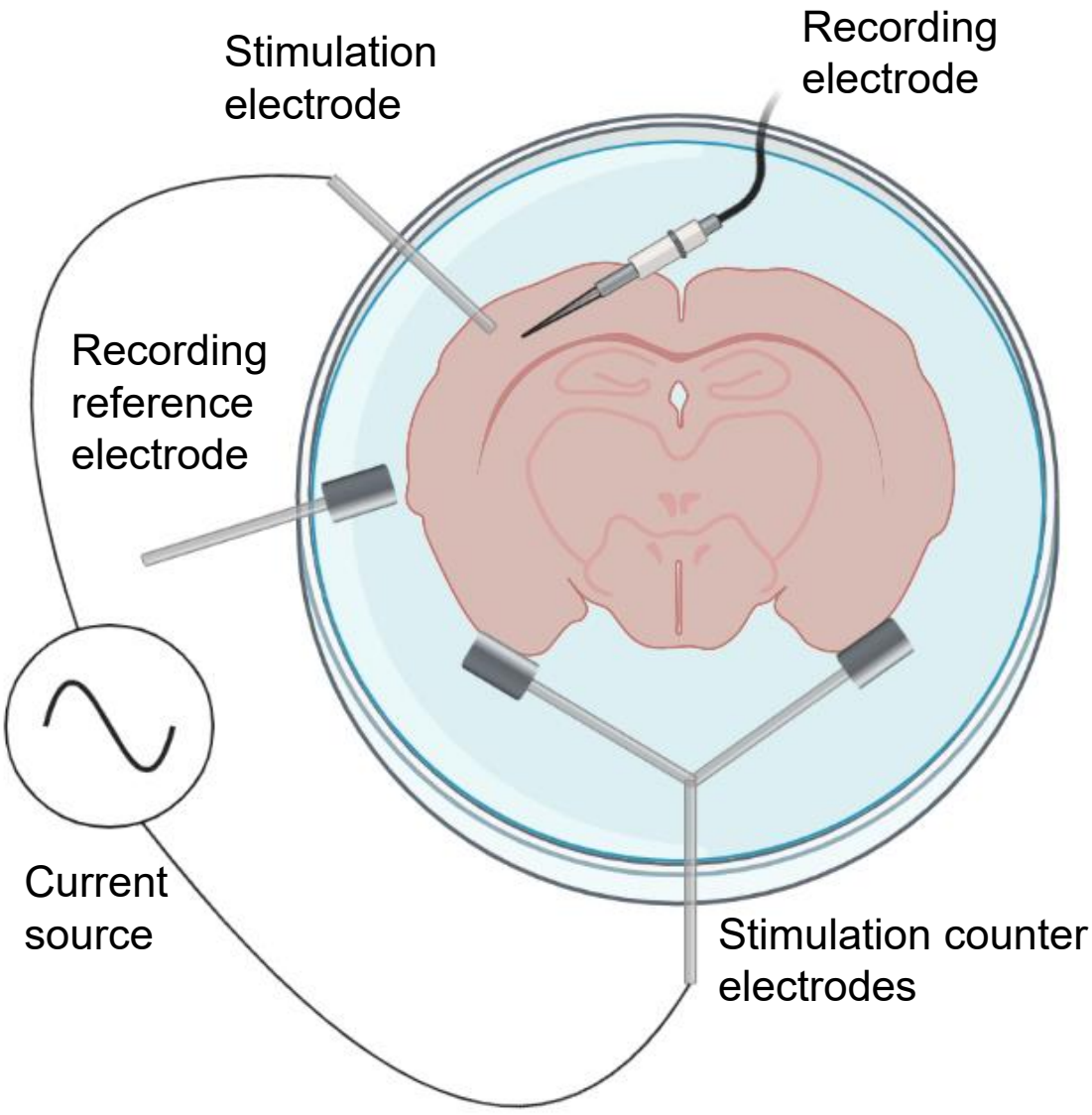


Figure 2.1: **Schematic of *ex vivo* whole cell patch clamp setup with extracellular stimulation**

2.3 Whole cell patch clamp electrophysiology

2.3.1 Principles

Given that the neuron can be thought of as an equivalent RC circuit, with the membrane resistance and capacitance as elements (see section 1.2.1), the voltage across these can be measured, and this is the membrane potential. The membrane potential is defined as the difference in potential inside the neuron relative to outside, and is a metric of great interest to neuroscience, as almost every aspect of a neuron's computation and signalling is controlled by its voltage (Koch, 1997).

Generally, the whole-cell patch clamp technique involves gaining access to the intracellular space of a single neuron via a glass micro-pipette electrode in order to record the transmembrane currents or potential. The technique is based on the cell-attached patch clamp technique developed for recording single channel currents (Neher and Sakmann, 1976). The pipette electrode is brought to the cell membrane and a seal is formed which has a resistance on the order of a gigaohm, and a small section of the membrane is removed via suction. The resistance of the seal with the membrane remains very high, however electrical access to the inside of the neuron is achieved, with access resistance being an order of magnitude smaller. The current, or voltage across the membrane (membrane potential) can be measured using an op-amp.

2.3.2 Measuring membrane potential

The data in this thesis was obtained using the current-clamp method however, no current was injected into the cell via the pipette electrode, which allows for the measurement of the resting membrane potential. The resting membrane potential is the potential recorded at the pipette recording electrode (intracellular), compared to the potential recorded at a reference electrode in the aCSF (extracellular). The membrane potential is thus a potential difference and is measured in volts. Membrane potential/voltage changes across the membrane were then measured during extracellular current stimulation (see section 2.2) and baseline (no stimulation).

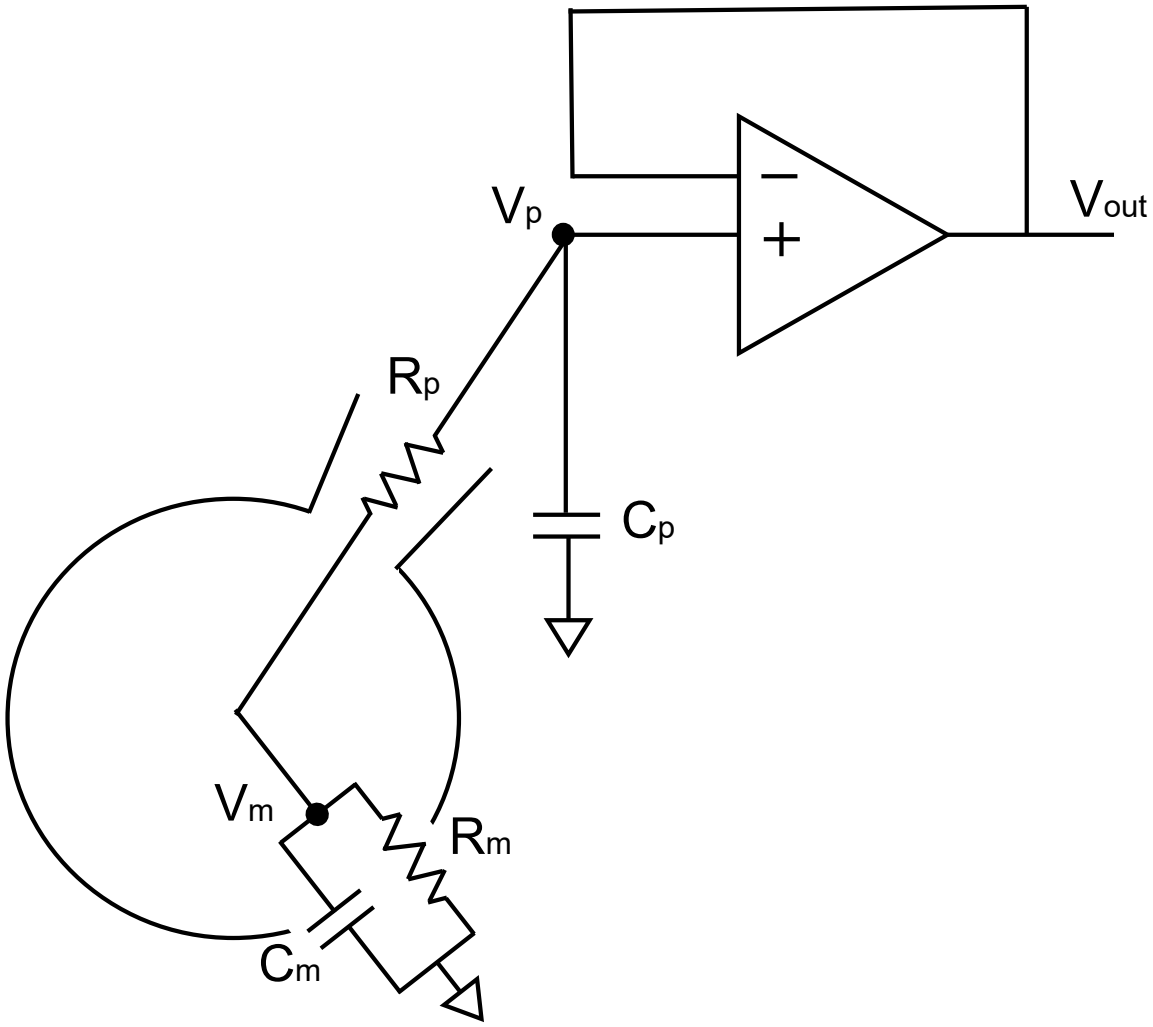


Figure 2.2: **Schematic of whole cell patch clamp equivalent circuit during voltage recording in the absence of injected current** Recording of membrane potential from a single neuron is achieved using an voltage follower op-amp. The op-amp is connected to the neuron via an pipette electrode which has resistance (R_p) and capacitance (C_p). The electrode measures the potential difference inside the cell relative to outside of the cell (measured with an extracellular reference electrode) and thus the membrane potential across the membrane resistance (R_m) and capacitance (C_m). When an electric field is applied across the membrane, C_m is charged, a capacitive current is induced and the membrane potential changes. Additionally, membrane potential changes when ions and thus current, flows through ion channels across the membrane, with R_m being inversely proportional to the number of open ion channels.

2.3.3 Principles of data analysis

Membrane potential traces acquired using whole-cell patch clamp can be analysed in the time domain and the frequency domain.

In the time domain, one can look at the membrane potential trace and calculate amplitude of events or oscillations detected at the single cell which are typically on the order millivolts. Additionally, the threshold for action potential firing can be established by looking at the data in this domain. When whole-cell patch clamp recordings (see section 2.3.2) are done in conjunction with extracellular stimulation (applied as described in section 2.2.3), a stimulation artefact is recorded as well as the single cell neural activity. This is due to the applied current creating a voltage difference between the recording and reference electrode.

One can also analyse the single neuron recordings in the frequency domain. A recording of a neuron's membrane potential contains signals of multiple frequencies and computation of the power spectral density reveals these frequency components. Power is a measure of energy or the strength of the signal at a specific frequency. If a neural membrane is oscillating at a specific frequency, this will be evident as an increase in power at that frequency.

2.4 Electroencephalography

2.4.1 Principles

Electroencephalography (EEG) is a measure of voltage fluctuations resulting from ionic current flow within the brain due to the activity of neurons and is a non-invasive method of measuring wide scale synchronous cortical neural activity. The electrical activity detected by an EEG electrode placed on the scalp represents the synaptic activity of thousands of similarly oriented cerebral cortical (mostly pyramidal) neurons underneath the electrode (Louis et al., 2016).

An EEG electrode detects the sum of the charges beneath it. If a postsynaptic neuron is depolarised at the dendrite, the extracellular voltage at the dendrite is more negative relative

to other regions of the neuron such as the soma. When a negative and positive charge are separated in space, this is referred to as a dipole. A neuron receiving a synaptic input can thus be considered to be a dipole. The charge of a single neuron dipole is too small to be detected by electrodes on the scalp. Additionally, as electrodes detect the sum of charges, they can only detect a dipole when they are closer to the negative or positive end, as if they are equidistant from each pole, the charges cancel and the electrode measures a net zero. Therefore, in order for an EEG electrode to detect anything, many neurons must receive synaptic input synchronously/simultaneously in order for the dipole charge to be large enough, and neurons being recorded must be parallel to one another, so that the charges from their dipoles do not cancel each other out. EEG cannot distinguish between excitatory and inhibitory neural activity as the measured extracellular charge that makes up the dipole depends on both the orientation of the neuron with respect to the electrode and where the synaptic input arrives at the neuron. A negative deflection of the EEG signal represents only a net negative charge being recorded by the electrode, and a positive deflection of the EEG signal represents only a net positive charge. It is thought that it is primarily cortico-cortical and thalamo-cortical connections that are captured in EEG recordings (Buzsaki, 2006).

The EEG signal is therefore a measure of synchronous cortical neural activity (postsynaptic potentials), and can be used to detect patterns of brain activity at different frequencies or oscillations (see section 1.1.1) produced by neuronal assemblies (Jackson and Bolger, 2014).

2.4.2 Measuring synchronous cortical neural activity

The EEG signal propagates through the brain via a process called volume conduction. Ions repel ions of the same charge, and this is true also in the brain extracellular space. Repelled ions repel other ions, and this continues through the medium and results in an effective "travelling wave" of charge. However, this wave cannot leave the volume it is travelling in, so for the EEG signal to continue through the dura, skull, and scalp and reach the electrodes during an EEG recording, capacitive conduction must occur. This is when an insulator, such as the dura, impedes for example positive charge flow, and positive charge builds up in the conductor on one

side of the insulator. This, in turn, repels positive charge from the conductor on the other side of the insulting layer. If this continues across a stack of insulating layers acting as capacitors, the positive charge can effectively move through these capacitors via capacitive conduction. Electrode gel is placed on the scalp, and once the positive charge builds in this medium, it can again flow to reach the electrode, which records the EEG signal.

The extracellular charges from the neural dipole propagate to the recording electrodes in the EEG montage in this way, inducing current in the recording electrode. Ideally, the reference electrode is not exposed to the ionic current from the dipole, thus there is a current/potential difference between the recording and reference electrodes, which is the measured voltage. If the measured voltage is larger, this indicates a larger current being detected at the recording electrode which is indicative of a larger dipole charge or neural polarisation signal. Thus, recorded EEG signal is typically on the order of micro-volts and shows the underlying neural activity.

2.4.3 Analysis of recorded signals

EEG records neural oscillations which represent the rhythmic activity of the brain (see section 1.1.1). These signals are typically analysed in the time-frequency domain and important features of these signals include the frequency, the phase and the power (Cohen, 2014). Frequency is a measure of the speed of oscillations, power represents the amount of energy in a specific frequency band and is a measure of the amplitude of the signal at that frequency, and phase represents the degree of synchrony in the activity of the neurons being recorded. The phase of an EEG signal represents the intra- and inter-region coherence. A phase-aligned signal within an EEG recording from a single channel indicates that the neuronal population firing being detected is in synchrony. The phase difference between signals can inform you of the coherence between the signals (Cohen, 2014).

2.5 Detecting frequency mixing using three-way phase relationships

A novel method for detection of three-way phase relationships between three signals with different frequencies, was developed by my co-workers, to detect the presence of FM in neural signals (both single cell and EEG recordings)(Figure 2.3). This relationship is a higher order nonlinear interaction. In this section, the method is introduced. Additionally, the method is tested using synthetic data to determine the robustness of the FM detection.

2.5.1 Three-way phase relationship detection method

Definition of a triplet

Going forward, a triplet is defined as a set of three signals which have frequencies $f_1/f_2/f_1$-f_2 (f_Δ) or $f_1/f_2/f_1{+}f_2$ (f_Σ). Only three-way phase relationships between triplets are tested. Henceforth, a triplet which has a significant three-way phase relationship is referred to as a FM triplet, i.e., a triplet that displays FM.

Spectral analysis

For detection of FM, the spectral power and instantaneous phase were calculated across both time and frequency (a time frequency decomposition) using a Wavelet transform. A complex Morlet mother wavelet with a sigma value of 15 was used. The instantaneous phase is represented in Figure 2.3i.

Detection of a three-way phase relationships using the total independence test

FM introduces a three-way phase relationship (Figure 2.4 A-C), or a dependence, between three signals of different frequencies. We thus require a way to test if, for a triplet with phase-angle observations $\mathcal{D} = \{(X_i, Y_i, Z_i), i = 1, \ldots, n\}$, the instantaneous phases X, Y, and Z, are

independent. A total independence test (Rubenstein, 2015; Rubenstein et al., 2016), is used between the array of phase-angles of each signal ($f_1/f_2/f_\Delta$ or f_Σ) to detect any significant three-way phase relationships, and thus identify the presence of FM. This involves the construction of a test statistic which must be compared to an appropriate null distribution. The wild bootstrap method (Davidson and Flachaire, 2008) is employed to generate temporally dependent null permutations of the phase-angle arrays, to create an appropriate null distribution, with which to compare the test statistic. A measure of FM, which we term the Higher Order Interaction (HOI) strength, is computed, using a normalisation of the test statistic relative to its null distribution (using the 95% quantile). Finally, depending on the given data set, permutation cluster tests are implemented to identify group-level significance and to control for multiple hypothesis testing.

Test statistic

A test statistic is constructed. Ideally, this has a large value when none of the signal phases are independent (i.e. they have dependence) and a small value when one of the phases is independent of the other two (i.e. no three-way phase relationship exists). To determine whether the test statistic is 'large' requires comparison with a null distribution, which is detailed in the wild bootstrap section of these methods.

First, a radial basis function kernel is used to determine the similarity of each phase-angle compared to every other phase-angle in each individual signal separately, generating a Reproducing Kernel Hilbert Space (RKHS), which is essentially a similarity matrix (Figure 2.3 ii). The RKHS is an embedding space where every individual phase-angle is positioned relative to every other phase-angle. Element-wise multiplication (Hadamard product of the matrices) of the three produced similarity matrices is performed to produce a test matrix (Figure 2.3 iii). If all three elements being multiplied are large at the same time, this indicates a relationship between the phase-angles of the three signals, thus a larger value in the test matrix indicates a relationship between the three phase-angles of the signals. Therefore, the mean value of all of the elements in the test matrix is a measure of the dependency between the phase-angles of

the three signals and this is defined as the test-statistic. The test-statistic is a singular value that is compared with its own distribution under the null hypothesis, i.e. relative to a null distribution, to see whether it is significant. When the test statistic is found to be greater than a defined threshold in the null distribution, the null hypothesis is rejected and the value for the test-statistic is considered to be significant (here we choose the significance level $\alpha = 0.05$ - meaning that the test statistic must be larger than 95% of the null test-statistics to reject independence) (Figure 2.3 v).

Wild bootstrap

Bootstrap methods must accurately approximate the distribution of test-statistics, given the chosen null hypothesis. It is important that the process for generating bootstrap samples should resemble closely the true data generating process of the observed data. Standard permutations (random shuffling of indices) of temporal data will remove any temporal dependence within the signals, generating bootstrap samples that do not accurately resemble the original signal. Here we use the wild bootstrap method (Davidson and Flachaire, 2008), to construct an appropriate null distribution. The wild bootstrap allows the phase-angles to be randomly permuted whilst still retaining the temporal dependence between consecutive phase-angles (Figure 2.3 iv). This creates a null distribution of test-statistics for a given triplet, such that the original test statistic can be evaluated for its significance. A p-value is computed which represents the proportion of the finite-sample null distribution for which the test-statistic is greater than, i.e., a small p-value is returned when the original test statistic is greater than the majority of wild bootstrap permutations. The p-value measures the probability that the relationship between the three frequency components would appear by chance (Figure 2.3 vi).

Higher order interaction strength

Whilst the three-way phase relationship/dependence either exists or it does not, i.e. FM is occurring or it isn't, and this is demonstrated by whether the test-statistic is significant or not, the strength of the three-way phase relationship or FM within the measured signals is likely

to be dependent on the power of inputs signals and is an interesting metric. Therefore, to measure the strength of FM, a Higher Order Interaction (HOI) strength is defined and this is computed by dividing the test statistic by the 95% confidence interval of the null distribution (Figure 2.3 vii). For this measure to be valid, it is important that sufficient null permutations are computed to stabilise the 95% confidence interval, such that the HOI strength is stable with repeated calculations. The number of permutations is set to 5000, which allows the HOI strength to be stable in robustness tests on synthetic data (see section 2.5.2).

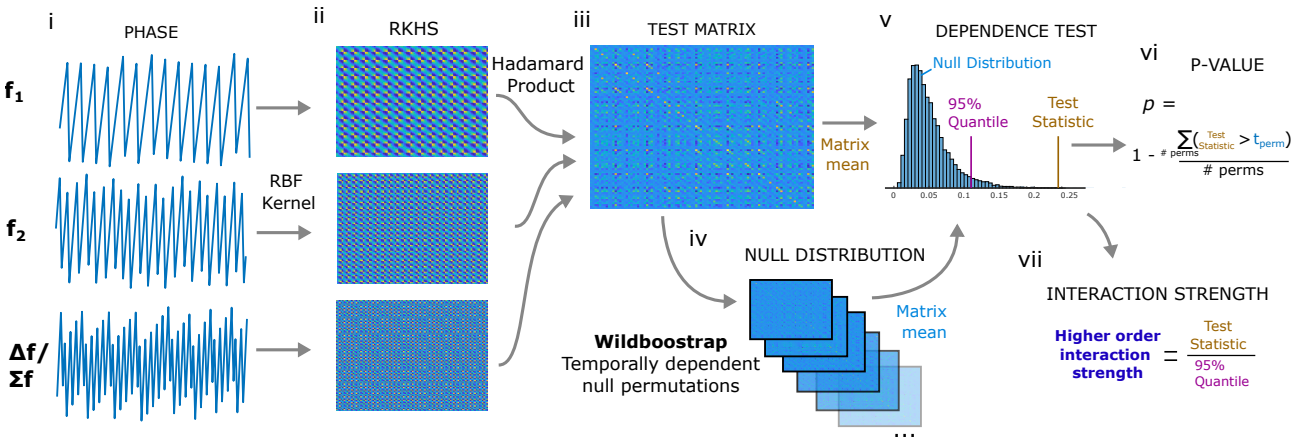


Figure 2.3: **Workflow for detection of significant three-way phase relationships** Significant three-way phase relationships are indicative of Frequency Mixing (FM). A three-way phase relationship, or a dependency, between the phases of three signals can be computed as follows. (i) Three arrays containing the instantaneous phases of three signals are created. The radial basis function kernel is used to compute (ii) a similarity matrix for each signal, which undergo element-wise multiplication to produce a (ii) test matrix. The mean of this test matrix is the test statistic, and a (iv) null distribution is created to compare this test statistic to. Comparison of the test-statistic to this null distribution generates a (vi) p-value, which indicates whether all three of the signals have phases which are significantly dependent on the phases of the other signals. (vii) Normalisation of the test-statistic to the null distribution creates a value termed the Higher Order Interaction (HOI) strength, which represents the strength of the dependency between the phases of the three signals.

2.5.2 Methodology testing

In the previous section, the generation of a measure of FM strength for a triplet of frequencies within a neural signal is outlined (see section 2.5.1). As this is a novel methodology, the validity of the HOI strength as a measure of FM strength was tested.

Synthetic data

The method for generating a HOI strength value for a triplet was tested using synthetic data. This synthetic data contains the output signal of two input signals applied to a nonlinear activation function, thus FM of signals occurs here, and specific triplets involving the applied signals (f_1 and f_2) and the FM product output signals (f_Δ and f_Σ), should be significant when the three-way phase relationship detection method is applied.

To create the synthetic data, two oscillatory signals components are combined by their simple addition (Figure 2.4 A) and provided as input to a nonlinear activation function (here a quadratic function)(Figure 2.4 B),

$$F(s) = B + Cs + Ds^2, \tag{2.1}$$

where $s = (S_1 + S_2)$ is comprised of two oscillatory signals and expansion of this result gives,

$$F(S_1 + S_2) = B + CS_1 + CS_2 + DS_2^1 + DS_2^2 + 2DS_1S_2. \tag{2.2}$$

The transformation of the two input signals results in an output signal which is comprised of:

1. Signals with frequencies of the original inputs.
2. The harmonics of the inputs.
3. Signals with frequencies equal to the difference and sum of the inputs.

See Figure 2.4 C for a visual description of this nonlinear process. White noise is also added to the resulting signal.

Two groups of synthetic data signals were used in Figure 2.4. Within each group, each synthetic data signal consisted of four oscillatory signals, which produced two FM interactions. The signals were constructed with a duration of 60 seconds and a sampling rate of 1000 Hz. Signals for group 1 were constructed with one common nonlinear FM interaction (f_1 = 7Hz and f_1

= 18Hz) and one random FM interaction (any pair of frequency components between 1-45 Hz). Signals for group 2 were constructed with two random FM interactions (any two pairs of frequency components between 1-45 Hz). At the group-level, only the FM interaction that is common to group 1 should be detectable.

Evaluation of individual signal The average time-frequency Wavelet decomposition of each group reveals distinct peaks at the expected sum (25Hz) and difference (11Hz) frequencies in group 1 (Figure 2.4 Ei) and no distinct peaks in group 2 (Figure 2.4 Eii). The significant triplets, as determined using the dependence test pipeline (see section 2.5.1), in a single synthetic signal from group 1 (mixing pairs: 7Hz/18Hz and 4Hz/35Hz) is displayed as a 3D scatter plot (Figure 2.4 F) and the expected sum and differences of each mixing pair is indeed observed.

Hypothesis driven approach Next, taking a hypothesis-driven approach, significant differences at the group level are examined. To compare at the group-level, the HOI strength is used to represent FM strength at a given triplet for each synthetic data signal (see section 2.5.1). As expected, a significantly larger HOI strength is seen in group 1 at both the sum (25Hz, $p = 1.92 \times 10^{-12}$) and difference (11Hz, $p = 2.05 \times 10^{-12}$) triplets, compared to group 2 (Figure 2.4 G).

Data-driven approach In circumstances when the input signals are not known, a hypothesis driven approach cannot be used. The aim is to detect any significant triplets (and by extension FM), and not compare the HOI strength of a specific triplet. To do this, permutation cluster testing is employed to identify significant clusters of triplets (see section 4.2.6) for details. As expected, significant clusters of significant triplets at the sum and difference frequencies are found (Figure 2.4Hi; sum=25Hz, $p = 0$, $n_{perm} = 1 \times 10^4$; diff=11Hz, $p = 0$, $n_{perm} = 1 \times 10^4$).

Robustness of methodology To examine the robustness of the methodology, we asked whether the three-way phase relationship is still significant (both at the sum and difference frequencies) after down-sampling of the synthetic signals prior to testing (Figure 2.5 A). For

each down-sampling value, 20 synthetic signals were constructed, each with FM pairs 7Hz/18Hz and 4Hz/35Hz. The HOI of all mixing triplets were averaged for a synthetic signal and the distribution across the 20 repeats are plotted in Figure 2.5A.

The expected triplets appear to retain the significant three-way phase relationship, up to a decimation factor of 0.005 (down-sampled by 200 times). At lower decimation factors (< 0.005) the expected nonlinear dependence is undetectable. This is relevant because the EEG recordings that this methodology is applied to, are down-sampled 20 times (decimation factor of 0.05). Down-sampling is not done prior to time-frequency decomposition - the down-sampling occurs on the instantaneous phase signal just prior to the total independence test. These results suggest that the methodology is robust to down-sampling of the instantaneous phase signals (within the range applied to human and mice data in this thesis), and that there exists a monotonic negative relationship between the average HOI strength and decimation factor.

We also examine the robustness of our methodology to the amplitude of the nonlinear interaction b and the signal to noise ratio. The triplet appears to retain the significant three-way phase relationship with a weak coefficient b of nonlinear interaction (Figure 2.5 B, $b > 0.1$), and with a poor signal to noise ratio (Figure 2.5 C, signal:noise ratio $< 1 : 10$). If the amplitude of the nonlinear coefficient in the activation function b ($a = 1, c = 1$) (Figure 2.4 B), is less than $b \sim 0.1$, dependence can no longer be detected. A monotonic negative relationship between average HOI strength and amplitude of nonlinear coefficient exists. If the the signal-to-noise ratio decreases beyond $1 : 10$, dependence can no longer be detected. Additionally, a gradual reduction of the average HOI strength is observed as noise is increased. Signal to noise ratio is defined as the ratio of the nonlinear interaction amplitude b and the noise amplitude c. Together, these results suggest that the method will be sufficient to detect FM in noisy signals such as neural signals recorded via EEG.

To summarise, here, a novel method for detecting three-way phase relationships between three signals has been described and tested. The input and output signals of a frequency mixer exhibit this three-way phase relationship. Thus, if this methodology is applied to signals with frequencies that can exist due to FM i.e. $f_1/f_2/f_1\text{-}f_2$ (f_Δ) or $f_1/f_2/f_1{+}f_2$ (f_Σ) (triplets),

FM can be detected. The methodology was validated on synthetic data, and robustness tests suggest that it should also be effective on noisy neural signals.

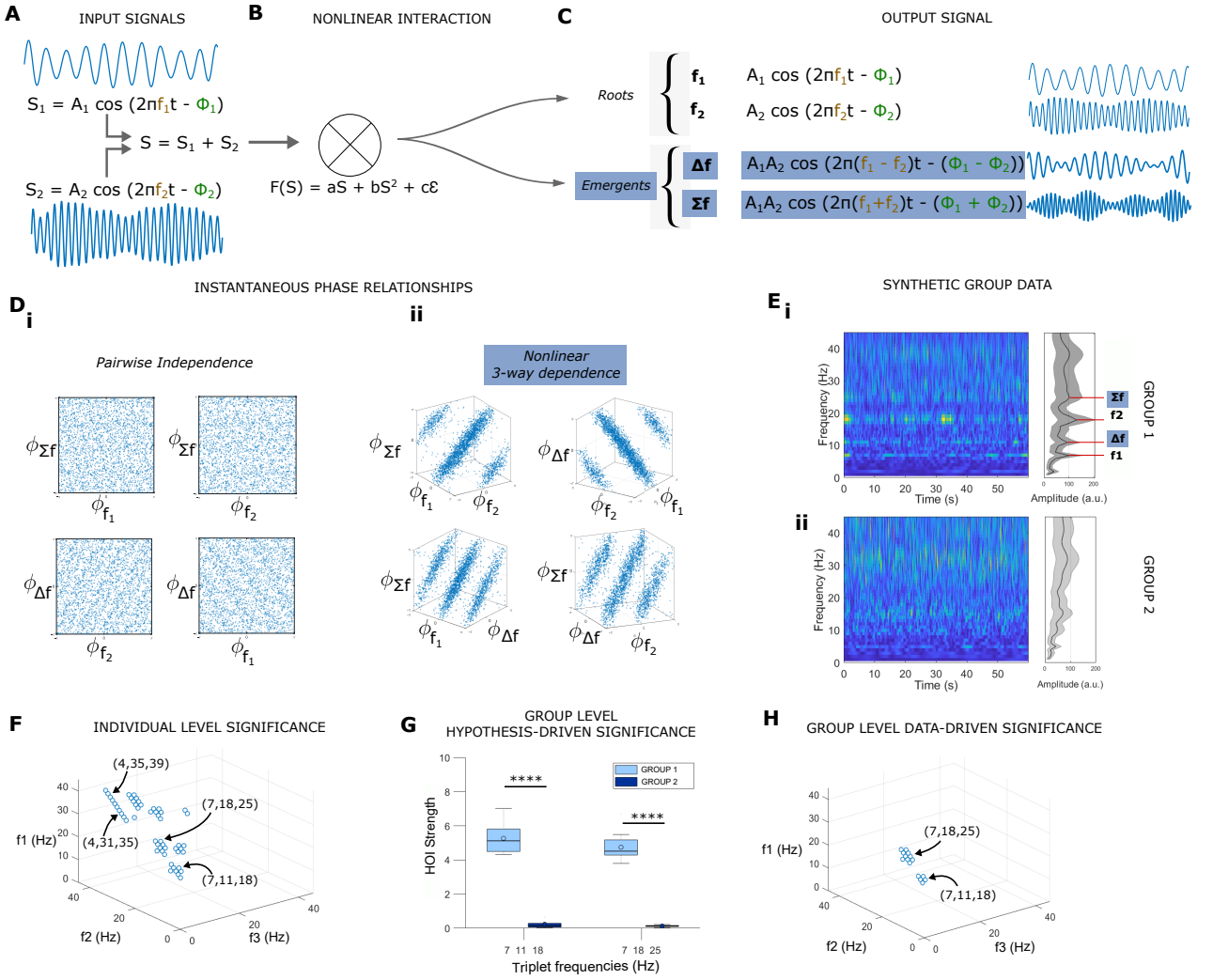


Figure 2.4: **Testing three-way phase relationship methodology with synthetic data** (A) Synthetic signals (S1 and S2) are first constructed and (B) provided as input into a quadratic nonlinear activation function (plus noise ϵ) resulting in (C) outputs at the applied frequencies (f_1, f_2) and the sum and difference frequencies (f_Δ, f_Σ). (D) Scatter plots of instantaneous phase relationships reveal (i) no pairwise dependence between any combination of the input and output signals and (ii) a three-way relationship between any combination of the input signals and output signals. (E) 10 synthetic samples are constructed with the nonlinear interaction of $f_1 = 7$ Hz and $f_2 = 18$ Hz and a second nonlinear interaction of two randomly chosen frequencies (between 1-45 Hz) forming group 1. A further 10 synthetic samples are constructed with two separate nonlinear interactions of randomly chosen frequencies forming group 2, i.e. total number of Frequency Mixing (FM) components within each sample is consistent, but only group 1 shares a common FM interaction. An average wavelet time-frequency decomposition across samples in (i) group 1 and (ii) group 2, shows the expected peaks at the sum and difference of $f_1 = 7$ Hz and $f_2 = 18$ Hz for group 1, but not group 2. (F) A scatter plot of significant FM triplets for a randomly chosen signal from group 1 (nonlinear mixing of $f_1 = 7$ Hz and $f_2 = 18$ Hz, plus mixing of $f_1 = 4$ Hz and $f_2 = 35$ Hz) displays the expected triplets. (G) A hypothesis driven approach to compare the two groups at the expected sum and difference triplets produced by mixing of $f_1 = 7$ Hz and $f_2 = 18$ Hz. A significantly larger HOI strength is observed in group 1 for both triplets. (H) A data-driven approach testing significance (using a cluster permutation test) across all frequency combinations (< 45 Hz) finds the expected sum and difference triplets at the group level.

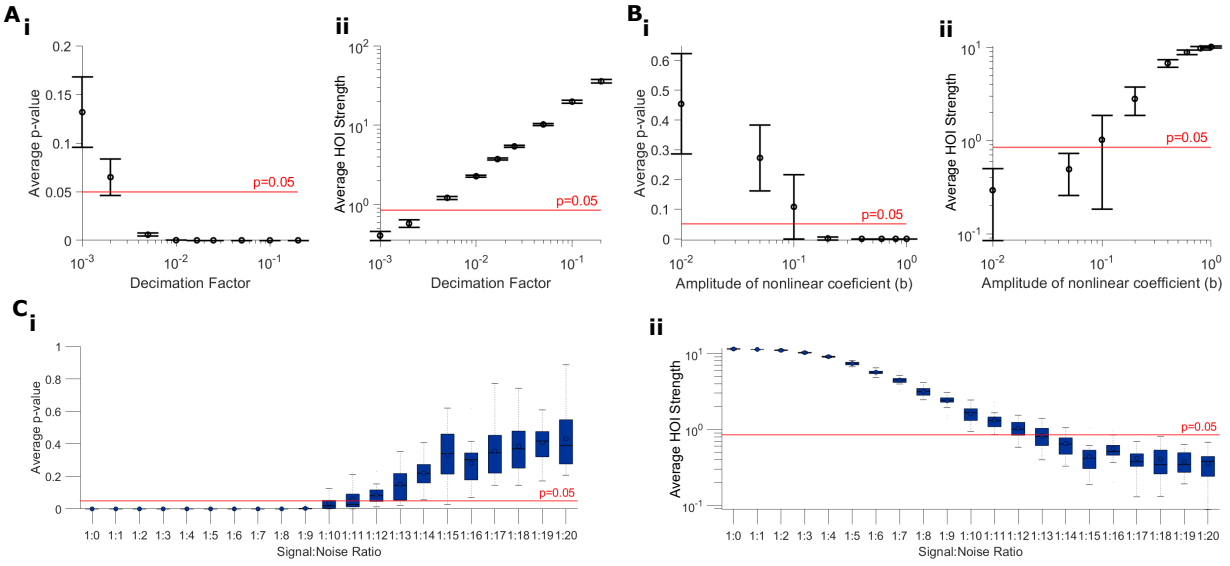


Figure 2.5: **Testing the robustness of frequency mixing detection** Using synthetic Frequency Mixing (FM) triplets, the robustness of the methodology is tested against (a) the decimation factor (down-sampling rate) of the phase signal, (b) the signal-to-noise ratio and (c) the amplitude of the nonlinear coefficient b used in the nonlinear interaction function.

Chapter 3

Nonlinear frequency conversion at the single neuron

3.1 Introduction

3.1.1 Mechanism of temporal interference

The mechanism by which TI of kHz electric fields stimulates neural activity is currently unknown (see section 1.1.5), and whether FM or another nonlinear frequency conversion process underlies the neurostimulation process is an open question (see section 1.3.4). In this chapter I aim to investigate these questions at the level of the single neuron. Below, I summarise the possible neurostimulation mechanisms that I will consider.

Mechanism option 1. Linear superposition of input fields (no subthreshold transmembrane oscillation at f_Δ)

The TI neurostimulation is mediated by a linear superposition of the applied electric fields (Figure 3.1 A). In this case, the membrane is polarised at the mean of the applied kHz frequencies and an AP is evoked when the amplitude of the combined field is sufficiently large. Since the amplitude of the combined field is modulated, i.e. the amplitude reaches maximal

value periodically at f_Δ, if the electric field strength at the maximal value is large enough and exceeds the threshold for neuronal firing, an AP is evoked at f_Δ. I expect that in this case, f_Δ should be observed in the suprathreshold neural activity but not in the subthreshold activity. A suprathreshold response at f_Δ has indeed been observed previously (Grossman et al., 2017).

Mechanism option 2. Nonlinear frequency mixing of input fields (subthreshold transmembrane oscillation at f_Δ and f_Σ must exist)

TI neurostimulation is mediated by a nonlinear FM process that leads to membrane polarisation at f_Δ and f_Σ of the applied field frequencies. To put this into context with the definition of nonlinearity at the neuron (see section 1.2.2 and section 1.2.3), the input to the system in this case is the extracellular ionic currents created by the applied extracellular electric fields. We can assume that these currents, like the applied electric fields, alternate at the applied frequencies f_1 and f_2. The output of the system is the transmembrane voltage. If our system is nonlinear, i.e. the change in the output amplitude (membrane potential) is not linearly proportional to the change in the input amplitude (extracellular ionic currents), the output will depend on the multiplication of the input components. A multiplication of the input components will convert the applied frequencies to new frequencies, i.e. f_Δ and f_Σ. Nonlinearity capable of this is well defined in neurons (see section 1.2.3), yet to-date there has not been direct evidence of such a frequency conversion at the level of the single neuron.

The phenomenon of generating f_Δ and f_Σ is called FM (Figure 3.1 B). FM is well characterised in electronics (see section 1.3.1)(Breed, 2011). In FM, input signals (e.g. an amplitude modulated signal that has frequency components at f_1 and f_2) are applied to a nonlinear mixer within a circuit. The frequency mixer multiplies the inputs to create a signal that contains frequency components at f_Δ and f_Σ. If it is a perfect frequency mixer, there will not be frequency components at f_1 and f_2 in the output signal. In reality this is rarely the case, even in electronics. If only f_Δ is desired, as in the case of envelope detection or heterodyne demodulation applications, a low-pass filter, for example in the form of a resistor and a capacitor, is added to the circuit to remove f_Σ.

To put this into the context of neural activity, in the case of TI stimulation, the membrane

is exposed to extracellular ionic currents oscillating at kHz frequencies f_1 and f_2, and via multiplication of these signals, it is polarised not just at f_1 and f_2, but also at f_Δ and f_Σ.

The origin of the FM phenomenon from the nonlinearity of the neural membrane polarisation dynamics can be explained mathematically using the Taylor series approximation of the membrane potential. A Taylor series is an approximation of a continuous function. The Taylor series represents a function $f(x)$ near a point $x = a$ via a power series

$$f(x) = \sum_{k=0}^{\infty} f^{(k)}(a) \frac{(x-a)^k}{k!} \tag{3.1}$$

Where $(x-a)^k$ is the k power of $(x-a)$, $f^{(k)}(a)$ is the value of the k derivative of $f(x)$ at $x = a$, and $k!$ is the factorial of k. In our case we use the Taylor series to approximate the membrane potential (V_m) as a function of the applied extracellular ionic currents (I_1 and I_2) near its resting potential, where

$$I1 = A_1 sin(2\pi f_1 t) \tag{3.2}$$

$$I2 = A_2 sin(2\pi f_2 t) \tag{3.3}$$

The first term in the Taylor Series is a constant (i.e. the resting membrane potential, V_0), the second term is a linear dependency on the input variables (i.e. $\alpha(\mathrm{I}_1 + \mathrm{I}_2)$), the third term is a square dependency on the input variables (i.e., $\beta(\mathrm{I}_1 + \mathrm{I}_2)^2$; the first nonlinear term of the equation) etc.

$$\mathrm{V}_m = \mathrm{V}_0 + \alpha(\mathrm{I}_1 + \mathrm{I}_2) + \beta(\mathrm{I}_1 + \mathrm{I}_2)^2 + \ldots \tag{3.4}$$

In the case of small fluctuations around a set value (in our case a fluctuation in the transmembrane potential around its resting potential), the function can be well described by the first few terms of the Taylor series. In this case, the significant bulk of nonlinearity is represented in the square term of the Taylor Series. Thus, if we assume that nonlinearity is present in the polarisation of the neural membrane, the membrane polarisation will be proportional not just to the sum of the applied TI currents, but also to the square of the sum of the applied TI currents and thus is equal to

$$A_1^2 sin^2(2\pi f_1 t) + 2A_1A_2 sin(2\pi f_1 t) sin(2\pi f_2 t) + A_2^2 sin^2(2\pi f_2 t) \tag{3.5}$$

and using the following trigonometric identities,

$$sin^2(\alpha) = \frac{1}{2}(1 - cos(2\alpha)) \tag{3.6}$$

$$sin(\alpha)sin(\beta) = \frac{1}{2}(cos(\alpha - \beta)cos(\alpha + \beta) \tag{3.7}$$

can be rewritten as

$$\frac{1}{2}(A_1^2 + A_2^2) + A_1A_2 cos(2\pi t(f_1 - f_2)) + \frac{1}{2}[A_1^2 cos(2\pi 2 f_1 t) + A_2^2 cos(2\pi 2 f_1 t)] + A_1A_2 cos(2\pi t(f_1 + f_2)) \tag{3.8}$$

resulting in membrane polarisation containing a DC component, and frequency components at f_Δ, f_Σ, and harmonics of the input frequencies

I expect that if TI neurostimulation is mediated by a nonlinear FM process, I should be able to

observe f_Δ and f_Σ, as well as $2f_1$ and $2f_2$, in the subthreshold neural response to TI stimulation. However, the low-pass filtering property of the cell membrane (Deans et al., 2007), attenuates the polarisation at f_Σ, $2f_1$, and $2f_2$, leading to a polarisation that is dominated by f_Δ. To increase the probability of detecting f_Σ, I will also test TI stimulation with low frequencies so that f_Σ is closer to the frequency range of endogenous neural activity.

Mechanism option 3. Nonlinear envelope detection via rectification (subthreshold transmembrane oscillation at f_Δ but not f_Σ must exist)

TI neurostimulation is mediated by an envelope detection phenomenon via a nonlinear rectification and smoothing filtering process (Figure 3.1 A). In electronics, a simple envelope detector can be implemented by applying the input signal to a diode for rectification and the output of the diode to a capacitor and resistor in parallel (i.e. parallel RC circuit) for smoothing. A diode conducts electric current in one direction and blocks it in the other direction (when it is forward biased). When an amplitude modulated AC signal is applied to the input of the diode, it will be half-wave rectified at the output of the diode, i.e. the diode will output only a half cycle of the input signal (only the positive half) while blocking the other half (i.e. outputting zero). In a parallel RC circuit, the capacitor and resistor have the same voltage. When the half-wave rectified voltage is fed to a parallel RC circuit, the capacitor is directly charged during the rising phase of the signal (i.e. the voltage of the signal is larger than the voltage of the capacitor) and discharged via the resistor during the falling phase (i.e. the voltage of the signal is smaller than the voltage of the capacitor). The discharging time constant of the capacitor is equal to the product of the capacitor and resistor values ($\tau = RC$).

In an envelope detector that works via half-wave rectification, the values of the capacitor and resistor are chosen so that the discharging time of the capacitor is significantly larger than the period of the input signal, i.e. $\tau >> T_c$, where $T_c = 1/f_c$, and f_c is the carrier frequency of the input signal. This is so the capacitor does not discharge (or discharges very little) during the falling phase of the input signal. In this case, the output voltage (i.e. the voltage across the capacitor) follows the envelope of the signal. Since the output contains both the AC and DC component of the envelope, a high-pass filter is typically added at the output of the parallel

RC circuit to remove the DC component.

If the discharging time constant (τ) is not sufficiently large compared to the period of the input signal (T_c), the output signal will have a strong ripple distortion since the capacitor will discharge during the falling (or constant) phase of the rectified signal. On the other hand, if the discharging time constant (τ) is too large compared to the modulation period of the input signal (T_m), the capacitor will not discharge sufficiently during the falling phase of the envelope (a phenomenon called negative peak clipping which is used in peak detection applications). Thus, the RC values must be carefully selected so that the discharging time constant is sufficiently larger than the signal's period and sufficiently smaller than the signal modulation period $T_c << \tau << T_m$. These requirements can only be achieved when the signal modulation frequency is much smaller than the signal frequency, i.e. $f_m << f_c$.

If TI neurostimulation is mediated by such a rectification-based envelope detection mechanism, I expect to observe a DC offset and f_Δ, but not f_Σ, $2f_1$, or $2f_2$ in the subthreshold membrane response. In addition, I expect that the subthreshold polarisation at f_Δ will fail if the TI stimulation is applied with a low carrier frequency such that $f_m \approx f_c$. In this case, I expect to observe a step response rather than oscillation at f_m.

If the nonlinear process (FM or rectification) is mediated by the ion channels, the applied extracellular ionic currents must first charge the bilipid membrane at f_1 and f_2, exposing the voltage-gated ion channels to transmembrane potential at those frequencies (kHz frequencies in the case of TI), something which has not yet been seen experimentally (Grossman et al., 2017; Deans et al., 2007).

The question of TI mechanism is of interest to neuroscience (see section 1.1.5, 1.3.4, and 1.4.2). Thus far, no definitive evidence for the role of nonlinear frequency conversion, either via multiplication or rectification, during TI exists. This is due to the neurostimulation technique being investigated purely in the suprathreshold domain. However, in suprathreshold activity, f_Δ could emerge from either of the three mechanisms. If nonlinear frequency conversion is found to occur during TI, it will aid in uncovering the role of the phenomenon during the stimulation. Whether nonlinear frequency conversion (via multiplication or rectification) is the driving force

of TI stimulation-induced neural activity is important for development of the technique and work aimed towards improving its focality.

3.1.2 Nonlinear frequency conversion by individual neurons

As stated previously FM, a form of nonlinear frequency conversion, has been detected in neural activity (see section 1.3.2). A related question to whether nonlinear frequency conversion is occurring during the application of electric fields in TI, is whether the single neuron is indeed able to directly mix/rectify and smooth these applied signals and additionally, whether mixing or rectification and smoothing of endogenous inputs/currents is performed. To date, FM in both evoked and spontaneous brain activity has only been detected using measures of widespread synchronous neural activity (see section 1.3.2). Evidence of FM of applied electric fields in the brain has never been observed. As FM has been detected only in LFP recordings, this would suggest that the FM being detected is from many neurons mixing the same root signals to produce the same emergent signals (Ahrens et al., 2002; Haufler and Paré, 2019). This gives insight into the network level effects of FM, but also means that potentially differing higher order mixing occurring at the single neuron due to varied intrinsic properties, cannot be detected. Furthermore the mixing that is detectable at the network level in rodent large-scale neural activity is assumed to be originating at the single neuron, however this has never been definitively tested, other than in the suprathreshold response of the paddlefish sensory nerve cell (see section 1.3.2).Thus, it is unclear what the origin of FM is and whether it is something that originates at the polarisation of the single neuron. Discovery of this would suggest that neurons are able to multiply input signals to produce signals at new frequencies and could have implications for understanding neuronal computation.

3.1.3 Nonlinear frequency conversion in subthreshold neural activity

Additionally, if neurons are able to mix endogenous currents, whether this frequency conversion is able to occur in the subthreshold domain is an open question. It has been hypothesised that FM, a form of nonlinear frequency conversion, could exist in brain activity due to the threshold firing properties of a neuron (Kleinfeld and Mehta, 2006). Other cellular nonlinearities such as voltage-gated ion channels or morphology, or specifically network level properties could however be paramount. Detection of nonlinear frequency conversion in subthreshold neural activity has not previously been attempted. If it is present, this could suggest that some other nonlinear property/properties of the neuron is/are capable of creating nonlinear mixing of input signals. Elucidation of nonlinear properties in the subthreshold domain may aid in further understanding of the origin and functional role of nonlinear frequency conversion in the brain, and ways it could potentially be manipulated.

3.1.4 Exploration of nonlinear frequency conversion and temporal interference parameter space

At the network level, FM occurring via the integration of two oscillations with endogenous frequencies, which are commonly associated with neural activity, has been observed (Ahrens et al., 2002; Haufler and Paré, 2019). Whether neural processes support FM at applied signals of higher frequencies is yet to be explored. Additionally, the dependence of the amplitude of the emergent signals, or the strength of the FM relationship on the frequency of the applied signals (or endogenous signals involved), is unknown. One would expect the phenomena to be dependent on the amplitude of the neuronal response at the fundamental, or applied, frequencies. Therefore, due to existence of low-pass filtering by the neuronal membrane (Deans et al., 2007), an interesting question is whether the amplitude of the the emergent signals (f_{Δ} and f_{Σ}) and the strength of the FM relationship, is dependent on the frequency of the applied or root signals. A full characterisation of FM across the frequency parameter space has the potential

to provide insight into the mechanism of the phenomenon.

The question of whether FM occurs at higher frequencies is obviously also directly related to the question of whether FM is occurring and mechanistically relevant in TI stimulation. If it is, as TI is delivered at the kHz frequency range, the effect of the frequency of f_1 & f_2 on emergent FM signal strength is of interest for both understanding the phenomenon further, and also guiding choice of stimulation parameters.

Lastly, regardless of the role of FM in TI but related to the question of its mechanism (see section 1.1.5), a full characterisation of the parameter space of TI has not been undertaken. Specifically, whether there is a dependence of the applied kHz frequency and f_Δ on TI-induced neural activity. Alongside the other aforementioned investigations, this will prove invaluable for gaining insight into the stimulation mechanisms, and also providing guidance for the most effective use of the technique.

3.1.5 Characterisation of nonlinear stimulation and recording artefacts

Investigation of the production of nonlinear polarisation products is challenging when input frequencies are applied via electrical stimulation. Both stimulation and recording hardware are composed of electrical circuits and components, which can introduce nonlinearity to a system and produce nonlinear stimulation and recording artefacts respectively (Kasten et al., 2018). Additionally, the electrode-electrolyte interfaces can have nonlinear electrical properties (McAdams et al., 1995). It is thus imperative that the setup is characterised to ensure that any nonlinear products observed in neural activity recordings are truly representing neural polarisation created by nonlinear mixing at the neuron and are not confounded by a) nonlinear recording artefacts produced by nonlinearity in the recording hardware or b) stimulation at nonlinear products due to nonlinearity in the stimulation hardware.

3.1.6 Aims

In this chapter I investigate the existence and origin of nonlinear frequency conversion of exogenous electric fields at the single neuron, and probe the parameter space of the phenomenon. Furthermore, I look specifically at the presence and mechanistic role of nonlinear processes in TI neurostimulation. More specifically, my aims for this chapter are as follows:

a) Characterise and control for nonlinear artefact in experimental setup

b) Determine whether neurons exert nonlinear frequency conversion on exogenous electric fields (including TI fields)

c) Investigate how the strength of evoked neural frequency conversion depends on the frequency of the applied signals

d) Probe the origin of nonlinearity underlying neural frequency conversion at the single neuron

e) Investigate whether strength of TI neurostimulation is mediated by a linear summation of the electric fields, or a nonlinear frequency conversion via multiplication (FM), or rectification.

3.2 Methods

3.2.1 *Ex-vivo* brain slice preparation

All single neuron recordings were obtained from the soma of L2/3 cortical neurons in coronal brain slices from 4-8 week old male C57BL/6 mice brains. Anaesthesia of mice was achieved via intraperitoneal injection of 100 mg/kg ketamine and 10 mg/kg xylazine. Mice were transcardially perfused with 0–5^{o}C carbogenated dissection Artificial Cerebrospinal Fluid (aCSF) containing (in mM): 108 $C_5H_{14}C_lNO$, 3 KCl, 26 $NaHCO_3$, 1.25 NaH_2PO_4, 25 Dextrose, 3 C_3H_3NaO, 1 $Mgcl_2$, and 2 $CaCl_2$. 350-μm-thick coronal slices around the somatosensory cortex were prepared using a Vibratome (Campden Instruments LTD, Loughborough, UK). Following

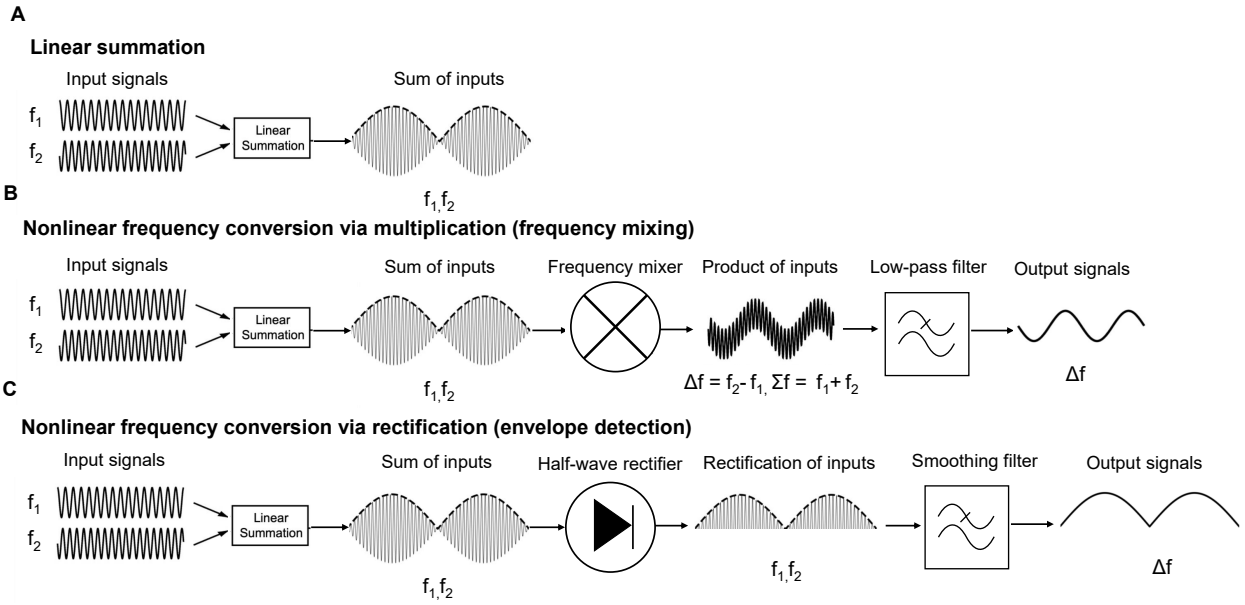


Figure 3.1: **Schematic of potential temporal interference mechanisms** (A) Linear summation of two signals with different frequencies (f_1 and f_2), results in an amplitude modulated signal with frequency components at f_1 and f_2. (B) Input of a signal with two different frequencies (e.g. an amplitude modulated signal with frequencies f_1 and f_2) to a frequency mixer results in an output signal that contains frequency components at the difference (f_Δ) and sum (f_Σ) of the two input signal frequencies. If this output signal is low-pass filtered, f_Δ can be isolated. (C) Input of a signal with two different frequencies (e.g. an amplitude modulated signal with frequencies f_1 and f_2) to a half-wave rectifier results in an output signal that contains frequency components at f_1, f_2, and f_Δ. If this output signal is subjected to a smoothing filter, f_Δ can be isolated.

sectioning, slices recovered for 2-4 hours at room temperature in carbogenated bath aCSF containing (in mM): 120 NaCl, 3 KCl, 23 $NaHCO_3$, 1.25 NaH_2PO_4, 1 $Mgcl_2$, and 2 $CaCl_2$. Following recovery, slices were placed in the recording chamber of an upright microscope (Scientifica, Uckfield, UK), and held down using a harp (Multi Channel Systems, Reutlingen, Germany). The recording chamber was continually perfused with room temperature carbogenated bath aCSF throughout the experiment.

3.2.2 Electrical stimulation

Hardware

A 0.25mm diameter platinum wire stimulating electrode (VWR, Lutterworth, UK) was positioned just touching the slice, on L2/3 cortex before commencement of whole cell patch clamp recordings. A return stimulation electrode consisting of two 2x2mm Ag/AgCl pellet electrodes (VWR, Lutterworth, UK) in a y-shape configuration, was placed in the bath (ventral side of the slice) (Figure 2.1). Electrical stimulation was delivered using a custom-written MATLAB GUI via a DAQ (USB-6216 BNC; National Instruments, Newbury, UK) and constant current isolator (LCI1107; Soterix Medical Inc, New York, NY, USA).

Waveforms

Amplitude modulated waveforms

Amplitude modulated (TI) stimulation waveforms were created by the summation of two biphasic sinusoidal waveforms (5s total, 0.5s ramp up, 0.5s ramp down, 4s stimulation) with two different frequencies, henceforth termed applied frequencies (Figure 3.2 B). Stimulation waveforms were created with a range of average applied frequencies (see Table 3.1). For clarity, subsequently when stimulation is referred to as having an average applied frequency of for example 1000Hz, it refers to an amplitude modulated waveform produced by the summation of two biphasic sinusoidal waveforms with frequencies $f_1 = 997$Hz and $f_2 = 1007$Hz. Summation

produces a waveform which oscillates at the mean of the two applied frequencies ($(f_1+f_2)/2$) and is amplitude modulated at f_Δ (f_1-f_2)(Figure 3.2 B). Stimulation was applied at a range of current amplitudes (in 0.5mA steps) and a 5s break (no stimulation or baseline period) preceded each 5s stimulation period. All waveforms were created in MATLAB with a sampling rate of 250kHz. This stimulation was delivered using a single electrode pair, thus emulating the electric field experienced during TI neurostimulation in the region of complete overlap, or full Amplitude Modulation (AM), of the two applied electric fields.

		Frequency (Hz)					
Stimulation frequencies		f_Δ **= 5**		f_Δ **= 10**		f_Δ **= 40**	
		f_1	f_2	f_1	f_2	f_1	f_2
	10	7	12	7	17	7	47
	50	47	52	47	57	47	87
Average	*100*	97	102	97	107	97	137
Applied	*500*	497	502	497	507	497	537
Frequency (Hz)	*1000*	997	1002	997	1007	997	1037
	2500	2497	2502	2497	2507	2497	2537
	5000	4997	5002	4997	5007	4997	5037

Table 3.1: **Frequencies of applied stimulation current waveforms**

Fixed current product, sum amplitude, and envelope amplitude waveforms

Amplitude modulated stimulation waveforms with fixed current product, fixed sum amplitude and fixed envelope amplitude were created to investigate the dependency of TI-induced neuromodulation on these parameters (see section 3.3.9). Sum amplitude is defined as the amplitude of the summed biphasic sinusoidal currents, envelope amplitude is defined as the amplitude of the summed signal envelope amplitude from peak to trough, and current product is defined as the simple multiplication of the two applied current amplitudes. For the fixed current product, three different waveforms were produced in which the current product is fixed across the three,

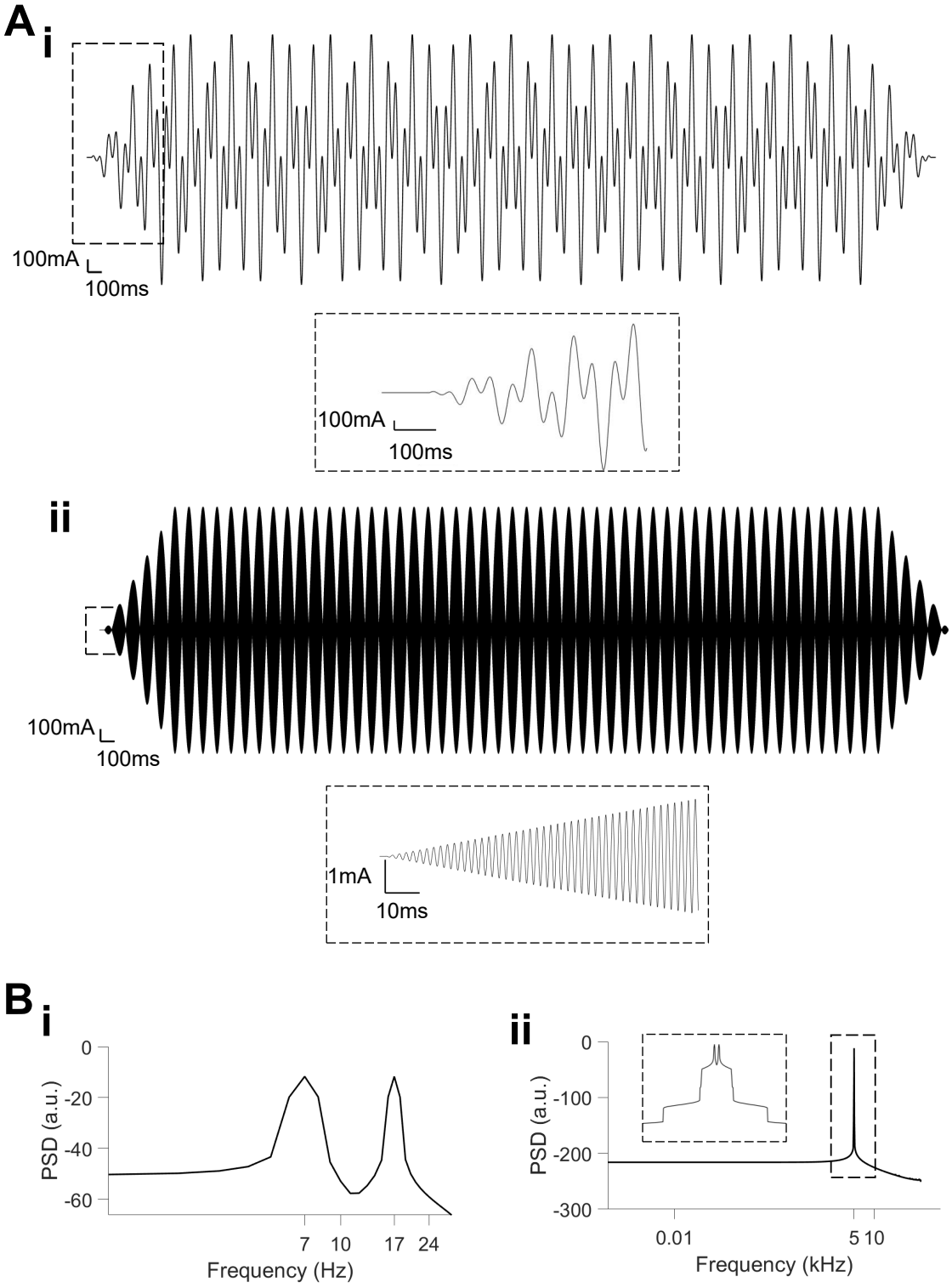


Figure 3.2: **Schematic of applied amplitude modulated stimulation waveforms** (A)(i) *Top* Example amplitude modulated stimulation waveform, created by the summation of two biphasic sinusoidal waveforms with frequencies $f_1 = 7$Hz and $f_2 = 17$Hz, $f_\Delta = 10$Hz. *Bottom* Zoom view of region inside dashed box. (ii) *Top* Example amplitude modulated stimulation waveform, created by the summation of two biphasic sinusoidal waveforms with frequencies $f_1 = 4997$Hz and $f_2 = 5007$Hz, $f_\Delta = 10$Hz. *Bottom* Zoom view of region inside dashed box. (B)(i) Power Spectral Density (PSD) of waveform in (A)(i). (ii) PSD of waveform in (A)(ii) Zoom view of region inside dashed box.

but the current sum and envelope amplitudes change (Figure 3.3 A). For the fixed envelope amplitude, three different waveforms were produced in which the envelope amplitude is fixed across the three, but the current sum and product change (Figure 3.3 B). For the fixed sum amplitude, three different waveforms were produced in which the sum amplitude is fixed across the three, but the current product and envelope amplitudes change (Figure 3.3 C).

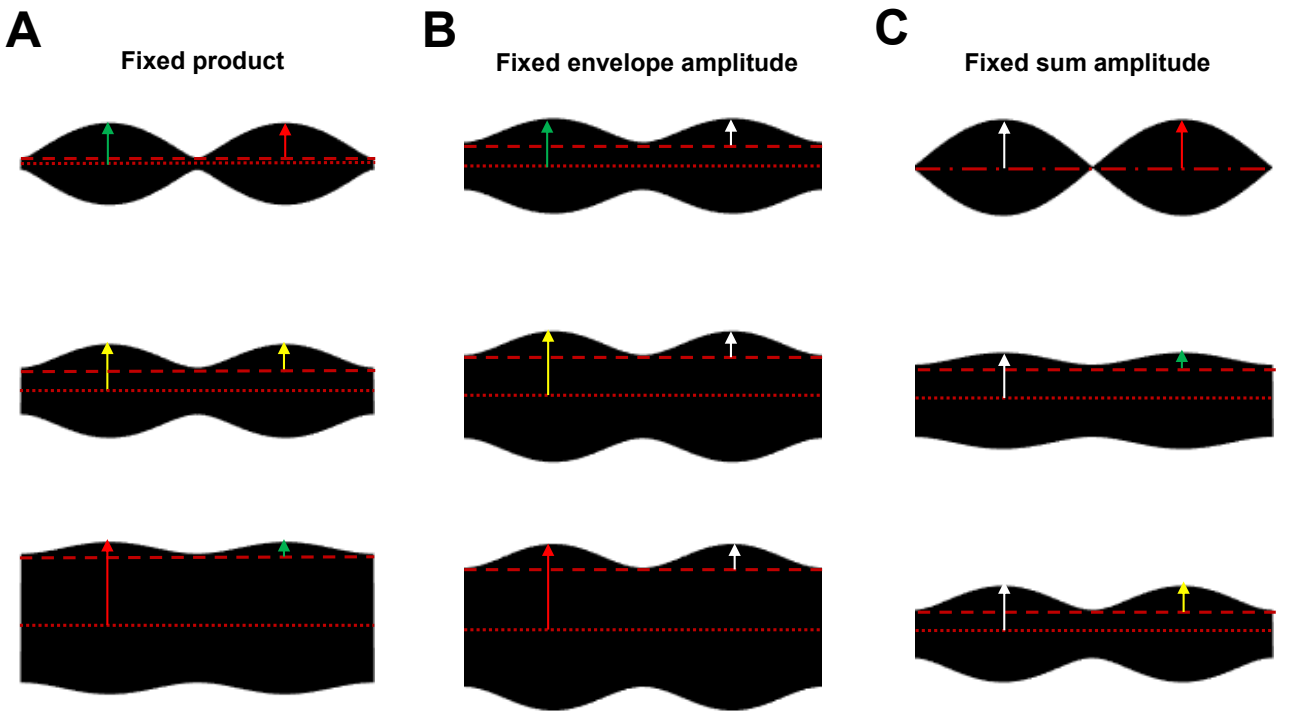


Figure 3.3: **Schematic of fixed sum amplitude, fixed envelope amplitude and fixed product waveforms** For all waveforms, the left arrow indicates the sum amplitude and the right arrow indicates the envelope amplitude. (A) Example stimulation waveforms for the three fixed current product conditions. In all three conditions, the current product is fixed but the current sum and envelope amplitudes change. Waveform amplitude is normalised to the smallest current sum across all conditions, which in this example is 1mA. (B) Example stimulation waveforms for the three fixed envelope amplitude conditions. In all three conditions, the envelope amplitude is fixed but the current sum and product change. Waveform amplitude is normalised to the smallest current sum across all conditions, which in this example is 1mA. (C) Example stimulation waveforms for the three fixed sum amplitude conditions. In all three conditions, the current sum is fixed but the current product and envelope amplitudes change. Waveform amplitude is normalised to the smallest current sum across all conditions, which in this example is 1mA

3.2.3 Whole cell patch clamp recording

Patch electrodes were pulled from filamented thin-walled borosilicate glass capillaries (World Precision Instruments, Hitchin, UK) using a horizontal Flaming–Brown micropipette puller (P1000; Sutter Instruments, Novato, CA, USA). Electrode tip resistance immediately after pulling ranged from 5-8 MΩ. Patch electrodes were filled with internal solution containing (in mM): 130 $KMeSO_4$, 8 NaCl, 2 KH_2PO_4,2 Dextrose and 10 HEPES. Whole cell patch clamp recordings were taken in current clamp mode (no holding current) using an amplifier (MultiClamp 700B; Molecular Devices Ltd) and digitiser (Digidata 1550b; Molecular Devices Ltd), and data were acquired using pClamp software (Molecular Devices Ltd, Wokingham, UK) with a sampling rate of 100kHz. The stimulation electrode was 50-100µm from the recorded neuron in the coronal plane. Following successful break-in and before each electrical stimulation, a membrane test was run on the cell to gather membrane statistics. Furthermore, a protocol comprising of current steps increasing in amplitude by 50pA was run, to determine viability of the cell, resting membrane potential, and threshold for AP firing.

3.2.4 Pharmacology

Full synaptic blockade was achieved by application of an AMPA receptor antagonist (NBQX; Merck Life Science UK Ltd, #N183), NMDA receptor antagonist (DAP-5; Merck Life Science UK Ltd, #A8054) and $GABA_A$ antagonist (Bicuculline; Merck Life Science UK Ltd, #14340) to the bath aCSF being perfused to the slice. The resulting bath aCSF solution contained (in µM): 10 NBQX, 50 DAP-5, and 10 Bicuculline. One minute of spontaneous membrane potential activity was recorded prior to drug application and 10 minutes following, to observe elimination of postsynaptic potentials. Elimination of postsynaptic potentials was observed in 100% of cells included in analysis.

Blockade of voltage-gated and persistent sodium currents was achieved by application of Tetrodotoxin (TTX)(Abcam Ltd, #ab120054) to the bath aCSF being perfused to the slice. The resulting aCSF solution contained in µM): 1 TTX. Membrane potential response to current steps of 50pA

was recorded prior to drug application and 10 minutes following, to observe elimination of APs. Disappearance of APs was observed in 100% of cells included in analysis.

Post drug stimulation and recordings commenced 10 minutes following drug application in all cases.

3.2.5 Data analysis

All data were analysed in MATLAB (MATLAB 2019a, The MathWorks Inc.).

Membrane potential traces

For plotting of mean membrane potential, individual membrane potential traces were high-pass filtered to remove any offset (butterworth; cutoff frequency: 1Hz, order: 3) then low-pass filtered to remove high-frequency stimulation artefact (butterworth; specific filter cut-off frequencies specified in figure legends, order 5). The 10Hz average applied frequency stimulation condition was excluded from mean membrane potential trace plots due to the stimulation artefact obscuring neural polarisation at f_{Δ}. Resting membrane potential was calculated for each cell for each stimulation (mean $\pm$ standard deviation displayed on figures), as the mean membrane potential in the 0.5s of baseline period (no stimulation) preceding a given stimulation, or for baseline traces, the mean membrane potential across the first 0.5s of baseline period.

Frequency domain analysis

Power Spectral Density (PSD) plots were created by computing the PSD estimate for each timeseres, via Thomson's Multitaper Method. PSD values were normalised to the maximum PSD value in that PSD (for stimulation conditions, this is f_1 or f_2). PSDs were computed using data that was only high-pass filtered (to remove some 1/f noise), thus power at stimulation artefact frequencies can be observed.

To determine whether significant peaks in PSD plots exist at the frequencies of interest (f_Δ and f_Σ), a comparison to the noise floor of the normalised PSD was undertaken. The value for the noise floor at the frequency of interest was calculated by applying a linear fit to the log transform of the normalised PSD surrounding the frequency of interest (± 5Hz). For the 10Hz average applied frequency condition, this was (± 0.25Hz) due to the stimulation artefact at f_1 or f_2 biasing the fit otherwise. The inverse log transform of the linear fit was then calculated to generate a value for the noise floor in units of normalised PSD. The value for the noise floor at the frequency of interest was then subtracted from the value of the normalised PSD at that frequency of interest to generate a Δ normalised PSD that represents the amplitude of the peak in the PSD (noise floor to peak). If this normalised PSD value was significantly greater than zero, the power at the frequency of interest was considered significantly greater than noise and thus it was considered that neural polarisation at that frequency was occurring.

Due to the potential for nonlinear stimulation artefacts to confound the measurement of neural polarisation at the frequencies of interest in the frequency domain, a strategy was developed to subtract any artefact from the PSD. The existence of nonlinear stimulation artefacts at the frequencies of interest was determined by calculating whether the power at each frequency was significantly larger than the noise floor (as described above) in recordings of extracellular stimulation applied to a brain phantom (aCSF in the recording chamber without a brain slice). If a significant artefact was determined to be present at a frequency of interest, the nonlinear-to-linear artefact ratio was computed by taking the normalised PSD value at the frequency of interest (PSDs are already normalised to the linear artefact at f_1 or f_2, which is the maximum value). This value was then used to compute a conservative estimate of the artefact-corrected normalised PSD value in neural recordings. The 90th percentile value of the nonlinear-to-linear ratio was simply subtracted from the normalised PSD value at the frequency of interest (as normalised PSD is also normalised to the maximum value, which is the linear artefact at f_1 or f_2). This artefact-corrected normalised PSD value can then be compared to the noise floor (as described above) to determine whether there is significant neural polarisation above artefact and noise at the frequency of interest in the recording.

PSD values were only included in statistical comparisons, if the artefact corrected normalised

PSD/normalised PSD/absolute PSD value at the frequency of interest was significantly larger than the noise floor of the PSD, so as to avoid simply comparing noise levels.

Normalised PSD is plotted to represent the magnitude of neural polarisation at the frequencies of interest and these values are used for statistical comparisons. This is with the exception of analysis comparing polarisation at the frequency of interest across different average applied frequencies. Absolute PSD was used in these plots and comparisons, due to the linear artefact being smaller at higher average applied frequencies (due to low-pass filtering of the recordings by parasitic pipette capacitance), which affects normalised PSD value at the frequency of interest across applied frequencies, purely because normalisation is to different values across the applied frequencies. As the same electric field strength was applied across the different applied frequencies being compared in this case, comparison of the absolute PSD value is valid. For the comparison across average applied frequencies, the 10Hz average applied frequency condition was excluded due to stimulation artefact peaks at f_1 (7Hz) and f_2 (10Hz) potentially affecting the PSD value at f_Δ (10Hz).

For all analysis in the frequency domain, only neural recordings during stimulation where the neuron did not exhibit a suprathreshold response were included, to ensure that the values being obtained were representative of purely subthreshold neural polarisation for that neuron.

Threshold for stimulation induced action potential firing

AP threshold was defined as the lowest applied current of a given stimulation required to evoke an AP if the next current step evoked at least 3 APs, to ensure the AP was due to the stimulation and not endogenous neural activity. Action potentials were detected in an automated fashion using a peak finding algorithm on the low-pass filtered membrane potential traces. For determination of low frequency stimulation threshold, recordings were high-pass filtered (butterworth, cut off: 100Hz, order: 3), to reveal action potentials obscured by the stimulation artefact and the peak finding algorithm was employed. Thresholds were normalised to threshold for stimulation with low frequency stimulation at f_Δ for that cell, to control for differences in electric field strength across preparations, unless otherwise stated.

Statistical analysis

All data is shown as mean ± SEM. Values are presented in tables which are referred to in the text. Statistical tests are specified in respective table and figure legends. All t-tests are two tailed unless stated. In all plots, the * notation represents a statistical significance that survived Bonferonni correction. If a p-value is < 0.05 but did not survive Bonferonni correction, it is displayed on the figure.

3.3 Results

3.3.1 Characterisation of nonlinear stimulation artefact

Significant nonlinear stimulation artefact exists at the sum frequency but not the difference

In TI stimulation, the stimulation artefact is at the applied kHz frequencies and not at the frequency of interest (typically f_Δ), thus unlike in traditional tACS, recording of subthreshold signals at frequencies of interest is possible. Nonlinearity in the signal pathway (e.g. current source circuit, electrode-electrolyte interface of stimulation and recording electrodes), however, can produce signal components at f_Δ, f_Σ, and higher order mixing products. Although, these signals are too weak to stimulate neurons, they can confound the detection of nonlinear frequency conversion performed by the neuron in subthreshold recordings of neural activity. I hence aim to systematically characterise the nonlinear stimulation artefacts (f_Δ and f_Σ) in a brain phantom (i.e. a recording chamber filled with aCSF) and establish proof of principle that the TI induced subthreshold neural oscillation at f_Δ and f_Σ can be recorded.

Firstly, the existence of detectable nonlinear artefacts at f_Δ and f_Σ produced by the stimulation hardware was investigated. Visual inspection of a representative PSD plot of a recording of extracellular current stimulation with approximate frequencies typically used in TI ($f_1 =$ 2497Hz and $f_2 =$ 2507Hz), applied to aCSF without neural tissue, reveal discernible peaks at

the linear stimulation artefact (applied frequencies f_1 and f_2), the nonlinear stimulation artefact f_Σ, and other higher order mixing components. A peak at the f_Δ nonlinear stimulation artefact is not present (Figure 3.4 A). This suggests the presence of stimulation artefact at f_Σ, that could potentially be detected in cell recordings of neural activity.

To calculate the change in normalised PSD above noise at the nonlinear stimulation artefact frequencies, I subtracted the PSD value at f_Δ and f_Σ from the 1/f noise at those frequencies, computed via a linear fit at the respective frequency range. The change in normalised PSD above the noise floor at f_Δ of aCSF recordings of extracellular current stimulation is not significantly greater than zero, across the range of applied frequencies ($p > 0.05$)(Figure 3.4 B)(see Table 3.2 for all values). The data used here is comprised of recordings at the full range of applied voltages, incorporating the largest applied current densities and voltages applied to the neurons during my experiments, to control for changes in stimulation nonlinearity occurring due to changes in applied voltage. This suggests that the nonlinear stimulation artefact at f_Δ is sufficiently small to be below the noise floor, and going forward, that any peak at f_Δ in cell recordings of neural activity will be due to polarisation of the cell membrane at that frequency. Conversely, the change in normalised PSD at f_Σ is significantly larger than the noise floor at all applied frequencies ($p < 0.05$)(Figure 3.4 Ci)(see Table 3.2 for all values). This suggests that the nonlinear stimulation artefact at f_Σ is large enough to be detected above the noise floor (evident in the normalised PSD (Figure 3.4 A)). Thus, a significant artefact at f_Σ is likely to be present in any cell recordings of neural activity and this must be controlled for if neural polarisation at f_Σ is to be detected.

Given the significant f_Σ nonlinear stimulation artefact, the nonlinear:linear artefact ratio (see (see section 3.2.5) for method), i.e. the ratio between the PSD at f_Σ and the applied frequencies f_1 and f_2, was calculated to determine the expected magnitude of the artefact at f_Σ in neural recordings for each applied frequency pair. These calculations suggests that in aCSF recordings of extracellular current stimulation across a range of average applied frequencies, the nonlinear artefact is approximately 4-7 orders of magnitude smaller than the linear artefact at the applied stimulation frequency (Figure 3.4 Cii)(see Table 3.3 for all values). Additionally, the artefact decreases in magnitude as the applied frequency increases. The 90th percentile of

the nonlinear:linear artefact ratio values can be used to conservatively calculate the nonlinear artefact expected in each neural recording PSD (see Table 3.3), as it is essentially taking the maximum value without risking including outliers. This can then be subtracted from the neural recording PSD value at f_Σ to reveal any polarisation of the neural membrane at this frequency.

These results suggest that the stimulation hardware nonlinearity which may create an artefactual peak at f_Δ, is sufficiently small to be within the noise at this frequency. Thus, it is possible to detect neural polarisation at f_Δ in subthreshold neural activity recorded in this setup without any artefact subtraction, as any detectable peak at f_Δ in the recordings above noise level can be assumed to be resulting from neural polarisation. Conversely a significant detectable artefact is present at f_Σ. This nonlinear artefact is approximately 1e-4 to 1e-7 times smaller than the linear artefact. Henceforth, I use the 90th percentile value of this computed nonlinear:linear ratio to conservatively subtract the artefact from measures of neural polarisation at f_Σ (see Table 3.3 for all values).

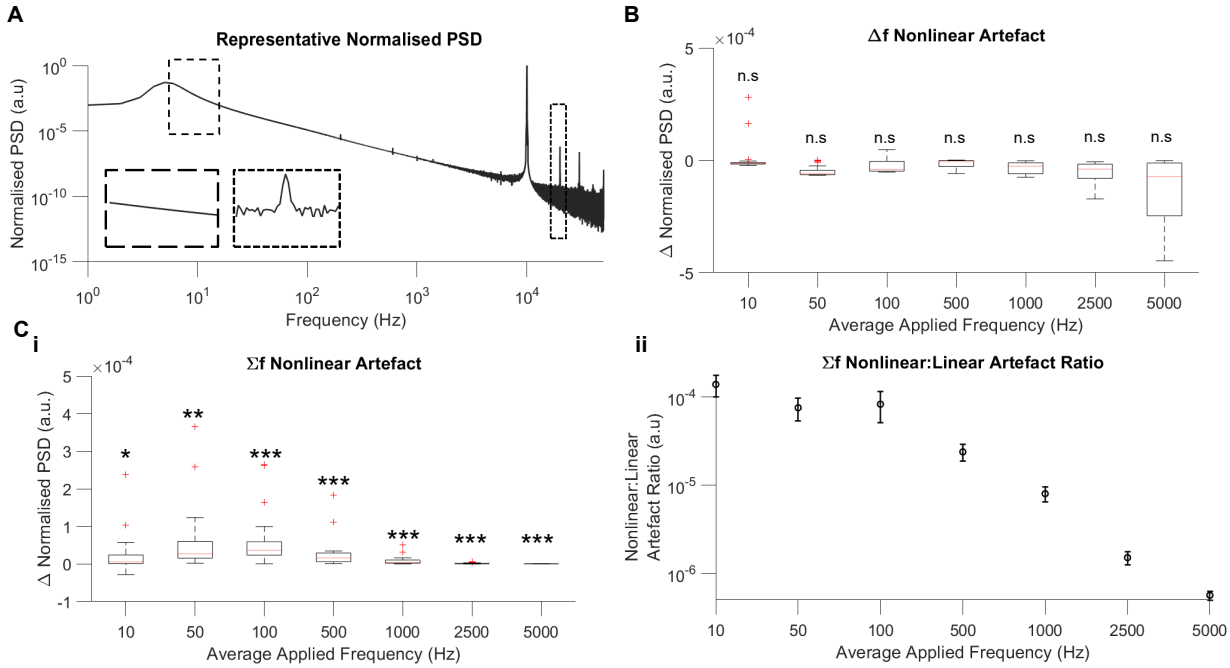


Figure 3.4: **Characterisation of nonlinear stimulation artefact in recordings** *(A-C) Significant nonlinear stimulation artefact at the sum frequency (f_Σ) but not the difference frequency (f_Δ) exists in recordings of stimulation current taken in Artificial Cerebrospinal Fluid (aCSF) without neural tissue.* (A) *Left* Representative normalised Power Spectral Density (PSD) of aCSF recording during extracellular stimulation with frequencies $f_1 = 2497$Hz, $f_2 = 2507$Hz. Zoom view of regions inside dashed boxes. Normalised to maximum value in PSD. Applied voltage is 1.5V. (B) Boxplot showing change in normalised PSD value from noise floor, at f_Δ (10Hz), of recordings taken in aCSF during stimulation with a range of average applied frequencies. One sample one tailed t-test. n.s = $p > 0.05$. Boxplots showing median (line), 25th (bottom edge) and 75th (top edge) percentiles. Whiskers extend to the most extreme data points not considered outliers. + indicates outliers. n = 40 recordings across a range of applied current densities/voltages. (C)(i) Boxplot showing change from normalised PSD value from noise floor, at f_Σ, of recordings taken in aCSF during stimulation with a range of average applied frequencies. * indicates a significantly greater difference from zero that survived Bonferroni correction. One sample one tailed t-test. * = $p < 0.05$, ** = $p < 0.005$, *** = $p < 0.0005$. Boxplots showing median (line), 25th (bottom edge) and 75th (top edge) percentiles. Whiskers extend to the most extreme data points not considered outliers. + indicates outliers. n = 40 recordings across a range of applied current densities/voltages. (C)(ii) Nonlinear:linear artefact ratio at f_Σ, of recordings taken in aCSF during stimulation with a range of average applied frequencies. Nonlinear:linear ratio was calculated by taking the PSD at f_Σ (as PSD is already normalised to maximum value (f_1 or f_2) in each aCSF recording). Mean nonlinear:linear ratio ± SEM is plotted. n = 40 recordings across a range of applied current densities/voltages.

Δ Normalised PSD	Average Applied Frequency (Hz)						
	10	***50***	***100***	***500***	***1000***	***2500***	***5000***
				f_Δ			
Mean ± (SEM)	-1.27e-06 (8.70e-06)	-4.86e-05 (3.62e-06)	-2.79-05 (3.84e-06)	-1.66e-05 (3.28e-06)	-3.32e-05 (4.09e-06)	-5.47e-05 (7.52e-06)	-0.00013 (2.10e-05)
p-value	0.56	1	1	1	1	1	1
				f_Σ			
Mean ± (SEM)	1.90e-05 (6.74e-06)	6.04e-05 (1.63e-05)	5.24e-05 (9.33e-06)	2.32e-05 (5.17e-06)	7.83e-06 (1.55e-06)	1.49e-06 (2.54e-07)	5.72e-07 (6.53e-08)
p-value	0.0039*	0.00033**	9.55e-07***	3.23e-05***	5.67e-06***	4.49e-07***	5.92e-11***

Table 3.2: **Nonlinear artefact across applied frequencies** One sample one tailed t-test. * indicates significance that survived Bonferroni correction. Bonferroni-corrected p-value = 0.0071.

Nonlinear:Linear Artefact Ratio	Average Applied Frequency (Hz)						
f_Σ	***10***	***50***	***100***	***500***	***1000***	***2500***	***5000***
Mean ± SEM	1.38e-04 (3.86e-05)	7.51e-05 (2.19e-05)	8.24e-05 (3.17e-05)	2.38e-05 (5.13e-06)	7.97e-06 (1.54e-06)	1.50e-06 (2.51e-07)	5.62e-07 (6.52e-08)
90th percentile	0.00014	0.00019	0.00013	3.39e-05	1.63e-05	4.40e-06	1.16e-06

Table 3.3: f_Σ **Nonlinear:linear artefact ratio**

3.3.2 Temporal interference evoked subthreshold neural oscillation at the difference frequency: evidence of neural frequency conversion

Conclusive verification that neural frequency conversion of two input signals of different frequencies (for example during TI neurostimulation), can be performed by a single neuron, requires evidence of the production of new frequencies in subthreshold neural activity (see section 3.1.1). These frequencies are either f_Δ (for nonlinear envelope detection via rectification), or f_Δ and f_Σ (for nonlinear frequency mixing). Hence in this section, I aim to investigate whether polarisation at the nonlinear products (f_Δ and f_Σ) in single neuron recordings of TI induced subthreshold neural activity exists. To test this, I applied the same currents as in figure 3.4 to a neuron and measured the transmembrane potential using whole cell patch clamp.

The subthreshold membrane potential of single neurons stimulated extracellularly with TI stimulation (f_1 = 2497Hz, f_2 = 2507Hz), oscillates at the difference frequency (f_Δ) of the two applied frequencies (Figure 3.5 Ai). A frequency component at the difference and sum of the two applied frequencies is present in the recorded membrane potential, as evidenced by a peak in the normalised PSD of the membrane potential trace (Figure 3.5 Bi). The normalised PSD also shows large peaks at the linear artefact frequencies (f_1 and f_2), as in the aCSF recording. To ensure that any power observed in the PSD of neural recordings is due to neural polarisation rather than nonlinear stimulation artefact, the artefact-corrected normalised PSD was computed for f_Σ. The expected stimulation PSD artefact was computed by multiplying the stimulation nonlinear:linear artefact ratio (Figure 3.4 Cii) by the linear artefact (in each neuron recording). This was then subtracted from the normalised PSD at f_Σ. As there is no detectable artefact at f_Δ, the normalised PSD was taken. A significant peak above the noise floor, at f_Δ in the normalised PSD is present in neural recordings suggesting neural polarisation at this frequency (p = 0.048)(see Tables 3.4 and 3.5). The artefact-corrected normalised PSD at f_Σ however, is not significantly larger than the noise floor (p = 0.24), suggesting either a) no neural polarisation at this frequency or b) polarisation of small enough magnitude to be hidden by the stimulation artefact (see Tables 3.4 and 3.5).

A no stimulation condition was also performed to ensure that any peaks in the PSD during stimulation are due to the stimulation. Indeed, there is no visible oscillation at f_Δ in the mean membrane potential (Figure 3.5 Aii). There are also no discernible peaks at f_Δ or f_Σ in the mean normalised PSD (Figure 3.5 Bii). Accordingly, the normalised PSD at f_Δ or f_Σ is not significantly larger than the noise floor during no stimulation (f_Δ: p = 0.15, f_Σ: p = 0.77)(Figure 3.5 Cii). These results confirm that polarisation of the neural membrane at f_Δ is due to the TI stimulation.

Overall, these results provide proof of principle that TI stimulation induces a neural subthreshold oscillation at f_Δ. Whether TI stimulation induces polarisation at f_Σ is inconclusive due to the nonlinear stimulation artefact at that frequency. A subthreshold oscillation at f_Δ suggests that the neuron is able to perform a nonlinear frequency conversion and that neural frequency conversion is occurring during TI stimulation, thus going forward this terminology will be used.

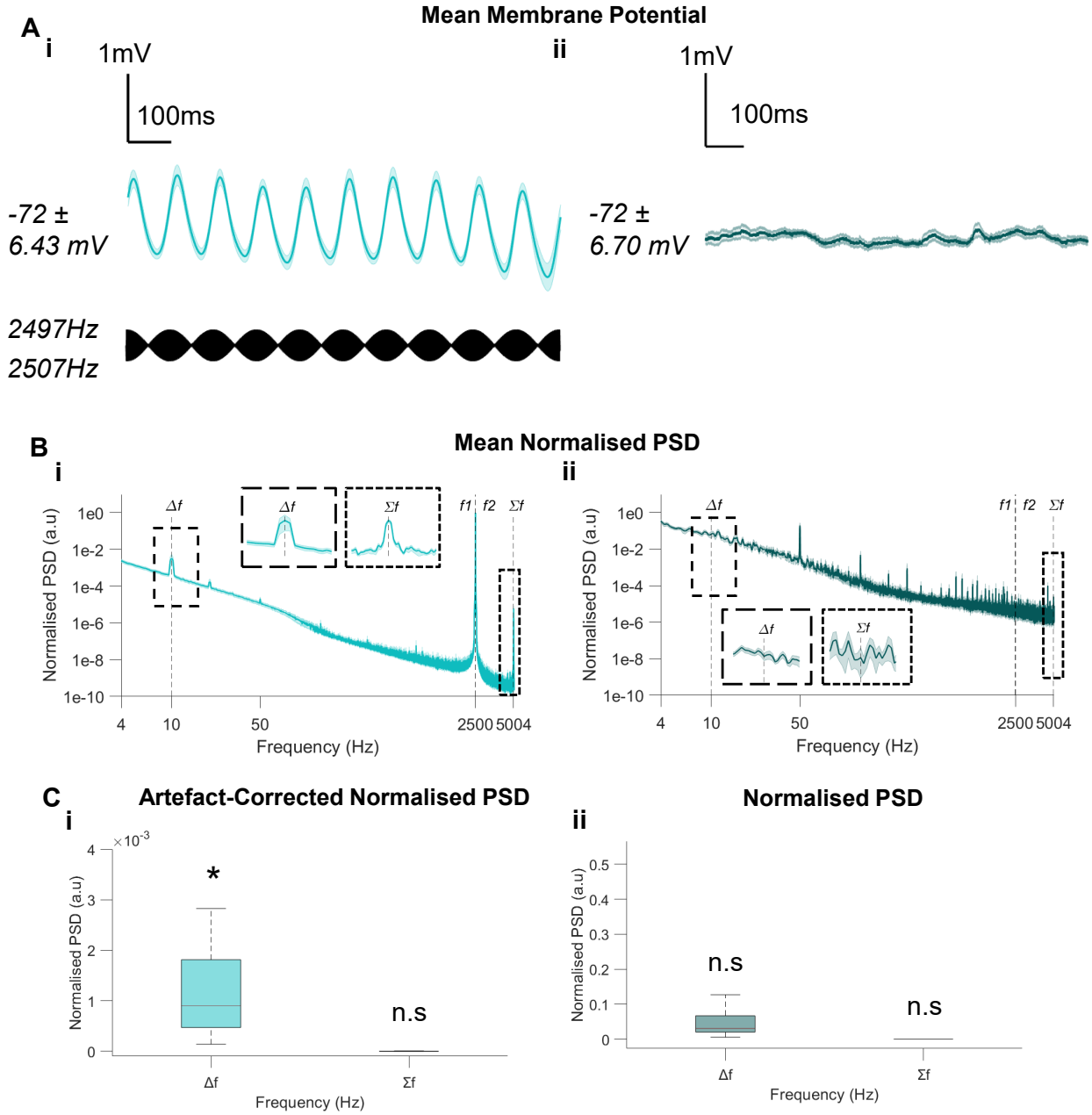


Figure 3.5: **Evoked neural frequency conversion in single neuron subthreshold activity during temporal interference stimulation**

Figure 3.5: **Evoked neural frequency conversion in single neuron subthreshold activity during temporal interference stimulation** *(A-C) Evidence for neural frequency conversion during temporal interference stimulation is presented in the form of significant neural polarisation at f_Δ during stimulation with kHz frequencies. This polarisation is not present in the no stimulation condition.* (A)(i) Mean membrane potential during extracellular stimulation (f_1 = 2497Hz, f_2 = 2507Hz). Showing mean ± SEM. Data is high-pass filtered at 1Hz, and low-pass filtered at 20Hz to remove stimulation artefact. Mean resting membrane potential across all cells ± standard deviation is displayed. (ii) As in (i) but without stimulation. (B)(i) Mean Power Spectral Density (PSD) of neural membrane potential during extracellular stimulation (f_1 = 2497Hz, f_2 = 2507Hz). Zoom view of regions inside dashed boxes. Normalised to maximum value in PSD. Showing mean ± SEM. (ii) As in (i) but without stimulation. (C)(i) Boxplot showing normalised PSD value at f_Δ (10Hz), and artefact-corrected normalised PSD at f_Σ (5004Hz) during stimulation (f_1 = 2497Hz, f_2 = 2507Hz). * indicates difference from linear fit at this value is significantly greater than zero, thus comparing the value to the noise floor. One sample one tailed t-test. n.s = p > 0.05, * = p < 0.05. Boxplots showing median (line), 25th (bottom edge) and 75th (top edge) percentiles. Whiskers extend to the most extreme data points not considered outliers. Values considered outliers were removed from the plot to aid visualisation, but included in statistical comparisons. (ii) As in (i) but showing normalised PSD value, at f_Δ (10Hz) and f_Σ (5004Hz), during no stimulation. n = 40 cells for all plots.

	Average Applied Frequency (Hz)						
Δ Artefact-Corrected Normalised PSD (linear fit subtracted)	***10***	***50***	***100***	***500***	***1000***	***2500***	***5000***
				f_Δ			
Mean	0.00042	0.00091	0.00036	0.00076	0.00096	0.0024	0.0019
± SEM	(8.34e-05)	(0.00035)	(8.63e-05)	(0.00032)	(0.00030)	(0.0013)	(0.00060)
p-value	1.38e-05***	0.011*	2.40e-04***	0.014*	0.0071*	0.048*	0.0015**
				f_Σ			
Mean	6.71e-05	-8.58e-05	-6.21e-05	-2.31e-06	2.32e-06	1.19e-06	5.10e-06
± SEM	(7.93e-05)	(2.90e-05)	(1.43e-05)	(9.94e-06)	(8.86e-06)	(1.57e-06)	(2.74e-06)
p-value	0.21	1	1	0.59	0.42	0.24	0.036

Table 3.4: **Δ Artefact-corrected normalised PSD at f_Δ and f_Σ** One sample one tailed t-test. * indicates significance that survived Bonferroni correction. Bonferroni-corrected p-value = 0.0071.

Artefact-Corrected Normalised PSD	Average Applied Frequency (Hz)						
	10	***50***	***100***	***500***	***1000***	***2500***	***5000***
				f_Δ			
Mean	0.00045	0.0012	0.00051	0.00098	0.00123	0.0029	0.0029
± SEM	(8.54e-05)	(0.00038)	(9.09e-05)	(0.00033)	(0.00030)	(0.0013)	(0.00065)
				f_Σ			
Mean	0.00015	-8.41e-05	-6.17e-05	-2.17e-06	2.49e-06	1.21e-06	5.12e-06
± SEM	(8.12e-05)	(2.95e-05)	(1.44e-05)	(9.99e-06)	(8.98e-06)	(1.58e-06)	(2.75e-06)

Table 3.5: **Artefact-corrected normalised PSD at f_Δ and f_Σ**

Δ Normalised PSD (linear fit subtracted)	***No stimulation***
	f_Δ **(10Hz)**
Mean ± SEM	0.017 (0.016)
p-value	0.15
	f_Σ **(5004Hz)**
Mean ± SEM	-1.37e-07 (1.70e-07)
p-value	0.77

Table 3.6: **Δ Normalised PSD at f_Δ and f_Σ (no stimulation)** One sample one tailed t-test.

Normalised PSD	***No stimulation***
	f_Δ **(10Hz)**
Mean ± SEM	6.34e-02 (1.81e-02)
	f_Σ **(5004Hz)**
Mean ± SEM	1.36e-06 (5.08e-07)

Table 3.7: **Normalised PSD at f_Δ and f_Σ (no stimulation)**

3.3.3 Neural subthreshold frequency conversion can be evoked across a broad range of frequencies

The previous section described evidence of nonlinear frequency conversion during TI stimulation at kHz frequencies. Given that endogenous neural activity falls within a much lower frequency range, I next aim to investigate whether evoked nonlinear frequency conversion occurs across a wide range of applied frequencies, using whole cell patch clamp recordings of single neuron activity.

The subthreshold membrane potential of single neurons stimulated extracellularly with average applied frequencies of 50Hz, 500Hz, and 5000Hz, oscillates at f_Δ of the two applied frequencies (Figure 3.6). A frequency component at the difference and sum of the two applied frequencies is present in the recorded membrane potentials. This can be seen as a peak in the PSD of the membrane potential trace (Figure 3.6 B). For average applied frequencies of 50Hz, 500Hz and 5000Hz, a peak significantly larger than the noise floor, at f_Δ in the normalised PSD, is observed in the neural recordings ($p < 0.05$)(Figure 3.6 C), suggesting neural polarisation at this frequency (see Tables 3.4 and 3.5). Conversely, the artefact-corrected normalised PSD at

f_Σ, is not significantly larger than the noise floor for average applied frequencies of 50Hz and 500Hz (Figure 3.6 Ci, ii), suggesting either a) a lack of neural polarisation at this frequency or b) amplitude of polarisation is smaller than the nonlinear stimulation artefact (see Tables 3.4 and 3.5). For 5000Hz on the other hand, the artefact-corrected normalised PSD at f_Σ is indeed significantly larger than the noise floor ($p = 0.036$), suggesting that there is some neural polarisation at this sum frequency (10004Hz) which is large enough to be detected above the nonlinear stimulation artefact (Figure 3.6Ci, ii)(see Tables 3.4 and 3.5).

A full range of applied frequencies were tested, spanning 10Hz-5000Hz average applied frequency, and results consistently support the production and existence of neural polarisation at f_Δ and thus neural frequency conversion ($p < 0.05$. For 50Hz, 500Hz and 2500Hz, significance did not survive Bonferroni correction)(Figure 3.7A). The results do not however suggest that neurons can consistently produce f_Σ across the range of applied frequencies (Figure 3.7 B)(see Tables 3.4 and 3.5 for all values). However, given that the results suggest some neural polarisation at f_Σ during the 5000Hz stimulation condition, where the nonlinear stimulation artefact is smallest (Figure 3.7 Cii), whether evoked f_Σ polarisation at lower applied frequencies is being masked by the larger nonlinear stimulation artefact is an open question.

Together, these results support the existence of evoked neural frequency conversion at the single cell across a range of frequencies spanning endogenous to kHz, including during TI stimulation.

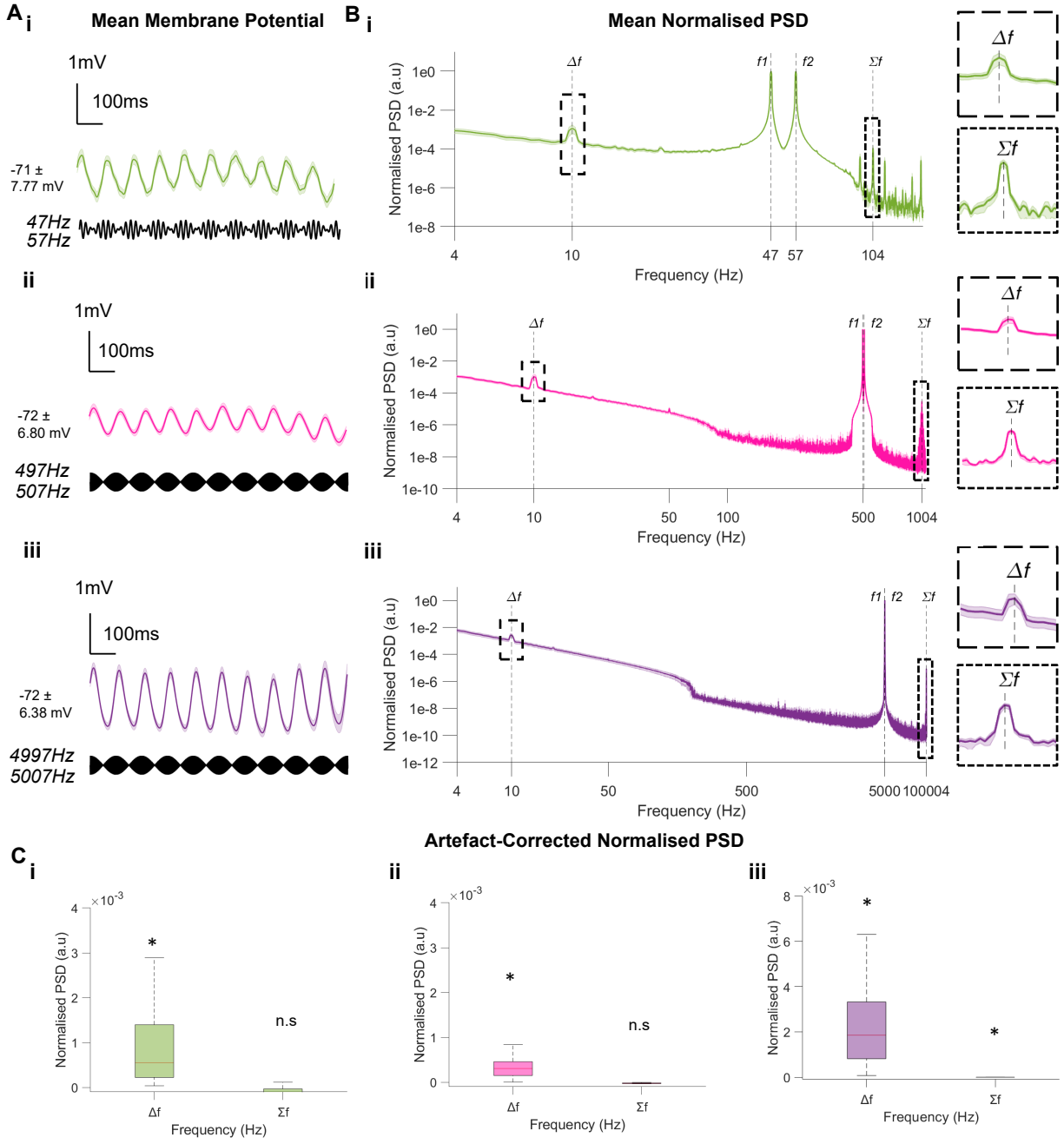


Figure 3.6: **Evoked neural frequency conversion in single neuron subthreshold activity across a range of applied stimulation frequencies**

Figure 3.6: **Evoked neural frequency conversion in single neuron subthreshold activity across a range of applied stimulation frequencies** *(A-C) Evidence for neural frequency conversion is presented in the form of significant neural polarisation at the difference frequency (f_Δ) during stimulation across a range of applied frequencies, as seen in the membrane potential and Power Spectral Density (PSD)* (A) Mean membrane potential during extracellular stimulation with frequencies (i) $f_1 = 47$Hz, $f_2 = 57$Hz, (ii) $f_1 = 407$Hz, $f_2 = 507$Hz, and (iii) $f_1 = 4997$Hz, $f_2 = 5007$Hz. Showing mean ± SEM. Data is high-pass filtered at 1Hz, and low-pass filtered at 20Hz to remove stimulation artefact. Mean resting membrane potential across all cells ± standard deviation is displayed. (B) Mean PSD of neural membrane potential during extracellular stimulation with frequencies (i) $f_1 = 47$Hz, $f_2 = 57$Hz, (ii) $f_1 = 407$Hz, $f_2 = 507$Hz, and (iii) $f_1 = 4997$Hz, $f_2 = 5007$Hz. Zoom view of regions inside dashed boxes. Normalised to maximum value in PSD. Showing mean ± SEM. (C) Boxplot showing normalised PSD value at f_Δ (10Hz), and artefact-corrected normalised PSD at f_Σ during stimulation with frequencies (i) $f_1 = 47$Hz, $f_2 = 57$Hz, (ii) $f_1 = 407$Hz, $f_2 = 507$Hz, and (iii) $f_1 = 4997$Hz, $f_2 = 5007$Hz. * indicates difference from linear fit at this value is significantly greater than zero, thus comparing the value to the noise floor. One sample one tailed t-test. n.s = $p > 0.05$, * = $p < 0.05$. Boxplots showing median (line), 25th (bottom edge) and 75th (top edge) percentiles. Whiskers extend to the most extreme data points not considered outliers. Values considered outliers were removed from the plot to aid visualisation, but included in statistical comparisons. n = 28 cells (50Hz), 34 cells (500Hz), 42 cells (5000Hz) for all plots.

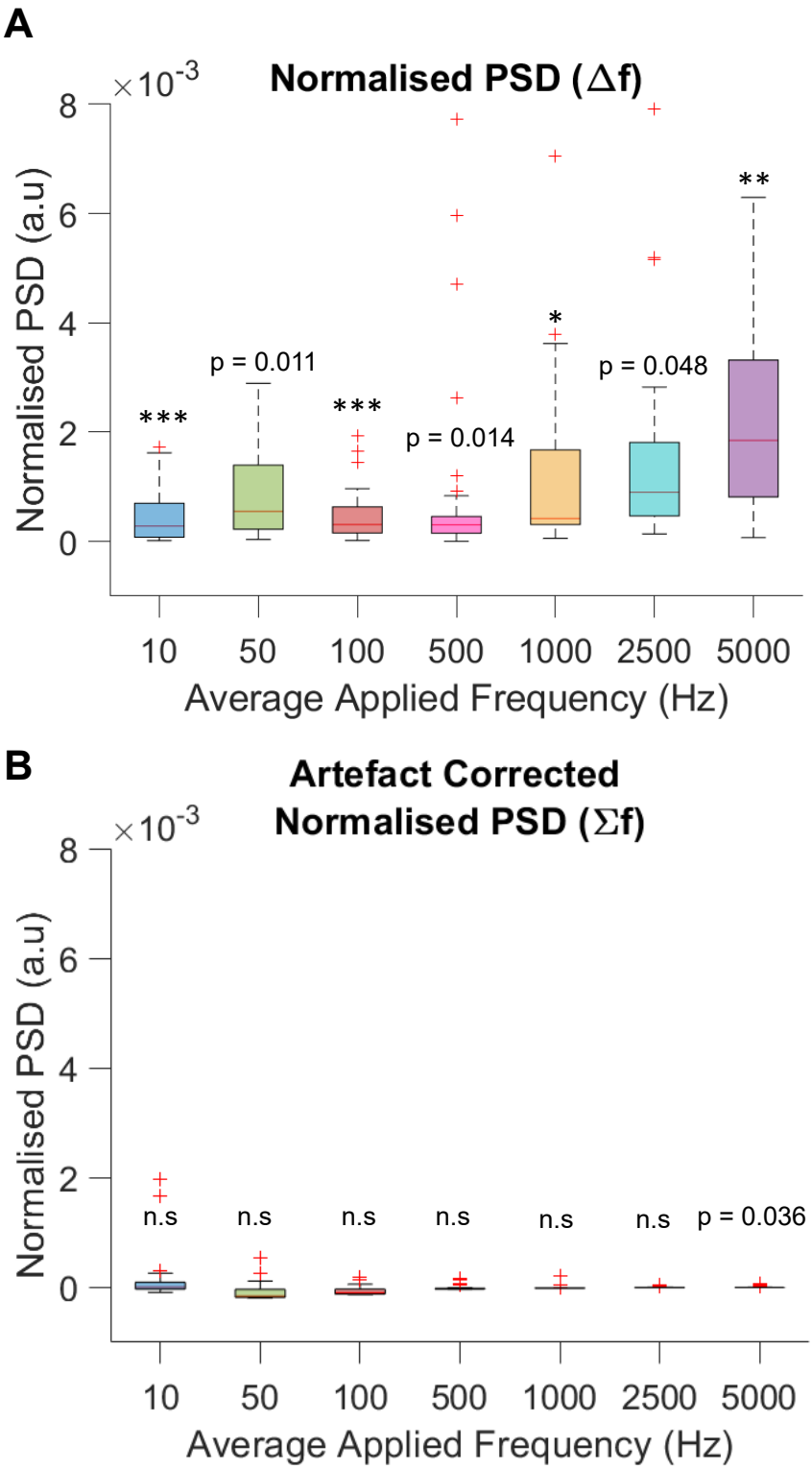


Figure 3.7: **Evoked neural frequency conversion in single neuron subthreshold activity across a range of applied frequencies cont.** Boxplot showing (A) normalised Power Spectral Density (PSD) value at f_Δ (10Hz), and (B) artefact-corrected normalised PSD at f_Σ, during stimulation with a range of applied frequencies. * indicates difference from linear fit at this value is significantly greater than zero, thus comparing the value to the noise floor. * indicates a significant difference that survived Bonferroni correction. One sample one tailed t-test. n.s = $p > 0.05$, * = $p < 0.05$, ** = $p < 0.005$, *** = $p < 0.0005$. Boxplots showing median (line), 25th (bottom edge) and 75th (top edge) percentiles. Whiskers extend to the most extreme data points not considered outliers. n = 28 cells (50Hz), 31 cells (100Hz), 34 cells (500Hz), 38 cells (100Hz), 40 cells (2500Hz), 42 cells (5000Hz).

3.3.4 Strength of evoked neural subthreshold frequency conversion drops at higher stimulation frequencies

Previous results involve the detection of neural frequency conversion in the maximum subthreshold evoked activity for each cell, at each average applied frequency (see section 3.3.2). However, whether the strength of evoked neural frequency conversion, and thus TI-induced subthreshold neural activity, depends on the applied frequency is of interest due to the implications for neural computation and clinical applications of TI. As before, the strength of neural frequency conversion can be measured by the amplitude of subthreshold polarisation at frequency conversion products, and also the threshold for TI-induced AP firing, as this is dependent on the magnitude of subthreshold polarisation. I thus aimed to characterise the strength of subthreshold neural frequency conversion/TI-induced neural activity, when the electric field strength is kept constant across the applied frequencies. Given that evidence of evoked neural polarisation at f_{Σ} across the range of applied frequencies is inconclusive, only evoked neural polarisation at f_{Δ} is used as evidence of neural frequency conversion, and thus characterised, going forward.

As seen previously, the subthreshold membrane potential in response to extracellular stimulation with an amplitude modulated electric field composed of two different frequencies, oscillates at f_{Δ} of the two applied frequencies. However if the amplitude is kept constant across the stimulation conditions with varying applied frequencies, the amplitude of this oscillation decreases as the applied frequency increases. This can be seen clearly with average applied frequencies of 50Hz, 500Hz, and 5000Hz (Figure 3.8 A).

In the PSDs of membrane potential traces when the average applied frequencies are 50Hz, 500Hz and 5000Hz and the current amplitude is fixed across frequency conditions, the peak at f_{Δ} can be seen in all frequency conditions however visual inspection of the size of the peak suggests that it decreases as applied frequency increases (Figure 3.8 B).

Across a range of applied frequencies from 50Hz to 5000Hz, a peak significantly larger than the noise floor, at f_{Δ} in the normalised PSD is observed in the neural recordings ($p < 0.05$ with the

exception of 500Hz)(see Table 3.8) (Figure 3.8 C). The absolute PSD values of all frequencies which showed significant neural frequency conversion at f_Δ were compared (see Table 3.9). A statistically significant effect of frequency on absolute PSD at f_Δ is observed ($F(4,96) = 5.81$, $p = 3.14e\text{-}04$, Figure 3.8 C)(see Table 3.10). The general trend in the data suggests a decrease in PSD as applied frequency increases (Figure 3.8 C). Indeed, post-hoc comparisons of frequency conditions show a significant increase in the normalised PSD at 50Hz compared to 100Hz ($p = 0.0043$) that survived Bonferroni correction. Other comparisons, (50Hz vs 500Hz, 2500Hz and 5000Hz) had p-values of < 0.05, however these did not survive Bonferonni correction (see Table 3.11 for full range of values).

Figure 3.8 D shows the stimulation threshold amplitude for evoking AP spiking vs the applied stimulation frequencies. The stimulation threshold amplitudes were normalized to the threshold amplitude of traditional AC stimulation, i.e. stimulation at f_Δ. The threshold for evoking APs via TI stimulation with 2500Hz is approximately 1.5 times larger than the threshold for evoking APs via traditional AC stimulation (see Table 3.9). There is a significant effect of applied frequency on normalised threshold, with threshold increasing as applied frequency increases ($F(5,135) = 22.33$, $p = 5.82e\text{-}17$, Figure 3.8 D)(see Table 3.10). At 5000Hz, threshold is significantly increased compared to 10Hz ($p = 4.43e\text{-}05$), 50Hz ($p = 2.94e\text{-}06$), 100Hz ($p = 5.44e\text{-}06$), 500Hz ($p = 8.63e\text{-}07$), 1000Hz ($p = 3.57e\text{-}07$) and 2500Hz ($p = 0.00046$)(Figure 3.8 E). Additionally, at 2500Hz, threshold is significantly increased compared to 50Hz ($p = 0.0022$) and 500Hz ($p = 5.56e\text{-}05$). Other comparisons did not survive Bonferonni correction (see Table 3.11).

Together these results suggest that strength of neural frequency conversion and thus TI stimulation, as measured by the amplitude of polarisation at the frequency conversion product f_Δ, is dependent on the frequency of the applied or input signals to the neuron. More specifically, that in the kilohertz domain, the strength of the neural frequency conversion product is reduced compared to in the endogenous frequency domain. Additionally, within the kilohertz domain, strength of neural frequency conversion and thus TI stimulation decreases as applied frequency increases.

3.3.5 Strength of evoked neural subthreshold frequency conversion is dependent on applied frequency across a range of difference frequencies

The dependence of neural frequency conversion on applied frequency is not only true with conditions where f_Δ is 10Hz. Normalised threshold for AP firing also depends on applied frequency when f_Δ is 5 Hz ($F(6,30) = 4.673$, $p = 0.0018$, Figure 3.8 E) and 40Hz ($F(6,24) = 2.68$, $p = 0.0039$, Figure 3.8 F). Individual post-hoc comparisons did not survive Bonferonni correction (see Table 3.11 for full range of values).

These results further support the conclusion that strength of neural frequency conversion is reduced as applied frequency increases.

Δ **Normalised PSD (linear fit subtracted)**	**Average Applied Frequency (Hz)**					
	50	*100*	*500*	*1000*	*2500*	*5000*
Mean ± SEM	0.00082 (0.00040)	0.00054 (3.04e-04)	0.00027 (0.00022)	0.00045 (0.00021)	0.00015 (8.59e-05)	0.00038 (0.00020)
p-value	0.025	0.044	0.11	0.018	0.045	0.032

Table 3.8: **Δ Normalised PSD at f_Δ** One sample one tailed t-test.

Measure of frequency conversion strength		Average Applied Frequency (Hz)						
Measure	**Frequency**	*10*	*50*	*100*	*500*	*1000*	*2500*	*5000*
					Mean (± SEM)			
Absolute PSD	f_Δ = *10Hz*	-	0.66 (0.21)	0.27 (0.10)	0.15 (0.042)	0.10 (0.019)	0.081 (0.023)	0.076 (0.020)
Normalised Threshold	f_Δ = *5Hz*	0.90 (0.072)	0.81 (0.076)	0.71 (0.080)	1.21 (0.37)	1.62 (0.57)	2.38 (0.91)	3.65 (1.24)
	f_Δ = *10Hz*	1.19 (0.26)	1.06 (0.21)	1.09 (0.15)	1.09 (0.069)	1.30 (0.32)	1.72 (0.39)	2.82 (1.37)
	f_Δ = *40Hz*	1.52 (0.36)	1.58 (0.31)	1.33 (0.20)	1.13 (0.096)	1.54 (0.43)	2.01 (0.62)	5.38 (2.68)

Table 3.9: **Measures of neural frequency conversion strength when electric field strength is of constant amplitude across applied frequency**

Measure of frequency conversion strength		Repeated Measures ANOVA	
Measure	**Frequency**	F	p
Absolute PSD	f_Δ = *10Hz*	5.81	3.14e-04
	f_Δ = *5Hz*	4.67	0.0018
Normalised Threshold	f_Δ = *10Hz*	22.33	5.82e-17
	f_Δ = *40Hz*	2.68	0.039

Table 3.10: **Repeated-measures ANOVA results for measures of neural frequency conversion strength when electric field strength is of constant amplitude across applied frequency**

Measure of frequency conversion strength			p-value						
			Average Applied Frequency (Hz)						
Measure	**Frequency**	**Average Applied Frequency (Hz)**	*10*	*50*	*100*	*500*	*1000*	*2500*	*5000*
Absolute PSD	f_Δ *= 10Hz*	*10*	-	-	-	-	-	-	-
		50	-	-	0.0043**	0.019	-	0.017	0.012
		100	-	0.0043**	-	0.11	-	0.010	0.088
		500	-	0.019	0.11	-	-	0.24	0.15
		1000	-	-	-	-	-	-	-
		2500	-	0.017	0.10	0.24	-	-	0.49
		5000	-	0.012	0.088	0.15	-	0.49	-
Normalised Threshold	f_Δ *= 5Hz*	*10*	-	0.17	0.043	0.41	0.23	0.16	0.073
		50	0.17	-	0.22	0.27	0.17	0.13	0.062
		100	0.043	0.22	-	0.15	0.11	0.10	0.051
		500	0.41	0.27	0.15	-	0.18	0.092	0.057
		1000	0.23	0.17	0.11	0.18	-	0.072	0.029
		2500	0.16	0.13	0.10	0.092	0.072	-	0.080
		5000	0.073	0.062	0.051	0.057	0.029	0.080	-
Normalised Threshold	f_Δ *= 10Hz*	*10*	-	0.23	0.30	0.58	0.48	0.018	4.43e-05***
		50	0.23	-	0.77	0.86	0.21	0.0021**	2.93e-06***
		100	0.30	0.77	-	0.98	0.24	0.0045	5.44e-06***
		500	0.58	0.86	0.98	-	0.0096	5.55e-05***	8.63e-07***
		1000	0.48	0.21	0.24	0.0096	-	0.018	3.5e-07***
		2500	0.018	0.0021**	0.0045	5.55e-05***	0.018	-	4.57e-04***
		5000	4.43e-05***	2.94e-06***	5.44e-06***	8.63e-07***	3.5e-07***	4.57e-04***	-
Normalised Threshold	f_Δ *= 40Hz*	*10*	-	0.75	0.58	0.33	0.98	0.20	0.14
		50	0.75	-	0.31	0.18	0.92	0.17	0.15
		100	0.58	0.31	-	0.34	0.62	0.22	0.19
		500	0.33	0.18	0.34	-	0.31	0.16	0.17
		1000	0.98	0.92	0.62	0.31	-	0.16	0.17
		2500	0.20	0.17	0.22	0.16	0.16	-	0.13
		5000	0.14	0.15	0.19	0.17	0.17	0.13	-

Table 3.11: **Post-hoc comparisons of measures of neural frequency conversion strength when electric field strength is of constant amplitude across applied frequency** Paired t-test. * indicates significance that survived Bonferroni correction. Bonferroni-corrected p-value = 0.005 (absolute PSD), 0.0021 (normalised threshold).

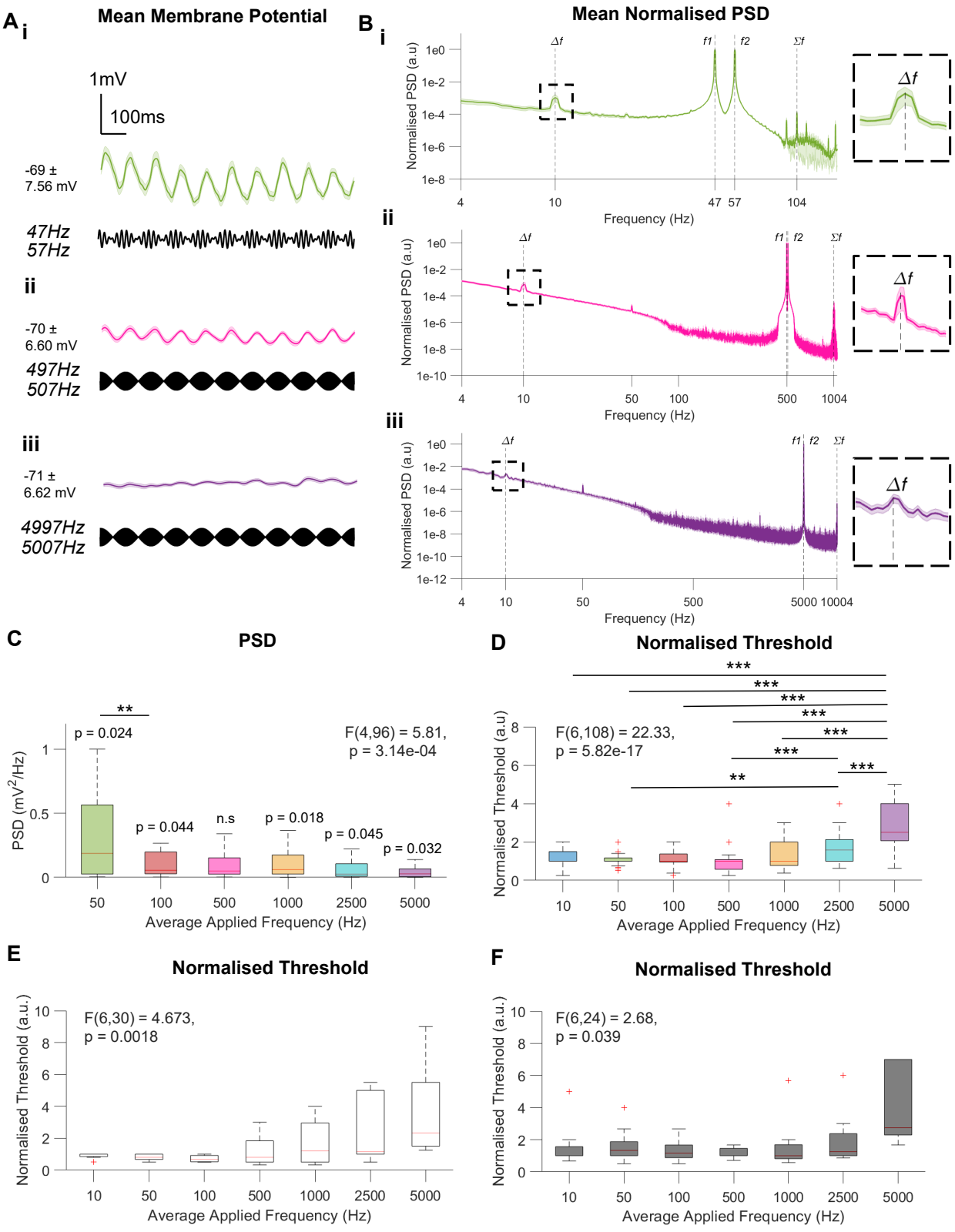


Figure 3.8: **Dependency of neural frequency conversion strength and temporal interference-induced neural activity on applied frequency**

Figure 3.8: **Dependency of neural frequency conversion strength and temporal interference-induced neural activity on applied frequency** *(A-G) Measures of TI/neural frequency conversion strength show dependence on applied frequency, with both decreasing as applied frequency increases.* (A) Mean membrane potential during extracellular stimulation with frequencies (i) f_1 = 47Hz, f_2 = 57Hz, n = 28 cells, (ii) f_1 = 497Hz, f_2 = 507Hz, n = 34 cells (iii) f_1 = 4997Hz, f_2 = 5007Hz, n = 42 cells. Difference frequency (f_Δ) across applied frequencies is 10Hz. Current amplitude across applied frequencies is the same. Data is high-pass filtered at 1Hz, and low-pass filtered at 20Hz to remove stimulation artefact. Showing mean ± SEM. Mean resting membrane potential across all cells ± standard deviation is displayed. (B) *Left*: Mean normalised Power Spectral Density (PSD) of neural membrane potential during extracellular stimulation with frequencies (i) f_1 = 47Hz, f_2 = 57Hz, n = 28 cells, (ii) f_1 = 497Hz, f_2 = 507Hz, n = 34 cells (iii) f_1 = 4997Hz, f_2 = 5007Hz, n = 42 cells. *Right*: Zoom view of region inside dashed box. f_Δ across carrier frequencies is 10Hz. Current amplitude across applied frequencies is the same. Normalised to maximum value in PSD. (C)(i) Boxplot showing absolute PSD value at f_Δ (10Hz), during stimulation across a range of applied frequencies. Current amplitude across applied frequencies is the same. Labelled p-values indicate result of comparison to the noise floor. One sample one tailed t-test. n.s = $p > 0.05$. * indicates a significant difference that survived Bonferroni correction. Repeated measures ANOVA of average applied frequencies which are significantly larger than noise floor ($p < 0.05$). ** = $p < 0.005$. n = 28 cells (50Hz), 31 cells (100Hz), 34 cells (500Hz), 38 cells (100Hz), 40 cells (2500Hz), 42 cells (5000Hz). (D) Boxplot showing normalised threshold for Action Potential (AP) firing, during stimulation across a range of applied frequencies as in (C). f_Δ across carrier frequencies is 10Hz. Thresholds are normalised to threshold for firing in response to 10Hz stimulation for each cell. * indicates a significant difference that survived Bonferroni correction. Repeated measures ANOVA. ** = $p < 0.005$, *** = $p < 0.005$. n = 22 cells (10/50Hz), 21 cells (100/500Hz), 20 cells (1000/2500Hz), 19 cells (5000Hz). (E) Boxplot showing normalised threshold for AP firing, during stimulation across a range of applied frequencies. f_Δ across carrier frequencies is 5Hz. Thresholds are normalised to threshold for firing in response to 5Hz stimulation for each cell. * indicates a significant difference that survived Bonferroni correction. Repeated measures ANOVA. n = 7 cells (10/50/100/500/1000Hz), n = 6 cells (2500/5000Hz). (F) Boxplot showing normalised threshold for AP firing, during stimulation across a range of applied frequencies. f_Δ across carrier frequencies is 40Hz. Thresholds are normalised to threshold for firing in response to 40Hz stimulation alone for each cell. Repeated measures ANOVA. n = 12 cells (10/50/100/500/1000Hz), n = 8 cells (2500Hz), n = 5 cells (5000Hz). All boxplots showing median (line), 25th (bottom edge) and 75th (top edge) percentiles. Whiskers extend to the most extreme data points not considered outliers. + indicates outliers.

3.3.6 Strength of evoked neural subthreshold frequency conversion does not depend on difference frequency

Full characterisation of the neural frequency conversion phenomenon requires elucidation of whether the frequency conversion exhibits dependency on f_Δ. Consequently, I aim to investigate this by performing whole cell patch clamp recordings of single neuron activity during stimulation

where the electric field strength across different applied difference frequencies is kept constant.

The subthreshold membrane potential, in response to extracellular stimulation with an amplitude modulated current composed of two frequencies, oscillates at f_Δ of the two applied frequencies, across a range of difference frequencies. However, if the amplitude of stimulation is kept constant across f_Δ stimulation conditions, on visual inspection, the amplitude of this oscillation appears to decrease as f_Δ increases. This can be seen with difference frequencies of 5Hz, 10Hz, and 40Hz, across representative average applied frequencies of 500Hz (Figure 3.9 A) and 1000Hz (Figure 3.9 B).

The normalised threshold for AP firing (normalised to 10Hz low-frequency stimulation threshold) across a range of average applied frequencies (10Hz-5000Hz) is not dependent on f_Δ. There was no significant effect of f_Δ on threshold at applied frequencies of 10Hz ($F(2,8) = 1.38$, $p = 0.31$), 50Hz ($F(2,8) = 0.30$, $p = 0.75$), 100Hz ($F(2,8) = 3.63$, $p = 0.076$), 500Hz ($F(2,8) = 2.78$, $p = 0.12$), 1000z ($F(2,6) = 0.47$, $p = 0.65$), 2500Hz ($F(2,6) = 0.34$, $p = 0.72$) or 5000Hz ($F(2,6) = 1.10$, $p = 0.42$). Accordingly, when comparing different applied frequencies, no clear trend in normalised threshold can be observed across the different difference frequencies.

These results suggest that strength of neural frequency conversion is not dependent on the difference in frequency between the two applied, or input, signals to the neuron. This manifests as no significant difference in AP firing threshold when stimulation is applied using two applied frequencies with different difference frequencies.

Measure of frequency conversion strength		Difference Frequency (Hz)		
Measure	Average Applied Frequency (Hz)	*5*	*10*	*40*
		Mean (± SEM)		
Normalised Threshold	*10*	0.97 (0.15)	1.17 (0.089)	0.87 (0.14)
	50	0.93 (0.066)	0.99 (0.046)	1.60 (0.25)
	100	0.80 (0.12)	1.07 (0.12)	1.60 (0.40)
	500	1.60 (0.78)	1.29 (0.30)	1.82 (0.51)
	1000	1.82 (0.91)	1.63 (0.45)	2.14 (0.58)
	2500	2.38 (0.97)	2.24 (0.58)	1.21 (0.18)
	5000	3.44 (0.78)	3.15 (0.36)	2.59 (0.46)

Table 3.12: **Normalised threshold across difference frequency when electric field strength is of constant amplitude**

Measure of frequency conversion strength		Repeated Measures ANOVA	
Measure	Average Applied Frequency (Hz)	*F*	*p*
Normalised Threshold	*10*	1.38	0.31
	50	0.30	0.75
	100	3.63	0.076
	500	2.78	0.12
	1000	0.47	0.65
	2500	0.34	0.72
	5000	1.10	0.42

Table 3.13: **Repeated-measures ANOVA results for normalised threshold when electric field strength is of constant amplitude across difference frequencies**

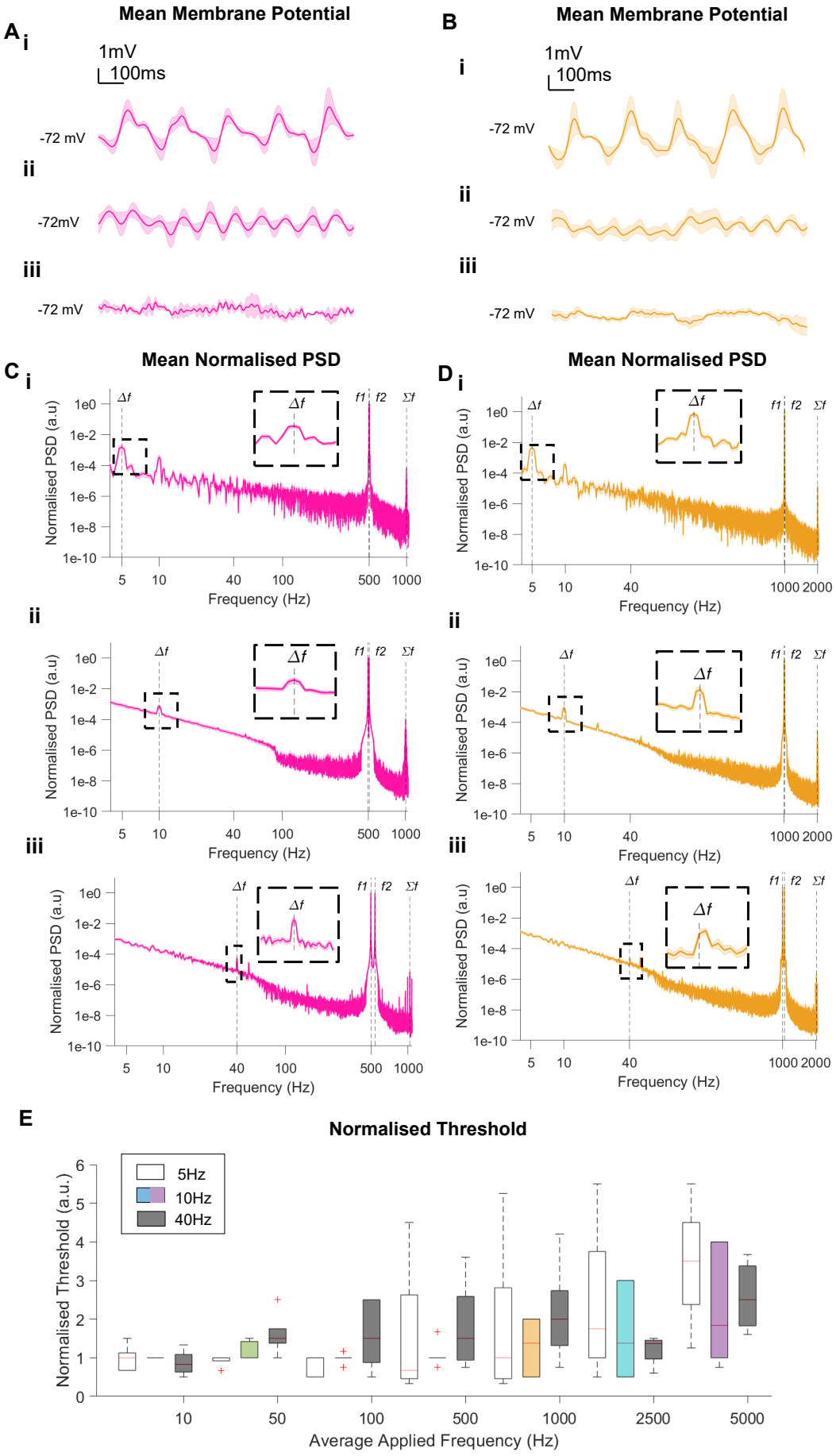


Figure 3.9: **No dependency of neural frequency conversion strength and temporal interference-induced neural activity on difference frequency**

Figure 3.9: **No dependency of neural frequency conversion strength and temporal interference-induced neural activity on difference frequency** *(A-F) Measures of Temporal Interference (TI)/frequency conversion strength show no dependence on difference frequency.* (A) Mean membrane potential during extracellular stimulation with frequencies (i) $f_1 = 497$Hz, $f_2 = 502$Hz, n = 5 cells, (ii) $f_1 = 497$Hz, $f_2 = 507$Hz, n = 7 cells, (iii) $f_1 = 497$Hz, $f_2 = 537$Hz, n = 5 cells. f_Δ across applied frequencies is 5Hz, 10Hz, and 40Hz respectively. Data is low-pass filtered at 100Hz. Current amplitude across difference frequencies is the same. Showing mean ± SEM. Mean resting membrane potential across all cells is displayed. (B) Mean membrane potential during extracellular stimulation with frequencies (i) $f_1 = 997$Hz, $f_2 = 1002$Hz, n = 5 cells, (ii) $f_1 = 997$Hz, $f_2 = 1007$Hz, n = 5 cells, (iii) $f_1 = 997$Hz, $f_2 = 1037$Hz, n = 5 cells. f_Δ across applied frequencies is 5Hz, 10Hz, and 40Hz respectively. Current amplitude across difference frequencies is the same. Showing mean ± SEM. Mean resting membrane potential across all cells is displayed. (C) *Left*: Mean normalised Power Spectral Density (PSD) of neural membrane potential during extracellular stimulation with frequencies (i) $f_1 = 497$Hz, $f_2 = 502$Hz, n = 5 cells, (ii) $f_1 = 497$Hz, $f_2 = 507$Hz, n = 7 cells, (iii) $f_1 = 497$Hz, $f_2 = 537$Hz, n = 5 cells. *Right*: Zoom view of regions inside dashed boxes. Current amplitude across difference frequencies is the same. Normalised to maximum value in PSD. (D) *Left*: Mean normalised PSD of neural membrane potential during extracellular stimulation with frequencies (i) $f_1 = 997$Hz, $f_2 = 1002$Hz, n = 5 cells, (ii) $f_1 = 997$Hz, $f_2 = 1007$Hz, n = 5 cells, (iii) $f_1 = 997$Hz, $f_2 = 1037$Hz, n = 5 cells. *Right*: Zoom view of regions inside dashed boxes. Current amplitude across difference frequencies is the same. Normalised to maximum value in PSD. (E) Boxplot showing normalised threshold for Action Potential (AP) firing, during stimulation across a range of applied frequencies and difference frequencies. Thresholds are normalised to threshold for firing in response to 10Hz stimulation alone for each cell. Repeated measures ANOVA. Absence of * = $p > 0.0167$ (Bonferroni-corrected p-value), for comparisons across difference frequencies. Thresholds were compared across difference frequencies for each applied frequency. No comparison across applied frequencies was performed. Boxplot showing median (line), 25th (bottom edge) and 75th (top edge) percentiles. Whiskers extend to the most extreme data points not considered outliers. + indicates outliers. n = 5 cells (5Hz), 7 cells (10Hz), 5 cells (40Hz).

3.3.7 Evoked neural subthreshold frequency conversion is sustained under synaptic input block: evidence of a cell membrane origin

The previously described results characterise the presence and strength of neural frequency conversion in evoked neural activity that is subthreshold at the neuron being recorded, at a range of applied and difference frequencies (see sections 3.3.2 - 3.3.6). At the level of the network however, suprathreshold processes are potentially occurring which could be contributing to the frequency conversion products being detected at the neuron via synaptic input onto the cell. For example, if the linear summation of applied signals is occurring, resulting in the production of suprathreshold f_Δ in neurons within the network, in theory, these neurons could

be synapsing onto the recorded neurons, producing subthreshold polarisation at f_Δ. Thus I aim to a) verify that f_Δ is being produced via solely subthreshold polarisation and thus that neural frequency conversion (rather than linear summation in the network) is occurring and b) investigate whether the single neuron has sufficient nonlinearity to be able to perform frequency conversion in isolation, that is, in the absence of a neuronal network and the suprathreshold activity within it. Additionally, I aim to investigate the origin of the nonlinearity underpinning nonlinear frequency conversion, and whether the nonlinear TTX-sensitive voltage-gated conductance is involved.

I aim to achieve this by characterising frequency conversion in the presence of synaptic blockade and TTX. In these experiments I used one low and one high average applied frequency from the previous section (synaptic blockers: 10Hz and 1000Hz; TTX: 10Hz and 5000Hz) (see section 3.3.2) to investigate the role of the network on evoked neural frequency conversion at both endogenous and kHz frequencies.

To probe the contribution of the neural network in neural frequency conversion, I recorded whole cell patch clamp measures of neural frequency conversion strength, before and after application of synaptic blockers.

Evoked neural frequency conversion in response to extracellular stimulation with an amplitude modulated current composed of two frequencies, can be observed in both the absence and presence of synaptic blockers (Figure 3.10). On visual inspection, the amplitude of this oscillation does not appear to change following drug application. This can be seen in a representative example when extracellular stimulation fields at the average applied frequency of 1000Hz are applied (Figure 3.10 A).

In the PSDs of membrane potential traces with and without synaptic blockers, the peak at f_Δ can be seen in both conditions across representative average applied frequencies of 10Hz (Figure 3.10 Bi) and 1000Hz (Figure 3.10 Bii). On visual inspection, the peak at f_Δ in the 10Hz average applied frequency condition, appears reduced in the presence of synaptic blockers, however this is not seen for the 1000Hz applied frequencies (Figure 3.10 Bi) (see Table 3.15).

Synaptic blockers do not have a significant effect (that survives Bonferonni correction) on normalised PSD at f_Δ, when average applied frequencies are 10Hz ($p = 0.027$) or 1000Hz ($p = 0.18$)(Bonferonni corrected p-value = 0.025)(Figure 3.10 C)(see Table 3.15). However, at 10Hz average applied frequency, a reduction occurs such that post-synaptic blockade, the amplitude of the peak at f_Δ is no longer significantly larger than the noise floor ($p = 0.055$). This suggests that indeed a reduction in polarisation at this frequency is occurring. Normalised PSD at f_Δ is significantly larger than the noise floor prior to synaptic blockade at applied frequencies of 10Hz ($p = 0.0093$) and 1000Hz ($p = 0.046$) and post-synaptic blockade at 1000Hz ($p = 0.048$), suggesting neural frequency conversion is occurring in these conditions (see Table 3.14 for all values).

Together these results suggest that the strength of evoked neural frequency conversion is attenuated, but not eliminated, by synaptic blockers at low applied frequencies, and that they have no effect on neural frequency conversion strength at kHz applied frequencies. Thus, polarisation of the single neuron at f_Δ does not require neural network input to occur suggesting that a) indeed neural frequency conversion is occurring, and b) the phenomena is originating at the single cell membrane.

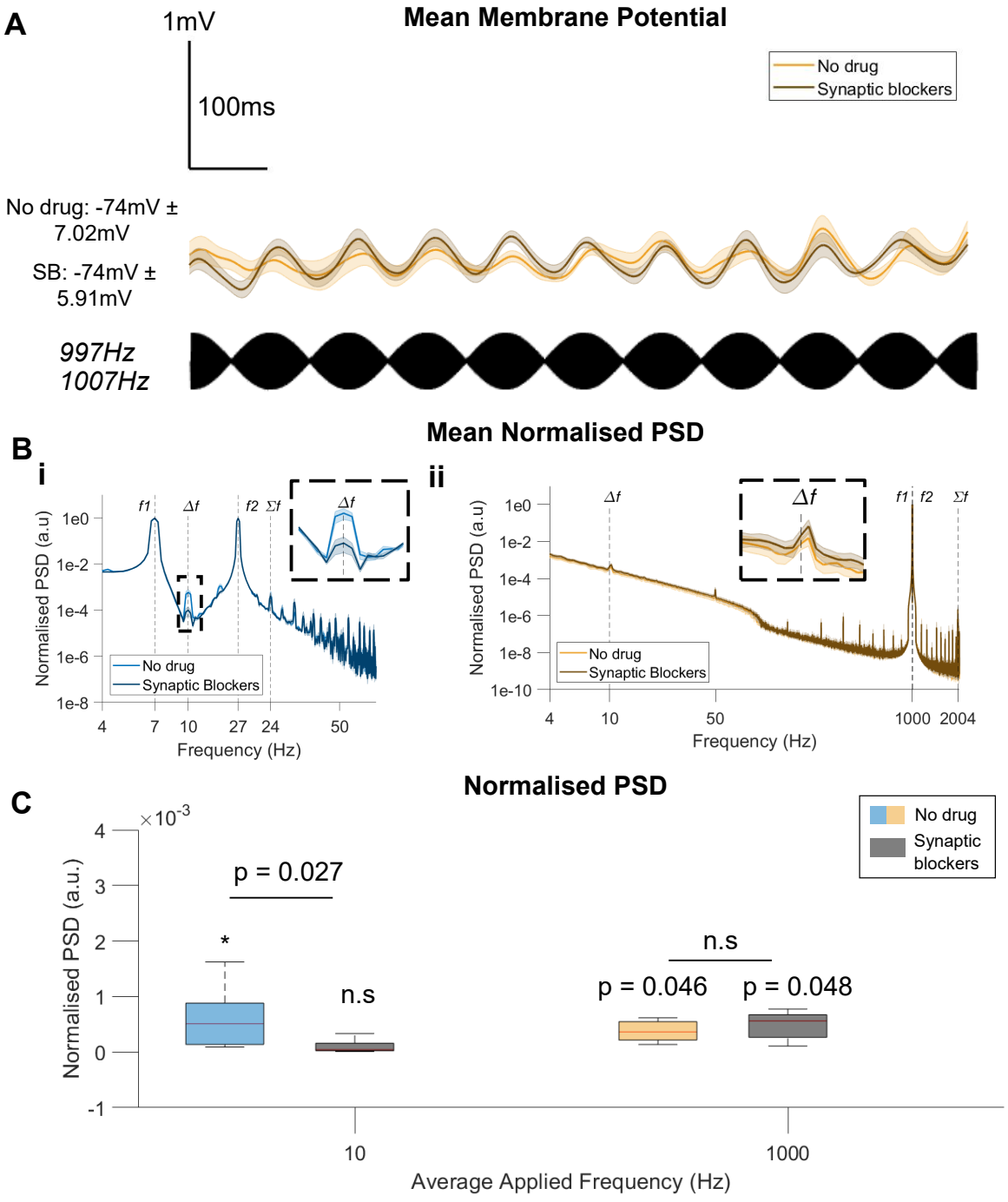


Figure 3.10: **Characterisation of the contribution of the neural network to neural frequency conversion**

Figure 3.10: **Characterisation of the contribution of the neural network to neural frequency conversion** *(A-C) Evidence of neural frequency conversion in the absence of neural network input is presented in the form of significant neural frequency conversion (power at f_Δ) during stimulation, which is not significantly attenuated when synaptic blockers are applied.* (A) Mean membrane potential during extracellular stimulation (f_1 = 997Hz, f_2 = 1007Hz), showing subthreshold oscillation at the difference frequency (f_Δ) of 10Hz, before drug application (yellow) and after synaptic blockers (grey). Showing mean ± SEM. Recordings are high-pass filtered at 1Hz, and low-pass filtered at 20Hz to remove stimulation artefact. Mean resting membrane potential ± standard deviation across all cells is displayed. n = 10. (B)(i) Mean PSD of neural membrane potential during extracellular stimulation (f_1 = 7Hz, f_2 = 17Hz), before and after application of synaptic blockers. Zoom view of region inside dashed box. Normalised to maximum value in PSD. Showing mean ± SEM. n = 7. (ii) As in (i) but with stimulation with frequencies f_1 = 997Hz, f_2 = 1007Hz. n = 10. (C)(i) Boxplot showing normalised Power Spectral Density (PSD), at f_Δ, during stimulation across 2 average applied frequencies, before drug application (colour) and after application of synaptic blockers (grey). Two sample t-test performed between drug conditions. One sample one tailed t-test performed between each condition and its respective noise floor. * indicates a significant difference that survives Bonferonni correction. n.s = p > 0.05, * = p < 0.05. n = 7, (10Hz), 10 (1000Hz).

Δ Normalised PSD	**Average Applied Frequency (Hz)**	
(linear fit subtracted)	*10*	*1000*
	Pre-Synaptic Blockers	
Mean ± SEM	0.00056 (0.00018)	9.43e-05 (4.99e-05)
p-value	0.0093*	0.046
	Post-Synaptic Blockers	
Mean ± SEM	7.46e-05 (4.09e-05)	0.00014 (7.42e-05)
p-value	0.056	0.048

Table 3.14: **Δ Normalised PSD at f_Δ** One sample one tailed t-test. * indicates significance that survived Bonferroni correction. Bonferroni-corrected p-value = 0.0125.

Normalised PSD	Average Applied Frequency (Hz)	
	10	*1000*
	Pre-Synaptic Blockers	
Mean ± SEM	0.00060	0.00038
	Post-Synaptic Blockers	
Mean ± SEM	9.96e-05	0.00050
	Pre vs Post	
p-value	0.027	0.18

Table 3.15: **Normalised PSD at f_Δ** Paired t-test.

3.3.8 Evoked neural membrane subthreshold frequency conversion involves voltage-gated ion channels

To probe the contribution of voltage-gated ion channels in neural frequency conversion, I recorded whole cell patch clamp measures of neural frequency conversion strength, before and after application of TTX.

The evoked subthreshold membrane potential oscillation produced when a neuron is exposed to extracellular stimulation with an amplitude modulated current composed of two frequencies, is at f_Δ of the two applied frequencies, both in the absence and presence of TTX. On visual inspection, the amplitude of this oscillation appears to decrease following drug application. This can be seen with representative average applied frequencies of 5000Hz (Figure 3.11 A). Interestingly, the oscillation is also phase-shifted.

In the PSDs of membrane potential traces with and without TTX, peaks at f_Δ can be seen pre- and post-TTX application with the representative average applied frequency of 10Hz (Figure 3.11 Bi). This peak does appear to reduce in amplitude following TTX mediated blockade of ion channels. Interestingly, at applied frequencies of 5000Hz, the power at f_Δ is reduced such that there is no longer a discernible peak (Figure 3.11 Bii).

TTX results in a significant reduction in normalised PSD amplitude at f_Δ when average applied frequencies are 10Hz ($p = 0.017$)(Figure 3.11 C). A reduction is also visible for 5000Hz, reflecting what is seen in the mean normalised PSD, however it is not significant ($p = 0.060$)(Figure 3.11 C)(Figure 3.11 Bii)(see Table 3.17). At both applied frequencies, a reduction occurs such that post-TTX, the amplitude of the peak at f_Δ is no longer significant compared to baseline (10Hz: $p = 0.099$, 5000Hz: $p = 0.98$), suggesting indeed a reduction in polarisation at f_Δ during these applied frequencies. Normalised PSD at f_Δ is significant compared to baseline prior to TTX at applied frequencies of 10Hz ($p = 0.011$) and 5000Hz ($p = 0.0043$), suggesting the presence of nonlinear frequency conversion in these pre drug conditions and a significant effect of TTX on f_Δ polarisation amplitude (see Table 3.16 for all values).

Together, these results suggest that strength of evoked neural frequency conversion is significantly reduced in the presence of TTX at both low and high applied frequencies. Some evidence for neural frequency conversion in the presence of TTX remains however, with polarisation at the frequency conversion product f_Δ being detectable in the membrane potential trace and mean PSD, albeit at a significantly reduced amplitude (not significantly larger than noise). Thus, it can be concluded that polarisation of the single neuron at f_Δ requires TTX-sensitive conduction to occur, suggesting that either a) TTX-sensitive voltage-gated ion channels are an origin of nonlinearity underlying neural frequency conversion or b) are involved in the amplification of the polarisation at f_Δ created by other nonlinearity originating at the cell membrane.

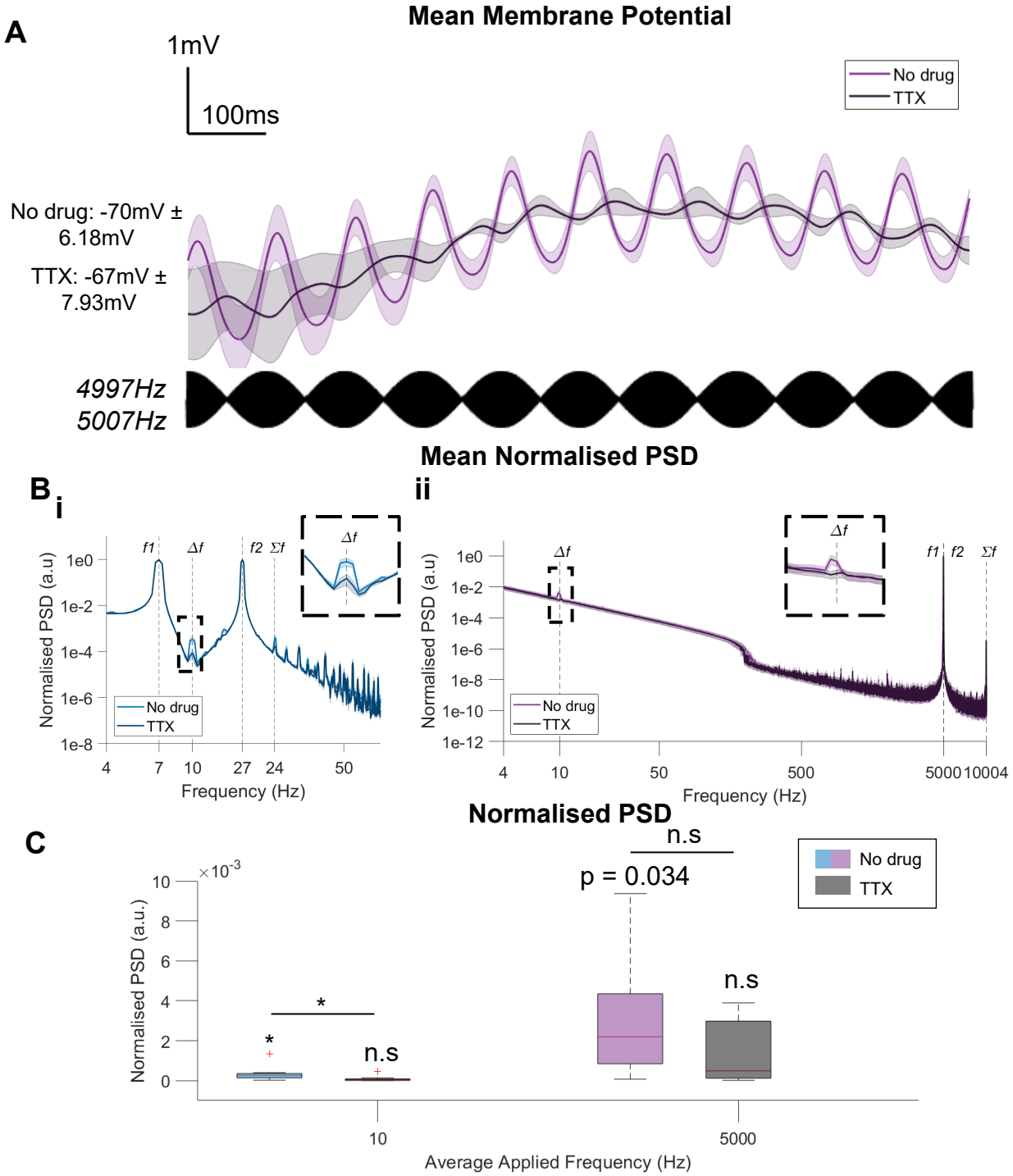


Figure 3.11: **Characterisation of the contribution of tetrodotoxin-sensitive conductance to neural frequency conversion**

Figure 3.11: **Characterisation of the contribution of tetrodotoxin-sensitive conductance to neural frequency conversion** *(A-C) Evidence of the contributing effect of Tetrodotoxin (TTX)-sensitive conductance on neural frequency conversion is presented in the form of a significant reduction in the strength of neural frequency conversion (power at the difference frequency (f_Δ)) during stimulation with TTX compared to stimulation without TTX.* (A) Mean membrane potential during extracellular stimulation (f_1 = 4997Hz, f_2 = 5007Hz), showing subthreshold oscillation at f_Δ of 10Hz, before drug application (purple) and after TTX (grey). Showing mean ± SEM. Recordings are high-pass filtered at 1Hz, and low-pass filtered at 20Hz to remove stimulation artefact. Mean resting membrane potential ± standard deviation across all cells is displayed. n = 8. (B)(i) Mean Power Spectral Density (PSD) of neural membrane potential during extracellular stimulation (f_1 = 7Hz, f_2 = 17Hz), before and after application of TTX. Zoom view of region inside dashed box. Normalised to maximum value in PSD. Showing mean ± SEM. n = 7. (ii) As in (i) but with stimulation frequencies f_1 = 4997Hz, f_2 = 5007Hz. n = 8. (C)(i) Boxplot showing normalised PSD, at f_Δ, during stimulation across 2 average applied frequencies, before drug application (colour) and after application of synaptic blockers (grey). Two sample t-test performed between drug conditions. n.s = p > 0.05. One sample one tailed t-test performed between each condition and its respective noise floor. * indicates a significant difference that survives Bonferonni correction. n.s = p > 0.05, * = p < 0.05. n = 7, (10Hz), 8 (5000Hz).

Δ Normalised PSD	**Average Applied Frequency (Hz)**	
(linear fit subtracted)	*10*	*5000*
	Pre-TTX	
Mean ± SEM	0.00031 (0.00011)	0.0015 (0.00073)
p-value	0.011*	0.034
	Post-TTX	
Mean ± SEM	5.83e-05 (4.19e-05)	-0.00013 (6.19e-05)
p-value	0.099	0.97

Table 3.16: **Δ Normalised PSD at f_Δ** One sample one tailed t-test. * indicates significance that survived Bonferroni correction. Bonferroni-corrected p-value = 0.0125.

Normalised PSD	Average Applied Frequency (Hz)	
	10	*5000*
	Pre-TTX	
Mean ± SEM	0.00034	0.0018
	Post-TTX	
Mean ± SEM	8.73e-05	0.0015
	Pre vs Post	
p-value	0.017*	0.060

Table 3.17: **Normalised PSD at** f_Δ Paired t-test. * indicates significance that survived Bonferroni correction. Bonferroni-corrected p-value = 0.025.

3.3.9 Strength of temporal interference stimulation and neural frequency conversion is dependent on the summed amplitude of the applied stimulating electric fields

I have presented evidence that neural frequency conversion is occurring during TI stimulation (see section 3.3.2 and section 3.3.3). Whether this nonlinear process is the driving force of the stimulation, that is, whether it determines the strength of the TI stimulation, is an important question for the development of the technique, specifically, the estimation of the stimulation spread and the development of models which predict this. It is currently assumed that TI stimulation strength is greatest where the envelope amplitude of the applied electric fields is maximal (Figure 1.1 C)(Grossman et al., 2017), however the spatial spread of TI-induced depolarisation has not been yet been investigated experimentally. The finding that TI neural stimulation involves nonlinear frequency conversion however, could have implications for the spatial spread of TI, as the site of maximal stimulation could in theory be determined by where the nonlinear frequency conversion is strongest, i.e. where the product of the applied fields is maximal. If the mechanism of TI is purely via linear summation of the electric fields, one would expect that the strength of TI stimulation to be dependent on the summed amplitude of the applied currents. If however, TI-induced neural depolarisation at f_Δ is produced only by neural

frequency conversion via multiplication (frequency mixing), one would expect the strength of TI stimulation to be dependent on the product of the applied currents. Thus, investigating the dependency of TI strength on these measures will help uncover the driving force of the stimulation.

The strength of TI stimulation and neural frequency conversion can be measured in two ways. Firstly by the threshold for TI-induced AP firing, and secondly by the strength of the evoked subthreshold polarisation at f_Δ (i.e. TI-induced neural frequency conversion). Thus, I aim to probe the driving force of TI stimulation by investigating how measures of TI strength, obtained using the whole cell patch clamp technique, depend on the envelope amplitude of the applied currents, the sum amplitude of the applied currents and the product of the applied currents. TI stimulation in these experiments uses typical stimulation frequencies, f_1 = 2000Hz and f_2 = 2010Hz.

When the current product is fixed, normalised threshold for TI-induced AP firing decreases as normalised sum amplitude increases and as normalised envelope amplitude decreases (Figure 3.12 Ai)(see Table 3.18). A step-wise Generalised Linear Model (GLM) indicates a significant negative effect of sum amplitude alone on normalised threshold (t_{stat} = -2.69, p = 0.013)(see Table 3.19). No post-hoc comparison of the thresholds across discrete normalised sum/envelope amplitudes however, survives Bonferonni correction (1 vs 1.14: p = 0.99, 1 vs 1.86: p = 0.049, 1.14 vs 1.86: p = 0.15)(Bonferonni corrected p-value = 0.017)(Figure 3.12 Ai).

When the envelope amplitude is fixed, normalised threshold for TI-induced AP firing decreases as both normalised sum amplitude and normalised product increase (Figure 3.12 Bi)(see Table 3.18). A step-wise Generalised Linear Model (GLM) again indicates a significant negative effect of sum amplitude alone on normalised threshold (t_{stat} = -2.23, p = 0.034)(see Table 3.19). No post-hoc comparison of the thresholds across discrete sum amplitude/product however are significant (1.14 vs 1.57: p = 0.50, 1.14 vs 2: p = 0.13, 1.57 vs 2: p = 0.15)(Bonferonni corrected p-value = 0.017)(Figure 3.12 Bi).

Conversely, when the sum amplitude is fixed, normalised threshold for TI-induced AP firing does not appear to change (Figure 3.12 Ci)(see Table 3.18). Indeed, a step-wise Generalised

Linear Model (GLM) again indicates no significant effect of envelope amplitude or product on normalised threshold ($p > 0.05$)(Figure 3.12 Ci).

The mean evoked membrane potential supports the findings from the threshold, i.e. visual inspection indicates that the evoked depolarisation at f_Δ increases as sum amplitude increases when both current product (Figure 3.12 Aii), and envelope amplitude are fixed (Figure 3.12 Bii), but does not change when sum amplitude is fixed (Figure 3.12 Cii). This is difficult to quantify however, as polarisation at f_Δ measured by the normalised PSD, is not significantly different from noise for any of the sum amplitude conditions when current product is fixed (1: $p = 0.89$, 1.14: $p = 0.11$, 1.86: $p = 0.30$)(Figure 3.12 Biii)(see Table 3.20). These should not be compared due to the possibility that simply the noise levels are being compared, but is likely due to the current amplitude used (the maximum product when all of the conditions are still subthreshold) being too small to evoke discernible polarisation in these experiments. Polarisation at f_Δ, is not significantly different from noise for the 1.14 or 1.57 sum amplitude conditions when envelope amplitude is fixed (1.14: $p = 0.85$, 1.57: $p = 0.45$)(Figure 3.12 Biii). The largest sum amplitude does evoke polarisation that is significantly larger than noise ($p = 0.027$), although this does not survive Bonferroni correction (Bonferonni corrected p-value $= 0.017$)(see Table 3.20 for all values). Nonetheless, this result does imply that polarisation is greater at a normalised sum amplitude of 2, compared to 1.57 and 1.14, when envelope amplitude is fixed. Polarisation at f_Δ, is not significantly different from noise for any of the normalised product conditions when sum amplitude is fixed (1: $p = 0.12$, 1.71: $p = 0.14$, 2.29: 0.13)(Figure 3.12 Ciii)(see Tables 3.18 and 3.20 for all values).

When taken together, these results suggest that the strength of TI stimulation is dependent on the summed amplitude of the applied electric fields.

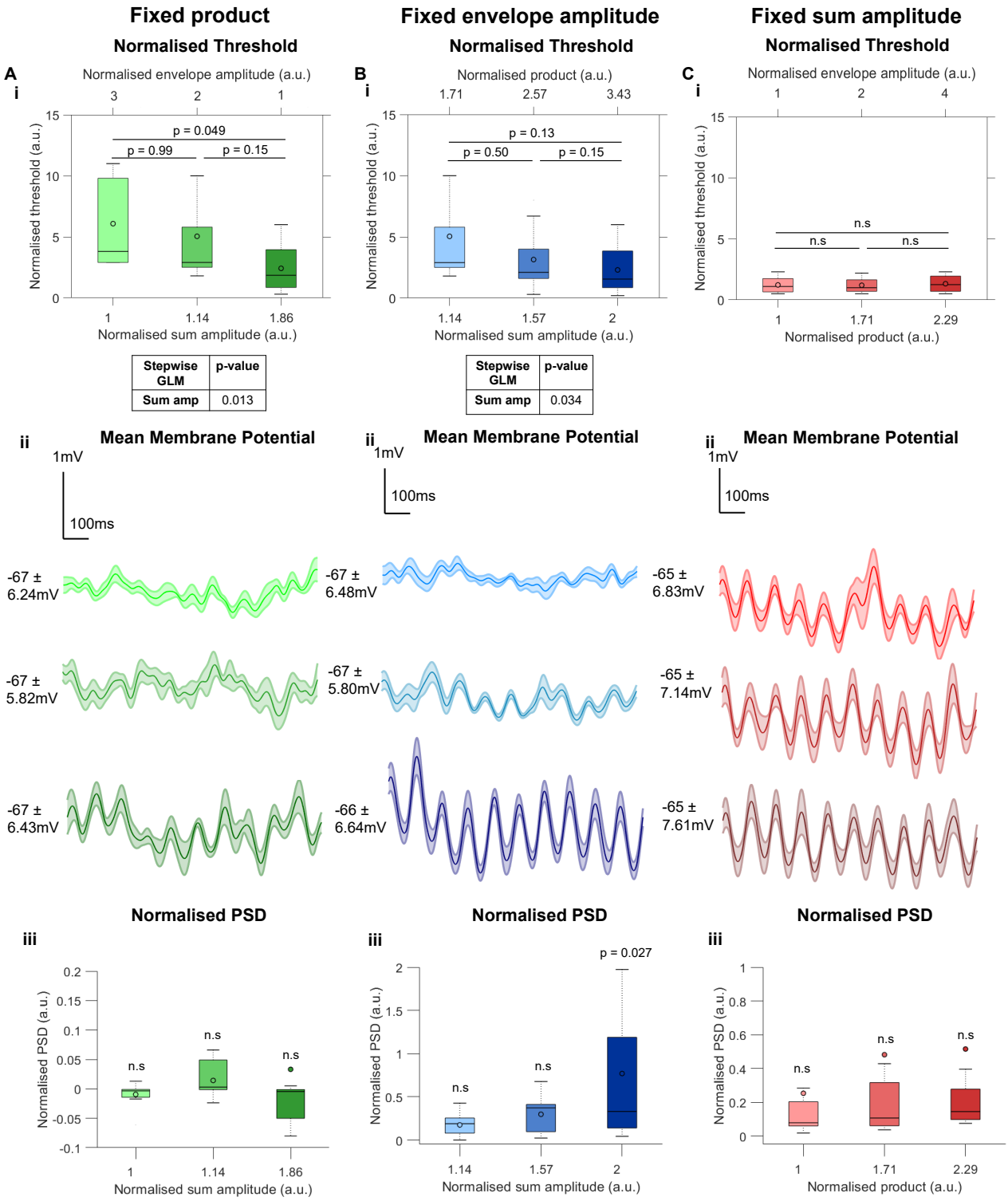


Figure 3.12: **Characterisation of the driving force of temporal interference stimulation**

Figure 3.12: **Characterisation of the driving force of temporal interference stimulation and neural frequency conversion** *(A-C) Strength of Temporal Interference (TI) stimulation as measured by the threshold for neural spiking and frequency conversion, is dependent on the summed amplitude of the applied fields.* (A)(i) *Top* Boxplot showing threshold for TI-induced Action Potential (AP)s evoked using extracellular stimulation (f_1 = 2000Hz, f_2 = 2010Hz) with varying sum and envelope amplitudes when current product is fixed. The threshold values are normalised to AP threshold for 10Hz stimulation. Sum and envelope amplitude values are normalised to the smallest sum and envelope amplitudes across all conditions respectively. Step-wise generalised linear regression model with post-hoc paired t-test. p-values are displayed. n = 12 cells. *Bottom* Results of a step-wise generalised linear regression model using threshold as the response variable, and sum amplitude and envelope amplitude as predictor variables. (ii) Mean membrane potential during extracellular stimulation with an AM current (f_1 = 2000Hz, f_2 = 2010Hz), of varying sum and envelope amplitudes (as in (i)), when current product is fixed. *Top* Normalised sum amplitude = 1, normalised envelope amplitude = 3. *Middle* Normalised sum amplitude = 1.14, normalised envelope amplitude = 1.86. *Bottom* Normalised sum amplitude = 1.86, normalised envelope amplitude = 1. For each cell, the maximum current that was still subthreshold for all three conditions was selected. Subthreshold oscillation at the difference frequency (f_Δ) of 10Hz is shown, across one second of stimulation. n = 9 cells. Mean resting membrane potential ± standard deviation across all cells is displayed. (iii) Boxplot showing normalised Power Spectral Density (PSD) at f_Δ, during extracellular stimulation (f_1 = 2000Hz, f_2 = 2010Hz) with varying sum amplitudes when current product is fixed. Included recordings were at the maximum fixed product while all sum amplitude conditions were still subthreshold. Sum amplitude values are normalised to the smallest sum amplitude across all conditions respectively. Stepwise generalised linear regression model with post-hoc paired t-test. n.s = neither sum amplitude or envelope amplitude are significant predictors of PSD at f_Δ. n.s $p > 0.05$. n = 9 cells. (B)(i) *Top* As in (A)(i) but with varying sum amplitudes and current products when envelope amplitude is fixed. n = 9. *Bottom* Results of a step-wise generalised linear regression model using threshold as the response variable, sum amplitude and current product as predictor variables. n = 12 cells. (ii) As in (A)(ii) but with varying sum amplitude and current product when envelope amplitude is fixed, (as in (B)(i)). *Top* Normalised sum amplitude = 1.14, normalised current product = 1.71. *Middle* Normalised sum amplitude = 1.57, normalised current product = 2.57. *Bottom* Normalised sum amplitude = 2, normalised current product = 3.43. n = 9 cells. (iii) As in (A)(iii), but with varying sum amplitude and current product when envelope amplitude is fixed. Included recordings were at the maximum envelope amplitude while all sum amplitude conditions were still subthreshold. n = 9 cells. (C)(i) As in (A)(i) but with varying envelope amplitudes and current products when sum amplitude is fixed. n = 8 cells. (ii) As in (A)(ii) but with varying envelope amplitude and current product when sum amplitude is fixed, (as in (C)(i)). *Top* Normalised current product = 1, normalised envelope amplitude = 1. *Middle* Normalised current product = 1.71, normalised envelope amplitude = 2. *Bottom* Normalised current product = 2.29, normalised envelope amplitude = 4. n = 8 cells. (iii) As in (A)(iii),but with varying envelope amplitude and current product when sum amplitude is fixed. Included recordings were at the maximum sum amplitude while all product conditions were still subthreshold. n = 8 cells. All boxplots showing median (line), mean (circle) and interquartile range (IQR).

Measure of TI strength		**Amp**		
		1	*2*	*3*
Measure	**Condition**	**Mean (± SEM)**		
Normalised Threshold	*Fixed product*	6.08 (1.78)	5.04 (1.45)	2.42 (0.53)
	Fixed envelope	5.04 (1.34)	3.14 (0.75)	2.30 (0.54)
	Fixed sum	1.23 (0.23)	1.20 (0.24)	1.33 (0.25)
Normalised PSD (Δ)	*Fixed product*	0.082 (0.028)	0.12 (0.039)	0.31 (0.10)
	Fixed envelope	0.18 (0.051)	0.23 (0.084)	0.77 (0.25)
	Fixed sum	0.25 (0.16)	0.48 (0.34)	0.51 (0.36)

Table 3.18: **Measures of temporal interference strength**

		Stepwise GLM			
Condition	**Variable**	*Estimate*	*SE*	*tStat*	*p-value*
Fixed product	Sum amplitude	-4.04	1.50	-2.69	0.013
Fixed envelope	Sum amplitude	-3.07	1.38	-2.23	0.034

Table 3.19: **Results of step-wise GLM for normalised threshold**

Δ Normalised PSD (linear fit subtracted)	**Amp**		
	1	*2*	*3*
Condition	**Mean (±) SEM**		
Fixed product	-0.0095 (0.0071)	0.014 (0.011)	0.033 (0.059)
Fixed envelope	-0.0056 (0.0051)	0.0023 (0.0176)	0.37 (0.16)
Fixed sum	0.20 (0.16)	0.41 (0.35)	0.45 (0.37)
	p-value		
Fixed product	0.89	0.11	0.30
Fixed envelope	0.85	0.45	0.027
Fixed sum	0.12	0.14	0.13

Table 3.20: **Δ Normalised PSD at** f_{Δ} One sample one tailed t-test.

3.4 Discussion

3.4.1 General discussion of results

In this chapter, I show evidence that applied signals undergo nonlinear frequency conversion at the single neuron. This neural frequency conversion is occurring both during TI stimulation, with stimulation frequencies in the kHz range, as well as in the low frequency range, i.e. those typical of endogenous brain signals. Additionally, I characterised the parameter space

of this phenomenon and found that strength of neural frequency conversion is dependent on the frequency of the applied signals, but not on the difference of the two signals. I show that neural frequency conversion originates at the cell membrane and involves voltage-gated ion channels. In order to investigate these questions, I characterised the nonlinear stimulation artefact present in recordings obtained with my experimental setup, and devised a method to remove these artefacts from neural recordings to determine whether neural polarisation exists. Lastly, whilst neural frequency conversion is occurring during TI stimulation, the strength of stimulation still depends on the summed amplitude of the applied electric fields, and not on the product.

Evoked neuronal subthreshold polarisation at f_Δ of two applied electric fields, indicates that a nonlinear process is occurring in the neural tissue. As outlined previously, this cannot occur if the neuronal response is due to a purely linear superposition of the two applied fields (see section 3.1). Whilst evidence of the nonlinear frequency mixing process has been detected in network level activity (Ahrens et al., 2002; Haufler and Paré, 2019), this is the first evidence of such a phenomenon being detected at the single neuron. Given that this polarisation persists when neural input to the neuron being recorded is blocked, I suggest that this nonlinear frequency conversion originates at the single neuron membrane. These experiments verified that the subthreshold polarisation at f_Δ being recorded in response to the stimulation, was not originating from the input of other neurons, (which could potentially be being polarised at f_Δ through the linear summation of the electric fields). Thus, the single neuron can exert such a nonlinear frequency conversion. It is interesting that the polarisation at f_Δ when stimulation frequencies are in the kHz frequency range ($f_1 = 997$Hz $f_2 = 1007$Hz) is not attenuated. However when stimulation frequencies are in the endogenous range, it is such that the peak at f_Δ is no longer significantly larger than the noise. I hypothesise that at lower frequencies (<100Hz), the neuron can receive synaptic input from neighbouring cells at f_1, f_2, and f_Δ (produced via nonlinear frequency conversion by the neighbouring cell) however at high frequencies (>100Hz), the neuron is only receiving synaptic input from neighbouring cells at f_Δ (as synaptic transmission cannot follow f_1 and f_2). If this is true, in the low applied frequency condition, synaptic input at f_1 and f_2 from neighbouring cells would contribute to polarisation at f_Δ. However,

synaptic input at f_Δ is not necessary, as the isolated cell itself can produce f_Δ (albeit at a smaller amplitude without synaptic input at f_1/f_2, as evidenced by a significantly reduced but still noticeable peak in the PSD). At the higher applied frequencies, synaptic input at f_Δ from neighbouring cells is not instrumental in creating f_Δ at the recorded cell, thus blockade of neural network input to the neuron does not decrease polarisation at f_Δ of the neuron, suggesting that the production of f_Δ at higher carrier frequencies is dominated by direct polarisation and neural frequency conversion at the recorded neuron. This hypothesis could also in part explain why the strength of neural frequency conversion and TI stimulation is reduced as stimulation frequency increases.

Further investigation into the origin of neural frequency conversion suggests that TTX-sensitive conductance, i.e. voltage-gated sodium channels (Stevens et al., 2011) and the persistent sodium channel (Taddese and Bean, 2002), contribute to neural frequency conversion. Evoked neural frequency conversion is attenuated greatly when TTX-sensitive conductance in the neuron is blocked, at both endogenous and kHz applied stimulation frequencies, such that the polarisation at f_Δ is no longer significantly larger than noise. This finding may seem logical because TTX effectively silences the network, as well as blocking subthreshold activated sodium conductance involved in subthreshold depolarisation (persistent sodium). However, given that the stimulation-evoked polarisation at f_Δ is typically on the order of 1mV above resting membrane potential ($\sim$-70mV), one would not expect TTX-sensitive channels to be open and allowing current to flow (activation gates open at $\sim$-55mV). Thus, one would not expect TTX-sensitive sodium currents to be contributing to the neural frequency conversion at this membrane potential. A possible explanation is that other compartments of the neuron, e.g. the dendrites, are more depolarised by the stimulation, to a point where TTX-sensitive channels are open, and the effects of blocking these are being observed at the soma. One way to test this would be by recording polarisation of of multiple compartments at once, for example via 2-photon imaging in conjunction with voltage/calcium imaging, or multiple concurrent patch clamp recordings. Similarly, given the unique electrical properties of dendrites and spines, the effects of kHz frequency neural stimulation on these structures should be of great interest to the field and may provide more insight into the mechanisms of TI stimulation. Further investigation into why

TTX has such as dramatic effect on polarisation at f_Δ may help uncover the origin of neural frequency conversion. As it stands, these results suggest that either a) nonlinearity of TTX-sensitive conductance i.e. mediated by voltage gated sodium channels, directly contributes to the production of neural frequency conversion, or b) depolarisation at f_Δ due to some cell membrane nonlinearity is amplified by these conductances.

Despite the significant reduction in neural frequency conversion following TTX, a small oscillation at f_Δ, when the average applied frequency is 5000Hz, is still visible. Whilst the peak at f_Δ in the PSD is not significantly greater than noise, the amplitude of the oscillation at f_Δ is greater than 0 (mean: 0.16mV, SEM: 0.11mV), which is representative of several cells which still exhibit the neural frequency conversion. This could potentially be indicative of another cell membrane nonlinearity, for example a nonlinear capacitance as previously discussed (see section 1.2.3). Whilst no APs could be evoked in any of these neurons, this certainly requires further investigation, to ensure that this result isn't just due to an incomplete block of TTX-sensitive conductance in some of these neurons. It is important to note an observation made during these experiments, that for both synaptic blocker and TTX application, the amplitude of the polarisation at f_Δ does seems to be recovered when stimulation amplitudes are further increased. The power behind this analysis was too low to include in this chapter and draw conclusions from, but warrants further study. If this is the case, it may provide more evidence that the neural network is not required (even at lower applied frequencies), and that another membrane nonlinearity is contributing to the neural frequency conversion. Additionally, this small oscillation that remains in the presence of TTX appears to be phase shifted. This is interesting and could be due to the change in effective membrane resistance.

The observed reductions in f_Δ power following drug application supports the conclusion that detection of a f_Δ polarisation in patched neurons is indeed neural polarisation and not artefact.

In this chapter, I aimed to determine the mechanism of action of TI stimulation. What is not clear from the results, due to the presence of significant stimulation artefact, is whether the nonlinear frequency conversion occurring at the neuron also results in polarisation at the sum frequency (f_Σ). I found that the power at f_Σ in my neural recordings was not significantly

greater than the noise level when the expected artefact amplitude was subtracted. This is with the exception of the 5000Hz condition, which does suggest some neural polarisation above noise and artefact, due to the artefact being very small at these frequencies. Whilst I used a very conservative estimate of the artefact, I interpret these results cautiously as potential sum frequency depolarisation. Due to potentially uncontrolled variability in the artefact size in neural recordings, this should be further characterised before making a conclusion, as I would expect polarisation at such a high frequency to be minute. The evidence that TI stimulation induces subthreshold depolarisation at f_Δ renders neurostimulation via a purely linear superposition impossible (mechanism option 1)(see section 3.1.1). Since both nonlinear FM (mechanism option 2), and nonlinear envelope detection via rectification (mechanism option 3) predict subthreshold depolarisation at f_Δ, the result showing this depolarisation during TI stimulation (kHz frequencies) is not enough to differentiate between the two. However, I found that neural frequency conversion can be evoked across a range of applied frequencies, including those that are of the same order of magnitude as f_Δ. This evidence strongly suggests that neural frequency conversion is not occurring via rectification (envelope detection), as envelope detection of a signal whose carrier frequency is on the same order of magnitude as f_Δ should not be possible (see section 3.1.1). This is due to the fact that the capacitor cannot be simultaneously not discharging in a period of the carrier (applied) frequency, and discharging during a period of the modulation (difference) frequency (which is what is required for envelope detection via rectification), if the two frequencies are similar. In other words, the envelope detection via rectification mechanism can only work for applied frequencies that are much larger than the difference frequencies. Given these results, I suggest that the mechanism by which f_Δ is being produced is Frequency Mixing (FM). The results presented in this chapter show the first evidence to suggest that the neuron can integrate and multiply signals in this way, to create signals with new frequency components.

FM occurs during TI stimulation across a range of applied frequencies. I showed that strength of this neural frequency conversion and thus TI, decreases as the stimulation frequencies increase. This result is expected when one considers the low-pass filtering properties of the neuron (see section 1.2.1). This result supports the conclusion that FM is driving neural activity during

TI, as depolarisation at the kHz frequency is required and if this depolarisation is of a smaller magnitude due to filtering, the magnitude of frequency mixing products will also be reduced. This finding has implications for the development of TI, as proposed strategies to improve focality of TI currently involve using much higher applied frequencies (Grossman et al., 2017). These findings would suggest that stimulation in the high kHz range would be very weak. Additionally, clinical application of TI can be guided by these results i.e. use of lower kHz frequencies will require less applied current. I found no significant difference in strength of neural frequency conversion or TI across difference frequencies suggesting that stimulation will be effective over a range of physiologically relevant difference frequencies.

Whilst frequency mixing is occurring during TI stimulation, whether it is the driving force of TI is important for understanding the spatial spread of stimulation and development of strategies to improve the strength and focality. If the stimulation strength is mediated entirely by frequency mixing, the production of polarisation at f_Δ should be dependent on the product of the applied current amplitudes, as it is this value that determines the magnitude of the emergent signal at f_Δ. In fact, the strength of the stimulation appears to be dependent on the summed amplitude of the applied currents. This is interesting because the magnitude of the frequency mixing product depends on the amplitude at the applied kHz frequencies, but it is known that nonlinearities in the neuron, such as the conductance of the membrane to an ion species such as sodium, depends on the membrane potential. That is, the ion channel opening probability vs. membrane potential is approximately a sigmoid curve (Colbert and Pan, 2002; Peters et al., 2017), leading to a combined sodium conductance (g) and the membrane potential (V) sigmoid shape relationship, aka the g-V curve. The coefficient of the linear term in the Taylor Series is g(v), and the coefficient of the first nonlinear term in the Taylor Series is g'(V)/2!, thus the magnitude of nonlinearity is is proportional to g'(V) and the relative magnitude g'(V)/g(V). If nonlinearity originates in the voltage-gated conductance to sodium, and it is represented by a sigmoid curve, g'(V) is greater when the membrane potential is more depolarised, which suggest that the magnitude of nonlinearity will also be greater. Thus in this case, as the sum amplitude increases, if depolarisation increases, the strength of nonlinearity may also increase, potentially explaining why we see this increase in nonlinear frequency conversion strength as the

sum increases. These results support the finding that TI strength depends on carrier frequency, as if TI is being driven by summed amplitude of the applied currents, it is being driven by direct polarisation at the kHz frequencies, and as the applied kHz frequency increases, polarisation at these frequencies will be attenuated due to low-pass filtering (see section 1.2.1). Together, these results suggest that frequency mixing is a contributing mechanism to TI stimulation, however TI stimulation may be strongest where the summed amplitude of the applied currents is greatest. This is different to the existing assumption, used in most modelling of the spatial spread of TI, that TI strength is strongest where envelope amplitude is largest (Grossman et al., 2017). Investigation into the spatial spread of TI stimulation using methods such as wide-scale calcium imaging, may aid in furthering our understanding.

The characterisation of the nonlinear stimulation artefact in my recording setup was pivotal for ensuring that depolarisation at frequency conversion products detected in neural recordings was real. The nonlinear stimulation artefact is significant at f_Σ but not at f_Δ. This is likely not due to there not being an artefact at f_Δ, but it being within the noise. The PSD of the nonlinear stimulation artefact at f_Σ is approximately 1e-4 to 1e-7 (% of the linear artefact) whilst the PSD of the noise floor is approximately 1e-7 to 1e-10 (% of the linear artefact)(depending on applied stimulation frequency). Thus the artefact at f_Σ can be detected above noise. If we assume that the nonlinear stimulation artefact at f_Δ is of the same order of magnitude (a reasonable assumption as they originate from the same nonlinear process in the stimulation hardware), it would be masked by the large noise floor of 1e-4 at f_Δ, thus neural polarisation, which is larger than the noise floor, is detectable. Secondly, the subthreshold neural polarisation at f_Σ is expected to be smaller than f_Δ due to the low-pass filtering property of the cell membrane, thus it is more likely to be masked by a large artefact. The origin of this nonlinearity is currently not clear but could be originating in the stimulation hardware, recording hardware or the electrode/electrolyte interfaces. Nonetheless, stimulation being applied directly at f_Δ is negligible due to the minute artefact at this frequency.

Lastly, I employed another method for FM detection (which is described in section 2.5 and utilised in chapter 4) on this single neuron data to see whether I could detect f_Σ (results not shown). This method involves the detection of a three-way phase relationship between signals,

to determine if a higher order nonlinear interaction is occurring. Preliminary testing of this method on these evoked nonlinear frequency conversion recordings suggested that the method was able to detect the strong phase relationship between the applied frequencies and the f_Δ and f_Σ nonlinear artefact signals. The measure used infers the strength of frequency mixing via the strength of the three way phase relationship, and is unable to significantly differentiate between artefactual frequency mixing and frequency mixing originating at the neuron. This is due to the artefactual frequency mixing phase relationship being very strong, as the applied signals and the artefact signals have constant phases, unlike neural signals.

3.4.2 Limitations

Firstly, significant nonlinear stimulation artefact at f_Σ in this setup prevented the detection of any neural polarisation present at this frequency. Evidence for production of f_Σ would greatly strengthen the conclusion that the neural frequency conversion being performed by the neuron is FM via multiplication of the signals, rather than envelope detection (see section 3.1.1).

In some instances, statistical comparisons were not significant or did not survive the conservative Bonferroni correction. These experiments are likely under powered and would benefit from a larger sample size. For example for the comparison of the effect of current product, sum amplitude and envelope amplitude on subthreshold neural frequency conversion, the normalised PSDs did not indicate polarisation at f_Δ was significantly larger than noise and thus could not be compared, despite the mean membrane potentials indicating a difference/no difference here.

For the investigation into the contribution of voltage-gated ion channels on neural frequency conversion, only TTX was applied. This neurotoxin blocks voltage-gated sodium channels but other voltage-gated ion channels mediating the movement of potassium and calcium exist in neurons (Armstrong and Hille, 1998). To investigate the contribution of all voltage-gated ion channels, and to investigate neural frequency conversion at the truly "passive" membrane, blockade of these would be required.

Investigation into the mechanism of TI stimulation in this chapter, has suggested that a)

neural frequency conversion is occurring during TI, b) strength of neural frequency conversion and TI depends on the applied stimulation frequency and c) strength of TI is determined by the summed amplitude of the applied currents. All of these findings strongly suggest that the neuron is being polarised at the kHz frequency and the magnitude of this polarisation is instrumental in determining the effects of the stimulation. This is in opposition to what has been previously reported, where it was shown that kHz frequencies are unable to depolarise the neuron (Grossman et al., 2017). Thus, further investigation into how neurons respond to kHz frequencies and whether the response to an amplitude modulated kHz frequency is different to a pure un-modulated kHz frequency is an open question and essential for the development of TI.

3.4.3 Future directions

Development of the work done in this chapter could include further investigation into the origin of the nonlinear stimulation artefact, so that it may be significantly reduced, and a conclusion regarding whether f_Σ is produced at the neuron can be made. This will strengthen the evidence that neural frequency conversion is via multiplication (FM). The nonlinear artefact at higher applied frequencies appears to be smaller, thus focusing on higher frequencies could be a good strategy here, although the polarisation at these frequencies will be much smaller.

Another potential method for probing whether FM is the mechanism by which the nonlinear frequency conversion is occurring is to do a more in-depth analysis on the higher frequency mixing products, e.g. the harmonics of the applied frequencies, to determine whether these are present in the evoked subthreshold activity. This would confirm that frequency conversion is via multiplication rather than via rectification.

In order to conclusively determine whether the passive membrane is able to exert neural frequency conversion, or whether the voltage-gated ion channels are the origin of nonlinearity underlying this, investigation into whether neural frequency conversion occurs on a truly passive membrane could be performed. For example application of the electric fields to cultured non-neuronal cells (e.g. Human Embryonic Kidney (HEK) cells) with endogenous conductance

blocked, or an artificial bilipid membrane, would reveal any nonlinearity in membrane elements typically considered to be passive (e.g. the capacitance).

I suggest that the strength of nonlinearity may be dependent on the sum of applied currents, due to nonlinearity at depolarised membrane potentials being stronger. This could potentially be directly tested, by investigating whether nonlinear frequency conversion strength is altered when the neuron membrane potential is depolarised or hyperpolarised.

As mentioned previously, investigation into the direct effects of simulation at non-amplitude modulated kHz frequencies will be instrumental in deciphering the mechanism and neurophysiological consequences of TI stimulation, potentially with implications for focality.

3.4.4 Conclusions

In conclusion, I show that nonlinear frequency conversion, likely FM, can be performed by the single neuron, and that this process originates at the cell membrane. Additionally, I investigate the mechanism of TI and show that it induces subthreshold depolarisation of the neuron at f_{Δ}, and thus that neural frequency conversion is occurring during TI stimulation. This will aid in the development and improvement of TI. Additionally, I show that evoked neural frequency conversion is occurring at a wide range of frequencies, including those typical of endogenous neural oscillations. This opens up the question of whether the neuron utilises this process to integrate endogenous neural signals, and as neural frequency conversion results in novel frequency components, also potentially create neural signals with new frequencies.

Chapter 4

Higher order nonlinear frequency interactions in spontaneous neural activity

The work presented in this chapter is part of a collaborative project. The method for detecting higher order interactions was developed by my colleague Dr. Robert Peach, under the supervision of Professor Mauricio Barahona. The human EEG data was collected by Dr. Emma-Jane Mallas, under the supervision of Professor David Sharp.

4.1 Introduction

In the previous chapter, I showed evidence of an evoked nonlinear frequency conversion phenomena that originates at the cell membrane (see chapter 3). Given that this neural frequency conversion occurs at low frequencies, I concluded that it is likely to be via a multiplicative nonlinear process (FM). This finding also raised the question of whether FM occurs also in spontaneous neural activity. Indeed, FM has been detected in LFP recordings of network level spontaneous neural activity in the rodent brain (Haufler and Paré, 2019). Additionally one study suggests that evoked FM is present in human brain activity, as evidenced by the pres-

ence of higher order mixing products in the evoked potential, in response to two modulated visual gratings of different frequencies (Regan and Regan, 1987). There does not yet appear to be any specific evidence of FM in spontaneous human brain activity. Thus, nothing is known about the presence of FM in human cortical activity, and whether alterations in higher order nonlinear frequency interactions (such as FM) in the brain are associated with alterations in cognitive processes or behaviour, is subsequently unknown.

When multiple brain regions exhibit patterns of activity that are coupled or associated, they can be thought of as being part of a large-scale functionally connected brain network (Friston, 2011). The definition of functional connectivity is the temporal coherence of neurophysiological activity separated in space. It has been hypothesised that if the activity between two regions exhibits a statistical dependency, they are likely to be components of the same network, and can be considered to show functional connectivity (Friston, 2011).

Traumatic Brain Injury (TBI) causes wide-scale disruption of functionally connected brain networks, including alteration of CFC (see section 1.3.3) (Sharp et al., 2011; Antonakakis et al., 2016; Sharp et al., 2014). This abnormal network activity is thought to underpin cognitive and memory impairment in TBI (De Simoni et al., 2018; Mallas et al., 2021a). Whether FM plays a similar role in the brain to CFC is unknown, but as it can be thought of as a higher order nonlinear frequency interaction, it could potentially represent a form of functional connectivity. Thus, investigation into whether FM is disrupted in brain activity where functional connectivity is altered, i.e TBI, could help reveal the role of FM in functionally connected networks.

As shown using synthetic data in section 2.5, FM, i.e. as produced by the application of two input signals to a nonlinear activation function, creates output signals at the difference and sum frequency (f_Δ and f_Σ) of the applied signals. A three-way phase relationship exists between each of these output signals and the two input signals, i.e. the phase of the f_Δ signal is the difference in phase of the two applied signals, and the phase of the f_Σ signal is the sum of the two applied signal phases. Thus, detection of this three-way phase relationship in neural activity could indicate the presence of signals involved in FM. Haufler and Paré (2019), suggest that detection of phase relationships is a more sensitive way to detect FM in neural signals,

given that resolving discernible peaks in noisy power spectra is difficult. Indeed, the method introduced in section 2.5 for detection of dependency between signal phases, is believed to be robust, such that it should be capable of detecting FM in a noisy signal such as an EEG recording (Figure 2.5).

In this chapter I investigate whether spontaneous FM can be detected at the single neuron utilising whole cell patch clamp and a novel methodology for detecting three-way phase relationships between neural signals (see section 2.5). Furthermore, using this method on EEG recordings, I investigate whether a) spontaneous FM can be detected in large-scale human cortical activity and b) these higher order nonlinear interactions change in conditions characterised by abnormal network activity, i.e. Traumatic Brain Injury (TBI).

4.2 Methods

4.2.1 *Ex-vivo* brain slice preparation

As in section 3.2.1.

4.2.2 Whole cell patch clamp recording

As in section 3.2.3.

4.2.3 Participants

Healthy adults

EEG recordings from twenty one healthy adults (18 males, 3 females; mean age 29, range 18-70 years) were included in the analysis. Human data was collected under approval by the West London Research Ethics Committee (09/HO707/82). Written informed consent was obtained for all participants judged to have capacity, according to the declaration of Helsinki.

Traumatic brain injury patients

EEG recordings from seventeen acute TBI patients (14 males, 3 females, mean age 41.12, range 19-73 years) were included. All patients had been diagnosed with a recent moderate-severe TBI, as defined by the Mayo TBI Classification System (Malec et al., 2007). Patients were recruited from the Major Trauma Ward, St Mary's Hospital, Imperial College Healthcare Trust, London, UK, within the first two weeks of injury. Exclusion criteria were as follows: significant psychiatric or neurological illness; previous significant brain injury; current or previous substance or alcohol abuse; current pregnancy or breastfeeding; recent neurosurgical intervention or other contraindication to scalp EEG. Further detail including clinical details and cognitive profiles of all TBI patients can be found in Mallas et al. (2021b).

4.2.4 Electroencephalogram acquisition

Recordings were obtained using a 32-channel active electrode standard actiCAP (Easycap, Woerthsee-Etterschlag, Germany). Five minutes of eyes-closed resting state EEG data was taken and 1 minute of artefact free recording from the middle of the recording was used in analysis. Signals being recorded were amplified using the actiCHamp system and data were recorded using the BrainVision Recorder software (Brain Products GmbH, Gilching, Germany) at a sampling rate of 1000 Hz. Full details can be found in Mallas et al. (2021b).

4.2.5 Cognitive testing

Sustained attention

Sustained attention was assessed using the Feature Match task, which was delivered via a custom-programmed application on a touchscreen tablet (Hampshire et al., 2012). A series of shapes were presented in two side-by-side grids. The shapes presented in each grid were identical for half of all trials, and differed by one shape in the other half. The participant had to state whether the shapes in the grid match each other or mismatch. The first trial contained

one shape in each grid and the number of shapes increased with each correct response. One less shape in each grid was presented after every incorrect response. The task lasted for 90 seconds, during which the participant had to solve as many trials as possible. The main outcome measure was the total score.

Working memory binding

The ability to integrate separate visual features is a feature of working memory (Schneegans and Bays, 2019). This was assessed using an precision recall object-location association task (Pertzov et al., 2012). Full details of the task procedure are outlined in Mallas et al. (2021b). In summary, the subject viewed 1 (20 trials) or 2 (60 trials) fractal images, displayed in various locations across the screen. Following a 2 second maintenance period, a target image (a previously displayed image), and a "distractor" image (one not previously displayed) were shown. The participant had to choose which item they saw previously, and move it across a free-recall space to where it was previously positioned. This task gives a measure of the participants ability to:

1. Remember the identity of an object.
2. Remember the location of an object.
3. Bind this information together.

Trials in which an object was correctly remembered, but the location was incorrectly assigned to the location of a different item, suggests that a misbinding error has taken place. A measure of entropy ratio was used to quantify the distribution of responses between the target and non-target location in a normalised space (see Mallas et al. (2021b) for further details). To summarise, a higher entropy ratio is indicative of a greater affinity towards the non-target item, suggesting a failure of object-location integration in working memory, or memory binding.

4.2.6 Detection of significant three-way phase relationships

Strength of FM can be represented by a measure termed the HOI strength. The larger the HOI strength, the stronger the three-way phase relationship between three signals with different frequencies. As three-way phase relationships are only tested on combinations of frequencies which could arise via FM, we assume that this value gives a measure of the FM at that triplet. Generation of the HOI strength measure is described previously (see section 2.5). It can be determined whether each triplet within a signal has a significant three-way phase relationship and is thus a significant triplet. Additionally, the HOI strength for each triplet can be computed. Significant triplets within a neural signal are either compared to significant triplets within a neural signal under a different condition, or alternatively, to the HOI strength that exists by chance.

When the HOI values in a set of neural signals drawn from one condition are compared to the HOI values of the triplets in another condition, a two-sample t-test can be performed. Determination of whether the HOI value obtained for a triplet in a neural signal is greater than the HOI value obtained by chance involves comparing to surrogate data sets, which are detailed below.

Surrogate Data

Surrogate data was used to determine the existence of significant higher order nonlinear interactions in spontaneous single neuron, and human cortical activity.

For single neuron recordings, surrogate data was constructed that replicated the membrane potential recording data, but without any nonlinear frequency interactions that could produce FM. To construct a surrogate for each membrane potential recording, we:

1. Applied a Fourier transform to the signal.
2. Took the magnitude (absolute) of the imaginary number, to remove phase information but to retain the power distribution.

3. Applied an inverse Fourier transform.

The resulting surrogate signal retained the power distribution of the original signal but the phase information was entirely removed (including any associated phase dependence between frequency components).

For the comparison with healthy human EEG data, surrogate data was constructed that replicated the healthy human data but without any nonlinear frequency interactions that could produce FM (n = 20). Synthetic participants with six EEG channels (Fp1,Fp2,Oz,Pz,T7,T8) at the same sampling rate and total duration (1 minute) of the participant EEG recordings were created. The surrogate signals included oscillatory signals at random frequencies to introduce temporal dependence, plus a noise term. The oscillatory signals were not mixed via a non-linear interaction, which created a baseline signal with non-interacting signals (absent of three-way phase dependence).

Surrogate Distribution

Surrogate distributions were created using the surrogate data detailed above.

For the single neuron recordings, paired samples of neuron recordings and their respective surrogates (where the phase dependence was removed) were taken. The HOI was calculated for all triplets in both the original signals and the surrogate signals. The surrogate HOI strengths for each triplet were compared to the HOI strengths for each triplet in the neural recordings using a paired t-test, which returned a t-value (and a p-value indicating the significance of the group test vs. surrogate). Triplets that were significant ($p < 0.05$) could then be clustered together during a cluster permutation test (see next section).

Similarly, for the healthy human EEG recordings for each of the 20 surrogate participant signals (produced as described in the above section), the HOI strength of each possible triplet was computed. This gives surrogate HOI strengths for each triplet which could be be compared to the HOI strengths in the neural recordings using a two sample t-test, returning a t-value and a p-value for each triplet, which indicated whether the HOI strength of a neural signal

triplet is significantly larger than the HOI strength of the surrogate distribution triplet. If a neural signal triplet was deemed to be significant in this way, it was included in the cluster permutation.

Cluster permutation tests

Multiple hypothesis testing was required to test whether all triplets have a significantly greater HOI strength than either a triplet under another condition or the surrogate. Bonferroni correction is too conservative in this case. Therefore, a cluster permutation test was implemented to identify clusters of FM triplets that were significant (either via a t-test between two groups, or for a regression against a behavioural measure score).

Cluster permutation t-test

For the cluster permutation t-tests, any triplets that were considered to have a significantly stronger HOI when compared to another condition (paired t-test for paired samples (comparison to another condition), or two-sample t-test for unpaired samples (comparison to surrogate)) were retained ($p < 0.05$). Significant triplets were then clustered according to their similarity, where similarity is defined by both distance in frequency space and spatial distance. Similarity inside frequency space is defined as a Euclidean distance, such that for two FM triplets (x_1, y_1, z_1) Hz and (x_2, y_2, z_2) Hz, if their distance $\sqrt{(x_1 - x_2)^2 + (y_1 - y_2)^2 + (z_1 - z_2)^2} <= 2$, they could be clustered together. The spatial distance between triplets was defined by the channels, such that clustering two triplets required two of the three frequency components to be found in the same channel.

For each cluster, the t-values of the significant triplets were summed and then compared against a null distribution. A null sample was generated by permuting the condition labels (permuting signals between conditions) and the triplet label (permuting the index of triplets). The process of identifying significant triplets at the group-level (t-test) was repeated and clusters of significant triplets were found in the null sample. The sum of t-values was calculated for each cluster

and the largest sum of t-values was returned for the null sample. This was repeated 50,000 times to generate a null distribution comprised of 50,000 values (where each element was the sum of t-values for the largest cluster from a null sample).

The sum of t-values of each cluster in the neural recording data was then compared to the null distribution. A p-value was obtained which represents the proportion of null samples where the sum of t-values for the largest cluster was larger than the sum of t-values for the cluster in the original data. Each cluster was considered a significant cluster if $p < 0.05$, and each triplet within a cluster could be considered to be a significant triplet.

Cluster permutation regression

To determine whether the HOI strength for a given triplet correlated with the score from a cognitive test, a cluster permutation regression test was performed. For each triplet, the HOI strengths and the cognitive test score for each participant was taken. A regression was performed to see whether a relationship between the two exists. A t-value and p-value was obtained for every triplet, and a permutation cluster test was performed (in a similar manner to the above section) to determine significant clusters of triplets, and significant triplets, that correlate either positively or negatively with the behaviour measure.

Triplet definitions

Triplets that were defined as intra-region were triplets where the instantaneous phases of three frequency components were found within a single measurement channel, e.g., the triplet 7Hz (Oz),18Hz (Oz),25Hz (Oz) would be an intra-region triplet. Inter-region triplets on the other hand, were triplets where the instantaneous phases of three frequency components came from at least two different measurement channels, e.g., the triplet 7Hz (Oz),18Hz (Pz),25Hz (Oz) would be an inter-region triplet.

A triplet could be considered a member of a frequency band if at least one frequency component falls into the respective frequency band.

Statistical analysis

All data is mean ± SEM. Values are presented in tables which are referred to in the text. Statistical tests are specified in table and figure legends. All t-tests are two tailed unless stated. In all plots, the * notation represents a statistical significance that survived Bonferonni correction.

4.3 Results

4.3.1 Three-way phase relationships indicative of frequency mixing are present in spontaneous neural activity detected at the single neuron

A three-way phase relationship between three signals with frequencies $f_1/f_2/f_\Delta$ or $f_1/f_2/f_\Sigma$ (a triplet) is indicative of FM (see section 2.5.1). FM is a higher order frequency interaction, which could have implications for neural processing, thus it is of interest whether it is present in spontaneous neural activity. As evoked FM can be detected at the single neuron (see section 3.3.1), I first asked whether spontaneous FM can also be detected at this level, using whole cell patch clamp and a novel method for detecting FM via the three-way phase relationship (see section 2.5.1).

Indeed, triplets with significantly larger HOI strength values, compared to those expected by chance are detectable in single neuron recordings of spontaneous activity (Figure 4.1 Ai). 2310 triplets have a significantly stronger HOI strength compared to surrogate. Significant triplets predominantly contain signals with frequencies in the alpha, theta and delta frequency bands, as indicated by the sum of the HOI strengths across all significant triplets that consist of a frequency within those frequency bands (Figure 4.1 Aii).

These results suggest that a) FM is occuring, b) it can be detected at the single neuron and c) that the novel method for detection of FM of three-way phase is effective.

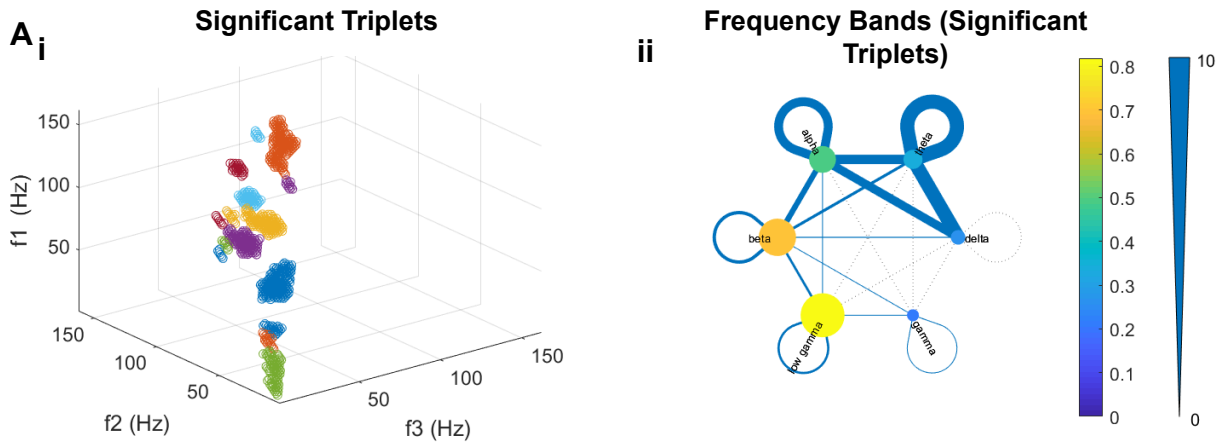


Figure 4.1: **Detection of frequency mixing in spontaneous single neuron activity** *(A) Evidence for Frequency Mixing (FM) is presented in the form of significant three-way phase relationships between neural signals of three different frequencies (triplets), that are detectable at the single neuron. The frequencies of the neural signals which have these three-way phase relationships range from delta to gamma, however most triplets are composed of three signals whose frequencies fall in the delta, theta, and alpha frequency bands.* (A)(i) Scatter plot indicating clusters of frequency triplets with significantly larger Higher Order Interaction (HOI) strength in spontaneous neural activity compared to surrogate. Each different colour group of triplets represents a significant cluster and each triplet within a cluster can be considered significant. Cluster permutation test vs surrogate. (ii) A frequency band interaction plot displaying the strength of HOI of the significant triplets within and between frequency bands. Nodes (colour and size) indicate the sum of HOI strengths across all significant triplets that consist of a frequency within that frequency band (normalised by total number of triplets tested). Edge width indicates the normalised sum of HOI strengths across all significant triplets containing frequencies that fall within the linked frequency bands. n = 20 cells.

4.3.2 Blockade of voltage-gated ion channels and synaptic input reduces frequency mixing strength in spontaneous neural activity detected at the single neuron

I found evidence of FM in spontaneous neural activity detected at the single neuron (see section 4.3.1), thus I next asked whether FM can still be detected at the single cell, in the absence of neural network input and when TTX-sensitive conductance is blocked. Additionally, I investigated whether the strength of FM, as indicated by the calculated HOI strength (see section 2.5.1), is different in the absence and presence of the network and TTX-sensitive conductance. I hypothesised that due to the absence of signals of different frequencies polarising the cell via the synapse in these conditions, both the amount of HOIs and the strength of FM, will be decreased compared to when neural network input is present. Additionally, as TTX was shown to decrease the amplitude of the evoked neural frequency conversion product at f_Δ (see section 3.3.7) (potentially due to the contribution of TTX-sensitive voltage-gated conductance to the nonlinearity underlying it), I expect the overall strength of FM to be decreased in spontaneous neural activity when TTX is applied. To investigate these questions, I computed the strength of FM in whole cell patch clamp recordings of single neuron activity when synaptic blockers and TTX were applied to the slice.

I found that both TTX and synaptic blockade reduce the FM clusters (Figure 4.2 A). Additionally, there are no triplets that have significantly larger HOI strengths in spontaneous neural activity during TTX application, or synaptic blockade, compared to in spontaneous neural activity with no drug (Figure 4.2 B, C). Conversely, 9 triplets have significantly larger HOI strengths prior to drug application compared to during TTX (Figure 4.2 B), and 148 triplets have significantly larger HOI strengths prior to synaptic blockade compared to during synaptic blockade (Figure 4.2 C). The HOI strength across all triplets prior to drug application is significantly stronger compared to with both synaptic blockers (no drug: 0.28 ± 0.046 a.u, synaptic blockers: 0.17 ± 0.0035)($p = 0.046$), and TTX (no drug: 0.36 ± 0.10 a.u, TTX: 0.23 ± 0.059)($p = 0.019$)(Figure 4.2 D).

Together, these results suggest that the neural network and TTX sensitive conductance, such as that from the voltage-gated ion sodium channel, play a role in spontaneous FM. Specifically, both of these factors contribute to the overall amount and strength of FM that occurs endogenously and can be detected at the single neuron. This is likely due to the reduction in signals of different frequencies reaching the neuron and the signals at the neuron being of a smaller amplitude respectively.

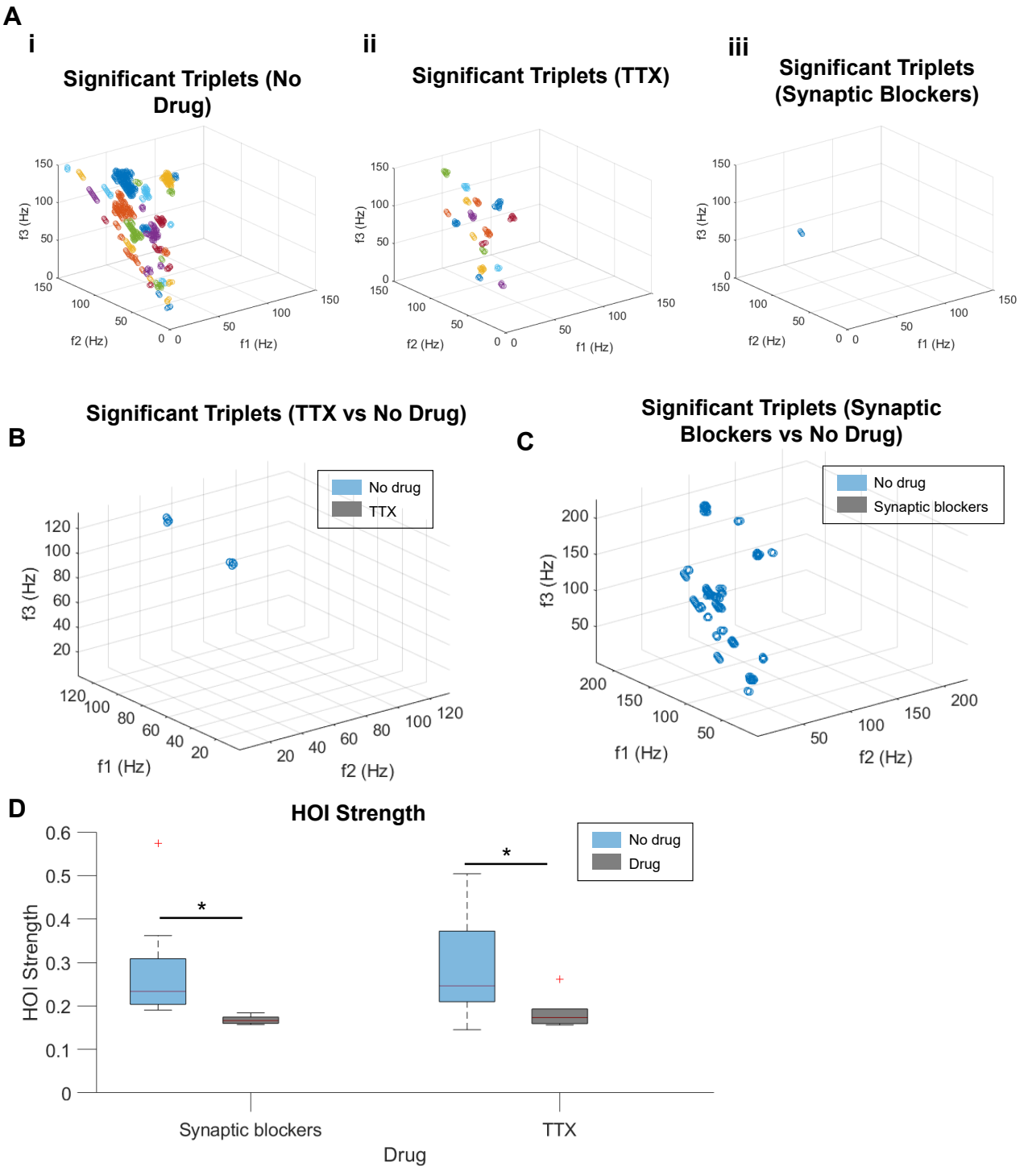


Figure 4.2: **Characterisation of frequency mixing in spontaneous single neuron activity in the absence of tetrodotoxin-sensitive conductance and synaptic input**

Figure 4.2: **Characterisation of frequency mixing in spontaneous single neuron activity in the absence of tetrodotoxin-sensitive conductance and synaptic input** *(A-B) The number of significant nonlinear frequency interactions between neural signals of three different frequencies (triplets) is reduced in the absence of Tetrodotoxin (TTX)-sensitive conductance and synaptic input (C) The strength of nonlinear frequency interactions between neural signals of three different frequencies is significantly reduced in the absence of both Tetrodotoxin (TTX)-sensitive conductance and synaptic input*(A)(i) Scatter plot indicating clusters of frequency triplets with significantly larger Higher Order Interaction (HOI) strength in spontaneous neural activity (no drug) compared to surrogate. Cluster permutation test vs surrogate. n = 10 cells. (ii) Scatter plot indicating clusters of frequency triplets with significantly larger Higher Order Interaction (HOI) strength in spontaneous neural activity (under TTX) compared to surrogate. Cluster permutation test vs surrogate. n = 10 cells. (iii) Scatter plot indicating clusters of frequency triplets with significantly larger Higher Order Interaction (HOI) strength in spontaneous neural activity (under synaptic blockers) compared to surrogate. Cluster permutation test vs surrogate. n = 8 cells. (B) Scatter plot indicating clusters of frequency triplets with significantly larger Higher Order Interaction (HOI) strength in spontaneous neural activity without TTX compared to with TTX (blue) and with TTX compared to without TTX (grey). Cluster permutation test, no drug vs TTX. n = 10 cells. (C) Scatter plot indicating clusters of frequency triplets with significantly larger Higher Order Interaction (HOI) strength in spontaneous neural activity without synaptic blockers compared to with synaptic blockers (blue) and with synaptic blockers compared to without synaptic blockers (grey). Cluster permutation test, no drug vs synaptic blockers. n = 8 cells. (D) Boxplot showing HOI strength across all possible triplets (combinations of frequencies between 1-45 Hz) before drug application (blue) and after blockade of synaptic input and TTX-sensitive ion channels (grey). Boxplot showing median (line), 25th (bottom edge) and 75th (top edge) percentiles. Whiskers extend to the most extreme data points not considered outliers. + indicates outliers. Paired t-test. * = $p < 0.05$. n = 8 cells (synaptic blockers), n = 10 cells (TTX).

4.3.3 Frequency mixing can be detected in large-scale spontaneous human cortical activity

Given that FM can be detected in spontaneous neural activity at the single neuron, I next asked whether FM can be detected in large-scale human cortical activity and whether differences in local and global FM exist. Additionally, I investigated whether the strength of FM, as indicated by the calculated HOI strength (see section 2.5.1) is related to the spectral power. To achieve this, I computed the strength of FM in EEG recordings of human cortical activity.

To investigate the presence of FM in human neural activity, all significant FM triplets from 1-45 Hz *within* and *between* EEG channels grouped into three regions (frontal: Fp1, Fp2; Temporal: T7, T8; Occipital/Parietal: Oz, Pz), to quantify the intra- and inter-region FM respectively,

were determined. More explicitly, intra-region FM refers to only those triplets whose component signals are all found within the same EEG channel, and thus can be considered to be local frequency mixing. Conversely, inter-region FM provides insight into more wide-spread FM by be being defined as only those triplets whose triplet components arise from two or more different EEG channels. The three brain regions (Frontal, Temporal, Occipital/Parietal) were chosen to provide channel representation across the whole scalp.

FM can be seen in spontaneous cortical activity of healthy humans within and between brain regions, across regions and frequency bands (Figure 4.3 A-C). The mean HOI strength across all triplets is significantly stronger in healthy human EEG compared to surrogate, for triplets that are both intra-region ($p < 0.0005$) and inter-region ($p < 0.0005$) (Figure 4.3 A). The mean HOI strength for intra-region FM (0.19 ± 0.0058 a.u) is significantly stronger than for inter-region FM (0.17 ± 0.0008 a.u) ($p < 0.0005$) (Figure 4.3 A). The mean HOI strength across all triplets is significantly stronger in healthy human EEG compared to surrogate, for both intra- and inter-region FM, across frontal, occipital and parietal, and temporal brain regions (Frontal; Intra: 0.18 ± 0.0081 a.u, p = 2.31e-08 Inter: 0.17 ± 0.0020 a.u, p = 6.96e-22, Occipital and Parietal; Intra: 0.18 ± 0.0027 a.u, p = 1.97e-18 Inter: 0.18 ± 0.0011 a.u, p = 1.95e-30, Temporal; Intra: 0.20 ± 0.014 a.u, p = 2.30e-08 Inter: 0.17 ± 0.0012 a.u, p = 7.11e-29)(Figure 4.3 B). Additionally, the mean HOI strength across all triplets is significantly stronger in healthy human EEG compared to surrogate, for both intra- and inter-region FM, across all frequency bands (Delta; Intra: 0.17 ± 0.0071 a.u, p = 3.25e-08 Inter: 0.17 ± 0.0047 a.u, p = 3.95e-11, Theta; Intra: 0.18 ± 0.0062 a.u, p = 2.45e-11 Inter: 0.18 ± 0.0037 a.u, p = 1.22e-15, Alpha; Intra: 0.20 ± 0.00354 a.u, p = 5.82e-15 Inter: 0.18 ± 0.0029, p = 6.64e-19, Beta; Inter: 0.20 ± 0.0070 a.u, p = 1.59e-12, Intra: 0.17 ± 0.00098 a.u, p = 2.90e-31, Low-gamma; Inter: 0.19 ± 0.0059 a.u, p = 1.19e-13, Intra: 0.17 ± 0.00066 a.u, p = 1.22e-35)(Figure 4.3 C).

The decrease in HOI strength for inter-region FM compared to intra-region FM persists across all conditions when data is stratified across brain regions and frequency bands with the exception of the delta frequency band (Figure 4.3 A-C).

The strength of within and between region FM is independent of amplitude of ongoing oscilla-

tory signals (Figure 4.3 D). There is no significant correlation between HOI strength and power across all frequency bands for either intra-region (Figure 4.3 Di) or inter-region FM (Figure 4.3 Dii) (see Table 4.1 for all values).

Correlation measure	**Frequency Band**				
	Delta	*Theta*	*Alpha*	*Beta*	*Low gamma*
Measure			**Intra-region**		
R^2	-0.028	-0.036	-0.059	-0.018	-0.054
p-value	0.48	0.55	0.99	0.41	0.73
Coefficient	4.79e-06	-1.73e-06	-3.11e-08	-6.72e-06	-3.43e-06
			Inter-region		
R^2	0.062	-0.056	0.18	-0.069	-0.067
p-value	0.17	0.84	0.04	0.87	1.00
Coefficient	3.63e-06	2.98e-07	2.95e-06	4.09e-07	-2.09e-09

Table 4.1: **Correlation measures for HOI strength vs average band power** Simple linear regression.

Across brain regions, the frequencies involved in FM differ (Figure 4.4 Ai). In the parietal and occipital regions, signals involved in FM fall in the beta and alpha frequency bands (Figure 4.4 Aiii). For frontal and temporal FM however, signals involved in FM fall in the beta and low-gamma bands (Figure 4.4 Aii, iv). For inter-region FM, the signals that make up triplets are detected across all EEG channels and thus regions (Figure 4.4 Bii). This intra-region FM typically involves signals in the theta and delta frequency bands (Figure 4.4 Biii). Together these results suggest that local FM (which occurs within a brain region) involves higher frequencies (alpha to low gamma), whereas inter-region FM involves lower frequencies (delta to alpha).

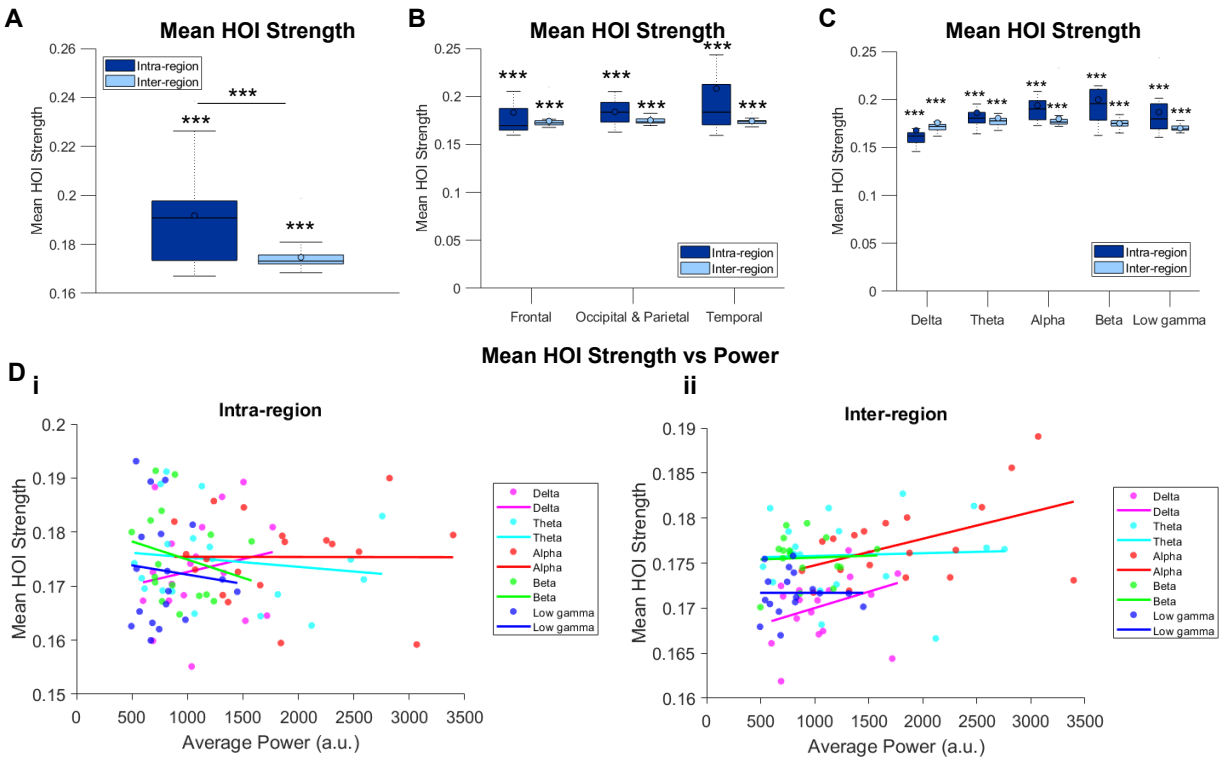


Figure 4.3: **Detection of frequency mixing in spontaneous cortical activity in the healthy human brain** *(A-C) Higher order nonlinear frequency interaction between neural signals of three different frequencies (triplets) occur across all brain regions and frequency bands, with within region Higher Order Interaction (HOI)s being significantly stronger than between region (D) Higher order interaction strength is independent of spectral power for both within and between region interactions* (A) Boxplot showing mean HOI strength of all higher order nonlinear frequency interactions occurring within a channel (intra-region) and between channels (inter-region) in healthy participant cortical activity. Two-sample t-test comparing mean HOI strength in healthy participants to surrogate data-set. Paired t-test comparing intra- and inter-region mean HOI strength. * indicates a significant difference that survived Bonferroni correction. *** = $p < 0.0005$. n = 20 healthy participants. (B) Boxplot showing mean HOI strength of all higher order nonlinear frequency interactions occurring within a channel (intra-region) and between channels (inter-region) in healthy participant cortical activity, stratified into brain region. Two-sample t-test comparing mean HOI strength in healthy participants in each region to surrogate data-set. * indicates a significant difference that survived Bonferroni correction. *** = $p < 0.0005$. n = 20 healthy participants. (C) Boxplot showing mean HOI strength of all higher order nonlinear frequency interactions occurring within a channel (intra-region) and between channels (inter-region) in healthy participant cortical activity, stratified into frequency band. Two-sample t-test comparing mean HOI strength in healthy participants in each region to surrogate data-set. * indicates a significant difference that survived Bonferroni correction. *** = $p < 0.0005$. n = 20 healthy participants. All boxplots showing median (line), mean (circle) and interquartile range (IQR). (D) Scatter plot showing relationship between mean HOI strength and normalised average power for (i) intra-region and (ii) intra-region higher order frequency interactions for each frequency band. For each participant, the average power at each frequency band was computed and plotted against the mean HOI strength for all frequency interactions containing a frequency within that frequency band. Average power for each band was normalised to the mean power across all bands in that participant.n = 20 healthy participants.

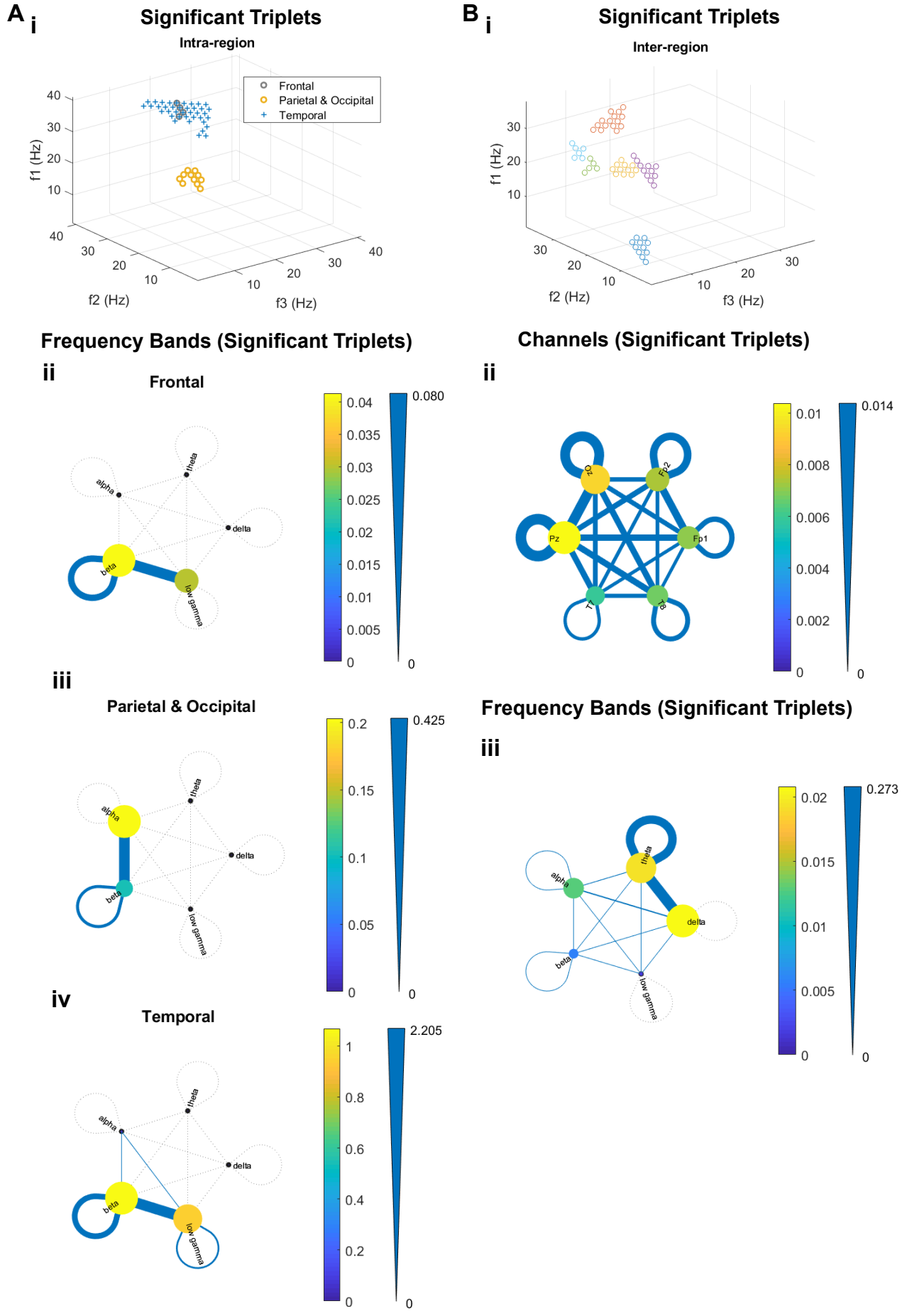


Figure 4.4: **Characterisation of frequency mixing in spontaneous cortical activity in the healthy human brain**

Figure 4.4: **Characterisation of frequency mixing in spontaneous cortical activity in the healthy human brain** *(A) Higher order frequency interactions are occurring between neural signals existing within a brain region, and the frequencies of the signals involved in these higher order interactions are different depending on the brain region. For within region higher order interactions, those involving neural signals with beta and low gamma frequencies are most common (B) Between region higher order frequency interactions are occurring across all brain regions and frequency bands, although Higher Order Interaction (HOI)s involving neural signals with delta and theta frequencies are most common* (A)(i) Scatter plot indicating clusters of frequency triplets with significantly larger HOI strength in healthy human cortical activity compared to surrogate. Plot shows only intra-region interactions, and each triplet within a cluster can be considered significant. Colours indicate brain region where the significant frequency intra-region interaction is occurring. Cluster permutation t-test, cluster permutation z-test vs surrogate. n = 20 healthy participants. (ii) A frequency band interaction plot displaying the strength of HOI of the significant triplets within and between frequency bands for intra-region frequency interactions in the frontal region. n = 20 healthy participants. (iii) As in (ii) for the parietal and occipital region. (iv) As in (ii) for the temporal region. For all interaction plots, nodes (colour and size) indicate the sum of HOI strengths across all significant triplets that consist of a frequency within that frequency band (normalised by total number of triplets tested). Edge width indicates the normalised sum of HOI strengths across all significant triplets containing frequencies that fall within the linked frequency bands. (B)(i) As in (A)(i), except plot shows only inter-region interactions. (ii) Brain region interaction plot displaying the strength of HOI of the significant triplets within and between brain regions for inter-region frequency interactions. n = 20 healthy participants. Nodes indicate (colour and size) the sum of HOI strengths across all significant triplets that consist of at least one neural signal that was detected within that brain region (normalised by total number of triplets tested). Edge width indicates the normalised sum of HOI strengths across all significant triplets containing two neural signals that were detected within the linked brain regions. (iii) Frequency band interaction plot displaying the strength of HOI of the significant triplets within and between frequency bands for inter-region frequency interactions across all brain regions. n = 20 healthy participants. Nodes (colour and size) indicate the sum of HOI strengths across all significant triplets that consist of a frequency within that frequency band (normalised by total number of triplets tested). Edge width indicates the normalised sum of HOI strengths across all significant triplets containing frequencies that fall within the linked frequency bands.

4.3.4 Frequency mixing is significantly different in spontaneous neural activity in traumatic brain injury compared to spontaneous neural activity in the healthy brain

I found that FM is occurring in spontaneous human cortical activity. An interesting question, which may aid in gaining further insight into this phenomenon and its role in the brain, is whether the strength of FM is altered in disease. To investigate this, I performed a preliminary investigation which computed, and compared, the strength of FM in EEG recordings of human cortical activity obtained from healthy participants, and TBI patients, who had significant impairments in memory binding and sustained attention.

TBI patients exhibit a greater degree of memory misbinding (0.91 $\pm$ 0.055 a.u)(as measured by the entropy ratio), compared to healthy participants (0.66 $\pm$ 0.063 a.u), as expected (p = 0.0062)(Figure 4.5 B). I found that distinct clusters of triplets, that is FM involving certain frequencies, correlate positively and negatively with memory misbinding (Figure 4.5 C). The channels that these triplets are found in (Figure 4.5 D) and the frequencies that make up the triplets (Figure 4.5 E) are different, for those that are positively and negatively correlated. For example, positively correlated triplets are mostly found in the temporal lobe (T8 electrode)(Figure 4.5 Di) and negatively correlated triplets are more dispersed across channels with a large proportion involving signals detected within the frontal region (Fp1 and Fp2 electrodes) (Figure 4.5 Dii). Triplets that positively correlate with memory misbinding involve signals in the theta, beta and low gamma bands only (Figure 4.5 Ei), whereas triplets that negatively correlate with memory misbinding are composed of signals with frequencies in the delta, theta, and alpha frequency bands (Figure 4.5 Eii).

The strength of FM across all triplets that are positively correlated with memory misbinding was compared across healthy participants and TBI patients. The mean HOI strength across all triplets that are positively correlated with memory misbinding is significantly stronger in TBI patients (0.2048 $\pm$ 0.022) compared to healthy participants (0.1568 $\pm$ 0.010)(p = 0.037)(Figure 4.5 Fi). The same was done for negatively correlated triplets and the inverse was found. The

mean HOI strength across all triplets that were negatively correlated with memory misbinding is significantly weaker in TBI patients (0.1589 ± 0.0074) compared to healthy participants (0.2391 ± 0.041)($p = 0.023$)(Figure 4.5 Fii).

Together, these results suggest that specific FM interactions may be involved in neural processes underlying memory misbinding.

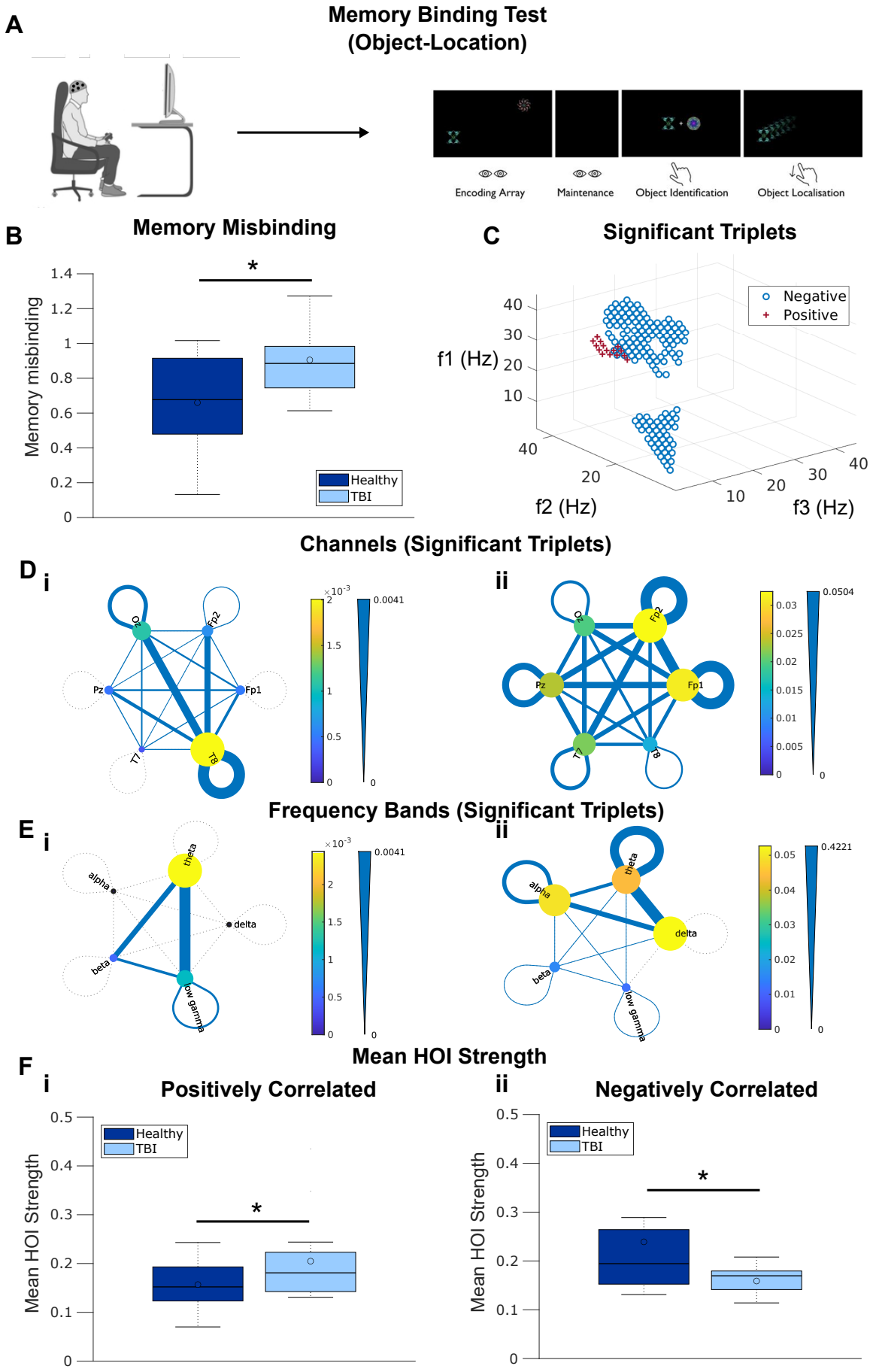


Figure 4.5: **Characterisation of frequency mixing interactions that correlate with memory misbinding in the spontaneous brain activity of healthy and traumatic brain injury patients**

Figure 4.5: **Characterisation of frequency mixing interactions that correlate with memory misbinding in the spontaneous brain activity of healthy and traumatic brain injury patients** *(A) Schematic of experimental setup. (B) Memory misbinding is significantly increased in Traumatic Brain Injury (TBI) patients compared to healthy participants. (C) Specific significant clusters of higher order nonlinear frequency interactions between neural signals of three different frequencies (triplets) significantly correlate with memory misbinding (both negatively and positively). (D) The brain regions in which the majority of triplets that positively and negatively correlate with memory misbinding occur, differ. (E) The main frequencies composing triplets that positively and negatively correlate with memory misbinding differ. (F) Triplets that positively correlate with memory misbinding are significantly stronger in TBI patients compared to healthy, and those that negatively correlate with memory misbinding are significantly stronger in healthy participants compared to TBI patients.* (A) Schematic of memory-binding (object-location) task undertaken by healthy participants and TBI patients. (B) Boxplot showing entropy ratio, a measure of memory misbinding, for healthy participants and TBI patients. Two-sample t-test. * = $p < 0.05$. (C) Scatter plot indicating clusters of triplets which significantly positively (red) and negatively (blue) correlate with memory misbinding. Each triplet within a cluster can be considered significant. Cluster permutation test vs surrogate, cluster permutation regression test. (D)(i) Brain region interaction plot displaying the strength of Higher Order Interaction (HOI) of the significant triplets within and between brain regions for triplets that are positively correlated with memory misbinding only. Nodes (colour and size) indicate the sum of HOI strengths across all significant triplets that consist of at least one neural signal that was detected within that brain region (normalised by total number of triplets tested). Edge width indicates the normalised sum of HOI strengths across all significant triplets containing two neural signals that were detected within the linked brain regions. (ii) As in (i) but of the significant triplets within and between brain regions for triplets that are negatively correlated with memory misbinding only. (E)(i) As in (D)(i) except for frequency band interactions. Nodes (colour and size) indicate the sum of HOI strengths across all significant triplets that consist of a frequency within that frequency band (normalised by total number of triplets tested). Edge width indicates the normalised sum of HOI strengths across all significant triplets containing frequencies that fall within the linked frequency bands. (ii) As in (i) but of the significant triplets within and between frequency bands for triplets that are negatively correlated with memory misbinding only. (F)(i) Boxplot showing the mean HOI strength of all triplets that were positively correlated with memory misbinding, for healthy participants and TBI patients. Two-sample t-test. * = $p < 0.05$. (ii) As in (i) except for all triplets that were negatively correlated with memory misbinding. n = 21 healthy and 17 TBI participants in all plots.

Compared to healthy subjects, TBI patients also exhibited an impaired ability to sustain attention (81.00 ± 6.94 a.u), compared to healthy (145.60 ± 9.07)(p = 5.82-06)(Figure 4.6 B). I found that distinct clusters of triplets, that is FM involving certain frequencies, correlate positively and negatively with sustained attention, as with memory misbinding (Figure 4.6 C). In the case of sustained attention, the EEG electrodes that make up these triplets do not differ for those that are positively and negatively correlated (Figure 4.6 D). The frequency bands that

make up the triplets however, do differ slightly, for those that are positively and negatively correlated (Figure 4.6 E). Triplets that positively correlate with sustained attention appear to involve signals that are mostly within the low gamma band, with a frequency in another band (Figure 4.6 Ei). Triplets that negatively correlate with sustained attention on the other hand, are composed of signals with frequencies mostly within the beta band with one frequency in the alpha, theta or low gamma frequency bands (Figure 4.6 Eii).

The strength of FM across all triplets that are positively correlated with sustained attention was compared across healthy participants and TBI patients. The mean HOI strength across all triplets that are positively correlated with sustained attention is significantly weaker in TBI patients (0.13 ± 0.0048 a.u), compared to healthy participants (0.20± 0.015 a.u)(p = 1.33e-05)(Figure 4.6 Fi). The same was done for negatively correlated triplets and the inverse was found. The mean HOI strength across all triplets that are negatively correlated with sustained attention is significantly stronger in TBI patients (0.21 ± 0.017 a.u), compared to healthy participants (0.14 ± 0.0068 a.u)(p = 4.15e-05)(Figure 4.6 Fii).

Together, these results suggest that FM involving specific frequencies may be involved in neural processes underlying sustained attention.

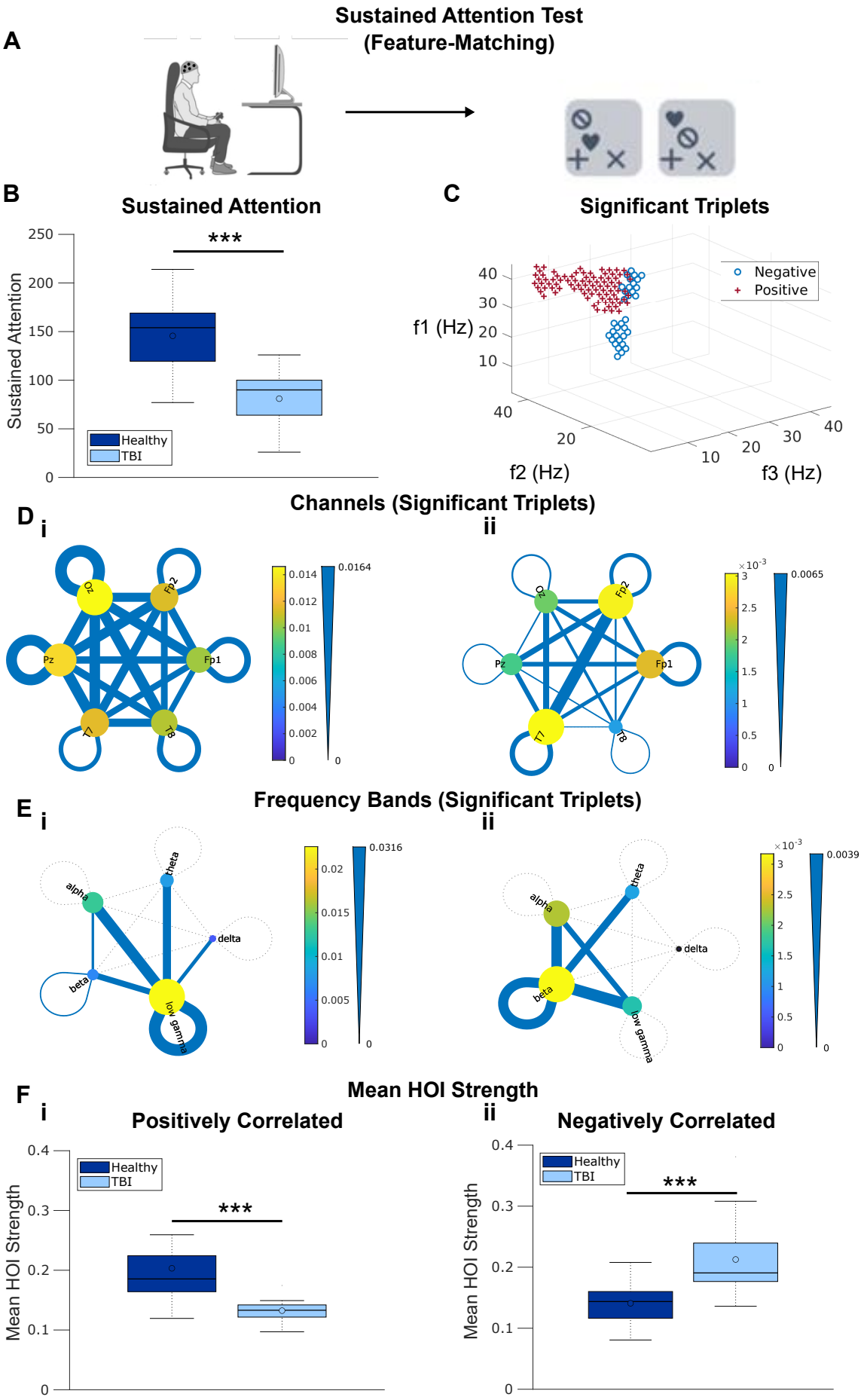


Figure 4.6: **Characterisation of frequency mixing interactions that correlate with sustained attention in the spontaneous brain activity of healthy and traumatic brain injury patients**

Figure 4.6: **Characterisation of frequency mixing interactions that correlate with sustained attention in the spontaneous brain activity of traumatic brain injury patients** *(A) Schematic of experimental setup. (B) Sustained attention is significantly decreased in Traumatic Brain Injury (TBI) patients compared to healthy participants. (C) Specific significant clusters of higher order nonlinear frequency interactions between neural signals of three different frequencies (triplets) significantly correlate with sustained attention (both negatively and positively). (D) The brain regions in which the majority of triplets that positively and negatively correlate with sustained attention occur, do not differ, although there are more positively correlated triplets (E) The main frequencies composing triplets that positively and negatively correlate with sustained attention differ only slightly. (F) Triplets that positively correlate with sustained attention are significantly weaker in TBI patients compared to healthy, and those that negatively correlate with sustained attention are significantly weaker in healthy participants compared to TBI patients.* (A) Schematic of sustained attention (feature-match) task undertaken by healthy participants and TBI patients. (B) Boxplot showing feature match score, a measure of sustained attention, for healthy participants and TBI patients. Two-sample t-test. *** = $p < 0.005$. (C) Scatter plot indicating clusters of frequency triplets which significantly positively (red) and negatively (blue) correlate with sustained attention. Each triplet within a cluster can be considered significant. Cluster permutation test vs surrogate, cluster permutation regression test. (D)(i) Brain region interaction plot displaying the strength of Higher Order Interaction (HOI) of the significant triplets within and between brain regions for triplets that are positively correlated with sustained attention only. Nodes (colour and size) indicate the sum of HOI strengths across all significant triplets that consist of at least one neural signal that was detected within that brain region (normalised by total number of triplets tested). Edge width indicates the normalised sum of HOI strengths across all significant triplets containing two neural signals that were detected within the linked brain regions. (ii) As in (i) but of the significant triplets within and between brain regions for triplets that are negatively correlated with sustained attention only. (E)(i) As in (D)(i) except for frequency band interactions. Nodes (colour and size) indicate the sum of HOI strengths across all significant triplets that consist of a frequency within that frequency band (normalised by total number of triplets tested). Edge width indicates the normalised sum of HOI strengths across all significant triplets containing frequencies that fall within the linked frequency bands. (ii) As in (i) but of the significant triplets within and between frequency bands for triplets that are negatively correlated with sustained attention only. (F)(i) Boxplot showing the mean HOI strength of all triplets that were positively correlated with sustained attention, for healthy participants and TBI patients. Two-sample t-test. *** = $p < 0.0005$. (ii) As in (i) except for all triplets that were negatively correlated with sustained attention. n = 21 healthy and 17 TBI participants in all plots.

4.4 Discussion

4.4.1 General discussion of results

FM has been detected in both evoked human neural activity (Regan and Regan, 1987), and spontaneous neural activity in rodents (Haufler and Paré, 2019). Methods used previously

however, have not been sensitive enough to detect FM in noisy spontaneous human neural activity. Due to this, we have very little insight into the potential role that FM plays in human brain dynamics and the behaviours underpinned by this. TBI causes disruption to functionally connected brain networks and the processes that determine this connectivity, such as CFC, thus higher order frequency interactions such as FM, may also be disrupted in these patients. In this chapter, I described a novel method for detecting FM in spontaneous neural activity and aimed to investigate whether spontaneous FM can be detected at the single neuron (see section 4.3.1). I previously found that evoked nonlinear frequency conversion (thought to be mediated by FM) at the single cell, likely has a cell membrane origin (see section 3.3.7) and involves voltage-gated ion channels (see section 3.3.8). Thus, I aimed to see whether blocking voltage-gated ion channels and synaptic input, affected spontaneous FM (see section 4.3.2). Lastly, I investigated whether spontaneous FM exists in human neural activity (see section 4.3.3), and whether it is altered in a condition associated with cognitive and memory impairment (see section 4.3.4).

First, I suggest that FM can be detected in single neuron activity, using a novel method utilising three-way phase relationships between three signals with different frequencies. These detected significant FM triplets fall within the range of spontaneous neural activity i.e. delta-low gamma. I found that the number and strength of FM interactions was reduced in the presence of TTX. This is to be expected for two reasons. Previously, I showed that the strength of evoked FM is affected by TTX (see section 3.3.8). I hypothesised that this could be due to the voltage-gated ion channels being an origin of the nonlinearity underlying FM. Thus, if these channels are blocked, the strength of FM in spontaneous activity should be reduced. Secondly, TTX effectively silences spontaneous network activity by abolishing supra-threshold activity. As APs cannot occur, neurotransmitters cannot be released from pre-synaptic terminals and synaptic transmission is abolished. If there is no synaptic input onto the cell, the range of frequencies that cell is exposed to will be reduced, as will the number of FM interactions occurring. This is also the case for synaptic blockers. One could ask the question, if there is no synaptic input to the neuron, where are the signals involved in FM coming from? One potential source of these signals in ephaptic coupling. It has been shown that the electric fields generated by endogenous

brain activity can polarise neurons via a process called ephaptic coupling (Anastassiou et al., 2011). Additionally, electrical gap junctions are a way by which cortical neurons communicate non-synaptically (Nadarajah et al., 1996).

My results suggest that FM is occurring in spontaneous human neural activity, as revealed by significant three-way phase relationships between neural signals. The method described in this chapter is sensitive enough to detect FM in human brain activity recorded using EEG. The results suggest that intra-region FM is stronger than inter-region FM. Additionally, that there is no correlation between FM strength and oscillatory band-power. These results suggest that FM is a feature of spontaneous human neural activity that is independent of spectral power.

Preliminary characterisation of spontaneous FM was also undertaken. I observe that intra-region or global FM involves lower frequencies, whereas inter-region or local FM involves primarily higher frequencies. This is potentially interesting as it is known that larger wide-spread networks are recruited during slow neural oscillations, whereas higher frequency neural oscillations are typically found in smaller, more local neuronal networks (Buzsáki and Draguhn, 2004). In summary, I show that endogenous FM is occurring in spontaneous neural activity and begin to characterise this phenomenon in healthy humans.

Lastly, I showed that specific groups of FM triplets correlate positively and negatively with TBI-associated memory misbinding and sustained attention deficits, and that the strength of these FM triplets is different in the neural activity of TBI patients compared to healthy controls. Interestingly, the strength of FM in TBI is reduced in the group of triplets that positively correlates with a positive behavioural outcome i.e. a higher sustained attention score and increased in the group of triplets that positively correlates with a negative behaviour outcome, i.e. increased memory misbinding. These results may indicate that FM at specific frequencies is involved in processes underlying memory and cognition. Additionally, they suggest that there may not simply be an overall increase or decrease in the strength of FM in disrupted neural activity, but rather, that the strength of FM at specific frequencies may be important.

4.4.2 Limitations and future direction

In experiments investigating spontaneous FM at the single neuron, the single neuron recordings were taken from cortical neurons in a slice. In this case, the neural network that this neuron is embedded within is obviously greatly reduced. If further work is to be done on spontaneous FM detected at the single cell, these experiments should be performed *in vivo*, so that mixing between the full range of neural signals in a network can be detected. Regardless, this experiment provided proof of principle that a novel methodology for detecting FM can be deployed.

The methodology for FM introduced in this chapter was tested on signals that had undergone a FM nonlinear process, and detection of a three-way phase relationship can certainly indicate FM. However, there are potentially other nonlinear processes that could introduce a three-way phase relationship between three signals. Previously, I described envelope detection via rectification, which is another way by which a triplet, i.e. three signals with frequencies $f_1/f_2/f_\Delta$, could be produced in a neural signal. Whether nonlinear frequency conversion via rectification results in signals with a similar three-way phase relationship should be tested, so that it can be determined if the triplets we observe could be produced via another nonlinear process. In any case, the discovery of a higher order frequency interaction that exists in human neural activity is of interest regardless.

With regards to the methodology, 1Hz frequency bins and relatively long time windows were used. As neural oscillations do not stratify themselves into such frequency bins, there is of course a chance that specific FM between signals are being missed. For example, a frequency mixing triplet at 1.1Hz, 1.9Hz and 3Hz could not be detected as both 1.1Hz and 1.9Hz would be considered to be in the same frequency bin and their phases would not be separately resolved. Computation of triplets across more frequency bins is computationally expensive so should only be considered for example, if specific FM across a smaller range of frequencies is of interest. As a 1 minute time window was used, it is currently not possible to detect FM that occurs over shorter timescales. Thus more transient HOIs are likely being missed. However, mixing between neural oscillations that exist for a longer time period may be more relevant to specific behaviour, therefore going forwards the time window used should be determined with the

scientific question in mind. Lastly, with this method we can detect FM triplets, but cannot say which two frequencies within the triplet combined to create the third, i.e. which are the root signals and which are the emergent signals. We can only conclude that the three frequencies are involved in a frequency mixing interaction. If the role of FM in spontaneous neural activity is to create signals with new frequencies within the brain, it is not possible to detect the occurrence of this with the method as it stands. Nonetheless, the finding that spontaneous FM occurs in the human brain may be of great interest to neuroscience. This process could be involved in the creation of new frequencies within the brain and is deserving of further investigation. Additionally, whether the three-way relationship itself is important in some large-scale brain property such as functional connectivity is an interesting question. CFC is a dependency between two neural signals and is thought to be important in information transfer across neural networks, thus there is a potential that a three-way dependency or relationship may do the same.

With regards to the analysis of healthy human and TBI patient data, the conclusions that can be drawn from these results are limited due to the methodology. A simple correlation between the HOI strength and behavioural measure cannot tell us whether HOI is important in determining this behavioural measure. The question of causality is difficult to answer, and future work building on the preliminary results presented in this chapter, could aim to determine indeed whether alterations in frequency mixing strength at specific frequencies, causally affect the ability to bind working memory and sustain attention. Furthermore, investigation into whether the difference in HOI strength in healthy humans and TBI patients is underlain by specific triplets, could be an interesting avenue. For example, elucidation of whether a relationship between three signals at specific frequencies plays a role in behaviour, such as in gamma theta CFC coupling, would be an impactful finding.

Additionally, the healthy human and TBI patient EEG data compared in this chapter was resting-state. That is, the participants were not undertaking the cognitive or memory task when the EEG recording was taken. Further work should include analysis of EEG signals obtained whilst the participants are performing the task, to see if there are changes in FM between healthy participants and TBI patients, whilst the brain is actively engaged in memory

binding or sustaining attention. This would provide further insight into whether FM is actually involved in the brain processes underlying these behaviours.

4.4.3 Conclusions

In conclusion, I show that FM is occurring in spontaneous neural activity, and can be detected at the single neuron. Additionally, I show the first evidence of FM in wide-scale human cortical activity. I present results that suggest that spontaneous FM is impacted when neural network inputs and voltage-gated ion channels are blocked. Lastly, I show that groups of FM triplets correlate with disease defining behavioural measures and that the strength of these FM triplets is different in healthy and diseased brains. The results in this chapter can be seen as a starting point for future work investigating FM in human neural activity.

Chapter 5

Pulse-width modulated temporal interference: validation and mechanistic investigation

5.1 Introduction

The concept of non-invasive deep brain stimulation via TI stimulation is based on the generation of a slow amplitude modulated waveform at depth, achieved by the overlap of two superficial kHz sinusoidal waveforms. The periodic modulation of the amplitude of the combined field at the difference frequency (f_Δ) results in the depolarization of the target neural cells at that frequency. In chapter 3 I investigated the mechanism by which amplitude modulated electric fields stimulate neural activity at the AM or difference frequency. In this chapter, I explore whether TI neurostimulation could be achieved via other periodic modulations of the kHz electric fields. Specifically, whether a periodic modulation in the pulse-width of the electric field waveform could drive neural activity at the modulation, or difference, frequency. If this was the case, a non-invasive DBS could be achieved by overlapping two square waveforms. In this case, the combined field has a constant amplitude but a pulse width that changes periodically at f_Δ of the applied fields.

A recent study, demonstrated that such a pulse-width modulation strategy, which will henceforth be referred to as Pulse-Width Modulated-Temporal Interference (PWM-TI) stimulation can effectively stimulate the mouse hippocampus, a deep brain structure. Evidence for this is in the form of the ability of PWM-TI to produce seizure-like events containing characteristic frequencies of rapid-discharges in this brain region, something which is typically achieved with intracranial electrodes situated close to the region of interest (Missey et al., 2021).

Whilst the aforementioned study introduces the concept of PWM-TI and suggests that its effects are analogous to traditional sinusoidal TI (which will henceforth be referred to as just TI), the two current waveforms applied to the brain, and thus the electric field in the region of overlap of the two in these two stimulation techniques are/is very different. PWM-TI involves the application of two waveforms consisting of biphasic bipolar pulses at two different frequencies to the brain. At the region of maximal overlap, as in TI, the current waveforms and thus electric fields are summed. In TI, which utilises sinusoidal electric fields, the neurons in the overlap are exposed to the summed electric field, which oscillates at the mean of the two applied field frequencies and is amplitude modulated at f_Δ (see section 3.2.2) (Figure 3.2). With PWM-TI however, the neurons in the overlap are exposed to an electric field which oscillates with bipolar biphasic pulses, the pulse-width of which, are periodically modulated at f_Δ. That is, the pulses have a frequency which is the mean of the two applied field frequencies and the width of these pulses increases and decreases, completing one full cycle in one period of f_Δ (Figure 5.1 B).

As the mechanism of action of TI, and thus the method by which the neuron extracts f_Δ from the stimulation current, is currently under investigation (see section 3.1.1), it is a large assumption that the PWM-TI waveform will produce comparable effects. In fact, no direct electrophysiological evidence that the stimulation is able to produce f_Δ has been presented (Missey et al., 2021). One could assume that neural polarisation can follow the kHz frequency pulsed current exactly, even at the smallest pulse-width. In this case, if TI exerts its effects via the purely linear summation of the two electric fields (see section 3.1.1), f_Δ could not be created during PWM-TI, as the amplitude of the electric field and thus the induced current does not vary. Similarly, if neurons are able to facilitate nonlinear frequency conversion via rectification, as hypothesised (see section 3.1.1), as the waveform does not have an envelope,

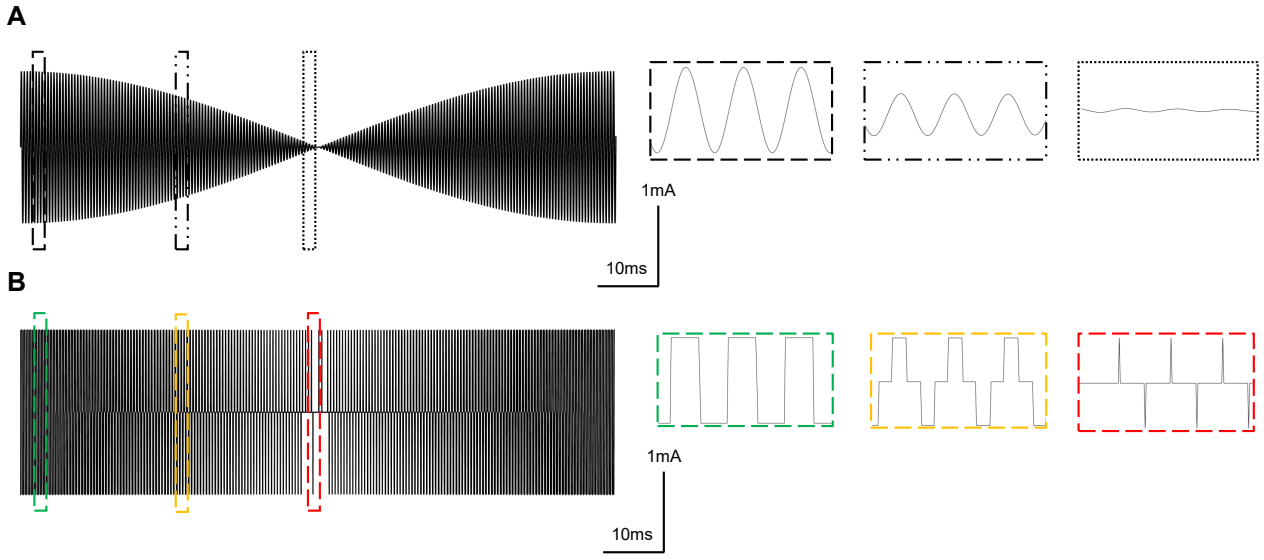


Figure 5.1: **Pulse-width modulated temporal interference waveform** (A) Temporal Interference (TI) stimulation current waveform created by the summation of two biphasic sinusoidal currents of two different frequencies ($f_1 = 2000$Hz and $f_2 = 2010$Hz). The current has a constant pulse-width however the amplitude changes periodically at a rate equal to the difference frequency (f_Δ) (10Hz). This waveform represents the electric field acting on the neurons in the perfect overlap of the two applied currents during TI. *Left* Zoom view of the regions inside the dashed boxes. (B) Right Pulse-Width Modulated-Temporal Interference (PWM-TI) stimulation current waveform created by the summation of two biphasic bipolar square wave currents of two different frequencies ($f_1 = 2000$Hz and $f_2 = 2010$Hz). The current has a constant current amplitude however the pulse-width of the pulses changes periodically at a rate equal to f_Δ (10Hz). This waveform represents the electric field experienced by the brain in the perfect overlap of the two applied currents during PWM-TI. *Left* Zoom view of the regions inside the dashed boxes.

envelope detection in this way would not be possible. These two mechanisms could in theory be possible, however only if the neuron was interpreting the electric field as an amplitude modulated electric field. This has never been suggested nor tested experimentally. Conversely, if neurons produce f_Δ by facilitating a nonlinear frequency conversion via multiplication (see section 3.1.1), f_Δ could indeed be produced with this current waveform as two frequencies exist within the signal and are applied as input, similarly to TI.

To investigate these key open questions, I first simulated, using neurophysiological models, and then measured, using whole patch clamp recording in brain slices (as in chapter 3), the response of individual neurons to PWM-TI stimulation and normal TI stimulation (i.e. with AM).

5.2 Methods

5.2.1 *Ex-vivo* brain slice preparation

As in section 3.2.1.

5.2.2 Electrical stimulation

Hardware

As in section 3.2.2.

Waveforms

Pulse-width modulated temporal interference waveform

PWM-TI stimulation waveforms were created by the summation of two constant amplitude biphasic bipolar square pulse waveforms (6s total, 0.5s ramp up, 0.5s ramp down, 5s stimulation) with duty cycles of 50% and frequencies of 2000Hz and 2010Hz (Figure 5.1 B). The

resulting waveform is a constant amplitude biphasic bipolar square waveform with a frequency of 2.005kHz, which has a pulse width that changes periodically at f_Δ (10Hz). The Inter-Pulse Interval (IPI) of the signal is equal to the period of the waveform (∼0.5ms). When the signal is fully constructive, the waveform has a symmetrical biphasic pulse-width equal to 50% of the IPI (∼0.25ms). When the signal is fully destructive, the waveform has a symmetric biphasic pulse-width equal to 0% of the IPI (0ms). When the signal is half constructive and half destructive, the waveform has a symmetrical biphasic pulse-width equal to 25% of the IPI (∼0.125ms).

Temporal interference waveform

TI stimulation waveforms were created as in section 3.2.2. Frequencies of the two summed waveforms were 2000Hz and 2010Hz (Figure 5.1 A).

Biphasic bipolar pulse waveform

A biphasic bipolar square pulse waveform with decreasing pulse-width was created. Pulse widths ranged from 50ms to 0.012ms.

5.2.3 Computational modelling

All modelling was performed in the NEURON environment (NEURON 7.8.1) (Carnevale and Hines, 2006; Hines et al., 2019).

Biophysically realistic pyramidal neuron model

Computational modelling was mostly performed using a single biophysically realistic multi-compartment layer 2/3 pyramidal neuron (Figure 5.2 A)(see Aberra et al. (2018)). Four other pyramidal cell neurons with different morphologies were also used when multiple cells were needed for statistical purposes. Typical Hodgkin-Huxley model parameters were used (Hodgkin and Huxley, 1952). All recordings were taken at the soma. Full blockade of voltage gated model

components was achieved by setting all ion channel conductance in the model to 0. Extracellular current stimulation with PWM-TI and TI waveforms (see section 5.2.2) were applied to these neurons (see Aberra et al. (2018)).

Simple RC model

Additionally, a single compartment model composed of a resistance representing the passive leak resistance/conductance, and a capacitance representing the membrane capacitance was used (Figure 5.2 B). Intracellular current stimulation with PWM-TI and TI waveforms (see section 5.2.2) was applied to this neuron. Time constant (τ) of the single compartment NEURON model was altered within the bounds of physiological neuronal time constants (1-100ms) (based on the literature, data obtained at https://neuroelectro.org), by changing the passive conductance. Specific membrane capacitance was fixed at 1µf/cm^2.

5.2.4 Whole cell patch clamp recording

As in section 3.2.3.

5.2.5 Data analysis

All data was analysed in MATLAB (MATLAB 2019a, The MathWorks Inc.).

Computational model data analysis

Threshold was defined as the current amplitude required to produce 1 AP. An unbiased approach to calculating envelope modulation in computational model membrane potentials was performed as follows:

1. Computing the upper and lower Hilbert envelope of the signal

2. Finding the peaks of the upper and lower envelopes and troughs of the upper envelope

3. Computing the peak-to-peak amplitude of the signal from the peaks of the upper and lower envelope

4. Computing the envelope amplitude from the peaks and troughs of the upper envelope

5. Calculating envelope amplitude as a percentage of amplitude (peak-to-peak amplitude divided by 2).

For the applied waveform, peaks and troughs of the upper and lower envelopes could not be detected due to the lack of envelope modulation, so envelope modulation was calculated as follows:

1. Computing the upper and lower Hilbert envelope of the signal

2. Finding the values of the upper and lower envelopes when pulse width was maximum and value of the upper envelope when pulse width was minimum (after 1/2 a period of f_Δ (50ms))

3. Computing the peak-to-peak amplitude of the signal from the values of the upper and lower envelopes when pulse width was maximum

4. Computing the envelope amplitude from the values of the upper envelope when pulse width was maximum and minimum

5. Calculating envelope amplitude as a percentage of amplitude (peak-to-peak amplitude divided by 2).

Peak to peak amplitude of single compartment neuron model membrane potential was computed using the Hilbert transform and normalised to the maximum amplitude for each time constant.

Patch-clamp data analysis

PSDs were computed using the multitaper method and normalised to the maximum PSD value. To determine whether magnitude of polarisation at the f_Δ was significant, the difference in PSD at the frequency of interest compared to noise was computed by applying a linear fit to the log transform of the normalised PSD and calculating the difference from this fit/the noise floor of

the PSD (as in (see section 3.2.5)). For patch clamp experiments, threshold was defined as the current amplitude required to produce 1 AP, if the next current amplitude step produced at least 3 APs. To calculate subthreshold oscillation amplitude in the time domain, the membrane potential trace in response to the maximum stimulation amplitude that had no APs for each cell, was filtered using a 50Hz Butterworth low-pass filter to remove stimulation artefact. Any peaks in the membrane potential separated by the f_Δ period were found. The amplitude of these peaks was computed relative to the minimum recorded membrane potential during this stimulation period, and an average stimulation-induced subthreshold oscillation amplitude for each cell was computed.

Statistical analysis

All data is mean ± SEM. Values are presented in tables which are referred to in the text. Statistical tests are specified in table and figure legends. All t-tests are two tailed unless stated. In all plots, the * notation represents a statistical significance that survived Bonferonni correction.

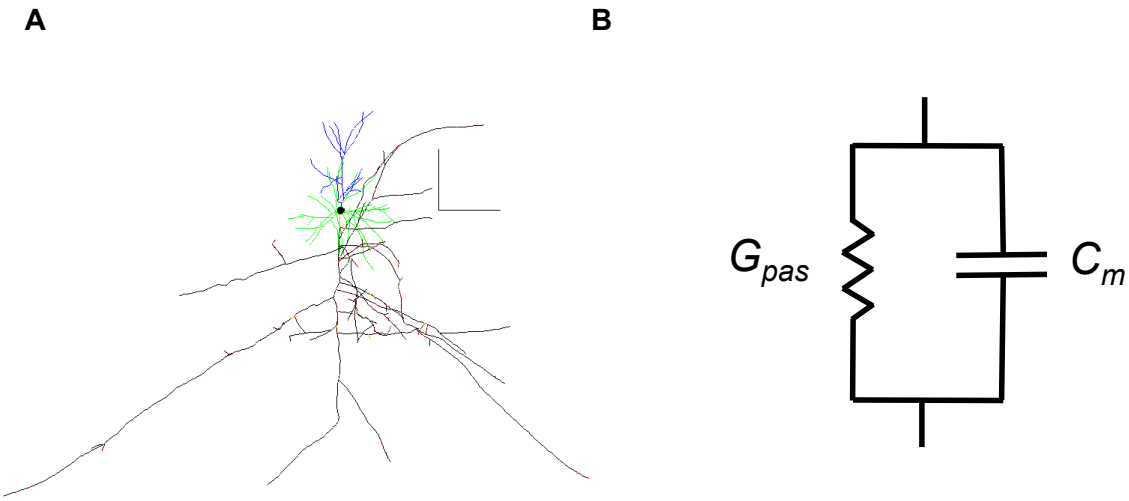


Figure 5.2: **Computational model schematics** (A) Schematic of a biophysically realistic layer 2/3 pyramidal neuron model. Soma is indicated by the black circle (Aberra et al., 2018). (B) Equivalent electrical circuit of a simple neuron model composed of only passive components

5.3 Results

5.3.1 Pulse-width modulated temporal interference can evoke action potentials at the difference frequency in a model pyramidal neuron

Whether PWM-TI-induced neural polarisation is comparable to TI-induced neural polarisation is an open question. First, I investigated this question by examining whether PWM-TI stimulation can evoke AP activity at f_Δ in a biophysically realistic pyramidal neuron model with Hodgkin-Huxley conductance, in response to extracellular electric fields. Simulations were performed on a range of biophysically realistic neuron models with different morphologies.

PWM-TI can evoke firing of APs at f_Δ in a model pyramidal neuron when average applied frequencies are 1000Hz (Figure 5.3 Aii) and 2000Hz (Figure 5.3 Bii), similarly to TI (Figure 5.3 Ai, Bi). The threshold for AP firing is approximately 5-20 times (depending on average applied frequency) larger than the threshold when the low frequency stimulation was applied at f_Δ, and similar to TI (Figure 5.3 F). The threshold for PWM-TI induced AP firing shows dependency on applied frequency, with threshold increasing as applied frequency increases ($F(2,8) = 34.51$ $p = 0.00012$)(Figure 5.3 F). Threshold for AP firing is significantly lower at 1000Hz applied frequency compared to 2000Hz and 10000Hz, and at 2000Hz compared to 10000Hz ($p = 0.0075$ (1000Hz vs 2000Hz) $p = 0.0042$ (1000Hz vs 10000Hz) $p = 0.0041$ (2000Hz vs 10000Hz), Bonferroni-corrected p-value = 0.017). Again, this is similar to what is observed with TI ($F(2,8) = 22.46$ $p = 0.00052$). Threshold for AP firing is significantly lower at 1000Hz compared to 2000Hz and 10000Hz, and at 2000Hz compared to 10000Hz ($p = 0.014$ (1000Hz vs 2000Hz) $p = 0.0092$ (1000Hz vs 10000Hz) $p= 0.0086$ (2000Hz vs 10000Hz), Bonferroni-corrected p-value = 0.017).

Next, I compared PWM-TI and TI-induced subthreshold polarisation. Interestingly, although the PWM-TI wavefrom has a constant amplitude, visual inspection of the subthreshold membrane potential polarisation of a model pyramidal neuron induced by PWM-TI, reveals a mem-

brane potential that is amplitude modulated at f_Δ and oscillates at the mean of the two applied frequencies when average applied frequencies are 1000Hz (Figure 5.3 Aiv) and 2000Hz (Figure 5.3 Biv). This amplitude modulation of membrane potential with PWM-TI (Figure 5.3 Aiv, Biv) looks comparable to that produced by TI of the same applied frequency (Figure 5.3 Aiii, Biii). Accordingly, depth of envelope modulation, as represented by the percentage (see section 5.2.5), with PWM-TI is not significantly different to depth of envelope modulation with TI ($p = 0.19$ (1000Hz), $p = 0.16$ (2000Hz))(Figure 5.3 C). Subthreshold polarisation also shows a dependency on stimulation frequency. The magnitude of polarisation is decreased as average applied frequency increases ($F(2,8) = 18.11$, $p = 0.0011$). This is evident in the peak to peak amplitude of the subthreshold membrane polarisation in response to PWM-TI, where polarisation at 1000Hz is significantly larger than polarisation at 10000Hz applied frequency, as is polarisation at 2000Hz (Figure 5.3 E)($p = 0.019$ (1000Hz vs 2000Hz), $p = 0.0011$ (2000Hz vs 10000Hz), $p = 0.013$(1000Hz vs 10000Hz), Bonferroni-corrected p-value = 0.017). This result is similar to TI stimulation where again polarisation at 1000Hz is significantly larger than polarisation at 10000Hz applied frequency. ($F(2,8) = 14.47$, $p = 0.0022$)($p = 0.024$ (1000Hz vs 2000Hz), $p = 0.0019$ (2000Hz vs 10000Hz), $p = 0.016$ (1000Hz vs 10000Hz), Bonferroni-corrected p-value = 0.017). In contrast to my ex-vivo measurements of single neurons (see chapter 3), there is no evidence of nonlinear frequency conversion (subthreshold polarisation at f_Δ) of PWM-TI currents in this neuron model (Figure 5.3 D). Polarisation at f_Δ in PWM-TI subthreshold membrane potential polarisation is not significantly greater than the noise floor, across a range of applied frequencies ($p = 1.00$ (1000Hz), $p = 1.00$ (2000Hz), $p = 1.00$ (10000Hz). Interestingly, this is also the case for TI ($p = 1.00$ (1000Hz), $p = 1.00$ (2000Hz), $p = 1.00$ (10000Hz)). In other words, the model fails to represent the nonlinear frequency conversion observed experimentally.

Regarding the relative strength of PWM-TI compared to TI, the model predicts that threshold for AP firing will be slightly reduced when TI stimulation is performed using PWM-TI compared to traditional sinusoidal TI, although none of these comparisons survived Bonferonni correction ($p = 0.090$ (1000Hz), 0.071 (2000Hz), 0.047 (10000Hz), Bonferroni-corrected p-value = 0.017). Additionally, the amplitude of subthreshold polarisation is somewhat increased with PWM-TI compared to traditional sinusoidal TI at all applied frequencies although these results again did

not survive Bonferonni correction (p = 0.028 (1000Hz), 0.027 (2000Hz), 0.066 (1000Hz))(Figure 5.3 E, F).

The result of the characterisation in the biophysically realistic neuron model suggest that indeed PWM-TI can drive APs at f_Δ. The stimulation strength is similar to TI. In this model, the subthreshold neural depolarisation during both PWM-TI and TI was mediated by a linear superposition of the fields, i.e. the cell did not show the nonlinear frequency conversion that was observed experimentally. Interestingly, the induced subthreshold neural depolarisation is amplitude modulated, similar to TI.

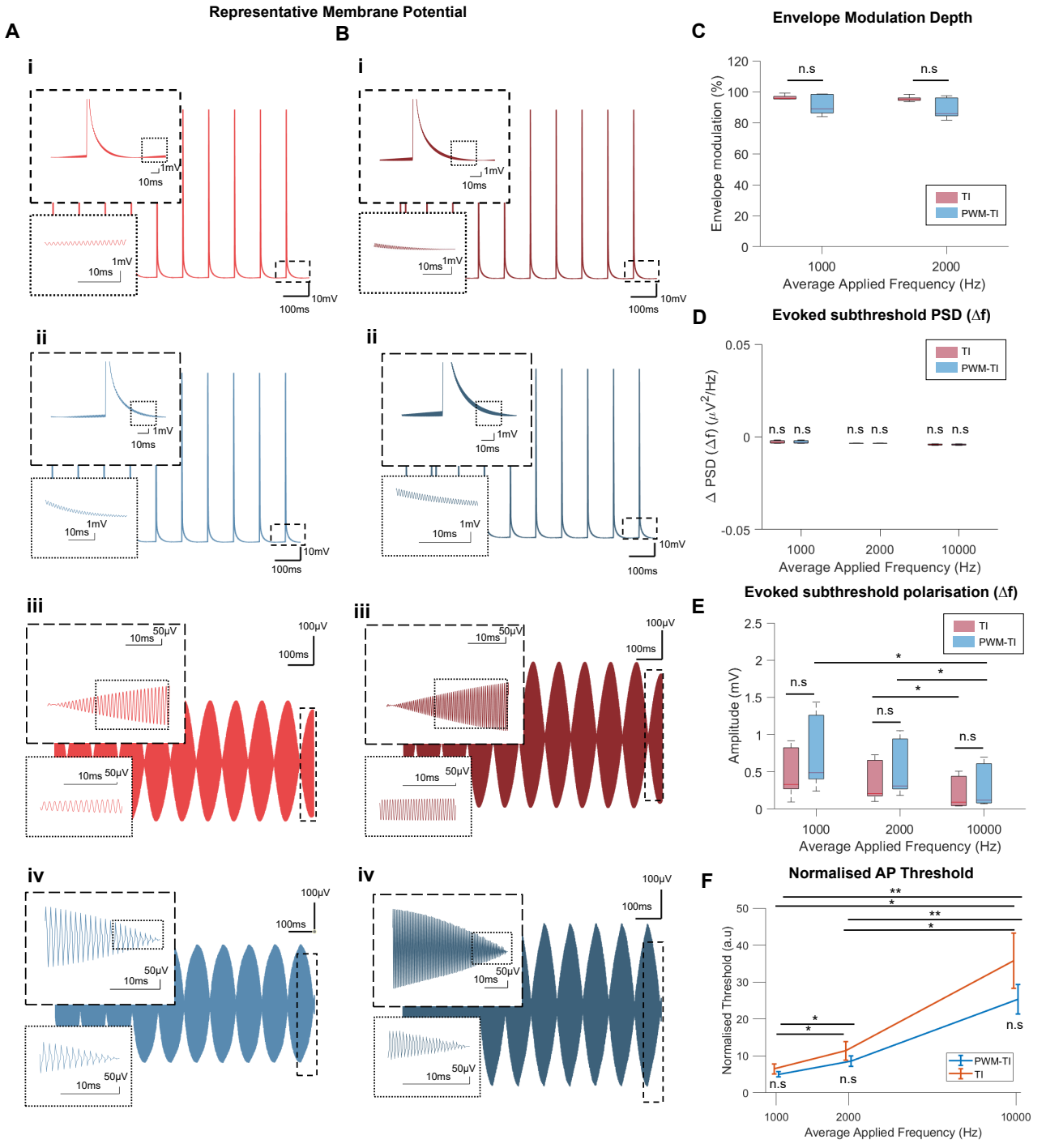


Figure 5.3: **Characterisation of pulse-width modulated temporal interference induced polarisation of a pyramidal neuron model, and comparison to traditional temporal interference stimulation**

Figure 5.3: **Characterisation of pulse-width modulated temporal interference induced polarisation of a pyramidal neuron model, and comparison to traditional temporal interference stimulation** *(A-C) Pulse-Width Modulated-Temporal Interference (PWM-TI) stimulates model pyramidal neurons in a comparable way to Temporal Interference (TI), as seen in subthreshold polarisation and Action Potential (AP) generation at the difference frequency (f_Δ) (D) Nonlinear frequency conversion in the subthreshold domain is not observed during PWM-TI or TI in a pyramidal neuron model (E-F) There is no significant difference between the strength of PWM-TI and TI and for both PWM-TI and TI, strength depends on applied frequency* (A) Representative membrane potential during extracellular stimulation with a (i) suprathreshold TI current, (ii) suprathreshold PWM-TI current, (iii) subthreshold TI current, and (iv) subthreshold PWM-TI current, with frequencies f_1 = 1000Hz, f_2 = 1010Hz. *Left* Zoom view of region inside dashed boxes. f_Δ across applied frequencies is 10Hz. Electric field strength is 10% below threshold for subthreshold stimulation and 150% above threshold for for suprathreshold simulation. (B) Representative membrane potential during extracellular stimulation with a (i) suprathreshold TI current, (ii) suprathreshold PWM-TI current, (iii) subthreshold TI current and, (iv) subthreshold PWM-TI current, with frequencies f_1 = 2000Hz, f_2 = 2010Hz. *Left* Zoom view of region inside dashed boxes. f_Δ across applied frequencies is 10Hz. Current amplitude across applied frequencies is the same. Electric field strength is 10% below threshold for subthreshold stimulation and 150% above threshold for for suprathreshold simulation. (C) Boxplot showing percentage of envelope modulation for TI- and PWM-TI-induced subthreshold polarisation of the membrane potential, across the two applied frequencies in (A) and (B). Electric field strength is 50V/m for all conditions. f_Δ across applied frequencies is 10Hz. n.s = p > 0.025 (Bonferroni-corrected p-value). Paired t-test. n = 5 pyramidal neurons with different morphologies. (D) Boxplot showing difference in absolute Power Spectral Density (PSD) at f_Δ compared to a linear fit (noise floor), of TI- and PWM-TI-induced subthreshold polarisation, across a range of applied frequencies. Electric field strength is 50V/m for all conditions. f_Δ across applied frequencies is 10Hz. n.s = p > 0.083 (Bonferroni-corrected p-value). One tailed one sample t-test to determine whether difference in PSD is significantly greater than 0. n = 5 pyramidal neurons with different morphologies. (E) Boxplot showing peak to peak amplitude of TI- and PWM-TI-induced subthreshold polarisation, across a range of applied frequencies. Electric field strength is 50V/m for all conditions. f_Δ across applied frequencies is 10Hz. * indicates a significant difference that survived Bonferonni correction. n.s = p > 0.0167 (Bonferroni-corrected p-value), * = p < 0.05. Paired t-test to compare between stimulation paradigms. Repeated measures ANOVA with post-hoc paired t-test to compare between applied frequencies. n = 5 pyramidal neurons with different morphologies. (F) Boxplot showing normalised threshold to evoke Action Potential (AP)s of TI and PWM-TI, across a range of applied frequencies. f_Δ across applied frequencies is 10Hz. Threshold at each applied frequency normalised to threshold for evoking APs with low frequency stimulation at f_Δ for that stimulation paradigm. * indicates a significant difference that survived Bonferonni correction. n.s = p > 0.0167 (Bonferroni-corrected p-value), * = p < 0.05, ** p < 0.005. Paired t-test to compare between stimulation paradigms. Repeated measures ANOVA with post-hoc paired t-test to compare between applied frequencies. n = 5 pyramidal neurons with different morphologies. All boxplots show median (line), 25th (bottom edge) and 75th (top edge) percentiles. Whiskers extend to the most extreme data points not considered outliers. + indicates outliers.

Envelope Modulation (%)		**Average Applied Frequency (Hz)**	
	Stimulation	*1000*	*2000*
Mean (± SEM)	TI	96.33 (0.72)	95.35 (0.78)
	PWM-TI	91.32 (2.98)	89.17 (3.09)
p - value	TI vs PWM-TI	0.19	0.16

Table 5.1: **Envelope modulation depth** Paired t-test.

Δ PSD (f_Δ)		**Average Applied Frequency (Hz)**		
	Stimulation	*1000*	*2000*	*10000*
Mean (± SEM)	TI	-0.0036 (0.00013)	-0.0035 (2.87e-05)	-0.0035 (1.38e-05)
p - value		1.00	1.00	1.00
Mean (± SEM)	PWM-TI	-0.0028 (0.00036)	-0.0035 (3.78e-05)	-0.0042 (0.00014)
p - value		1.00	1.00	1.00

Table 5.2: **Δ PSD at f_Δ** One sample one tailed t-test.

Measure of TI strength		**Average Applied Frequency (Hz)**		
Measure	**Stimulation**	*1000*	*2000*	*10000*
		Mean (± SEM)		
	TI	0.49 (0.16)	0.37 (0.13)	0.22 (0.10)
Amplitude (mV)	**PWM-TI**	0.75 (0.23)	0.55 (0.18)	0.31 (0.14)
		p-value		
	TI vs PWM-TI	0.028	0.026	0.066
		Mean (± SEM)		
Normalised	**TI**	6.48 (1.38)	11.36 (2.50)	35.73 (7.47)
	PWM-TI	4.97 (0.70)	8.63 (1.41)	25.33 (4.04)
Threshold (a.u)		**p-value**		
	TI vs PWM-TI	0.089	0.071	0.047

Table 5.3: **Measures of temporal interference strength** Paired t-test.

Measure of temporal interference strength	**Repeated Measures ANOVA**		
Measure	**Stimulation**	F	p
Amplitude	**TI**	14.46	0.0022
Normalised Threshold		22.46	0.00052
Amplitude	**PWM-TI**	18.10	0.0011
Normalised Threshold		34.51	0.00012

Table 5.4: **Repeated measures ANOVA results for measures of temporal interference strength**

Measure of TI strength			p-value		
			Average Applied Frequency (Hz)		
Measure	**Stimulation**	**Average Applied Frequency (Hz)**	*1000*	*2000*	*10000*
Amplitude	**TI**	*1000*	-	0.024	0.019
		2000	0.024	-	0.016*
		10000	0.019	0.016*	-
Normalised Threshold		*1000*	-	0.014*	0.0092*
		2000	0.014*	-	0.0086*
		10000	0.0092*	0.0086*	-
Amplitude	**PWM-TI**	*1000*	-	0.019*	0.013*
		2000	0.019*	-	0.0091*
		10000	0.013*	0.0091*	-
Normalised Threshold		*1000*	-	0.0075*	0.0042*
		2000	0.0075*	-	0.0041*
		10000	0.0042*	0.0041*	-

Table 5.5: **Post-hoc comparisons of measures of temporal interference strength** Paired t-test. * indicates a comparison that survived Bonferroni correction. Bonferonni corrected p-value = 0.0167.

5.3.2 The neuronal membrane interprets pulse-width modulated temporal interference as an amplitude modulated signal due to passive neuronal resistor-capacitor properties

I hypothesised that the PWM-TI stimulation, which has a constant amplitude, induces an amplitude modulated subthreshold depolarisation due to the low-pass filtering property of the membrane leading to depolarisation that is dependent on pulse-width. To test this hypothe-

sis, I repeated the simulation in the biophysical neuron model but with all the ion channels conductance removed.

The membrane potential of a biophysically realistic pyramidal neuron is amplitude modulated at f_Δ in response to stimulation with a PWM-TI current (Figure 5.4 Ai) when ion channels of the model are blocked. The envelope modulation of the membrane potential (89.37 ± 3.49)is significantly larger than the envelope modulation of the applied current waveform (0 ± 0) (p = 5.73e-09) (Figure 5.4 Aii).

Additionally, a simplified RC model composed of just a fixed value resistor and capacitor, representing the leak resistance/conductance and cell membrane capacitance respectively, has a membrane potential that is amplitude modulated at f_Δ (Figure 5.4 Bi). Application of a test biphasic bipolar square current pulses with varying pulse-widths reveals that as pulse-width decreases, evoked amplitude of membrane potential decreases (Figure 5.4 Bii, Biii). The RC properties of a neuronal membrane determine the time constant (τ) and thus the low-pass filtering properties of the neural membrane. When τ for the model neuron is varied for a given pulse-width, the amplitude of the evoked membrane potential in dependent on τ, with amplitude decreasing as τ increases, as expected (Figure 5.4 Biii).

These and the results in the previous section (see section 5.3.2), suggest that the passive properties of the neuronal membrane are sufficient for PWM-TI to be interpreted as an amplitude-modulated signal by the neuron. Additionally, the creation of this is mediated by filtering produced by these RC properties, and thus is dependent on the time constant of the neuronal membrane.

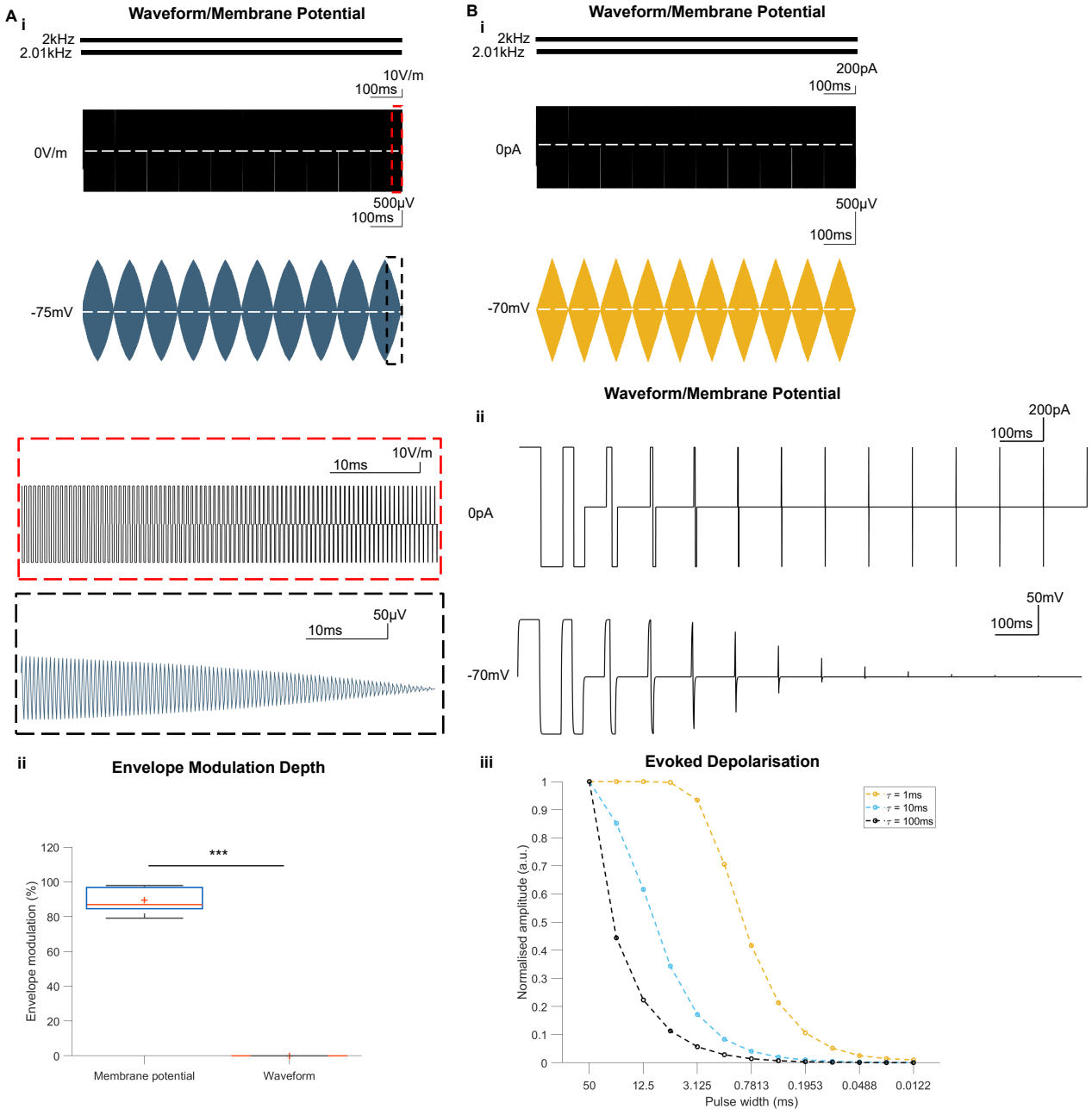


Figure 5.4: **Passive neural membrane response to pulse-width modulated temporal interference-induced polarisation**

Figure 5.4: **Passive neural membrane response to pulse-width modulated temporal interference-induced polarisation** *(A-B) Pulse-Width Modulated-Temporal Interference (PWM-TI) current is interpreted as an amplitude modulated signal by passive neuron models due to Resistor-Capacitor (RC) filtering.* (A)(i) *Top* PWM-TI extracellular current waveform ($f_1 = 2000$Hz, $f_2 = 2010$Hz). *Middle* Membrane potential response to the PWM-TI stimulation waveform as measured from a biophysically realistic neuron (Figure 5.2 A), with complete blockade of ion channels. Applied electric field is 50V/m. *Bottom* Zoom view of areas inside dashed boxes. (ii) Boxplot showing envelope modulation depth for the membrane potential and waveform in (A)(i). Paired t-test, *** = $p < 0.0005$. Boxplots showing median (line), 25th (bottom edge) and 75th (top edge) percentiles. Whiskers extend to the most extreme data points not considered outliers. n = 5 model pyramidal cells with different morphology, averaged across 10 envelopes. (B)(i) *Top* PWM-TI intracellular current waveform ($f_1 = 2000$Hz, $f_2 = 2010$Hz). *Bottom* Corresponding membrane potential response, as measured from a simple passive neuron model (Figure 5.2 B) with a time constant (τ) of 1ms. Injected current is 1nA. (ii) *Top* Waveform of intracellular current stimulation applied to the simple passive neuron model. *Bottom* Corresponding membrane potential response as measured from a simple passive neuron model with a τ of 1ms. Injected current is 1nA. (iii) Normalised amplitude of membrane potential depolarisation induced by a train of biphasic bipolar square pulses vs pulse-width. Plot shows responses of simple model neurons with different τ values. Plot showing peak to peak amplitude, normalised to the maximum peak to peak amplitude for each τ.

5.3.3 Pulse-width modulated temporal interference produces neural polarisation at the difference frequency with similar efficiency to traditional temporal interference

Next, I aimed to validate the modelling results by investigating the effect of extracellular PWM-TI on mouse cortical neuron polarisation. This was done via whole cell patch clamp recording of neurons in a brain slice (Figure 2.1), with stimulation frequencies $f_1 = 2000$Hz and $f_2 = 2010$Hz. I hypothesised that PWM-TI would be able to drive APs at f_Δ. Additionally, I hypothesised that subthreshold polarisation at f_Δ would be evoked due to nonlinear neural frequency conversion (see chapter 3), either via frequency mixing, or rectification of the amplitude modulated signal created by low-pass filtering by the neuron (see section 5.3.2).

A representative membrane potential trace shows evoked sub- (Figure 5.5 Ai), and suprathreshold (Figure 5.5 Bi) polarisation of the neuron at f_Δ, created by PWM-TI current stimulation.

I investigated whether the evoked polarisation at f_Δ by PWM-TI is significantly greater than

noise floor using the comparison to the linear fit method. Indeed, the normalised PSD at f_Δ, during subthreshold stimulation with the maximum current amplitude that was still subthreshold for both stimulation conditions for that cell, is significantly greater than the noise floor for PWM-TI stimulation (Δ normalised PSD: 0.0016 $\pm$ 4.57e-04 a.u, p = 0.0027) (data not shown in figure). This is also the case for traditional TI stimulation in these neurons (Δ normalised PSD: 0.0029 $\pm$ 8.96e-04 a.u, p = 0.0040) (data not shown in figure). This suggests neurons perform nonlinear frequency conversion of PWM-TI electric fields, similarly to TI fields (see chapter 3), resulting in subthreshold polarisation at f_Δ. To compare the relative strength of subthreshold polarisation during PWM-TI compared to TI, the same electric field strength (stimulation at the maximum current amplitude that was subthreshold for both stimulation paradigms) was applied to the neurons. In this case, there is no significant difference between normalised PSD at f_Δ during PWM-TI (0.0020 $\pm$ 0.00048 a.u), compared to TI (0.0017 $\pm$0.00092 a.u)(p = 0.79), however the polarisation during PWM-TI is significantly larger than the noise floor at this electric field strength (Δ normalised PSD: 0.0014 $\pm$ 4.37e-04 a.u, p = 0.0054), whereas during TI it is not (Δ normalised PSD: 0.0014 $\pm$ 8.65e-04 a.u, p = 0.072) (Figure 5.5 Aiii). This suggests that PWM-TI exerts a slightly stronger stimulation on the neuron. During the no stimulation condition (not shown), there is no significant increase in normalised PSD at f_Δ, compared to the noise floor of the PSD (Δ normalised PSD: -0.0039 $\pm$ 0.0027 a.u, p = 0.90), suggesting that power at f_Δ and thus polarisation at this frequency is due to the stimulation.

Similar results are obtained when suprathreshold polarisation is analysed in this way. Normalised PSD at f_Δ, during suprathreshold stimulation is significantly larger than the noise floor for PWM-TI stimulation (Δ normalised PSD: 0.010 $\pm$ 0.003 a.u, p = 0.0041). This is also seen for TI stimulation (Δ normalised PSD: 0.017 $\pm$ 0.0072 a.u, p = 0.021)(Figure 5.5 Aiii). These results suggest that PWM-TI evoked suprathreshold polarisation/APs are indeed at f_Δ. There is no significant difference in the magnitude of suprathreshold polarisation at f_Δ evoked by PWM-TI (normalised PSD: 0.012 $\pm$ 0.0032 a.u) compared to TI (normalised PSD:0.020 $\pm$ 0.0079 a.u)(p = 0.41), suggesting that the strength of these two stimulation techniques is comparable.

In line with these results, the normalised threshold for AP firing, is not significantly different for PWM-TI (1.15 ± 0.219 a.u) compared to TI (1.30 ± 0.28 a.u)(p = 0.38). For both PWM-TI and TI, normalised threshold for AP firing is on average approximately 1-1.5 times larger than the threshold for sinusoidal stimulation at f_Δ, at these applied frequencies (f_1 = 2000Hz, f_2 = 2010Hz). In the subthreshold membrane potential trace however, visual inspection suggests that at the same electric field strength, PWM-TI elicits larger subthreshold oscillatory polarisation of the membrane at f_Δ (Figure 5.5 Di), and indeed the average amplitude of this oscillatory polarisation is significantly larger during PWM-TI (1.70 ± 0.15mV), compared to TI (1.22 ± 0.18mV)(p = 0.039)(Figure 5.5 Dii).

Together, these results suggest that PWM-TI can efficiently stimulate neurons at f_Δ, comparably to TI. Additionally in the subthreshold domain, as with TI (see section 3.3.2), nonlinear conversion of frequencies is also occurring when two different frequencies are applied to the neuron during PWM-TI, as evidenced by the significant polarisation at f_Δ in the subthreshold domain. Additionally, PWM-TI stimulates the single neuron more strongly than TI in the subthreshold domain, although this is not translated to a significant decrease in AP threshold.

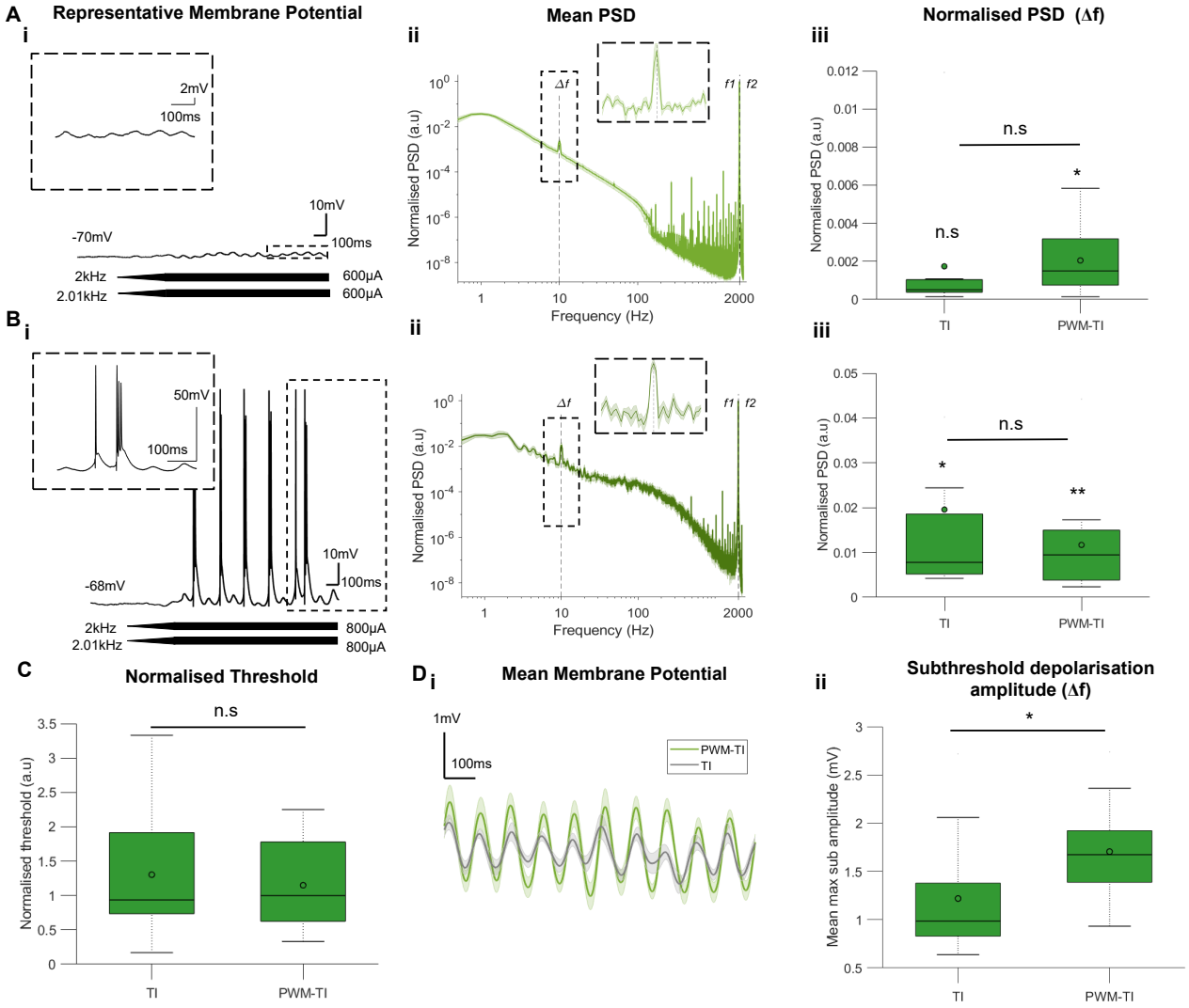


Figure 5.5: **Pulse-width modulated-temporal interference can stimulate single neurons at the difference frequency with comparable efficacy to traditional sinusoidal temporal interference**

Figure 5.5: **Pulse-width modulated-temporal interference can stimulate single neurons at the difference frequency with comparable efficacy to traditional sinusoidal temporal interference** *(A-B) PWM-TI is capable of both sub- and supra-threshold stimulation of the neuron at the difference frequency (f_Δ), as seen in the membrane potential trace and its respective Power Spectral Density (PSD) (A-D) PWM-TI is at least as effective at stimulating neurons as TI, as evidenced by no significant difference in the evoked power at f_Δ, and threshold for Action Potential (AP) firing between both stimulation conditions* (A)(i) Representative membrane potential trace of a cortical neuron during extracellular stimulation with subthreshold PWM-TI stimulation. (f_1 = 2000Hz, f_2 = 2010Hz). Membrane potential trace is filtered with a 500Hz low-pass Butterworth filter to remove stimulation artefact. Zoom view is of region inside dashed box. (ii) Mean normalised PSD of neuron membrane potential when cells are subjected to the maximum current amplitude that evoked a subthreshold response in all cells. Zoom view is of region inside dashed box. f_1 = 2000Hz, f_2 = 2010Hz for both stimulation conditions. Showing mean ± SEM. PSD normalised to maximum PSD value. n = 12. (iii) Boxplot showing difference from fit, a measure of PSD, at f_Δ (10Hz) in the PSD of subthreshold stimulation membrane potential across all cells for TI, PWM-TI and baseline. Two tailed paired t-test, n.s = $p > 0.05$, * = $p < 0.05$, ** = $p < 0.005$. Boxplot showing median (line), mean (circle) and interquartile range (IQR). n = 12. (B)(i) As in (A) but with suprathreshold PWM-TI stimulation. *** = $p < 0.0005$. (C) Boxplot showing the normalised threshold for AP generation for extracellular TI and PWM-TI. f_1 = 2000Hz, f_2 = 2010Hz for both stimulation conditions. Thresholds normalised to the threshold for AP generation when the cell is stimulated with a sinusoidal waveform at f_Δ (10Hz). Two tailed paired t-test, n.s = $p > 0.05$. Boxplots showing median (line), mean (circle) and interquartile range (IQR). n = 12. (D)(i) Mean membrane potential during extracellular stimulation with TI (grey) and PWM-TI (green) (f_1 = 2000Hz, f_2 = 2010Hz), showing subthreshold oscillation at f_Δ of 10Hz. Showing mean ± SEM. For each cell, the maximum current amplitude that was still subthreshold for both stimulation conditions was taken. Membrane potential traces are low pass filtered at 20Hz to remove stimulation artefact. n = 12. (ii) Boxplot showing the mean amplitude of subthreshold oscillations in (i), for extracellular TI and PWM-TI stimulation (f_1 = 2000Hz, f_2 = 2010Hz). Two tailed paired t-test, * = $p < 0.05$. Boxplots showing median (line), mean (circle) and interquartile range (IQR). n = 12.

5.4 Discussion

5.4.1 General discussion of results

PWM-TI neurostimulation using current waveforms composed of square pulses is a proposed alternative to TI, which is traditionally achieved through the application of currents with sinusoidal waveforms (Missey et al., 2021; Grossman et al., 2017). In some clinical settings, the available hardware for brain stimulation supports only the delivery of square waves, thus PWM-TI has been suggested as a viable alternative to TI to deliver DBS in these instances

(Missey et al., 2021). It has not previously been verified that this technique has the same electrophysiological effect as TI, or that it is capable of evoking neural activity at f_Δ. In this chapter I show that PWM-TI stimulation can stimulate neurons to fire at f_Δ with a similar strength to TI stimulation, and propose a mechanism by which PWM-TI exerts its effects.

Stimulation of biophysically realistic multi-compartment models of pyramidal neurons and mouse cortical neurons suggest that PWM-TI polarises neurons in a way that is capable of stimulating a neuron to fire APs at f_Δ.

Modelling indicates that in both PWM-TI and TI, the membrane potential is polarised at the kHz frequency. Interestingly, polarisation of the membrane potential in response to PWM-TI is amplitude modulated (as in TI) despite a lack of amplitude modulation in the applied waveform. Amplitude modulation of the membrane potential response to PWM-TI waveform occurs in multi-compartment pyramidal neuron models in the absence of ion channel conductance, suggesting that this process is underlain by the passive membrane components. In line with these results, a simple single compartment neuron model with only passive resistance and capacitance also demonstrates significant amplitude modulation of membrane potential. As described previously, the cell membrane passive components act as a low-pass filter, with filtering properties being determined by the time constant (τ). It is logical that pulse-width dependent filtering occurs by such a filter when the spectrum of a square waveform is considered. This is because the power spectrum of a square wave at a frequency f_1 has a peak at f_1 and decaying peaks at the odd harmonics (i.e. $3f_1$, $5f_1$ etc,). The harmonics are essential in creating the sharpness of the pulse. The peak at the f_1 is largest when the pulse has a duty cycle of 50%, when it is closest to a sine wave. Duty cycles that are larger or smaller than 50% have smaller amplitude/power at f_1 as more amplitude/power is at the higher harmonics, to represent the sharper transition (thus the shorter the pulse, the higher the frequencies needed to create it are). The RC properties of the neuron, create a low pass filter for the ionic current induced by the stimulation. The filter attenuates the amplitude at f_1 and its harmonics, however of course, the smaller the pulse-width, the greater the proportion of the signal power that is at higher frequencies. Thus more of the signal will be attenuated by the filter. Since duty cycles larger or smaller than 50% have more power at the higher harmonics they will be attenuated

more by the filter and if the square duty cycle changes periodically from 50%, after filtering, it will show maximum amplitude periodically when the duty cycle is 50%. A square wave will be outputted as a saw-tooth wave, with an amplitude that depends on the pulse-width. I saw that membrane potential polarisation in response to current pulses is dependent both on pulse-width of the resulting waveform and the time constant of the neuron in the simple neuron model, suggesting that amplitude modulation resulting from PWM-TI is due to filtering mediated by passive neuronal components.

With PWM-TI stimulation, there is no polarisation at f_Δ in purely subthreshold neural polarisation in this model. This is also the case with TI, despite evidence of nonlinear frequency conversion in subthreshold polarisation creating polarisation at f_Δ in mouse cortical neurons (see section 3.3.2). As the neuron interprets the PWM-TI waveform as an amplitude modulated signal, one can assume that in the model, any suprathreshold stimulation at f_Δ via PWM-TI and TI is purely by linear summation of the two applied fields (see section 3.1.1). Conversely in an *ex vivo* preparation, PWM-TI is able to exert both subthreshold and suprathreshold stimulation of mouse neurons at f_Δ. This evidence is in the form of significant subthreshold polarisation at f_Δ and suggests that that the neuron is performing nonlinear frequency conversion of PWM currents similarly to TI currents (see section 3.1.1). Due to the amplitude modulation of the membrane potential, frequency conversion could be occurring via either multiplication or rectification (see section 3.1.1). These results suggest that sub- and suprathreshold PWM-TI induced stimulation can occur both via nonlinear frequency conversion of applied frequencies, but potentially also via linear summation of applied currents mediated by direct polarisation at the kHz frequencies. The exact contribution of these mechanisms is yet to be fully characterised.

If the neuron is being activated by the purely linear summation of the two applied currents, as in the model, it is to be expected that neuronal activation has a dependency on the applied frequency. This is what is seen in the model, with threshold for PWM-TI AP firing increasing as applied frequency increases for both PWM-TI and TI. This is due to the neuron being solely polarised at the kHz frequency, and as the neuron acts as a low pass filter, amplitude of polarisation decreases as frequency increases. This is evident in the dependency of subthreshold

amplitude polarisation on applied frequency which is also observed.

The magnitude of PWM-TI-evoked polarisation is comparable to polarisation evoked by TI stimulation. The neuron model suggests that the threshold for neuronal activation with PWM-TI trends towards being lower than with TI although this result is not significant. A similar story emerges with the amplitude of subthreshold polarisation at the kHz frequency, with PWM-TI showing a non-significant increase in amplitude of polarisation compared to TI. In the *ex-vivo* preparation, there is no significant difference in threshold for evoking APs, suggesting that future application of PWM-TI will require similar electric field strengths to TI. Interestingly, in mouse cortical neurons, subthreshold polarisation at f_Δ evoked by PWM-TI is significantly larger than that evoked by TI. This indicates that PWM-TI is stronger in the subthreshold domain, and may require less current to exert similar effects to TI in clinical applications. It also suggests that the nonlinear frequency conversion is stronger with PWM-TI. The mechanism behind this increased strength remains unclear although, it is interesting to note that the simple multiplication of two biphasic square waveforms with different frequencies results in a signal at f_Δ that is 50% larger than the resulting signal at f_Δ if the two multiplied signals are sinusoidal. Hence, this result could be further evidence of a FM phenomenon occurring.

5.4.2 Limitations

As implied previously (see section 5.4.1), the pyramidal neuron model utilised in this chapter does not encapsulate sufficient nonlinearity to exhibit nonlinear frequency conversion in the subthreshold domain. The model also suggests that the neuronal membrane is capable of polarising at kHz frequencies, something which has not been fully investigated in previous studies of TI stimulation (Grossman et al., 2017). However, it seems that indeed polarisation at this frequency is minute due to low-pass filtering by the neuron, and this is illustrated in the large current amplitude required to evoke APs in the model compared to physiological neurons ($\sim$ five-fold greater than stimulation with low frequency compared to $\sim$ two-fold). Thus, it is possible that the effect of PWM-TI stimulation on the neuron is mediated by a combination of linear summation and nonlinear frequency conversion, however disentangling the contribution

of each of these is difficult as modelling only exhibits polarisation via linear summation and direct polarisation via linear summation in the neuron recorded via patch-clamp is confounded by artefact. This requires further investigation. Nonetheless, comparison of the two stimulation techniques, relative thresholds, and investigation into filtering by the membrane as recorded from a neuronal model, as well as evidence of nonlinear frequency conversion in the neuron is valid.

Investigation into the conversion of the PWM-TI current to an amplitude modulated membrane potential was performed solely in the neuron model. This is due to challenges relating to the whole cell patch-clamp technique alluded to in the previous paragraph. When extracellular current stimulation is applied during recording of membrane voltage, a stimulation artefact at the applied frequencies is created (see section 2.3.3). Thus, visual inspection of the membrane potential at the applied frequencies is not possible and hence any production of an amplitude modulated membrane potential is not detectable. Alternatively, current can be injected into the neuron. This removes the artefact and reveals only polarisation of the neuronal membrane, however the recording pipette in the setup has a parasitic capacitance which must be charged in order for a change in membrane voltage to be recorded. When this capacitance is combined with the pipette resistance, a low-pass filter is formed and rapid voltage changes occurring at the cell membrane, such as those when the pulse-width of our current is very small, are unable to be recorded at the amplifier without attenuation. Thus whilst an amplitude modulation of the membrane potential is recorded in this configuration, there is no way to determine whether this is due to filtering of the applied current being done by the neuronal membrane or filtering of the recorded signal being performed by the pipette resistance and capacitance. Consequently, modelling of these configurations was implemented to investigate this question.

5.4.3 Future directions

The results outlined in this chapter suggest that PWM-TI is comparable to TI at the level of the single neuron. This is an important first step in the validation of the approach however when it comes to applications of brain stimulation techniques, modulation of network activity

is pivotal for efficacy and clinically relevant alteration of behaviour (see section 1.1.5). Thus, future work regarding PWM-TI should investigate the efficacy of PWM-TI in entrainment of neural activity at the network level, and the relative strength of this with regards to existing techniques.

Related to this is the question of focality. Network level studies of PWM-TI should investigate focality of evoked neural activity at f_Δ and contrast this to TI and other currently used techniques for brain stimulation. This is important for behavioural consequences of applied brain stimulation (see section 1.1.5). In the experiments outlined in this chapter, PWM-TI current was applied via one pair of electrodes and emulated the field in the region of overlap of the two applied fields of different frequency required for DBS via temporally interfering fields. An important validation for the focality of this technique is that one of these electric fields, which is composed of a single kHz frequency, does not modulate neural activity (for example through entrainment or other increases/decreases in excitability). Modelling results suggest that direct polarisation at kHz frequencies occurs but amplitude is small, thus further investigation into this is warranted. This will be possible with network level measures of neuronal activity in conjunction with application of current through two electrode pairs, as well as further investigation into the single neuron response to the applied kHz electric fields which are not pulse-width modulated.

The finding that the passive neuronal membrane facilitates conversion of a constant amplitude PWM-TI waveform to an amplitude modulated membrane potential is novel and potentially of interest to neuroscience. Absolute validation that this is occurring in the neuron could potentially be achieved by reduction of the pipette capacitance in the whole cell patch clamp set up, such that the smallest pulse width in the waveform is not being filtered. This poses a technical challenge although could be achieved through increasing the distance between the conductive internal solution and external aCSF (for example by coating the pipette in sylgard) or decreasing the area of the pipette capacitance (for example by reducing bath height). Investigation into whether the neuron a) still interprets PWM-TI stimulation as an amplitude modulated waveform and b) still performs nonlinear frequency conversion in the subthreshold domain whilst being subjected to pharmacological synaptic and voltage-gated ion channel

blockade, would support the finding that the effects of PWM-TI are underlain by the passive membrane. Additionally, whether the differential filtering of current pulses with varying widths can be exploited in other novel strategies for non-invasive brain stimulation is an interesting question.

If indeed, the effects of PWM-TI are partially mediated by direct polarisation at the applied kHz frequencies and thus by linear summation of the applied fields, the filtering properties of neurons will determine the magnitude of PWM-TI induced stimulation. For example, the amplitude of the amplitude modulated subthreshold polarisation, or the degree of envelope modulation could vary. Filtering cut off frequency is inversely proportional to the specific membrane resistance and capacitance (see section 1.2.1), the former being determined by ion channel conductance and is thus dependent on the number, and properties, of ion channels in the neuronal membrane. Thus, one could hypothesise that different neuron types, may deferentially filter and hence respond to PWM-TI currents. Future work could aim to investigate potential cell-type specificity of the technique.

5.4.4 Conclusions

PWM-TI is proposed as an effective alternative to TI. Suprathreshold stimulation of neurons at f_Δ with PWM-TI can be achieved with similar currents/electric field strengths to TI. Additionally, the strength of subthreshold stimulation appears to be greater.

Modelling results suggest that neurons polarise at frequencies matching the applied kHz frequencies; however, they interpret the PWM-TI current waveform as an amplitude modulated signal due to RC filtering by passive neuronal membrane components. This creates suprathreshold stimulation of the neuron at f_Δ via linear summation of the applied fields. *Ex vivo* experiments recording from mouse neurons suggest that nonlinear frequency conversion of the applied signals creates subthreshold polarisation of the neuron at f_Δ, via multiplication of the applied frequencies, or alternatively rectification of the amplitude modulated signal.

In conclusion, PWM-TI is a novel neuromodulatory technique, that may be used as an al-

ternative to TI to achieve non-invasive deep brain stimulation, although future work should investigate focality and cell-type specificity before clinical application is attempted.

Chapter 6

General Discussion

6.1 Overview of experimental chapters

6.1.1 Chapter 3

In the first experimental chapter, I showed that nonlinear frequency conversion of input signals with different frequencies, can be performed by the single neuron. This results in subthreshold neural polarisation at the difference frequency of the two applied signals. This evoked nonlinear frequency conversion occurs when applied signals are in the kHz range, i.e. the frequencies of signals utilised in Temporal Interference (TI) stimulation, but also when applied signals are in the frequency range of endogenous neural activity, i.e. < 100Hz. I showed the first evidence that neural frequency conversion is occurring during TI stimulation, and that it is involved in TI-induced neural polarisation. I found that evoked neural frequency conversion can still occur in the absence of the neural network and that the strength of neural frequency conversion is reduced when voltage-gated ion channels are blocked. These results suggest that the phenomenon has a cell membrane origin, and that the nonlinearity of voltage-gated conductance contributes may contribute to the strength of the process.

Additionally, I characterised the parameter space of evoked neural frequency conversion/TI-induced neural activity, and found that the strength of neural frequency conversion/stimulation

decreases as the applied frequency increases to the kHz range. The fact that the phenomenon occurs at applied frequencies close to the difference frequency at all, suggests that the nonlinear frequency conversion occurring at the single neuron cannot be via rectification. Thus, this nonlinear process is concluded to be Frequency Mixing (FM). The difference in frequency between the two applied signals has no effect on the strength of stimulation, when this frequency is within the bounds of endogenous neural activity.

Lastly, as FM is occurring during TI stimulation, I conducted an investigation into whether this nonlinear process is the driving force of TI. I found that strength of TI stimulation is dependent on the sum of the applied electric fields, suggesting that strength of FM is not the main determining factor in the strength of stimulation.

6.1.2 Chapter 4

In this chapter, I investigated whether higher order nonlinear interactions such as FM, occur in spontaneous neural activity.

I found that endogenous FM can be detected in neural activity recorded at the single neuron as well as in wide-scale recordings of human cortical activity.

Strength and amount of endogenous FM recorded in single neuron activity is reduced by blockade of neural inputs and voltage-gated ion channels. This suggests that the neural network, and the nonlinearity conferred by voltage-gated conductance, contribute to the phenomenon of FM in spontaneous neural activity.

I showed the first evidence of FM in spontaneous human neural activity, and conducted a preliminary characterisation of the frequencies and brain regions involved. Additionally, I established that endogenous FM differs in the neural activity of healthy participants, and TBI patients who show deficits in working memory and sustained attention.

The work contained within this chapter verified a novel methodology for detecting FM in noisy neural signals, developed by my colleague.

6.1.3 Chapter 5

In the final experimental chapter, I investigated a novel technique for non-invasive deep brain stimulation called Pulse-Width Modulated-Temporal Interference (PWM-TI) stimulation.

I showed the first direct evidence that PWM-TI can stimulate single neurons at the difference frequency of the two applied fields. Additionally, I demonstrated that this technique is as effective as (stimulates neurons with comparable strength to), traditional TI stimulation. I showed that nonlinear frequency conversion is occurring during PWM-TI, as with TI, as evidenced by subthreshold neural polarisation at the difference frequency.

Computational modelling suggests that the constant amplitude PWM-TI electric field, is interpreted as an amplitude modulated electric field by the neuronal membrane. I showed that this conversion appears to mediated by the low-pass filtering properties of the passive neuronal membrane. Thus, I suggest that the mechanism of PWM-TI is likely similar to that of TI.

6.2 Implications

The implications of the work presented in this thesis, are potentially far reaching and can be split into three main categories.

Development of temporal interference stimulation

The development of TI stimulation is mainly focused on strategies to improve its focality, such that it can rival current Deep Brain Stimulation (DBS) techniques, and be adopted as a clinical intervention for disorders underlain by aberrant neural activity. The investigation into the mechanism and driving force of TI stimulation presented in this thesis will aid in this endeavour. The work presented in chapter 3, had the broad aim of furthering our understanding of how TI stimulation is able to stimulate neurons at the difference frequency. The discovery that nonlinear frequency conversion is occurring at the level of the single neuron when TI electric

fields are applied to the brain, confirms that subthreshold depolarisation at the difference frequency can be exerted. This is important, as Transcranial Alternating Current Stimulation (tACS) techniques in humans are typically thought to evoke subthreshold depolarisation. The finding that TI stimulation is dependent on the summed amplitude of the electric fields potentially has implications for the spatial spread of the the stimulation and may need to be taken into account when modelling of the spatial distribution of the stimulation is undertaken. The finding that TI strength is dependent on applied frequency, with strength decreasing as applied frequency increases, should be taken into consideration when studies using TI are designed, and new strategies for improving the technique are in development.

The results demonstrating the existence of a neural frequency conversion phenomenon may have implications for understanding how neurons integrate signals. The results suggest that a single neuron is able multiply input signals to create signals with new frequency components. The potential that this process is playing a role in the creation of neural signals with new frequency components, suggests that it should be investigated further.

Furthering understanding of nonlinear frequency interactions in brain activity

I showed that higher order frequency interactions, mediated by the FM process, are occurring in the human brain. How FM might contribute to the creation of signals with new frequencies in neural activity is currently unclear. However, if it is found to be the case, whether the process is involved in changing the frequency of brain activity is a very interesting question, that could have implications for understanding how the brain switches between states, for example wakefulness and sleep. Additionally, the FM discovered in human brain activity is characterised by a three-way phase relationship. As two-way relationships, i.e. coupling, are known to play important roles in functionally connected brain networks (Canolty and Knight, 2010), whether this is also the case for the higher order interaction, should be of interest to neuroscience.

Application of pulse-width modulated temporal interference stimulation

Chapter 5 validates a novel non-invasive deep brain stimulation technique called PWM-TI. The finding that this stimulation technique is a) effective at stimulating at the difference frequency, and b) effective at similar strengths to traditional TI stimulation, suggests that the technique should be adopted and used in experimental work that requires a non-invasive method to stimulate deep brain structures.

Additionally, the finding that the neuron deferentially filters current pulses of different pulse-widths, could potentially be exploited in future novel brain stimulation techniques.

6.3 Future directions

There are several broad ways in which the work presented in this thesis should be expanded on.

Firstly, the work characterising and investigating the mechanism of TI stimulation at the single neuron should be investigated at the network level. For example, when TI is applied to an intact brain using two pairs of electrodes. It should be determined whether the dependency of TI stimulation on the applied frequency, and the summed amplitude of the electric fields, can be observed at this level, as this is more applicable to clinical applications of the stimulation. Additionally, whether evoked neural frequency conversion originating at the single cell is detectable in wide-scale measures of neural activity during TI is important. These experiments would aid in validating the results presented in this thesis.

Secondly, the work presented showing FM in spontaneous neural activity, including in humans can be thought of as a proof of principle investigation. Whether FM plays a functional role in brain dynamics is a big question, but is worth further investigation. Additionally, investigation into whether alterations in FM causally effect behavioural outcomes, in both healthy and aberrant neural activity, is something that could be focused on in the future.

Lastly, the next stage of experiments investigating PWM-TI should focus on investigating the focality of this novel technique relative to TI and other currently used tACS strategies, to see whether it confers an advantage in this area. Whether the mechanism by which PWM-TI exerts its effects can be exploited to improve the technique, is a final interesting avenue for research.

Bibliography

A. S. Aberra, A. V. Peterchev, and W. M. Grill. Biophysically realistic neuron models for simulation of cortical stimulation. *Journal of neural engineering*, 15(6):066023, 2018.

E. Ahissar and D. Kleinfeld. Closed-loop Neuronal Computations: Focus on Vibrissa Somatosensation in Rat. *Cerebral Cortex*, 13(1):53–62, 01 2003. ISSN 1047-3211. doi: 10.1093/cercor/13.1.53. URL https://doi.org/10.1093/cercor/13.1.53.

K. F. Ahrens, H. Levine, H. Suhl, and D. Kleinfeld. Spectral mixing of rhythmic neuronal signals in sensory cortex. *Proceedings of the National Academy of Sciences*, 99(23):15176–15181, 2002. ISSN 0027-8424. doi: 10.1073/pnas.222547199. URL https://www.pnas.org/content/99/23/15176.

R. L. Albin, A. B. Young, and J. B. Penney. The functional anatomy of basal ganglia disorders. *Trends in Neurosciences*, 12(10):366–375, 1989. ISSN 0166-2236. doi: https://doi.org/10.1016/0166-2236(89)90074-X. URL https://www.sciencedirect.com/science/article/pii/016622368990074X.

O. Alvarez and R. Latorre. Voltage-dependent capacitance in lipid bilayers made from monolayers. *Biophysical Journal*, 21(1):1–17, 1978. ISSN 0006-3495. doi: https://doi.org/10.1016/S0006-3495(78)85505-2. URL https://www.sciencedirect.com/science/article/pii/S0006349578855052.

C. A. Anastassiou, R. Perin, H. Markram, and C. Koch. Ephaptic coupling of cortical neurons. *Nature neuroscience*, 14(2):217–223, 2011.

A. Antal, I. Alekseichuk, M. Bikson, J. Brockmöller, A. Brunoni, R. Chen, L. Cohen, G. Dowthwaite, J. Ellrich, A. Flöel, F. Fregni, M. George, R. Hamilton, J. Haueisen, C. Herrmann, F. Hummel, J. Lefaucheur, D. Liebetanz, C. Loo, C. McCaig, C. Miniussi, P. Miranda, V. Moliadze, M. Nitsche, R. Nowak, F. Padberg, A. Pascual-Leone, W. Poppendieck, A. Priori, S. Rossi, P. Rossini, J. Rothwell, M. Rueger, G. Ruffini, K. Schellhorn, H. Siebner, Y. Ugawa, A. Wexler, U. Ziemann, M. Hallett, and W. Paulus. Low intensity transcranial electric stimulation: Safety, ethical, legal regulatory and application guidelines. *Clinical Neurophysiology*, 128(9):1774–1809, 2017. ISSN 1388-2457. doi: https://doi.org/10.1016/j.clinph.2017.06.001. URL `https://www.sciencedirect.com/science/article/pii/S1388245717302122`.

M. Antonakakis, S. I. Dimitriadis, M. Zervakis, S. Micheloyannis, R. Rezaie, A. Babajani-Feremi, G. Zouridakis, and A. C. Papanicolaou. Altered cross-frequency coupling in resting-state meg after mild traumatic brain injury. *International Journal of Psychophysiology*, 102: 1–11, 2016.

C. M. Armstrong and B. Hille. Voltage-gated ion channels and electrical excitability. *Neuron*, 20(3):371–380, 1998.

N. Axmacher, M. M. Henseler, O. Jensen, I. Weinreich, C. E. Elger, and J. Fell. Cross-frequency coupling supports multi-item working memory in the human hippocampus. *Proceedings of the National Academy of Sciences*, 107(7):3228–3233, 2010. ISSN 0027-8424. doi: 10.1073/pnas.0911531107. URL `https://www.pnas.org/content/107/7/3228`.

M. J. Begemann, B. A. Brand, B. Ćurčić Blake, A. Aleman, and I. E. Sommer. Efficacy of non-invasive brain stimulation on cognitive functioning in brain disorders: a meta-analysis. *Psychological Medicine*, 50(15):2465–2486, 2020. doi: 10.1017/S0033291720003670.

I. Beheshti and J. H. Ko. Modulating brain networks associated with cognitive deficits in parkinson's disease. *Molecular Medicine*, 27(1):24, Mar 2021. ISSN 1528-3658. doi: 10.1186/s10020-021-00284-5. URL `https://doi.org/10.1186/s10020-021-00284-5`.

M. A. Belluscio, K. Mizuseki, R. Schmidt, R. Kempter, and G. Buzsáki. Cross-frequency phase–phase coupling between theta and gamma oscillations in the hippocampus. *Journal*

of Neuroscience, 32(2):423–435, 2012. ISSN 0270-6474. doi: 10.1523/JNEUROSCI.4122-11.2012. URL https://www.jneurosci.org/content/32/2/423.

A. Benazzouz, C. Gross, J. Féger, T. Boraud, and B. H. Bioulac. Reversal of rigidity and improvement in motor performance by subthalamic high-frequency stimulation in mptp-treated monkeys. *European Journal of Neuroscience*, 5, 1993.

A. Benussi, V. Cantoni, M. S. Cotelli, M. Cotelli, C. Brattini, A. Datta, C. Thomas, E. Santarnecchi, A. Pascual-Leone, and B. Borroni. Exposure to gamma tacs in alzheimer's disease: A randomized, double-blind, sham-controlled, crossover, pilot study. *Brain Stimulation*, 14 (3):531–540, 2021. ISSN 1935-861X. doi: https://doi.org/10.1016/j.brs.2021.03.007. URL https://www.sciencedirect.com/science/article/pii/S1935861X21000589.

M. E. Berryhill and D. Martin. Cognitive effects of transcranial direct current stimulation in healthy and clinical populations: An overview. *The Journal of ECT*, 34(3), 2018. ISSN 1095-0680. URL https://journals.lww.com/ectjournal/Fulltext/2018/09000/Cognitive_Effects_of_Transcranial_Direct_Current.10.aspx.

M. Bikson, A. Datta, A. Rahman, and J. Scaturro. Electrode montages for tdcs and weak transcranial electrical stimulation: role of "return" electrode's position and size. *Clinical neurophysiology : official journal of the International Federation of Clinical Neurophysiology*, 121(12):1976–1978, Dec 2010. ISSN 1872-8952. doi: 10.1016/j.clinph.2010.05.020. URL https://pubmed.ncbi.nlm.nih.gov/21035740. 21035740[pmid].

F. Bove, D. Mulas, F. Cavallieri, A. Castrioto, S. Chabardès, S. Meoni, E. Schmitt, A. Bichon, E. Di Stasio, A. Kistner, P. Pélissier, E. Chevrier, E. Seigneuret, P. Krack, V. Fraix, and E. Moro. Long-term outcomes (15 years) after subthalamic nucleus deep brain stimulation in patients with parkinson disease. *Neurology*, 97(3):e254–e262, 2021. ISSN 0028-3878. doi: 10.1212/WNL.0000000000012246. URL https://n.neurology.org/content/97/3/e254.

G. Breed. The mathematics of mixers: basic principles. *URL http://www. highfrequencyelectronics. com/Jan11/HFE0111 {_} Tutorial. pdf*, 2011.

G. Buzsaki. *Rhythms of the Brain*. Oxford university press, 2006.

G. Buzsáki and A. Draguhn. Neuronal oscillations in cortical networks. *science*, 304(5679): 1926–1929, 2004.

G. Buzsáki, L. Lai-Wo S., and C. H. Vanderwolf. Cellular bases of hippocampal eeg in the behaving rat. *Brain Research Reviews*, 6(2):139–171, 1983. ISSN 0165-0173. doi: https://doi.org/10.1016/0165-0173(83)90037-1. URL https://www.sciencedirect.com/science/article/pii/0165017383900371.

G. Buzsáki, N. Logothetis, and W. Singer. Scaling brain size, keeping timing: Evolutionary preservation of brain rhythms. *Neuron*, 80(3):751–764, 2013. ISSN 0896-6273. doi: https://doi.org/10.1016/j.neuron.2013.10.002. URL https://www.sciencedirect.com/science/article/pii/S0896627313009045.

R. T. Canolty and R. T. Knight. The functional role of cross-frequency coupling. *Trends in Cognitive Sciences*, 14(11):506–515, 2010. ISSN 1364-6613. doi: https://doi.org/10.1016/j.tics.2010.09.001. URL https://www.sciencedirect.com/science/article/pii/S1364661310002068.

N. T. Carnevale and M. L. Hines. *The NEURON book*. Cambridge University Press, 2006.

A. Chaturvedi, C. Butson, S. Lempka, S. Cooper, and C. Mcintyre. Patient-specific models of deep brain stimulation: Influence of field model complexity on neural activation predictions. *Brain stimulation*, 3:65–7, 04 2010. doi: 10.1016/j.brs.2010.01.003.

Z. Cheng and G. Liu. *Chapter 4. Amplitude modulation, demodulation and frequency mixing*, pages 145–190. De Gruyter, 2020. doi: doi:10.1515/9783110593822-004. URL https://doi.org/10.1515/9783110593822-004.

S. Chiken and A. Nambu. Mechanism of deep brain stimulation: Inhibition, excitation, or disruption? *The Neuroscientist*, 22(3):313–322, 2016. doi: 10.1177/1073858415581986. URL https://doi.org/10.1177/1073858415581986. PMID: 25888630.

M. X. Cohen. *Analyzing neural time series data : theory and practice*. Issues in clinical and cognitive neuropsychology. The MIT Press, Cambridge, Massachusetts, 2014. ISBN 0-262-31955-1.

C. M. Colbert and E. Pan. Ion channel properties underlying axonal action potential initiation in pyramidal neurons. *Nature neuroscience*, 5(6):533–538, 2002.

A. Datta, V. Bansal, J. Diaz, J. Patel, D. Reato, and M. Bikson. Gyri-precise head model of transcranial direct current stimulation: improved spatial focality using a ring electrode versus conventional rectangular pad. *Brain stimulation*, 2(4):201–207.e1, Oct 2009. ISSN 1876-4754. doi: 10.1016/j.brs.2009.03.005. URL https://pubmed.ncbi.nlm.nih.gov/20648973. 20648973[pmid].

R. Davidson and E. Flachaire. The wild bootstrap, tamed at last. *Journal of Econometrics*, 146(1):162–169, 2008.

S. De Simoni, P. O. Jenkins, N. J. Bourke, J. J. Fleminger, P. J. Hellyer, A. E. Jolly, M. C. Patel, J. H. Cole, R. Leech, and D. J. Sharp. Altered caudate connectivity is associated with executive dysfunction after traumatic brain injury. *Brain*, 141(1):148–164, 2018.

J. K. Deans, A. D. Powell, and J. G. R. Jefferys. Sensitivity of coherent oscillations in rat hippocampus to ac electric fields. *The Journal of physiology*, 583(Pt 2):555–565, Sep 2007. ISSN 0022-3751. doi: 10.1113/jphysiol.2007.137711. URL https://pubmed.ncbi.nlm.nih.gov/17599962. 17599962[pmid].

B. Degos, J.-M. Deniau, M. Chavez, and N. Maurice. Subthalamic nucleus high-frequency stimulation restores altered electrophysiological properties of cortical neurons in parkinsonian rat. *PLOS ONE*, 8(12):1–15, 12 2014. doi: 10.1371/journal.pone.0083608. URL https://doi.org/10.1371/journal.pone.0083608.

D. Desmaisons, J.-D. Vincent, and P.-M. Lledo. Control of action potential timing by intrinsic subthreshold oscillations in olfactory bulb output neurons. *Journal of Neuroscience*, 19(24): 10727–10737, 1999. ISSN 0270-6474. doi: 10.1523/JNEUROSCI.19-24-10727.1999. URL https://www.jneurosci.org/content/19/24/10727.

J. P. Dmochowski, A. Datta, M. Bikson, Y. Su, and L. C. Parra. Optimized multi-electrode stimulation increases focality and intensity at target. 8(4):046011, jun 2011. doi: 10.1088/1741-2560/8/4/046011. URL https://doi.org/10.1088/1741-2560/8/4/046011.

D. Edwards, M. Cortes, A. Datta, P. Minhas, E. M. Wassermann, and M. Bikson. Physiological and modeling evidence for focal transcranial electrical brain stimulation in humans: A basis for high-definition tdcs. *NeuroImage*, 74:266–275, 2013. ISSN 1053-8119. doi: https://doi.org/10.1016/j.neuroimage.2013.01.042. URL https://www.sciencedirect.com/science/article/pii/S105381191300089X.

Z. Esmaeilpour, G. Kronberg, D. Reato, L. C. Parra, and M. Bikson. Temporal interference stimulation targets deep brain regions by modulating neural oscillations. *Brain Stimulation*, 14(1):55–65, 2021.

B. Farrell, C. Do Shope, and W. E. Brownell. Voltage-dependent capacitance of human embryonic kidney cells. *Phys. Rev. E*, 73:041930, Apr 2006. doi: 10.1103/PhysRevE.73.041930. URL https://link.aps.org/doi/10.1103/PhysRevE.73.041930.

J. T. Francis, B. J. Gluckman, and S. J. Schiff. Sensitivity of neurons to weak electric fields. *Journal of Neuroscience*, 23(19):7255–7261, 2003. ISSN 0270-6474. doi: 10.1523/JNEUROSCI.23-19-07255.2003. URL https://www.jneurosci.org/content/23/19/7255.

K. J. Friston. Functional and effective connectivity: A review. *Brain Connectivity*, 1(1):13–36, 2011. doi: 10.1089/brain.2011.0008. URL https://doi.org/10.1089/brain.2011.0008. PMID: 22432952.

C. Gabriel, S. Gabriel, and y. E. Corthout. The dielectric properties of biological tissues: I. literature survey. *Physics in medicine & biology*, 41(11):2231, 1996.

L. M. Giocomo, E. A. Zilli, E. Fransén, and M. E. Hasselmo. Temporal frequency of subthreshold oscillations scales with entorhinal grid cell field spacing. *Science*, 315(5819):1719–1722, 2007. ISSN 0036-8075. doi: 10.1126/science.1139207. URL https://science.sciencemag.org/content/315/5819/1719.

G. C. Goats. Interferential current therapy. *British journal of sports medicine*, 24(2):87–92, Jun 1990. ISSN 0306-3674. doi: 10.1136/bjsm.24.2.87. URL https://pubmed.ncbi.nlm.nih.gov/1702337. 1702337[pmid].

C. González, D. Baez-Nieto, I. Valencia, I. Oyarzún, P. Rojas, D. Naranjo, and R. Latorre. K+ channels: function-structural overview. *Comprehensive physiology*, 2(3):2087–2149, 2012.

S. Grillner. Biological pattern generation: The cellular and computational logic of networks in motion. *Neuron*, 52(5):751–766, 2006. ISSN 0896-6273. doi: https://doi.org/10.1016/j.neuron.2006.11.008. URL https://www.sciencedirect.com/science/article/pii/S0896627306009020.

N. Grossman, D. Bono, N. Dedic, S. B. Kodandaramaiah, A. Rudenko, H.-J. Suk, A. M. Cassara, E. Neufeld, N. Kuster, L.-H. Tsai, A. Pascual-Leone, and E. S. Boyden. Noninvasive deep brain stimulation via temporally interfering electric fields. *Cell*, 169(6):1029–1041.e16, 2017. ISSN 0092-8674. doi: https://doi.org/10.1016/j.cell.2017.05.024. URL https://www.sciencedirect.com/science/article/pii/S0092867417305846.

N. Grossman, M. S. Okun, and E. S. Boyden. Translating Temporal Interference Brain Stimulation to Treat Neurological and Psychiatric Conditions. *JAMA Neurology*, 75(11): 1307–1308, 11 2018. ISSN 2168-6149. doi: 10.1001/jamaneurol.2018.2760. URL https://doi.org/10.1001/jamaneurol.2018.2760.

A. Hampshire, R. R. Highfield, B. L. Parkin, and A. M. Owen. Fractionating human intelligence. *Neuron*, 76(6):1225–1237, 2012.

C. Hardman, J. Henderson, D. Finkelstein, M. Horne, G. Paxinos, and G. Halliday. Comparison of the basal ganglia in rats, marmosets, macaques, baboons, and humans: Volume and neuronal number for the output, internal relay, and striatal modulating nuclei. *The Journal of comparative neurology*, 445:238–55, 04 2002. doi: 10.1002/cne.10165.

T. Hashimoto, C. M. Elder, M. S. Okun, S. K. Patrick, and J. L. Vitek. Stimulation of the subthalamic nucleus changes the firing pattern of pallidal neurons. *Journal of Neuroscience*, 23(5):1916–1923, 2003. ISSN 0270-6474. doi: 10.1523/JNEUROSCI.23-05-01916.2003. URL https://www.jneurosci.org/content/23/5/1916.

D. Haufler and D. Paré. Detection of multiway gamma coordination reveals how frequency mixing shapes neural dynamics. *Neuron*, 101(4):603–614.e6, 2019. ISSN 0896-6273. doi: https:

//doi.org/10.1016/j.neuron.2018.12.028. URL https://www.sciencedirect.com/science/article/pii/S0896627318311486.

T. Heimburg. The capacitance and electromechanical coupling of lipid membranes close to transitions: The effect of electrostriction. *Biophysical Journal*, 103(5):918–929, 2012. ISSN 0006-3495. doi: https://doi.org/10.1016/j.bpj.2012.07.010. URL https://www.sciencedirect.com/science/article/pii/S0006349512007825.

R. Helfrich, T. Schneider, S. Rach, S. Trautmann-Lengsfeld, A. Engel, and C. Herrmann. Entrainment of brain oscillations by transcranial alternating current stimulation. *Current Biology*, 24(3):333–339, 2014. ISSN 0960-9822. doi: https://doi.org/10.1016/j.cub.2013.12.041. URL https://www.sciencedirect.com/science/article/pii/S096098221301600X.

M. Hines, T. Carnevale, and R. A. McDougal. *NEURON Simulation Environment*, pages 1–7. Springer New York, New York, NY, 2019. ISBN 978-1-4614-7320-6. doi: 10.1007/978-1-4614-7320-6_795-2. URL https://doi.org/10.1007/978-1-4614-7320-6_795-2.

A. L. Hodgkin and A. F. Huxley. A quantitative description of membrane current and its application to conduction and excitation in nerve. *The Journal of Physiology*, 117(4):500–544, 1952. doi: https://doi.org/10.1113/jphysiol.1952.sp004764. URL https://physoc.onlinelibrary.wiley.com/doi/abs/10.1113/jphysiol.1952.sp004764.

J. C. Horvath, J. D. Forte, and O. Carter. Evidence that transcranial direct current stimulation (tdcs) generates little-to-no reliable neurophysiologic effect beyond mep amplitude modulation in healthy human subjects: A systematic review. *Neuropsychologia*, 66:213–236, 2015. ISSN 0028-3932. doi: https://doi.org/10.1016/j.neuropsychologia.2014.11.021. URL https://www.sciencedirect.com/science/article/pii/S0028393214004394.

G. Hsu, F. Farahani, and L. C. Parra. Cutaneous sensation of electrical stimulation waveforms. *Brain Stimulation*, 14(3):693–702, 2021. ISSN 1935-861X. doi: https://doi.org/10.1016/j.brs.2021.04.008. URL https://www.sciencedirect.com/science/article/pii/S1935861X21000784.

S. Huang, S. Hong, and E. De Schutter. Non-linear leak currents affect mammalian neuron physiology. *Frontiers in Cellular Neuroscience*, 9:432, 2015. ISSN 1662-5102. doi: 10.3389/fncel.2015.00432. URL https://www.frontiersin.org/article/10.3389/fncel.2015.00432.

Y. Huang and L. C. Parra. Can transcranial electric stimulation with multiple electrodes reach deep targets? *Brain Stimulation*, 12(1):30–40, 2019. ISSN 1935-861X. doi: https://doi.org/10.1016/j.brs.2018.09.010. URL https://www.sciencedirect.com/science/article/pii/S1935861X18303127.

Y. Huang, A. A. Liu, B. Lafon, D. Friedman, M. Dayan, X. Wang, M. Bikson, W. K. Doyle, O. Devinsky, and L. C. Parra. Measurements and models of electric fields in the *in vivo* human brain during transcranial electric stimulation. *eLife*, 6:e18834, feb 2017. ISSN 2050-084X. doi: 10.7554/eLife.18834. URL https://doi.org/10.7554/eLife.18834.

B. Hutcheon and Y. Yarom. Resonance, oscillation and the intrinsic frequency preferences of neurons. *Trends in Neurosciences*, 23(5):216–222, 2000. ISSN 0166-2236. doi: https://doi.org/10.1016/S0166-2236(00)01547-2. URL https://www.sciencedirect.com/science/article/pii/S0166223600015472.

A. F. Jackson and D. J. Bolger. The neurophysiological bases of eeg and eeg measurement: A review for the rest of us. *Psychophysiology*, 51(11):1061–1071, 2014.

T. J. Jentsch, M. Poët, J. C. Fuhrmann, and A. A. Zdebik. Physiological functions of clc clchannels gleaned from human genetic disease and mouse models. *Annual Review of Physiology*, 67(1):779–807, 2005. doi: 10.1146/annurev.physiol.67.032003.153245. URL https://doi.org/10.1146/annurev.physiol.67.032003.153245. PMID: 15709978.

F. H. Kasten, E. Negahbani, F. Fröhlich, and C. S. Herrmann. Non-linear transfer characteristics of stimulation and recording hardware account for spurious low-frequency artifacts during amplitude modulated transcranial alternating current stimulation (am-tacs). *Neuroimage*, 179:134–143, 2018.

D. Kleinfeld and S. B. Mehta. Spectral Mixing in Nervous Systems: Experimental Evidence and Biologically Plausible Circuits. *Progress of Theoretical Physics Supplement*, 161:86–98,

01 2006. ISSN 0375-9687. doi: 10.1143/PTPS.161.86. URL https://doi.org/10.1143/PTPS.161.86.

C. Koch. Computation and the single neuron. *Nature*, 385(6613):207–210, 1997.

C. Koch, M. Rapp, and I. Segev. A brief history of time (constants). *Cerebral cortex*, 6(2): 93–101, 1996.

S. Kohli and A. J. Casson. Removal of gross artifacts of transcranial alternating current stimulation in simultaneous eeg monitoring. *Sensors (Basel, Switzerland)*, 19(1):190, Jan 2019. ISSN 1424-8220. doi: 10.3390/s19010190. URL https://pubmed.ncbi.nlm.nih.gov/30621077.30621077[pmid].

S. Lee, F. Urbano, and E. Garcia-Rill. The critical role of intrinsic membrane oscillations. *Neurosignals*, 26:66 – 76, 2018.

D. B. Lindsley. Psychological phenomena and the electroencephalogram. *Electroencephalography and Clinical Neurophysiology*, 4(4):443–456, 1952. ISSN 0013-4694. doi: https://doi.org/10.1016/0013-4694(52)90075-8. URL https://www.sciencedirect.com/science/article/pii/0013469452900758.

A. Liu, M. Vöröslakos, G. Kronberg, S. Henin, M. Krause, Y. Huang, A. Opitz, A. Mehta, C. Pack, B. Krekelberg, A. Berényi, L. Parra, L. Melloni, O. Devinsky, and G. Buzsáki. Immediate neurophysiological effects of transcranial electrical stimulation. *Nature Communications*, 9, 12 2018. doi: 10.1038/s41467-018-07233-7.

R. R. Llinás, A. A. Grace, and Y. Yarom. In vitro neurons in mammalian cortical layer 4 exhibit intrinsic oscillatory activity in the 10- to 50-hz frequency range. *Proceedings of the National Academy of Sciences*, 88(3):897–901, 1991. ISSN 0027-8424. doi: 10.1073/pnas.88.3.897. URL https://www.pnas.org/content/88/3/897.

E. K. S. Louis, L. Frey, J. Britton, J. Hopp, P. Korb, M. Koubeissi, W. Lievens, and E. Pestana-Knight. Electroencephalography (eeg): An introductory text and atlas of normal and abnormal findings in adults. *Children, and Infants*, 2016.

A. M. Lozano, N. Lipsman, H. Bergman, P. Brown, S. Chabardes, J. W. Chang, K. Matthews, C. C. McIntyre, T. E. Schlaepfer, M. Schulder, Y. Temel, J. Volkmann, and J. K. Krauss. Deep brain stimulation: current challenges and future directions. *Nature Reviews Neurology*, 15(3):148–160, Mar 2019. ISSN 1759-4766. doi: 10.1038/s41582-018-0128-2. URL https://doi.org/10.1038/s41582-018-0128-2.

R. Ma, X. Xia, W. Zhang, Z. Lu, Q. Wu, J. Cui, H. Song, C. Fan, X. Chen, J. Wei, G. Ji, K. Wang, X. Wang, B. Qiu, and X. Zhang. High gamma and beta temporal interference stimulation in the human motor cortex improves motor functions. *bioRxiv*, 2021. doi: 10.1101/2021.03.26.437107. URL https://www.biorxiv.org/content/early/2021/04/13/2021.03.26.437107.

J. F. Malec, A. W. Brown, C. L. Leibson, J. T. Flaada, J. N. Mandrekar, N. N. Diehl, and P. K. Perkins. The mayo classification system for traumatic brain injury severity. *Journal of neurotrauma*, 24(9):1417–1424, 2007.

E.-J. Mallas, S. De Simoni, G. Scott, A. E. Jolly, A. Hampshire, L. M. Li, N. J. Bourke, S. A. Roberts, N. Gorgoraptis, and D. J. Sharp. Abnormal dorsal attention network activation in memory impairment after traumatic brain injury. *Brain*, 144(1):114–127, 2021a.

E.-J. Mallas, N. Gorgoraptis, S. Dautricourt, Y. Pertzov, G. Scott, and D. J. Sharp. Pathological slow-wave activity and impaired working memory binding in post-traumatic amnesia. *medRxiv*, 2021b.

E. McAdams, A. Lackermeier, J. McLaughlin, D. Macken, and J. Jossinet. The linear and nonlinear electrical properties of the electrode-electrolyte interface. *Biosensors and Bioelectronics*, 10(1):67–74, 1995. ISSN 0956-5663. doi: https://doi.org/10.1016/0956-5663(95)96795-Z. URL https://www.sciencedirect.com/science/article/pii/095656639596795Z.

G. C. McConnell, R. Q. So, J. D. Hilliard, P. Lopomo, and W. M. Grill. Effective deep brain stimulation suppresses low-frequency network oscillations in the basal ganglia by regularizing neural firing patterns. *The Journal of Neuroscience*, 32:15657 – 15668, 2012.

E. Mirzakhalili, B. Barra, M. Capogrosso, and S. F. Lempka. Biophysics of temporal interference stimulation. *Cell Systems*, 11(6):557–572.e5, 2020. ISSN 2405-4712. doi: https://doi.org/10.1016/j.cels.2020.10.004. URL https://www.sciencedirect.com/science/article/pii/S2405471220303720.

F. Missey, E. Rusina, E. Acerbo, B. Botzanowski, A. Trébuchon, F. Bartolomei, V. Jirsa, R. Carron, and A. Williamson. Orientation of temporal interference for non-invasive deep brain stimulation in epilepsy. *Frontiers in Neuroscience*, 15:656, 2021. ISSN 1662-453X. doi: 10.3389/fnins.2021.633988. URL https://www.frontiersin.org/article/10.3389/fnins.2021.633988.

L. D. Mosgaard, K. A. Zecchi, T. Heimburg, and R. Budvytyte. The effect of the nonlinearity of the response of lipid membranes to voltage perturbations on the interpretation of their electrical properties. a new theoretical description. *Membranes*, 5(4):495–512, 2015. ISSN 2077-0375. doi: 10.3390/membranes5040495. URL https://www.mdpi.com/2077-0375/5/4/495.

S. Mottaghi, O. Buchholz, and U. G. Hofmann. Systematic evaluation of dbs parameters in the hemi-parkinsonian rat model. *Frontiers in Neuroscience*, 14:1018, 2020. ISSN 1662-453X. doi: 10.3389/fnins.2020.561008. URL https://www.frontiersin.org/article/10.3389/fnins.2020.561008.

C. Munari, P. Kahane, L. Tassi, S. Francione, D. Hoffmann, G. L. Russo, and A. L. Benabid. Intracerebral low frequency electrical stimulation: a new tool for the definition of the "epileptogenic area"? In B. A. Meyerson, G. Broggi, J. Martin-Rodriguez, C. Ostertag, and M. Sindou, editors, *Advances in Stereotactic and Functional Neurosurgery 10*, pages 181–185, Vienna, 1993. Springer Vienna. ISBN 978-3-7091-9297-9.

A. Muralidharan, J. Zhang, D. Ghosh, M. Johnson, K. Baker, and J. Vitek. Modulation of neuronal activity in the motor thalamus during gpi-dbs in the mptp nonhuman primate model of parkinson's disease. *Brain Stimulation*, 10, 10 2016. doi: 10.1016/j.brs.2016.10.005.

B. Nadarajah, D. Thomaidou, W. H. Evans, and J. Parnavelas. Gap junctions in the adult

cerebral cortex: regional differences in their distribution and cellular expression of connexins. *Journal of Comparative Neurology*, 376(2):326–342, 1996.

E. Neher and B. Sakmann. Single-channel currents recorded from membrane of denervated frog muscle fibres. *Nature*, 260(5554):799–802, 1976.

A. B. Neiman and D. F. Russell. Two distinct types of noisy oscillators in electroreceptors of paddlefish. *Journal of neurophysiology*, 92(1):492–509, 2004.

Y. Nir, R. J. Staba, T. Andrillon, V. V. Vyazovskiy, C. Cirelli, I. Fried, and G. Tononi. Regional slow waves and spindles in human sleep. *Neuron*, 70(1):153–169, 2011.

M. A. Nitsche, L. G. Cohen, E. M. Wassermann, A. Priori, N. Lang, A. Antal, W. Paulus, F. Hummel, P. S. Boggio, F. Fregni, and A. Pascual-Leone. Transcranial direct current stimulation: State of the art 2008. *Brain Stimulation*, 1(3):206–223, 2008. ISSN 1935-861X. doi: https://doi.org/10.1016/j.brs.2008.06.004. URL `https://www.sciencedirect.com/science/article/pii/S1935861X08000405`.

N. Noury, J. Hipp, and M. Siegel. Physiological processes non-linearly affect electrophysiological recordings during transcranial electric stimulation. *NeuroImage*, 140, 04 2016. doi: 10.1016/j.neuroimage.2016.03.065.

J. O'Keefe and M. L. Recce. Phase relationship between hippocampal place units and the eeg theta rhythm. *Hippocampus*, 3(3):317–330, 1993. doi: https://doi.org/10.1002/hipo.450030307. URL `https://onlinelibrary.wiley.com/doi/abs/10.1002/hipo.450030307`.

A. Opitz, A. Falchier, C.-G. Yan, E. M. Yeagle, G. S. Linn, P. Megevand, A. Thielscher, R. Deborah A, M. P. Milham, A. D. Mehta, et al. Spatiotemporal structure of intracranial electric fields induced by transcranial electric stimulation in humans and nonhuman primates. *Scientific reports*, 6(1):1–11, 2016.

S. Ozen, A. Sirota, M. A. Belluscio, C. A. Anastassiou, E. Stark, C. Koch, and G. Buzsáki. Transcranial electric stimulation entrains cortical neuronal populations in rats. *Journal of Neu-*

roscience, 30(34):11476–11485, 2010. ISSN 0270-6474. doi: 10.1523/JNEUROSCI.5252-09.2010. URL https://www.jneurosci.org/content/30/34/11476.

J. S. Perlmutter and J. W. Mink. Deep brain stimulation. *Annual Review of Neuroscience*, 29 (1):229–257, 2006. doi: 10.1146/annurev.neuro.29.051605.112824. URL https://doi.org/10.1146/annurev.neuro.29.051605.112824. PMID: 16776585.

Y. Pertzov, M. Y. Dong, M.-C. Peich, and M. Husain. Forgetting what was where: The fragility of object-location binding. *PLoS One*, 7(10):e48214, 2012.

B. Pesaran, J. S. Pezaris, M. Sahani, P. P. Mitra, and R. A. Andersen. Temporal structure in neuronal activity during working memory in macaque parietal cortex. *Nature Neuroscience*, 5(8):805–811, Aug 2002. ISSN 1546-1726. doi: 10.1038/nn890. URL https://doi.org/10.1038/nn890.

C. H. Peters, A. Yu, W. Zhu, J. R. Silva, and P. C. Ruben. Depolarization of the conductance-voltage relationship in the nav1. 5 mutant, e1784k, is due to altered fast inactivation. *PLoS One*, 12(9):e0184605, 2017.

G. Popescu. Superposition principle. In *Principles of Biophotonics, Volume 1*, 2053-2563, pages 1–1 to 1–6. IOP Publishing, 2018. ISBN 978-0-7503-1641-5. doi: 10.1088/2053-2563/aae121ch1. URL https://dx.doi.org/10.1088/2053-2563/aae121ch1.

S. Rampersad, B. Roig-Solvas, M. Yarossi, P. P. Kulkarni, E. Santarnecchi, A. D. Dorval, and D. H. Brooks. Prospects for transcranial temporal interference stimulation in humans: A computational study. *NeuroImage*, 202:116124, 2019. ISSN 1053-8119. doi: https://doi.org/10.1016/j.neuroimage.2019.116124. URL https://www.sciencedirect.com/science/article/pii/S1053811919307153.

D. Reato, A. Rahman, M. Bikson, and L. C. Parra. Low-intensity electrical stimulation affects network dynamics by modulating population rate and spike timing. *Journal of Neuroscience*, 30(45):15067–15079, 2010. ISSN 0270-6474. doi: 10.1523/JNEUROSCI.2059-10.2010. URL https://www.jneurosci.org/content/30/45/15067.

D. Regan and M. P. Regan. Nonlinearity in human visual responses to two-dimensional patterns, and a limitation of fourier methods. *Vision Research*, 27(12):2181–2183, 1987. ISSN 0042-6989. doi: https://doi.org/10.1016/0042-6989(87)90132-5. URL https://www.sciencedirect.com/science/article/pii/0042698987901325.

D. Ren. Sodium leak channels in neuronal excitability and rhythmic behaviors. *Neuron*, 72(6): 899–911, 2011.

A. R. Rezai, B. H. Kopell, R. E. Gross, J. L. Vitek, A. D. Sharan, P. Limousin, and A.-L. Benabid. Deep brain stimulation for Parkinson's disease: surgical issues. *Movement Disorders*, 21 Suppl 14:S197–218, June 2006. doi: 10.1002/mds.20956. URL https://www.hal.inserm.fr/inserm-00390714.

P. K. Rubenstein. Three variable kernel independence testing with time series. Master's thesis, University College London, London, Sept. 2015.

P. K. Rubenstein, K. P. Chwialkowski, and A. Gretton. A kernel test for three-variable interactions with random processes. In *Proceedings of the Thirty-Second Conference on Uncertainty in Artificial Intelligence*, pages 637–646, 2016.

Y. Salimpour and W. S. Anderson. Cross-frequency coupling based neuromodulation for treating neurological disorders. *Frontiers in Neuroscience*, 13:125, 2019. ISSN 1662-453X. doi: 10.3389/fnins.2019.00125. URL https://www.frontiersin.org/article/10.3389/fnins.2019.00125.

G. B. Saturnino, H. R. Siebner, A. Thielscher, and K. H. Madsen. Accessibility of cortical regions to focal tes: Dependence on spatial position, safety, and practical constraints. *NeuroImage*, 203:116183, 2019. ISSN 1053-8119. doi: https://doi.org/10.1016/j.neuroimage.2019.116183. URL https://www.sciencedirect.com/science/article/pii/S1053811919307748.

R. Scheffer-Teixeira and A. B. Tort. On cross-frequency phase-phase coupling between theta and gamma oscillations in the hippocampus. *eLife*, 5:e20515, dec 2016. ISSN 2050-084X. doi: 10.7554/eLife.20515. URL https://doi.org/10.7554/eLife.20515.

S. Schneegans and P. M. Bays. New perspectives on binding in visual working memory. *British Journal of Psychology*, 110(2):207–244, 2019.

M. G. Shapiro, K. Homma, S. Villarreal, C.-P. Richter, and F. Bezanilla. Infrared light excites cells by changing their electrical capacitance. *Nature communications*, 3(1):1–11, 2012.

D. J. Sharp, C. F. Beckmann, R. Greenwood, K. M. Kinnunen, V. Bonnelle, X. De Boissezon, J. H. Powell, S. J. Counsell, M. C. Patel, and R. Leech. Default mode network functional and structural connectivity after traumatic brain injury. *Brain*, 134(8):2233–2247, 2011.

D. J. Sharp, G. Scott, and R. Leech. Network dysfunction after traumatic brain injury. *Nature Reviews Neurology*, 10(3):156–166, 2014.

F. Siebenhühner, S. H. Wang, G. Arnulfo, A. Lampinen, L. Nobili, J. M. Palva, and S. Palva. Genuine cross-frequency coupling networks in human resting-state electrophysiological recordings. *PLOS Biology*, 18(5):1–40, 05 2020. doi: 10.1371/journal.pbio.3000685. URL `https://doi.org/10.1371/journal.pbio.3000685`.

M. Stevens, S. Peigneur, and J. Tytgat. Neurotoxins and their binding areas on voltage-gated sodium channels. *Frontiers in Pharmacology*, 2, 2011. ISSN 1663-9812. doi: 10.3389/fphar.2011.00071. URL `https://www.frontiersin.org/article/10.3389/fphar.2011.00071`.

A. Taddese and B. P. Bean. Subthreshold sodium current from rapidly inactivating sodium channels drives spontaneous firing of tuberomammillary neurons. *Neuron*, 33(4):587–600, 2002.

C. A. Terzuolo and T. H. Bullock. Measurement of imposed voltage gradient adequate to modulate neuronal firing. *Proceedings of the National Academy of Sciences*, 42(9):687–694, 1956. ISSN 0027-8424. doi: 10.1073/pnas.42.9.687. URL `https://www.pnas.org/content/42/9/687`.

J. Teselink, K. K. Bawa, G. K. Koo, K. Sankhe, C. S. Liu, M. Rapoport, P. Oh, S. Marzolini, D. Gallagher, W. Swardfager, N. Herrmann, and K. L. Lanctôt. Efficacy of non-invasive brain stimulation on global cognition and neuropsychiatric symptoms in alzheimer's disease

and mild cognitive impairment: A meta-analysis and systematic review. *Ageing Research Reviews*, 72:101499, 2021. ISSN 1568-1637. doi: https://doi.org/10.1016/j.arr.2021.101499. URL https://www.sciencedirect.com/science/article/pii/S1568163721002464.

G. Thut, C. Miniussi, and J. Gross. The functional importance of rhythmic activity in the brain. *Current Biology*, 22(16):R658–R663, Aug 2012. ISSN 0960-9822. doi: 10.1016/j.cub.2012.06.061. URL https://doi.org/10.1016/j.cub.2012.06.061.

V. Tohidi and F. Nadim. Membrane resonance in bursting pacemaker neurons of an oscillatory network is correlated with network frequency. *Journal of Neuroscience*, 29(20): 6427–6435, 2009. ISSN 0270-6474. doi: 10.1523/JNEUROSCI.0545-09.2009. URL https://www.jneurosci.org/content/29/20/6427.

A. B. L. Tort, M. A. Kramer, C. Thorn, D. J. Gibson, Y. Kubota, A. M. Graybiel, and N. J. Kopell. Dynamic cross-frequency couplings of local field potential oscillations in rat striatum and hippocampus during performance of a t-maze task. *Proceedings of the National Academy of Sciences*, 105(51):20517–20522, 2008. ISSN 0027-8424. doi: 10.1073/pnas.0810524105. URL https://www.pnas.org/content/105/51/20517.

S. P. Vaidya and D. Johnston. Temporal synchrony and gamma-to-theta power conversion in the dendrites of ca1 pyramidal neurons. *Nature Neuroscience*, 16(12):1812–1820, Dec 2013. ISSN 1546-1726. doi: 10.1038/nn.3562. URL https://doi.org/10.1038/nn.3562.

M. Vinck, B. Lima, T. Womelsdorf, R. Oostenveld, W. Singer, S. Neuenschwander, and P. Fries. Gamma-phase shifting in awake monkey visual cortex. *Journal of Neuroscience*, 30(4):1250–1257, 2010. ISSN 0270-6474. doi: 10.1523/JNEUROSCI.1623-09.2010. URL https://www.jneurosci.org/content/30/4/1250.

M. Vöröslakos, Y. Takeuchi, K. Brinyiczki, T. Zombori, A. Oliva, A. Fernández-Ruiz, G. Kozák, Z. T. Kincses, B. Iványi, G. Buzsáki, and A. Berényi. Direct effects of transcranial electric stimulation on brain circuits in rats and humans. *Nature Communications*, 9(1):483, Feb 2018. ISSN 2041-1723. doi: 10.1038/s41467-018-02928-3. URL https://doi.org/10.1038/s41467-018-02928-3.

T. Wichmann and M. Delong. Basal ganglia discharge abnormalities in parkinson's disease. *Journal of neural transmission. Supplementum*, 70:21–5, 02 2006.

M. Wischnewski, D. J. Schutter, and M. A. Nitsche. Effects of beta-tacs on corticospinal excitability: A meta-analysis. *Brain Stimulation*, 12(6):1381–1389, 2019. ISSN 1935-861X. doi: https://doi.org/10.1016/j.brs.2019.07.023. URL https://www.sciencedirect.com/science/article/pii/S1935861X19303079.

D. Yang, Y.-I. Shin, and K.-S. Hong. Systemic review on transcranial electrical stimulation parameters and eeg/fnirs features for brain diseases. *Frontiers in Neuroscience*, 15:274, 2021. ISSN 1662-453X. doi: 10.3389/fnins.2021.629323. URL https://www.frontiersin.org/article/10.3389/fnins.2021.629323.

H. Ye and A. Steiger. Neuron matters: electric activation of neuronal tissue is dependent on the interaction between the neuron and the electric field. *Journal of neuroengineering and rehabilitation*, 12(1):1–9, 2015.

S. Zaghi, M. Acar, B. Hultgren, P. S. Boggio, and F. Fregni. Noninvasive brain stimulation with low-intensity electrical currents: Putative mechanisms of action for direct and alternating current stimulation. *The Neuroscientist*, 16(3):285–307, 2010. doi: 10.1177/1073858409336227. URL https://doi.org/10.1177/1073858409336227. PMID: 20040569.